The Dissertation Committee for John W. McClintic certifies that this is the approved version of the following dissertation:

Diffused-Exit Film Cooling Holes Fed by an Internal Crossflow

Committee:

David G. Bogard, Supervisor

Robert D. Moser

Noel T. Clemens

Vaibhav Bahadur

Thomas E. Dyson

Frederick T. Davidson

Diffused-Exit Film Cooling Holes Fed by an Internal Crossflow

by

John W. McClintic, B.S.M.E., M.S.E.

Dissertation

Presented to the Faculty of the Graduate School of

The University of Texas at Austin

in Partial Fulfillment

of the Requirements

for the Degree of

Doctor of Philosophy

The University of Texas at Austin

May, 2017

Dedication

solo sapienti Deo per Iesum Christum cui honor in saecula saeculorum amen

Acknowledgements

This work would not have been possible without the contribution of a great number of people who lent their guidance, expertise, and encouragement to me throughout the process. I would first like to thank my advisor, David Bogard for his support and guidance throughout the nearly six years that I worked with him. I do not think I could have asked for a better advisor – he is incredibly knowledgeable and insightful and has been an excellent teacher. He was incredibly patient with all of my many questions and concerns and knew how to encourage me to do good work. I am also appreciative of the trust he placed in me to do my work well and the confidence I have developed in my abilities under his leadership.

I would also like to thank all the people who I have worked with in my laboratory over these past years. Much of my thanks and appreciation goes to my fellow Ph.D. candidate and good friend Josh Anderson. Many of the experimental facilities and techniques presented in the paper worked as well as they did due to his brilliant work in developing and improving them, especially the cooling loop for the wind tunnel, the automatic traversing program for the thermal field measurements, and the method used to measure heat transfer coefficients. I would also like to thank Tom Dyson, who taught me how to do research in the lab when I was a new master's student and I had little to no idea what I was doing. I am also appreciative of his continued support of my research as an industry contact in his current position with GE Global Research and for serving on my dissertation committee. I would also like to thank Todd Davidson (who is also serving on my committee) and Emily Boyd who also helped me learn to become a better researcher. The crossflow channel used in this study was designed and assembled by Sean Klavetter

and James Winka. The conduction correction technique used in this study would not have been developed without the help of Kyle Chavez, who showed me Comsol and taught me how to use it. I would also like to thank Ellen Wilkes who collaborated with me on a number of projects and performed a study that laid much of the groundwork for the current work. I am also grateful to Dale Fox and Fraser Jones who assisted me with the velocity field measurements performed for this study. And I would be remiss to mention everyone else who helped me with a great number of things not listed here, and more importantly, made my time in the lab more enjoyable, and most importantly, celebrated the weekly holiday of Taco Tuesday (on Wednesday) with me: Dave Kistenmacher, Marc Nathan, Gavin Packard, Noah Mosberg, Robbie Stewart, Adam Vaclavik, Jabob Moore, Owen O'Neil, and Christopher Yoon.

Finally, I would like to thank my wonderful family who have been incredibly supportive and encouraging throughout this process, and my beautiful, intelligent, and caring fiancé Rebecca, who has been a wonderful blessing to me these past few years. Also, to all my friends in Austin who have made life outside of grad school (if indeed such a thing exists) incredibly enjoyable, thank you.

Diffused-Exit Film Cooling Holes Fed by an Internal Crossflow

John W. McClintic, Ph.D.

The University of Texas at Austin, 2017

Supervisor: David G. Bogard

Film cooling is an essential technology to the operation of modern gas turbine engines, allowing for greater efficiency and part durability. Due to film cooling's complexity, laboratory studies of film cooling isolate various effects by intentionally simplifying or neglecting various aspects of the film cooling problem. One such aspect that had been consistently neglected by film cooling studies is how the internal flow within the turbine blade affects film cooling performance. Studies have found that feeding the holes with an internal crossflow, directed perpendicular to the mainstream flow, can cause up to a 50% reduction in film cooling effectiveness. This result is of concern because internal crossflow is a common internal flow condition in gas turbine engines. However, none of the former studies have made a concerted effort to examine the important scaling parameters governing this effect. Nor have they provided experimental evidence showing the cause of this reduction in effectiveness due to internal crossflow.

In this study, a wide range of flow conditions was studied for two common film cooling hole geometry types: axial and compound angle diffused-exit film cooling holes. Internal crossflow-to-mainstream velocity ratios of VR_c = 0.2-0.6 were tested along with jet-to-mainstream velocity ratios of VR = 0.2-1.7. Film cooling effectiveness and discharge coefficients were measured for this full range of flow conditions for both geometries in

order to produce a sufficiently large data set to observe important trends in the data. It was found that the discharge coefficients, centerline effectiveness, and centerline location all scaled with the crossflow-to-jet velocity ratio, VR_i for the axial holes. Temperature and velocity fields showed that VR_i also scaled the in-hole temperature and velocity fields. A swirling flow within the hole was shown to cause ingestion of mainstream into the diffused exit of the hole and biasing of the issuing jet in the outlet diffuser, which reduced film cooling effectiveness. The direction of bias at the exit resulted from the direction of the internal crossflow and was critical for compound angle holes. Crossflow directed counter to the lateral direction of coolant injection caused improved film cooling effectiveness relative to the in-line crossflow direction.

Table of Contents

List of Tables

List of Figures

Nomenclature

Symbols:

A	area
AR	area ratio between diffused hole exit and cylindrical inlet
Bi	Biot number
C	airfoil chord length
C_d	discharge coefficient
d	diameter
d_H	hydraulic diameter
DR	coolant-to-mainstream density ratio
f	focal length, Darcy friction factor used in Gnielinski's correlation
h	heat transfer coefficient
H	turbine blade span, height of channel, boundary layer shape factor
$h_{f,norm}$	normalized heat transfer coefficient
I	coolant-to-mainstream momentum flux ratio
k	thermal conductivity
L	film cooling hole length
L_m	length of metering (cylindrical) section of shaped film cooling hole
$\dot{m}$	mass flow rate
M	blowing ratio
Ma	Mach number
Nu	Nusselt number
p	pressure, film cooling hole pitch
P	perimeter

Pr	Prandtl number
PR	pressure ratio
q''	heat flux
R	ideal gas constant
Re	Reynolds number
r_x	extraction ratio
s	equivalent slot width, airfoil surface streamwise coordinate
S	jet profile skew
t	time, wall thickness
T	temperature
Tu	turbulence intensity
U	mean velocity
v'	fluctuating velocity in the y^*-direction
VR	jet-to-mainstream velocity ratio
VR_c	crossflow-to-mainstream velocity ratio
VR_i	inlet velocity ratio (crossflow-to-jet velocity ratio)
w'	fluctuating velocity in the z-direction
W	jet profile width
x	streamwise coordinate
y	wall-normal coordinate
y^*	modified y coordinate in velocity field plane
z	spanwise coordinate

Greek:

α	injection angle
β	lateral diffusion angle, ratio of orifice throat to pipe diameters
γ	forward expansion angle, ratio of specific heats
δ	uncertainty
δ^*	boundary layer displacement thickness
δ_{99}	99% boundary layer thickness
ε	compound angle, emissivity
η	film cooling effectiveness
θ	normalized gas temperature, boundary layer momentum thickness
Λ_x	turbulence integral length scale
μ	dynamic viscosity
ρ	density
σ	Stefan-Boltzmann constant
φ	overall cooling effectiveness
χ	coolant warming factor

Subscripts and Accents:

0	without film cooling
$\bar{}$	laterally averaged
∞	pertaining to the mainstream flow
amb	ambient
atm	atmospheric
aw	adiabatic wall
b	bias

c	pertaining to internal coolant flow
CL	centerline
dp	dew point
f	with film cooling
g	gauge
j	pertaining to the film cooling jet
m	pertaining to the surface of the metal part
p	precision, pipe, predicted
s	pertaining to swirling flow in the film hole
t	total
th	throat

Chapter 1: Introduction

1.1 Gas Turbine Heat Transfer

The results of the research presented in this dissertation are intended to provide insight into the operation of gas turbine engines, in the hope that the understanding gained will lead toward the development of more efficient and durable engines. This work is of primary relevance to the hot gas path section of the gas turbine engine where active cooling is necessary to protect engine components that are subject to extreme temperatures in excess of material limits. Active cooling permits a higher turbine inlet temperature, resulting in increased efficiency. Gas turbine engines can be modeled as a Brayton cycle, for which increased turbine inlet temperature results in increased thermal efficiency. Therefore, modern gas turbine engines increasingly operate at higher turbine inlet temperatures – up to 2300 K in military jet engines [1]. Active cooling also benefits the durability of engine parts. It has been reported that for industrial gas turbine engines, a reduction of turbine airfoil temperature of just 25 K can double part life [2]. The downside to active cooling, however, is that the air used to cool the hot gas components would otherwise be used to produce useful work (either power generation or thrust). The cooling air is typically removed from the late stages of the high pressure compressor and delivered to the hot gas components. Using too much cooling air results in a reduction in efficiency due to the loss of working fluid so it is crucial to use the air that is removed for cooling as effectively as possible. In advanced engines, the amount of air used as coolant can exceed 20% of the total flow through the engine [2].

Gas turbine airfoils are cooled both internally and externally. Figure 1.1 diagrams a representative cooling design for an early stage gas turbine blade. Cooling air is supplied to the base of the blade and passes through an array of internal channels designed to

maximize the heat transfer between the cooling air and the blade. Impingement cooling is commonly used near the leading edge where the heat load on the blade is the highest. Much of the rest of the blade is cooled by internal channels oriented perpendicularly to the direction of the overflowing mainstream. These internal channels often feature rib turbulators or other features designed to enhance heat transfer between the coolant and the part. Near the trailing edge, it is common to use pin fins as the flow area narrows down. The blade is also cooled externally by film cooling holes machined into the blade to inject the coolant out onto the exposed surface. In a well-designed film cooling scheme, a thin film of coolant develops between the hot combustion products and the surface of the airfoil. Often, a densely packed array of film cooling holes oriented radially to the mainstream flow called the showerhead protects the leading edge and the region immediately downstream. Further downstream, rows of axially oriented film cooling holes ensure the rest of the blade is protected. The air that is not injected as film cooling is typically ejected out of slots in the trailing edge to enhance trailing edge cooling. Because film cooling holes are short, the manner in which the coolant enters the film cooling hole can have a strong effect on the issuing film cooling jet and its efficacy at protecting the external surface. This study specifically considers the downstream region of the blade where the internal supply channel is oriented perpendicularly to the overflowing mainstream.

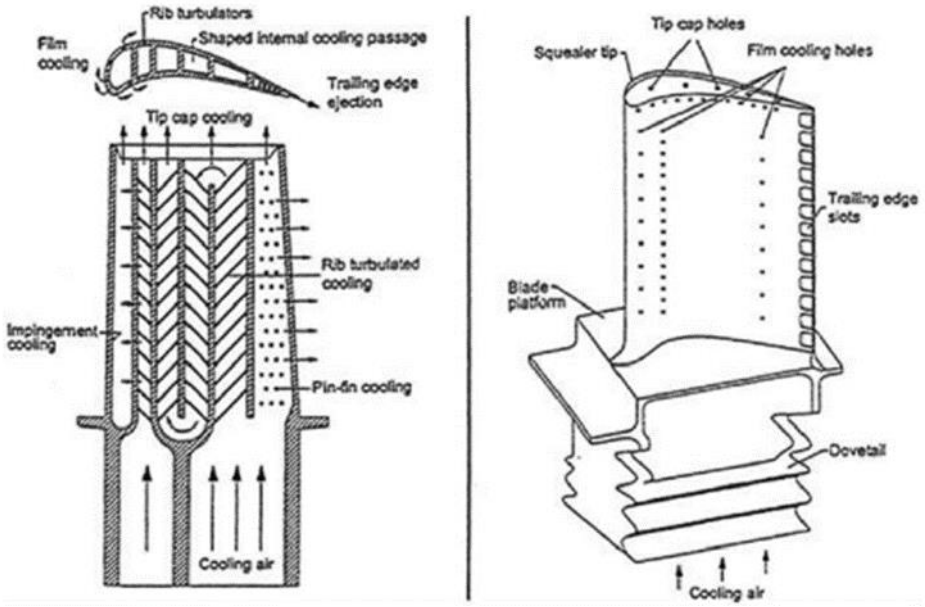

Figure 1.1: Diagram of an early-stage turbine blade featuring internal and external cooling [3]

1.2 Film and Internal Cooling Analysis

This section overviews parameters that are used to scale and evaluate internal cooling, film cooling, and the interaction between the two. Figure 1.2 diagrams a row of axially oriented film cooling holes fed by an internal crossflow. The direction of the mainstream flow is perpendicular to that of the internal flow, similar to the mainstream-internal flow orientation in Figure 1.1. The film cooling jets are injected at an angle to the surface to better allow the coolant to stay attached to the surface as it moves downstream. The exits of the holes are diffused both in the forward and lateral direction in order to reduce the momentum of the issuing jet and thus reduce the likelihood that the coolant detaches from the wall. Originally, film cooling holes were cylindrical, but diffused-exit or "shaped" holes perform more effectively than cylindrical holes and are commonly used in advanced film cooling designs.

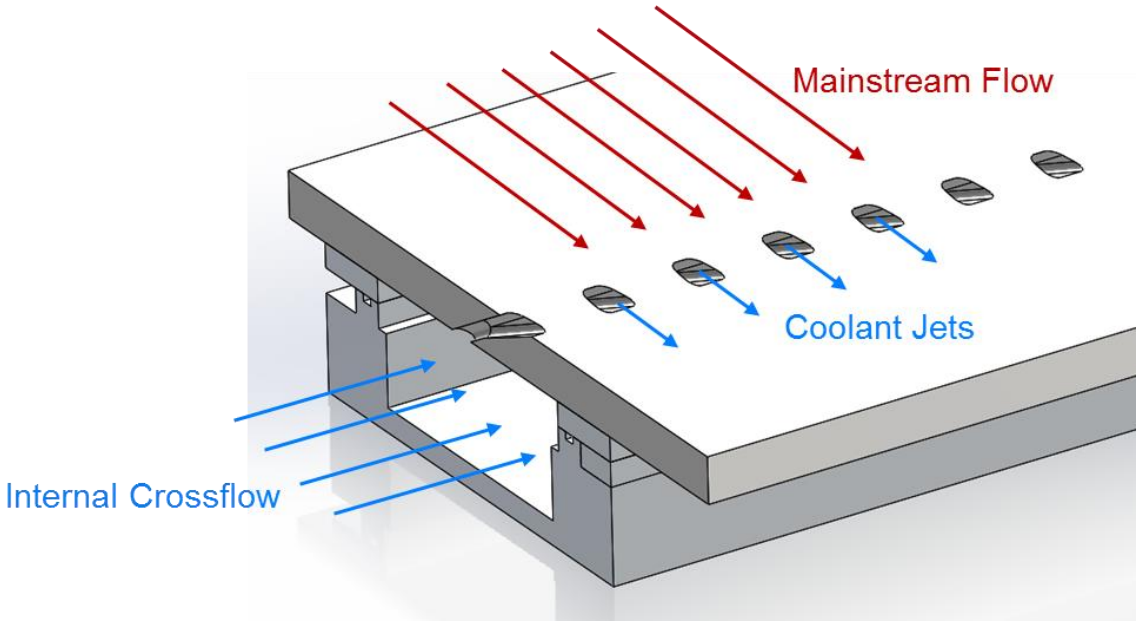

Figure 1.2: Diagram of axial film cooling holes fed by an internal crossflow

1.2.1 Important Flow Parameters

The flow portrayed in Figure 1.2 can be divided into three distinct regimes: the mainstream flow, the internal crossflow, and the coolant jet. When considering a single row of holes, the mainstream flow is commonly characterized by the approach flow characteristics upstream of the film cooling holes. Therefore, the mainstream flow affecting a row of film cooling holes can vary considerably depending on where on the airfoil the holes are located. Mainstream velocity is often normalized as an approach flow Reynolds number, Re_d, defined as:

$$Re_d \equiv \frac{\rho_\infty U_\infty d}{\mu_\infty} \tag{1.1}$$

This Reynolds number thus scales the mainstream velocity and properties by the film cooling hole diameter. A typical range for engine conditions is Re_d = 5,000-25,000. The mainstream turbulence level, Tu_∞, and integral length scale, Λ_x, characterize the turbulence

parameters of the approaching mainstream flow. The flow exiting the combustor is highly turbulent, with intensities around Tu_∞ = 20% [2], and can have integral length scales that are several times larger than the diameters of the film cooling holes. As the flow accelerates around the airfoil, the turbulence intensity is reduced to around 5-12%. As with the mainstream velocity, the boundary layer character and thickness vary considerably over the surface of the airfoil. Figure 1.3 (a) plots the shape of the boundary layer at different locations on the suction side of a C3X airfoil as measured by Dees [4]. Closer to the leading edge (SS1, SS2) the boundary layer profiles were laminar as can be seen by their close comparison to the Pollahausen correlation, while further downstream (SS3 and SS4) the boundary layer profiles became fully turbulent. Figure 1.3 (b) plots the heat transfer coefficient without film cooling, h_0, over the airfoil. It can be observed that transition to turbulence occurred between the SS2 and SS3 measurement locations as evidenced by the sharp increase in h_0 around s/C = 0.45.

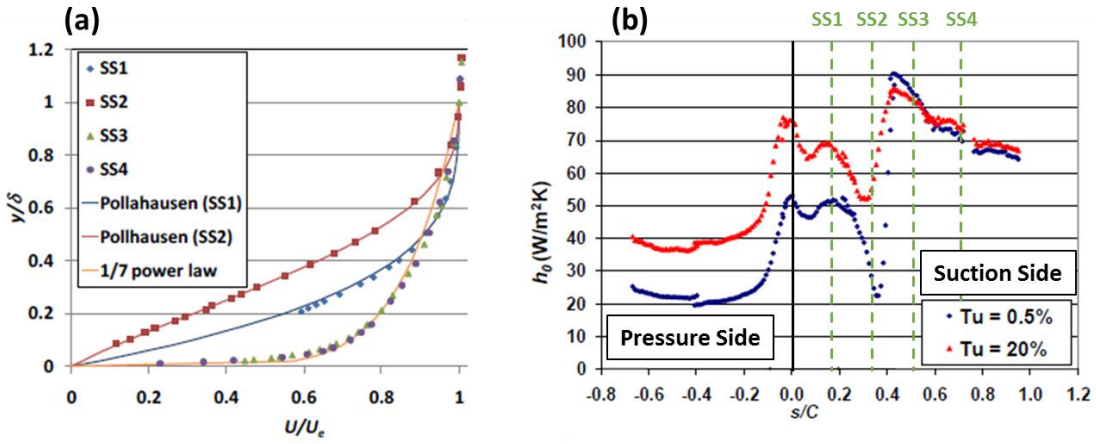

Figure 1.3: (a) Suction side boundary layer profiles and (b) heat transfer coefficient without film cooling on a low speed model C3X blade from Dees [4]

While a number of studies have endeavored to examine the effects of mainstream Reynolds number, turbulence intensity, and approach boundary layer, variation of these parameters is outside the scope of this study. However, it was desirable to simulate engine-relevant conditions, so an effort was made to simulate the downstream suction side of a turbine blade by setting an elevated turbulence intensity in the mainstream, with large turbulent length scale structures, and a thick turbulent boundary layer.

Most turbine heat transfer studies featuring internal flow through a channel characterize the flow in terms of an internal Reynolds number defined as:

$$Re_c \equiv \frac{\rho_c U_c d_H}{\mu_c} \tag{1.2}$$

where d_H is the hydraulic diameter of the channel, U_c is the mean velocity through the channel, and ρ_c and μ_c are the coolant density and dynamic viscosity respectively. The Reynolds number is the important flow parameter for heat transfer in the channel and is often correlated to a Nusselt or Stanton number. A number of studies focused on the effect of internal crossflow on film cooling performance repot an internal velocity in terms of a crossflow Mach number, Ma_c, which scales compressible flow effects. A recent study by Wilkes *et al.* [5] showed that the ratio of the internal crossflow velocity to the overflowing mainstream velocity, or crossflow velocity ratio, was important:

$$VR_c \equiv \frac{U_c}{U_\infty} \tag{1.3}$$

The velocity ratio at the inlet of the hole was also considered – that is, the ratio of the crossflow velocity to the jet velocity in the metering section of the hole.

$$VR_i \equiv \frac{U_c}{U_j} \tag{1.4}$$

This velocity ratio is expected to characterize how the coolant enters the film hole.

For the purposes of this study, a range of engine-relevant crossflow velocity ratios was chosen: VR_c = 0.2-0.6. It was deemed important to consider such a wide range of crossflow velocity ratios to encompass possible engine conditions and because as flow passes through a film-cooled blade, the film holes remove the coolant from the passages such that the crossflow velocity is reduced going through the passage.

A number of different parameters have been used to scale and quantify the film cooling injection rate throughout the literature. Those relevant to this study are shown in Table 1.1. Most common is the blowing ratio, *M*, which is a mass flux ratio between the coolant and the mainstream gas. Of the parameters listed, the blowing ratio most directly represents the cost of injecting coolant – as more mass flow is redirected for use as coolant, the less is available as a working fluid. In terms of film cooling performance, blowing ratio represents the amount of coolant mass available to cool the surface. The momentum flux ratio, *I*, is the ratio of the coolant and mainstream momentum fluxes. This ratio is often associated with jet detachment from the wall as a higher momentum cooling jet is more likely to separate from the wall and penetrate into the freestream where it can no longer protect the wall. The velocity ratio, *VR*, is simply the ratio between the coolant jet and mainstream velocities. When matched, it scales the coolant jet-mainstream shear layer interaction which determines how the coolant disperses both laterally and vertically. The density ratio, *DR*, is the ratio between the coolant and mainstream gas, and is the result of the temperature ratio between the two. Engines often run at a density ratio of $DR \approx 2.0$, which is difficult to simulate in laboratory conditions. Because density ratio is not commonly matched in laboratory conditions, only one of the three previously discussed

injection parameters, *M*, *I*, or *VR*, can be matched. A number of studies, such as Greiner *et al* [6], have examined the effect of density ratio and performed scaling analyses to determine the most appropriate blowing parameter. The results are often mixed, with no single parameter perfectly scaling film cooling performance in all cases. The final parameter listed is the pressure ratio, which is the ratio of the total coolant pressure in the channel to the static mainstream pressure. This parameter is commonly used by engine designers and rarely tested in low speed experimental studies of film cooling. At engine conditions, where flow around the airfoil is transonic, the required pressure ratio is greater than at low speed experimental conditions. For example, at a mainstream Mach number of $Ma_\infty = 0.8$, a film hole with a discharge coefficient of $C_d = 0.8$ at $DR = 2.0$ would require a pressure ratio of $PR = 2.0$ to achieve a blowing ratio of $M = 2.0$. In laboratory studies, such as this one, however, the pressure ratio for the same blowing ratio is very close to $PR = 1$. It is generally assumed that when translating laboratory results to engine conditions that *M*, *I*, or *VR* is the appropriate scaling factor, rather than pressure ratio.

Table 1.1: Common film injection parameters

Parameter	**Definition**	**Significance**
Blowing Ratio	$M \equiv \frac{\rho_j U_j}{\rho_\infty U_\infty}$	Represents the mass of coolant injected relative to mainstream
Momentum Flux Ratio	$I \equiv \frac{\rho_j U_j^2}{\rho_\infty U_\infty^2}$	Represents momentum of jet, governs jet separation from wall
Velocity Ratio	$VR \equiv \frac{U_j}{U_\infty}$	Represents velocity of jet, governs shear layer interaction and coolant dispersal
Density Ratio	$DR \equiv \frac{\rho_j}{\rho_\infty}$	Density ratio due to temperature difference between mainstream and coolant
Pressure Ratio	$PR \equiv \frac{p_{t,c}}{p_\infty}$	Driving potential for coolant injection, not generally matched in laboratory conditions

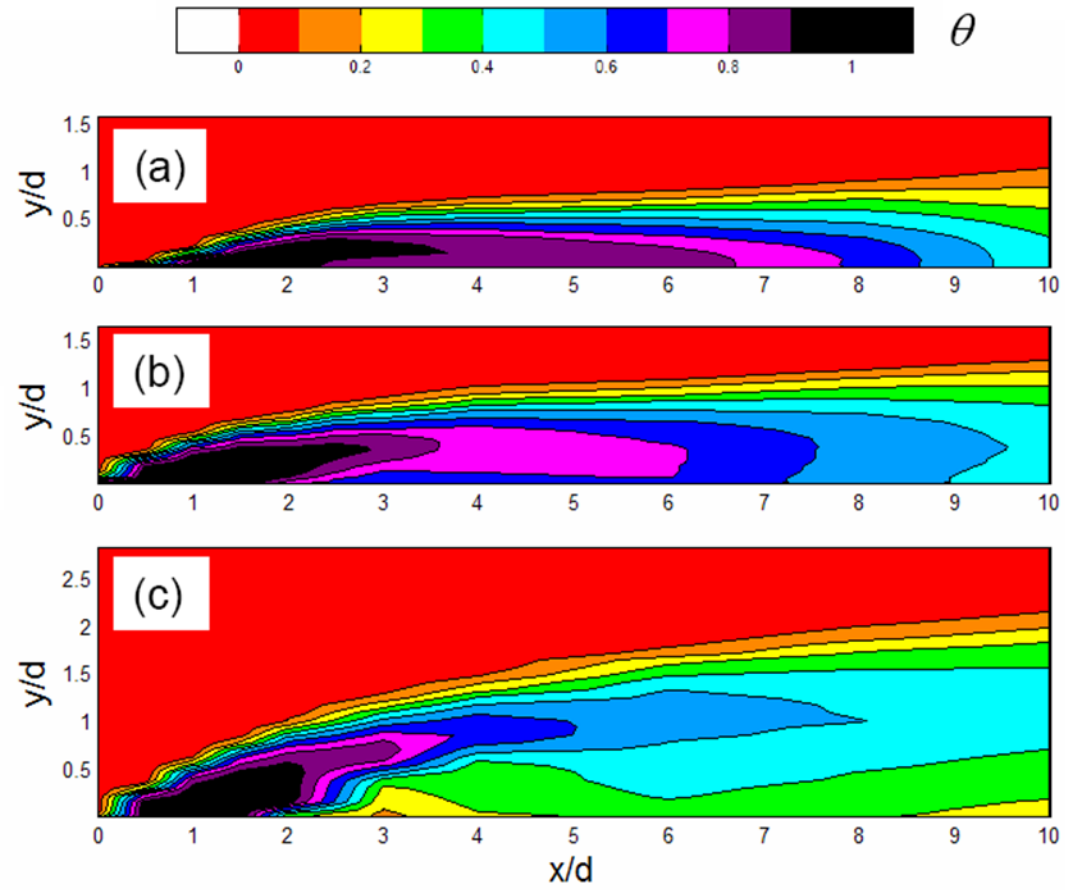

Figure 1.4: Thermal field of film cooling jets showing the behavior of a jet as injection rate is increased: (a) an attached jet, (b) a partially detached jet, (c) a fully detached jet [7]

While the effect of increasing the film cooling injection rate is geometry dependent, there are three regimes in which most film cooling jets can be categorized based on the injection rate: attached, partially detached, and fully detached. The jet detaches from the wall as the film cooling rate is increased, as can be seen in Figure 1.4, which shows thermal field data for cylindrical film cooling holes measured by Thole *et al.* [7] (figure produced by [2]). Starting from $VR = 0$, as injection rate increases, the film effectiveness increases as more coolant is supplied to cool the surface. However, at a certain point, the momentum

of the jet causes the jet to start detaching from the wall, yielding diminishing returns for the addition of more coolant. Usually the peak film cooling performance for a given geometry occurs in the partially detached jet regime. As the jet continues to separate, the coolant pulls away from the surface, and the film cooling is rendered less effective with increasing injection rate. Selecting an appropriate injection rate is therefore critical to appropriately cool the surface. Modern film cooling holes are therefore designed with the intent of reducing the tendency of the film cooling jets to separate from the surface. In this study a wide range of injection rates, VR = 0.2-1.7, was tested to examine a variety of coolant jet behaviors.

1.2.2 Evaluation of Cooling Performance

Most gas turbine cooling systems are primarily designed to manage the temperature of the exposed metal surface, T_m. Therefore, the dimensionless parameter of interest is the overall effectiveness, defined as follows:

$$\varphi \equiv \frac{T_\infty - T_m}{T_\infty - T_{c,inlet}} \tag{1.5}$$

The coolant temperature, $T_{c,inlet}$, typically used to define φ is the temperature at the inlet of the blade, such that φ = 1 corresponds to a region of a part that is perfectly cooled by the incoming coolant, while φ = 0 corresponds to a region of the part that is completely uncooled. A number of factors contribute to φ, including the mainstream and internal heat transfer coefficients, film cooling effectiveness, and part material. Given the considerable complexity of gas turbine heat transfer, it is often useful to isolate these various factors from each other to determine how each factor contributes to the overall cooling effectiveness.

The introduction of film cooling changes the boundary conditions for heat transfer at the external surface of the wall by changing the driving temperature for heat transfer and the heat transfer coefficients. The driving temperature of a film cooled wall is commonly evaluated in terms of an adiabatic effectiveness:

$$\eta \equiv \frac{T_\infty - T_{aw}}{T_\infty - T_j} \tag{1.6}$$

Similar to overall effectiveness, adiabatic effectiveness is the normalized adiabatic wall temperature, T_{aw}, of the film cooled part. Adiabatic effectiveness represents the gas temperature immediately above the surface and can also be thought of as how effectively the coolant covers the film cooled surface. Note that at greater Mach numbers, the recovery temperature is used instead of T_∞. The assumption that adiabatic effectiveness is the driving temperature is not fully justifiable due to conjugate heat transfer effects, but it has been found to be appropriate in many cases [8].

While adiabatic effectiveness provides a measure of the temperature boundary condition for a film-cooled wall, it does not take into account how film cooling jets alter the heat transfer coefficient between the mainstream and the surface. Due to turbulence production within the film cooling hole and in the secondary flows that result from the jet-to-mainstream interaction, film cooling jets often increase the heat transfer coefficient at the surface. This increase in heat transfer coefficient due to film cooling is often reported as heat transfer coefficient augmentation, h_f/h_0, or the ratio between the heat transfer coefficients with and without film cooling.

The efficacy of internal cooling, while not a focus of this study is an important consideration. Internal cooling is often evaluated as a Nusselt number and is dependent on both the flow rate through the internal channel and internal features such as rib turbulators.

$$Nu_c = \frac{h_c d_H}{k} \tag{1.7}$$

Like the adiabatic effectiveness and the heat transfer coefficient augmentation, Nu_c is used as a boundary condition to evaluate the overall cooling effectiveness. The internal temperature is also an important consideration, as the coolant is expected to warm up as it passes through the internal channels of the part.

The one-dimensional analysis of Williams *et al* [9] can be used to show the relationship between the adiabatic effectiveness, heat transfer coefficient with film cooling, and the internal cooling. Assuming a film-cooled and internally cooled wall of thickness, t, and thermal conductivity, k, the heat transfer through the wall can be calculated as:

$$q_f{}'' = h_f(T_{aw} - T_m) = \frac{T_m - T_c}{t/k - 1/h_i} \tag{1.8}$$

By substituting η and φ into the above equation, it can be shown that:

$$\varphi = \frac{1 - \chi\eta}{1 + Bi + h_f/h_c} + \chi\eta \tag{1.9}$$

where:

$$\chi = \frac{T_\infty - T_j}{T_\infty - T_c} \tag{1.10}$$

$$Bi = \frac{h_f t}{k} \tag{1.11}$$

The coolant warming factor, χ, is used to account for the difference in coolant temperature in the definitions of η and φ. The coolant temperature increases within the internal airfoil passages and as it passes through the film hole. Note that in the above derivation, the internal channel temperature, T_c, was used in place of the blade inlet temperature, $T_{c,inlet}$, to define φ – thus, the overall effectiveness is evaluated locally on a region of the airfoil, rather than for the airfoil as a whole. Doing so makes this model applicable to the case depicted by Figure 1.2, which is the focus of this study. Equation 1.9 demonstrates how the various factors contribute to overall effectiveness. For example, in the limiting case of $\eta = 1$ (perfect film coverage) and $\chi = 1$ (no warming through the hole), the overall effectiveness is $\varphi = 1$ because in that case the film perfectly isolates the part from the mainstream. In the other extreme where $\eta = 0$ (no film coverage), the overall effectiveness is determined only by the internal and external heat transfer coefficients and the wall Biot number. Note that in the absence of film cooling, $\varphi > 0$ due to the presence of internal cooling. The ratio of the external to internal heat transfer coefficients, h_f/h_c, is also important. As this ratio increases, the overall effectiveness decreases, due to increased external heat transfer relative to the internal heat transfer. It should be noted that these parameters, η, h_f, and h_c, are not independent of one another. For example, increasing the internal crossflow velocity increases h_c, but can have a detrimental effect on η and increase h_f. Whether this change in crossflow velocity has a net positive or negative effect on φ depends on how strongly linked each parameter is to the internal crossflow.

1.3 Effect of Internal Crossflow on Film Cooling

As previously stated, the primary aim of this study is to develop a better understanding of how an internal crossflow feed affects film cooling injection. This effect is an important consideration for engine designers because film cooling holes in turbine

airfoils are commonly fed by an internal crossflow. However, the majority of film cooling studies feed film holes by means of a quiescent plenum, which does not suitably approximate the internal flow in engine parts. The studies that consider an internal crossflow are rare and only consider a small range of flow conditions and film cooling geometries.

This study focuses on shaped holes as they have been overwhelmingly shown to outperform cylindrical film cooling holes and thus represent a state of the art. Bunker [10] provides a good review of film cooling with shaped holes. It should be noted that within the various geometries classified as "shaped" holes there is considerable variation in geometry and film cooling performance. It is therefore not expected that trends that hold true for one geometry will hold for all geometries. While there are a number of sub-categories of shaped holes, the present review will consider the two most common: fan-shaped (FS) holes and laidback fan-shaped (LFS) holes. Both types of holes have symmetric lateral diffusion such that the exit of the hole is in the shape of a fan. The difference between the two is that FS holes have no forward diffusion, while LFS holes do. Figure 1.5 shows a schematic of a shaped film cooling hole. The geometry used in this study is the 7-7-7 LFS hole originally presented by Schroeder and Thole [11]. The first two 7's in the name give the lateral diffusion angles, β, in degrees, while the last 7 gives the forward diffusion angle, γ. Therefore, the FS version of this geometry would be a 7-7-0 hole. Other parameters necessary to define the shape of a LFS or FS hole are the injection angle, α, the metering length of the hole, L_m, which is the length of the cylindrical portion of the hole, and the length of the hole, L, which is the overall length of the hole. For certain geometries, the forward and lateral expansions begin at different points. Because in some cases, it is necessary to for the hole to have a compound angle, ε, such that the coolant injection has a radial component, compound angle LFS holes were also tested in this study.

The hole shown in Figure 1.5 is a compound angle hole. For an axial hole, $\varepsilon = 0$. The following sections summarize what is known about how internal crossflow affects axial and compound angle shaped film cooling holes.

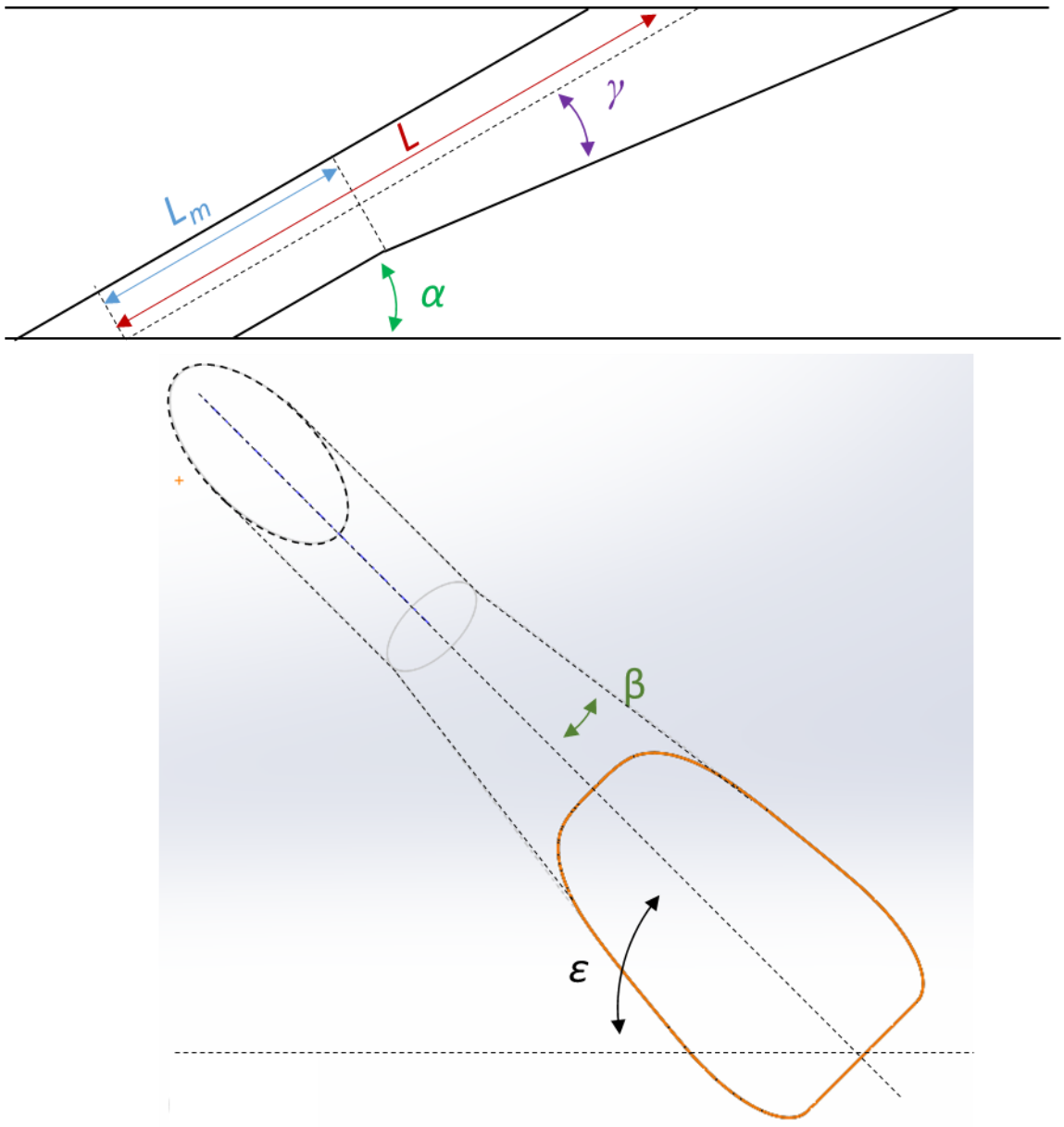

Figure 1.5: Schematic of a compound angle laidback fan-shaped film cooling hole

1.3.1 Axial Shaped Holes

The majority of internal crossflow studies have tested axial shaped holes, a significant number of which were performed in a laboratory at Universität Karlsruhe. While these studies only tested a single film hole and only measured effectiveness a short distance downstream of the hole (x/d = 8-12), they provide a useful dataset at realistic engine Mach numbers (Ma_∞ = 0.3 and Ma_c= 0.0-0.6) and considerable insight into the internal crossflow effect. These studies primarily featured FS and LFS holes with wide-angle diffusers (14-14-0 and 14-14-15 respectively) and examined the effect of crossflow on adiabatic effectiveness.

In general, it was found that internal crossflow caused a degradation in effectiveness for axial shaped holes. Figure 1.6 shows adiabatic effectiveness measurements from Gritsch *et al.* [12] for LFS holes for a range of crossflow Mach numbers and blowing ratios. The left column shows holes fed by Ma_c = 0.0, effectively a plenum feed. That condition resulted in a symmetric effectiveness profile on the surface and it appears that the coolant is filling out the diffused section of the film cooling hole, resulting in highly effective jets. The crossflow Mach number was increased to Ma_c = 0.3 and 0.6 for the center and right columns respectively. The internal crossflow resulted in asymmetric jets that did not cover the surface effectively and had spatially averaged effectiveness that was up to 30% lower compared to the plenum-fed condition. Instead of filling out the diffuser, the coolant instead biased toward the extreme edges of the diffuser, with most of the coolant favoring one side. For all but the Ma_c = 0.6, M = 0.5 and 1.0 conditions, the coolant favored the windward side of the diffuser relative to the direction of internal crossflow. These results confirmed and expanded those made earlier by Gritsch *et al.* [13].

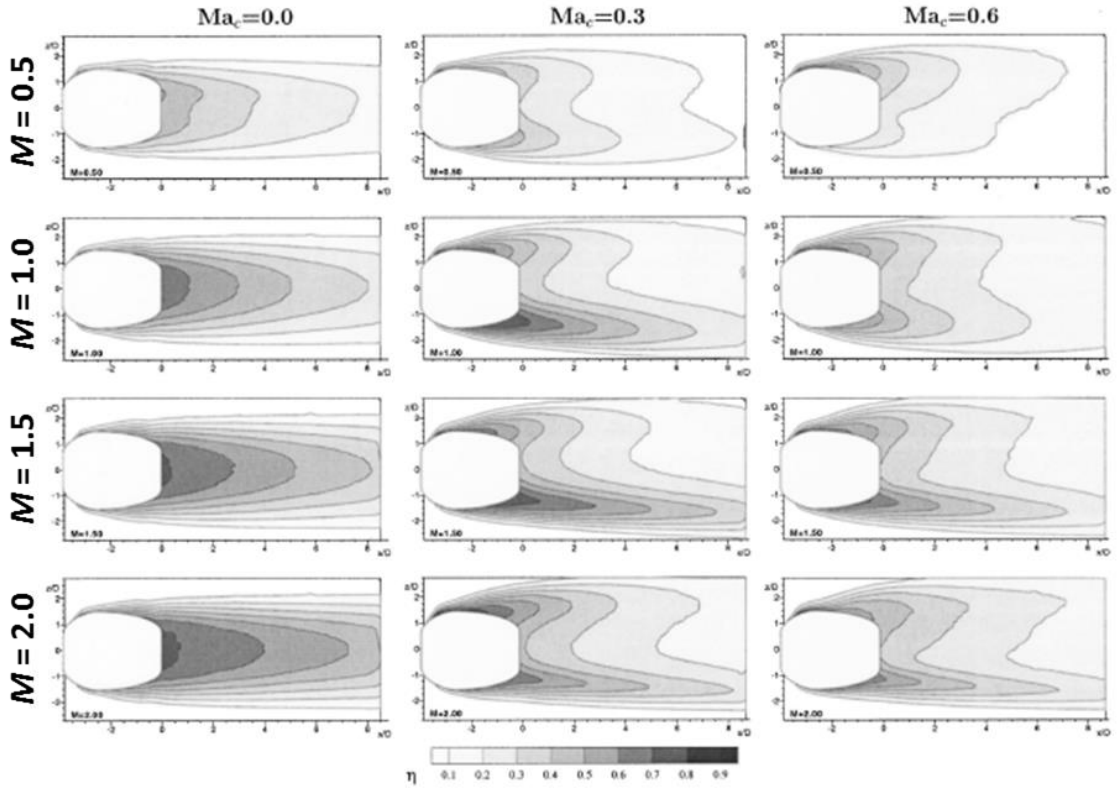

Figure 1.6: Degradation in η due to internal crossflow for laidback fan-shaped holes at Ma_∞ = 0.3 [12]. Internal crossflow was directed from bottom to top

The fan-shaped holes from [12] also experienced a degradation in effectiveness due to internal crossflow. Similar to the laidback fan-shaped holes, the reduced effectiveness for the FS holes occurred due to coolant biasing toward one or both sides of the diffuser. Unlike the LFS holes, however, the biasing in the FS holes occurred on the leeward side of the diffuser. The range of flow conditions for FS holes was expanded by Saumweber and Schulz [14]. That study similarly observed that crossflow reduced film cooling effectiveness by causing biasing in the diffuser. At the highest blowing ratio tested, M = 2.5, introducing internal crossflow reduced the area averaged effectiveness by about 40%. It was found that for a blowing ratio of M = 1.0, reducing the internal Mach number to Ma_c = 0.1, the direction of the biasing flipped to the windward side of the diffuser. The direction

of biasing also flipped at $Ma_c = 0.29$ when blowing ratio was increased to $M = 2.5$. Another study by Saumweber and Schulz [15] further expanded the experimental regime by testing a number of variations on the 14-14-0 FS hole, by varying the lateral expansion angle, β, the inclination angle, α, and the hole length-to-diameter ratio, L/d. Reducing the lateral expansion angle to $\beta = 10°$ and 6° caused a reduction in effectiveness for both plenum and crossflow-fed conditions. The 6-6-0 hole experienced degradation due to internal crossflow that was similar to the crossflow effect for the 14-14-0 hole, as shown in Figure 1.7. Unlike the 14-14-0 hole, the 6-6-0 only biased toward one side of the diffuser and did not have the same double-peak effectiveness profile due to the reduced lateral diffusion angle. The 6-6-0 hole was biased toward the leeward side of the hole (same as for the majority of the 14-14-0 hole conditions) except at $Ma_c = 0.6$ and $M = 0.5$, where the biasing direction flipped. The 14-14-0 hole from Gritsch *et al.* [12] was biased toward the windward side for that condition. And as mentioned previously, the 14-14-0 jet was biased toward the leeward side of the hole at $Ma_c = 0.3$ and $M = 2.5$, which was not the case for the 6-6-0 jet. Saumweber and Schulz [14] also found that changing the injection angle and the length of the hole could reverse the direction of biasing in the diffuser. While the aforementioned studies showed that internal crossflow could have a substantial effect on film cooling effectiveness, they did not make any effort to determine the important internal cooling parameters, such as VR_c or Re_c, governing this effect.

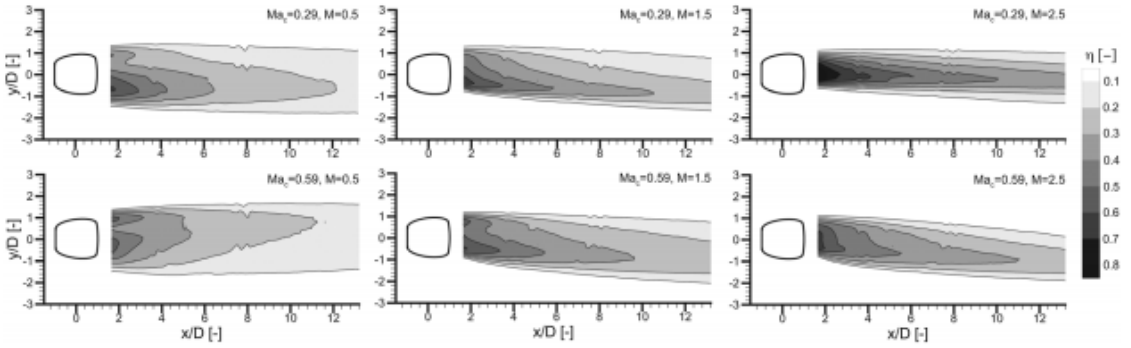

Figure 1.7: Effectiveness downstream of a 6-6-0 fan-shaped hole from [15]. The internal crossflow is directed from top to bottom.

There are very few experimental studies that have examined the effect of internal crossflow on adiabatic effectiveness of axial shaped holes outside those described above. There are a number of studies performed on simulated airfoils where there is an internal crossflow present, but those studies did not make an effort to control for the internal crossflow velocity. A study by Peng and Jiang [16] studied the same 14-14-0 fan-shaped holes tested by Universität Karlsruhe at low speeds (Ma_c = 0.06) and similarly found that internal crossflow reduced effectiveness. However, the data was not of sufficient resolution to draw any further conclusions. A study performed here at the University of Texas by Wilkes *et al.* [5] tested the same configuration which is the focus of this present study: the 7-7-7 laidback fan-shaped hole. Experiments for that study were performed at low speed, over a much larger stream-wise range (x/d = 0-50) and for a row of eight holes instead of a single hole. The test model was scaled at both 4x and 8x engine scale in order to independently vary the internal crossflow-to-mainstream velocity ratio, VR_c, and the internal Reynolds number, Re_c. It was found that the adiabatic effectiveness was sensitive to VR_c and not Re_c. Similar to the wide-angle 14-14-15 LFS hole of Gritsch *et al.* [12], the narrow-angle 7-7-7 LFS holes biased predominantly toward the windward side of the

diffuser, resulting in film cooling jets that were less effective than the reference plenum-fed condition. The exception to that rule occurred at $VR_c = 0.63$ and $VR = 0.54$ where the jet instead biased toward the leeward side of the diffuser.

While only a few studies have measured film cooling effectiveness for crossflow-fed axial shaped holes, even fewer have measured heat transfer coefficient augmentation. Saumweber and Schulz [14] report laterally averaged heat transfer coefficient measurements that show h_f/h_0 decreased when fed by internal crossflow relative to a plenum-fed configuration. There was little sensitivity to the magnitude of the crossflow velocity however and h_f/h_0 was primarily a function of injection rate. They claimed that the reduction in heat transfer coefficient augmentation for the internal crossflow configurations was due to reduced interaction between the jet and the surface in the crossflow cases. They made this assertion based on a computational simulation showing that the thermal gradient above the wall in the y-direction was reduced for the crossflow condition.

1.3.2 Compound Angle Shaped Holes

Film cooling holes often have a compound angle to allow for a shallow injection angle in regions of high curvature on a turbine airfoil. However, there are very few studies in the literature that test compound angle shaped holes and thus their performance is not well defined. Taslim and Khanicheh [17] measured higher adiabatic effectiveness for 10-10-10 LFS compound angle shaped holes than for axial shaped holes. Bell *et al.* [18] measured adiabatic effectiveness and heat transfer coefficient augmentation for both compound and axial 12-12-0 fan-shaped holes. It was found that the compound angle holes had both higher effectiveness and heat transfer coefficient augmentation. A net heat flux reduction analysis, which takes both adiabatic effectiveness and heat transfer coefficient augmentation into account to show how film cooling changes the net heat flux into the

wall, showed that the compound angle shaped holes outperformed the axial shaped holes. Ganzert *et al.* [19] found that compound angle shaped holes had higher aerodynamic losses and heat transfer coefficient augmentation relative to axial shaped holes. That study was performed on the suction side of a model gas turbine blade. The comparison between compound angle and axial shaped holes was for 10-10-10 LFS holes. These holes had similar expansion angles but shorter length than those of Taslim and Khanichech [17].

Only one study in the literature, Dittmar *et al.* [20], has studied compound angle shaped holes fed by an internal crossflow. That study tested a row of compound angle shaped holes machined onto a convex surface designed to simulate the suction side of a turbine blade. The holes tested were 14-14-0 fan-shaped holes. Unlike the studies mentioned previously, which all tested holes with a compound angle of $\varepsilon = 45°$, the holes in Dittmar *et al.* [20] had a compound angle of $\varepsilon = 35°$. No details were given regarding the magnitude of the crossflow velocity (and only one crossflow velocity was tested). Also, a direct comparison to the axial FS holes tested by that study is not possible because the axial holes were fed by a plenum and not internal crossflow. Both crossflow directions were tested for the compound angle holes and it was found that crossflow that was directed in-line with the spanwise direction of coolant injection resulted in approximately 50% higher effectiveness than when crossflow was directed counter to the lateral direction of injection. The heat transfer coefficient measurements showed that at $M = 1.0$ the in-line crossflow condition had much higher h_f/h_0 than the counter crossflow condition, but at $M = 3.0$, they had similar laterally averaged h_f/h_0 (peak laterally averaged h_f/h_0 was 60% greater for in-line crossflow). The distribution of h_f/h_0 was quite different between the two cases at $M = 3.0$ – the counter crossflow condition had a higher peak h_f/h_0, while the in-line condition had a more uniform distribution of high h_f/h_0 across the pitch.

Given the dearth of experimental data for compound angle shaped holes, it is worth noting that the effect of internal crossflow was investigated for compound angle cylindrical holes here at the University of Texas by McClintic *et al.* [21] for a smooth internal channel (the same one used in this study). It was found that internal crossflow directed counter to the lateral direction of coolant injection caused a significant improvement in effectiveness relative to an in-line crossflow direction.

1.4 Flow Physics of Film Cooling

The effect of crossflow on film cooling effectiveness and heat transfer coefficient augmentation must necessarily be initiated at the inlet of the film cooling hole. The manner of inlet flow must then have some effect on the flow within and at the exit of the hole, determining the manner of biasing within the diffuser and dispersal of the coolant above the surface. While the flow field within crossflow-fed shaped film cooling hole has never been experimentally measured, results from a number of experimental and computational studies can be gleaned to provide insight into the root cause of the crossflow effect.

1.4.1 Discharge Coefficients

The discharge coefficient through a film cooling hole provides a measure of the losses through the hole relative to an idealized case of $C_d = 1$. The losses through the film cooling hole can largely be attributed to separation at the hole inlet, flow through the hole itself, and mixing losses as the jet exits the hole. Shaped holes typically have higher discharge coefficients than cylindrical holes due to pressure recovery as the flow expands in the diffused section of the hole. Hay *et al.* [22] was the first study to consider the effect of crossflow on film cooling holes, and did so for both normal ($\alpha = 90°$) and inclined ($\alpha = 30°$) axial cylindrical holes fed both by an internal coflow, crossflow, and a plenum feed ($Ma_c = 0.0\text{-}0.4$). The internal coflow was directed parallel to the mainstream flow. For the

inclined holes, coflow increased C_d, while crossflow decreased C_d relative to the plenum-fed holes. This result is unsurprising given that the turning angle into the holes was reduced for coflow and increased for crossflow. Bunker and Bailey [23] performed a similar study for cylindrical holes fed by coflow and crossflow, but introduced rib turbulators to the internal channel, which had a significant effect. Coflow still had higher C_d than crossflow overall.

Discharge coefficients for shaped holes fed by internal crossflow and coflow were first measured by Gritsch *et al.* [24]. The shaped hole geometries used were the same 14-14-0 FS and 14-14-15 LFS holes tested in other studies at Universität Karlsruhe. They found that, similar to round holes, coflow increased and crossflow decreased C_d relative to a plenum feed, and that C_d was highly sensitive to Ma_c but relatively insensitive to Ma_∞. This result suggests that the losses in these holes were primarily governed by the separation at the inlet of the hole. It was also shown that, when fed by an internal crossflow, there was little difference in discharge coefficients between the FS and LFS holes. A scaling analysis was performed in that study where C_d was normalized by $C_{d,plenum}$ at constant pressure ratio and presented as a function of jet-to-crossflow momentum flux ratio. When scaled in this manner, the data from cylindrical holes for the full range of crossflow and injection flow rates collapsed to within uncertainty. The shaped holes data collapsed reasonably well, but with notably more scatter than the cylindrical holes. This result suggests a strong coupling between the inlet flow and losses through a film cooling hole.

1.4.2 Hole Inlet Effects

Flow entering a film cooling hole is forced to navigate a turning angle, often a sharp angle. Because film cooling holes are short ($L/d < 8$), the effect of separation at the inlet of the hole can propagate through the hole to affect the issuing jet. The manner in which the

flow turns to enter a crossflow-fed hole differs substantially from a plenum-fed hole. Pietzryk *et al.* [25, 26] measured the flow field at the exit of short (L/d = 3.5), inclined (α = 35°), cylindrical holes using a three-component LDV system. The holes were fed from below by a quiescent plenum. Measurements at the exit of the hole showed that the velocity profile at the exit of the hole was skewed and varied with the injection rate. At a low coolant flow rate, VR = 0.5, the majority of the coolant exited form the downstream portion of the hole, while the reverse was true for a higher injection rate of VR = 1.0. They hypothesized that a separation region occurred on the downstream side of the inlet as the flow navigated a sharp 55° turn into the hole, which would have caused the coolant to favor the upstream side of the film cooling hole. At VR = 0.5, the mainstream flow was dominant and served to block the coolant flow from exiting from the upstream side of the hole, but at VR = 1.0, the coolant flow had sufficient momentum to resist the mainstream and thus exited primarily from the upstream side of the hole. A computational prediction by Leylek and Zerkle [27] for the same geometry of Pietzryk *et al.* [25] showed this separation and jetting effect, shown in Figure 1.8 for VR = 1.0. The flow separated at the downstream edge of the hole inlet, resulting in jetting on the upstream side of the hole and a low momentum region on the downstream side. It should be noted that computational simulations of film cooling, especially those using Reynolds Averaged Navier Stokes (RANS) turbulence closure models, tend to poorly predict film cooling effectiveness (as indeed this one did). Computational studies are therefore most effective at providing insight into experimental observations. The effects observed by Leylek and Zerkle [27] were also observed experimentally by Issakhanian *et al.* [28], who used magnetic resonance velocimetry to resolve the full three-dimensional flow field within a cylindrical film cooling hole fed by a plenum and observed a similar pattern of separation and jetting for a plenum-fed hole. Similar computational studies were performed for plenum-fed axial and compound angle

12-12-0 fan-shaped holes by Hyams and Leylek [29] and Brittingham and Leylek [30] respectively. These studies similarly observed separation regions at the hole inlet, but the jetting effect was somewhat mitigated by the lateral diffusion at the hole exit. More recently, Oliver *et al.* [31] simulated flow through an axial 7-7-7 LFS hole (the same geometry used in this study using an implicit LES method, which should provide a more accurate prediction of the film cooling performance. That study showed separation both at the inlet of the film hole and also in the diffuser as the flow failed to navigate the forward expansion angle. This separation resulted in the coolant jetting and primarily exiting near the upstream edge of the hole.

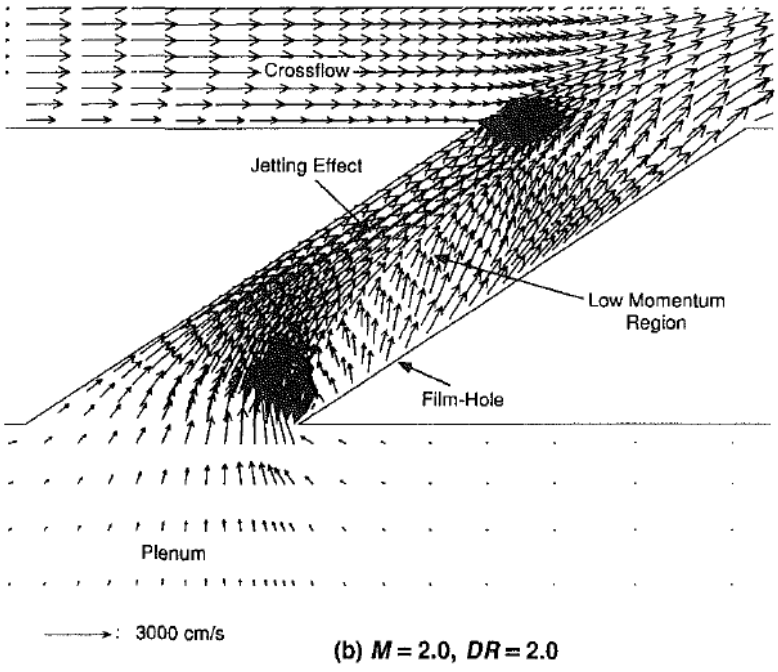

Figure 1.8: Computational prediction of flow through a short cylindrical film cooling hole fed by a quiescent plenum [27]

The previously discussed studies all provided coolant to the holes by means of a quiescent plenum. Those studies are useful to consider because it is expected that the crossflow likewise causes a separation region at the hole inlet that affects the flow development in the hole, which results in biasing in the diffuser and reduced film cooling effectiveness. A study by Lloyd and Brown [32] used hot wire anemometry to measure the flow field in a pipe fed by a perpendicular crossflow. They found that the inlet velocity profile was highly skewed toward the leeward side of the pipe relative to the crossflow direction, which is expected given that the flow is expected to separate on the windward side of the pipe. They also measured very high turbulence levels in the pipe (Tu = 55%, which is well outside of the turbulence levels that can accurately be measured by a hot wire probe). The high turbulence and skewed profile persisted for about four diameters into the pipe before beginning to subside. Interestingly, the location of the peak velocity rotated by about 45°, suggesting that a swirl was imparted to the flow by the crossflow at the inlet. This study also tested the influence of different pipe-to-crossflow velocity ratios, finding that as the pipe-to-crossflow velocity ratio was decreased, the inlet velocity profile became more skewed. The geometry tested by this study was somewhat analogous to crossflow-fed film cooling holes, with the primary difference being that film cooling holes are typically inclined relative to the internal crossflow, which would likely change this result somewhat. Thole *et al.* [33] measured the inlet velocity profile for an axial cylindrical hole fed by an internal coflow using a two-component LDV system. It was shown that the velocity profile was dependent on the magnitude of the internal coflow and that the inlet velocity profile influenced the manner in which the jet exited the hole.

1.4.3 Jet Secondary Flows

Separation at the inlet of the hole can influence the secondary flow within the hole. It is expected that the nature of this separation would change considerably from a plenum-fed hole to a crossflow-fed hole. However, there are no experimental studies that make that comparison directly, primarily due to the difficulty of measuring flow within a film cooling hole. These types of measurements were made by Peterson and Plesniak [34, 35, 36], who used particle image velocimetry (PIV) to measure the secondary flows inside of a normal (α = 90°) cylindrical hole fed by either a terminating internal coflow or counterflow. The term "terminating" refers to an internal channel configured such that all the flow entering the channel exits through the film cooling holes, and the term "counterflow" refers to internal flow in the opposite direction as the overflowing mainstream. They observed a secondary flow featuring a pair of symmetric counter-rotating vortices within the hole. The strength and location of these vortices was highly dependent on the direction of the internal coolant feed. While [34-36] did not test a geometry that is directly applicable to this study, their results give a sense of how a changing coolant feed can impact the secondary flow. Issakhanian *et al.* [28], mentioned previously, measured three-dimensional flow fields in cylindrical holes with varying injection angles: α = 30°, 60°, and 90°. The holes were nominally fed by a plenum, but the coolant supply to the plenum had a lateral component of velocity, so there was a slight lateral crossflow present in the plenum (on the order of $0.20 \cdot U_\infty$). Because of the lateral flow in the plenum, an asymmetric swirling secondary flow formed in the holes and was strongest for the shallowest injection angle, α = 30°. For that condition, the peak strength of the swirl was on the order of $0.3 \cdot U_\infty$ at a plane two diameters from the hole inlet. Because the holes tested in that study were cylindrical holes and because the crossflow velocity was relatively weak, there was little evidence of the

asymmetry found within the hole impacting the performance of the issuing jet outside the hole.

There have been a few computational studies that have aimed to investigate how crossflow affects the performance of shaped film cooling injection. Kohli and Thole [37] studied the impact of crossflow, co-flow, and counterflow on a 15-15-15 laidback fan-shaped hole. In addition to crossflow direction they also studied the effect of different crossflow velocities (given as Reynolds numbers), blowing ratios, and hole metering lengths. For the crossflow-fed holes, they observed biasing in the holes similar to that observed experimentally by Gritsch *et al.* [12], although they only saw a forked jet shape for the highest crossflow velocity. They also reported that the crossflow resulted in increased ingestion of mainstream flow into the diffused exit of the hole relative to the plenum and co-flow conditions. They predicted that the separation at the inlet of the hole resulted in the formation of a strong swirl within the hole that resulted in the observed biasing in the diffuser. A similar phenomenon was predicted by Saumweber and Schulz [14], who performed computational simulations of their experiments featuring 14-14-0 fan-shaped holes. Figure 1.9 shows the predicted vortical structures within the hole two diameters from the inlet. The plenum-fed hole, as expected, had a symmetrical counter-rotating vortex pair, while the crossflow-fed hole had a strong asymmetric swirling secondary flow. They attributed the biasing in the diffuser to this swirling flow patter in the hole.

Near the exit of plenum-fed holes, a counter-rotating vortex pair is formed as a result of the issuing jet blocking the mainstream flow, which forms these vortices as it wraps around the jet. This effect has been observed by a number of studies, including Crabb *et al.* [38], Andreopoulos and Rodi [39], Pietzryk *et al.* [25, 26], Kelso *et al.* [40], and Issakhanian *et al.* [28] for cylindrical holes and Haven *et al.* [41], Berger and Liburdy [42],

and Schroeder and Thole [43] for shaped holes. Berger and Liburdy [42] found that this vortex pair was stronger for round holes than for shaped holes. The orientation of this vortex pair is detrimental to film cooling because the vortices pull hot mainstream gas up into the core of the jet, reducing the film cooling effectiveness. The computational results of Oliver *et al.* [31] for the same 7-7-7 laidback fan-shaped hole tested in this study found that this counter-rotating vortex pair was the primary secondary flow transport mechanism for heat transfer.

There have been no measurements of the secondary flow above the wall for crossflow-fed holes. The computational prediction of Saumweber and Schulz [14] found that the crossflow feed resulted in an asymmetric vortex pair with increased vorticity relative to that of the plenum-fed hole. The asymmetric vortex pair also notably increased the dispersion of coolant away from the surface. This vortex pair likely developed due to a skewed velocity profile at the exit of the film cooling hole.

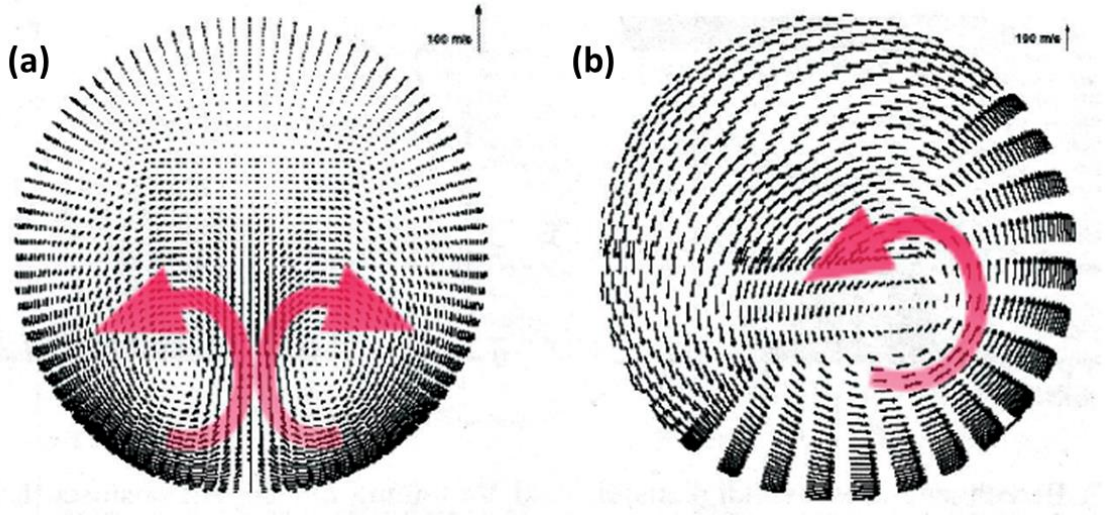

Figure 1.9: Computational predictions of secondary flows within a film cooling hole fed by (a) a plenum and (b) internal crossflow, 2*d* from the inlet of the hole [14]

1.5 PRESENT STUDY

The following conclusions can be drawn or inferred from the literature regarding axial shaped holes fed by and internal crossflow:

- Internal crossflow has been shown to reduce film cooling effectiveness relative to plenum conditions for a small range of axial hole geometries.
- This reduction in effectiveness can be attributed to biasing of the coolant within the diffuser at the exit of the holes.
- The manner of this biasing has been found to be dependent on hole geometry (hole length, inclination angle, lateral expansion angle, forward expansion angle) and flow conditions (crossflow velocity, injection rate).
- One study showed that internal crossflow Reynolds number had a negligible effect compared with crossflow-to-mainstream velocity ratio.
- One study found that heat transfer coefficient augmentation was reduced for crossflow-fed holes relative to plenum-fed holes for a single fan-shaped geometry.
- A compilation of computational and tangentially related experimental studies suggest that the biasing in the diffuser is the result of a swirling flow within the hole that is initiated by the crossflow at the hole inlet.

While the above conclusions are indeed valuable and provide engine designers with considerable insight, there are many questions concerning the nature of the crossflow effect left to be answered. This is especially true for compound angle shaped holes, for which there exists almost no useful data in the literature. And while there are certainly more questions to be answered than can be addressed in the scope of this study, the following have been investigated:

How does internal crossflow velocity and injection rate affect film cooling? The literature indicates that both crossflow-to-mainstream velocity ratio, VR_c, and coolant jet-to-mainstream velocity ratio, VR, are important to understanding how internal crossflow affects film cooling performance. To investigate this effect, the following parameter ranges were tested for both axial and compound angle shaped holes: VR_c = 0.2-0.6 and VR = 0.2-1.7. This is the first study to systematically vary these parameters in this manner in the open literature. Furthermore, no open literature experimental study has tested the effect of internal crossflow velocity on compound angle shaped film cooling holes. Film cooling effectiveness was measured for both hole types and heat transfer coefficient augmentation was measured for the compound angle holes at selected conditions. To enhance the analysis of the results, a number of jet characteristic parameters were defined in order to quantify the behavior of the film effectiveness profiles. A major goal of this analysis was to identify any parameters or relationships that scaled the interaction between VR_c and VR.

What impact does density ratio have on the crossflow effect? As mentioned previously, the coolant-to-mainstream density ratio in a gas turbine engine is approximately DR = 2.0. However, in laboratory conditions, it is usually easier to test at lower density ratios. The axial holes were tested at both DR = 1.2 and 1.8 to determine what similarities were maintained across the difference in density ratio. These types of density ratio sensitivity analyses have been performed for plenum-fed holes, but never for holes fed by an internal crossflow.

What is the root cause behind the behavior of crossflow-fed holes? A few computational studies have predicted that internal crossflow results in a strong swirl within the film hole, causing the experimentally observed biasing within the diffuser and reduction in film

cooling effectiveness. And, as previously mentioned, there are a few tangentially relevant experimental studies that suggest the existence of such a swirl. However, this phenomenon has never been directly experimentally investigated. In pursuit of this root cause thermal field measurements within and just downstream of the diffused section of the hole were performed. The purpose of the thermal fields is to investigate the nature of the biased coolant within the diffuser and how that influences the spread of coolant downstream. Additionally, velocity field measurements within the diffuser were made in order to determine whether the crossflow effect was indeed the result of swirling flow within the hole. Experimental evidence of this phenomenon is essential to confirm previous computational predictions and highly valuable to developing better hole designs that will perform more effectively when fed by crossflow.

How do these results influence film cooling design? It is desired that the results of this study provide insight into gas turbine film cooling in a manner sufficient to inform better design practices. Therefore, as much as possible, the results and observations of this study will be discussed in terms of their applicability to engine design. Additionally, the one-dimensional model for overall cooling effectiveness given in Equation 1.9 was used to predict overall effectiveness, taking into account both the benefits and disadvantages of increasing internal crossflow velocity. This model also proved to be a useful tool for investigating various design parameters that were outside the experimental scope of this study.

Chapter 2 describes the experimental facility and methods used to investigate these questions. These questions are addressed separately for axial holes and compound angle holes in Chapters 3 and 4 respectively, and conclusions are presented in Chapter 5.

Chapter 2: Experimental Facility and Procedures

The experimental facility and measurement techniques used to acquire the data for this study are presented in this chapter along with a description of data processing techniques where applicable. An assessment of repeatability and uncertainty for each technique is also presented.

2.1 Flat Plate Facility

All experiments for this study were performed in a low speed recirculating wind tunnel at the University of Texas at Austin. The facility was set up in a flat plate configuration, which isolated film cooling performance for a row of holes from the effects of curvature, mainstream pressure gradient, and upstream film injection present on an airfoil. Mainstream conditions, such as relative boundary layer thickness, turbulence intensity, and integral length scale were set to simulate the low curvature region on the suction side of an airfoil. Where possible, important dimensionless parameters, including external Reynolds number, injection and crossflow velocity ratios, and coolant-to-mainstream density ratio, were held at engine-relevant conditions. Prior to the initiation of this study, substantial upgrades were performed to increase the velocity in the test section and to increase the ease of operation. The following sections provide further detail regarding the facility, its subsystems, and the upgrades that were made to the system.

2.1.1 Main Flow Loop

The main flow loop, shown in Figure 2.1, was driven by a 22 kW belt-driven centrifugal fan. This fan replaced the previous 3.7 kW direct drive centrifugal fan as part of an effort to increase the maximum velocity in the test section from 25 m/s ($Ma_\infty = 0.07$) to 68 m/s ($Ma_\infty = 0.20$). A variable frequency drive (VFD) was used to modulate the speed of the motor, allowing a wide range of mainstream velocities.

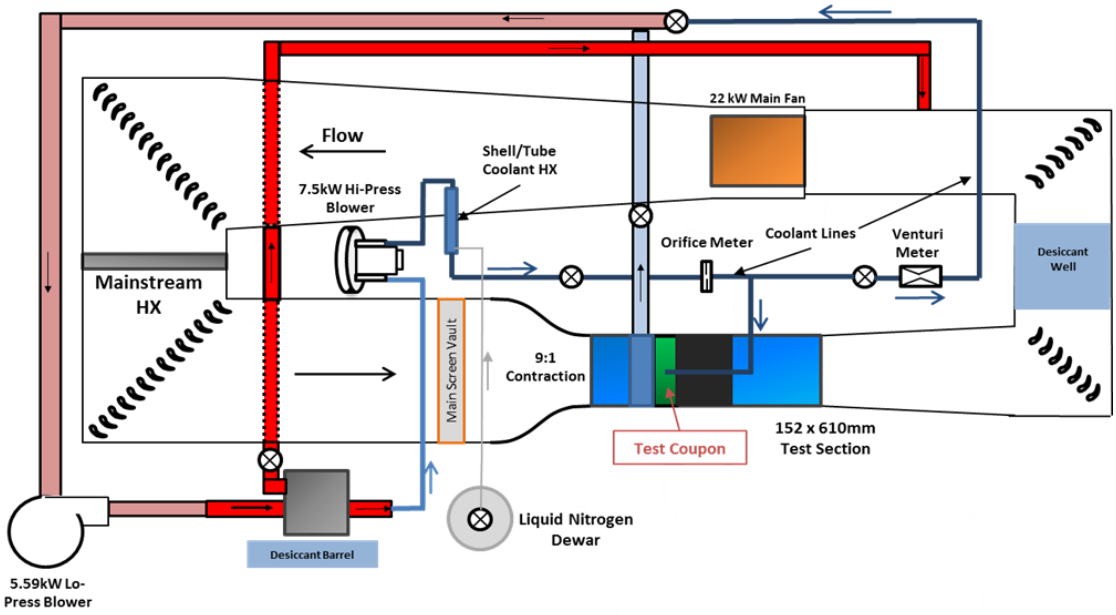

Figure 2.1: Schematic of the recirculating flat plate film cooling experimental facility

A cooling loop was used to control the temperature of the main flow loop. A 5-ton chiller (not shown) was installed and connected to a water-to-air heat exchanger that removed the heat added to the system by the main fan. A 60 gallon buffer tank and a PID-controlled Belimo modulating valve were used to isolate the mainstream heat exchanger from the chiller in order to reduce the fluctuations that the cycling of the chiller would otherwise impose on the mainstream temperature. Additionally, at lower velocities, a variac-controlled heating element was used to heat the cooling loop to reduce chiller cycling or to maintain a higher mainstream temperature if desired. The system was capable of maintaining a set mainstream temperature to within ±0.5 K over a range of T_∞ = 290-310 K.

Moisture was removed from the air in the main and secondary loops to minimize the buildup of frost in the system due to coolant injection at cryogenic temperatures. Six packs of desiccant containing about 27 kg of 13x molecular sieve were installed in two

locations. Three packs were installed in the main flow loop, oriented parallel to the flow to limit pressure loss, and another three packs were installed in a repurposed oil drum for the purpose of drying the air to be used as coolant. The desiccant was regenerated in an oven at a temperature of 230°C overnight between experiments. At the beginning of each experiment the desiccant packs were inserted to the tunnel and the system was allowed to dry for about 30 minutes. Over that time period, the relative humidity in the tunnel was reduced to < 0.5% and the dew point was suppressed to T_{dp} < -35°C.

Additional flow elements were used in the main flow loop. A series of screens and honeycomb elements installed upstream of the test section straightened the flow and removed large scale turbulence structures. A 9:1 contraction nozzle ensured a uniform flow into the test section at a turbulence level of Tu_{inlet} = 0.5%. After the test section, the flow was diffused in stages to its maximum width at the mainstream heat exchanger. Turning vanes in the corners reduced losses in the main flow loop.

2.1.2 Coolant Supply

The temperature difference between the hot mainstream gas and coolant in a gas turbine engine was simulated by injecting coolant at cryogenic temperatures. A 5.6 kW blower drove a secondary flow loop that provided air for the cooling loop and allowed for boundary layer suction control in the test section (discussed in Section 2.1.3). A portion of the secondary flow was drawn into the coolant loop by a 7.5 kW regenerative blower after being dried in the desiccant barrel. The speed of the regenerative blower was controlled by a VFD to allow for fine control of the flow rate of air through the coolant loop. The dry air exchanged heat with liquid nitrogen in a shell and tube heat exchanger. The system was configured to allow either the air from the secondary loop or the superheated nitrogen gas as coolant. It was easier to modulate the flow rate of coolant when air was used as coolant

but using pure nitrogen eliminated the formation of frost in the coolant loop for higher density ratio experiments. The coolant supply to the test section was designed in such a way that the coolant could either all be exhausted through the film cooling holes, or, more often, a fraction of it would be used for film cooling while the rest would be exhausted back into the secondary flow loop. The inlet and outlet coolant flow rates were measured using obstruction flow meters, the use and accuracy of which is discussed in Section 2.3.4.

2.1.3 Test Section and Models

The test section was configured for film cooling measurements over a zero pressure gradient flat plate. Prior to the experiments performed for this study, considerable effort was applied to upgrading the test section for improved control of the turbulence level and the approach boundary layer as well as improved ease of use. Figure 2.2 shows a side-view schematic of the test section. The inlet of the test section was 6" x 24" (152 x 610 mm). The inlet air had a low turbulence intensity and a uniform velocity profile due to upstream flow conditioning.

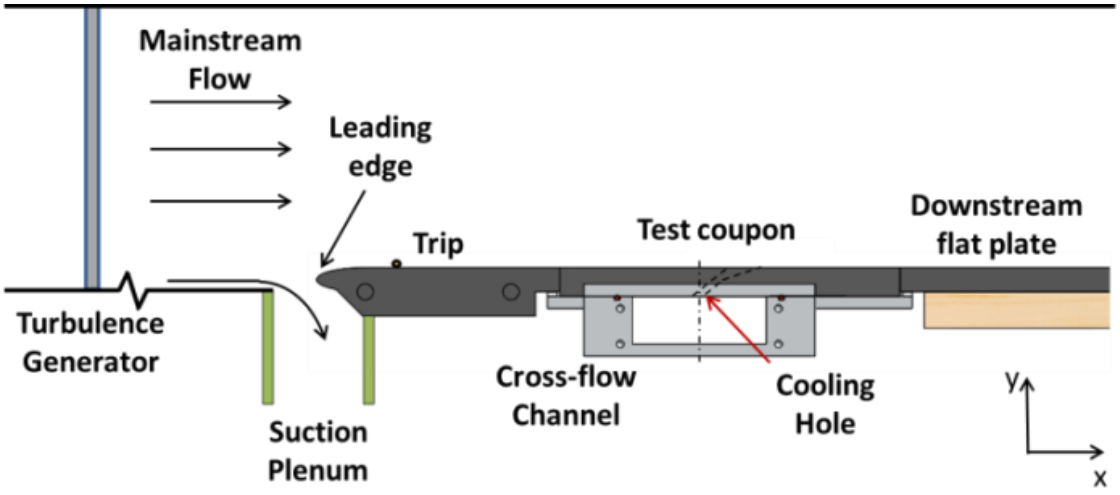

Figure 2.2: Schematic of the flat plate test section

Control over the turbulence level was afforded by a passive turbulence grid composed of an array of vertical aluminum bars. The grid was removable and could be installed in one of three slots at different streamwise locations, allowing for variable turbulence intensity at the injection location. The bars of the grid were 3/8" (9.5 mm) in diameter and spaced at a pitch of 1" (25.4 mm) apart for a solidity of 0.375. The construction of the turbulence grid made it possible to install different sized rods to adjust both the turbulence level and the turbulence integral length scale. For the experiments performed in this study, the grid was located 600 mm upstream of the hole breakout plane ($x/d = 0$) and produced a measured turbulence intensity of $Tu_\infty = 4.8\%$ at that location that was uniform across the span of the test section. The freestream turbulence integral length scale for this grid location was measured to be $\Lambda_x = 10$ mm. Both of these parameters were measured for the mainstream velocity of $U_\infty = 25$ m/s tested in this study.

Boundary layer control was enabled by a suction plenum which removed the boundary layer developing on the bottom wall of the test section and allowed a new boundary layer to develop starting at an elliptical leading edge located 250 mm upstream of the film cooling holes. A butterfly valve installed in the suction line was used to modulate the flow rate through the suction plenum so that the flow stagnated at the leading edge where desired. Pitot-static probes were mounted upstream and downstream of the suction plenum to measure the mainstream velocity at each location. A conservation of mass analysis was used to show that the ratio of the downstream and upstream velocities should be set to 1.04. In practice it was found that setting the ratio to 1.00 or less produced the thinnest boundary layer just upstream of the film cooling hole location. Minimizing the thickness of the boundary layer was important for experiments where a very thin boundary layer or even a laminar approach boundary layer was desired. If an experiment called for a thicker boundary layer, a cylindrical rod could be adhered to the surface upstream of the

film cooling holes to cause transition to a turbulent boundary layer prematurely. For the purpose of this study, a thick turbulent boundary layer was desired, so a 1/8" (3.175 mm) cylindrical trip was installed 105 mm upstream of the film cooling hole break out location. This produced a boundary layer thickness of δ_{99} = 11.5 mm, or three times the hole diameter. Boundary layers far downstream on the suction side are commonly thick relative to the hole diameter due to upstream coolant injection. McClintic *et al* [44] measured a boundary layer thickness of about 2*d* in this region with upstream injection. While this thickness is shorter than what was used in this study, that study also measured a region of increased turbulence due to upstream injection that persisted to about 3.5*d* above the surface.

The test section was designed with removable and adjustable floors to allow for ease of changing out the coolant supply and downstream run-out plate. The coolant channel and floors were supported by four threaded rods that allowed for the height and tilt of the test coupon and run-out plate to be adjusted such that they were level and flush with each other and with the upstream leading edge. The gap between the test coupon and the run-out plate was filled with a lightweight spackle to ensure a smooth transition between the plates that minimally disturbed the flow.

For all experiments in this study, flow was provided to the film cooling holes by an aluminum channel oriented perpendicularly to the mainstream flow. This channel was first used and is described in detail in McClintic *et al.* [21]. A schematic of the channel is shown in Figure 2.3. The channel had a cross-sectional area of 25 x 70 mm and a hydraulic diameter of d_H = 36.8 mm. Screens at the inlet removed gradients in the flow to promote a fully developed velocity profile within the channel. An approach profile was measured 250 mm or 6.8 d_H downstream of the inlet and is shown in Figure 2.4. The measured approach profile was symmetric and compared well to a long development measurement profile

measured on the other side of the test section with the holes taped off. The similarity of the approach and long development profiles to each other and to the 1/7 power law indicates that the approach flow in the channel was turbulent fully developed internal flow.

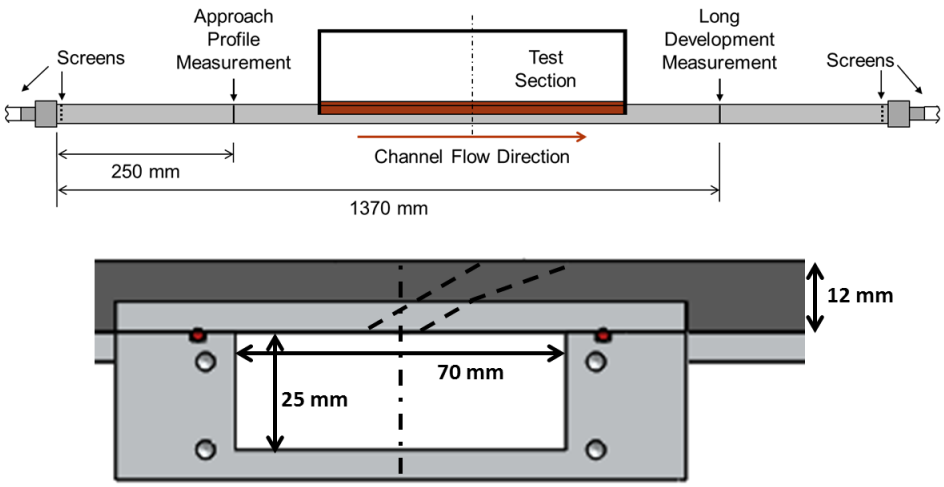

Figure 2.3: Schematic of the coolant supply channel

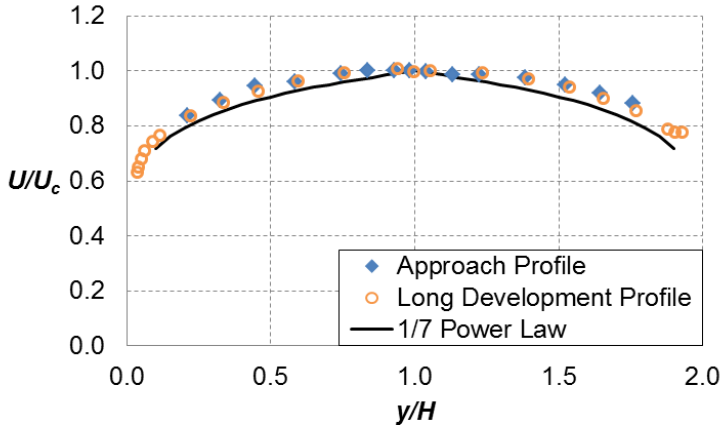

Figure 2.4: Channel velocity profile measurements

The test coupons were machined out of a closed cell polyurethane foam (General Plastics Last-a-Foam R-3315). The foam had a reported thermal conductivity of $k = 0.044$ W/m·K, which was suitable for approximating an adiabatic surface. A single row of eight film cooling holes was machined into each test coupon. The film cooling geometry selected for this study was the open-literature laidback fan-shaped hole introduced by Schroeder and Thole [11]. A detail of the hole geometry, hereafter referred to as the "7-7-7" hole, is shown in Figure 2.5. The hole had an injection angle, of $\alpha = 30°$, lateral expansion and forward expansion angles of $\beta = \gamma = 7°$, a length of $L = 6d$, a metering hole length of $L_m = 2.5d$, and an area ratio of $AR = 2.5$. In this study both axial holes ($\varepsilon = 0°$) and compound angle holes ($\varepsilon = 45°$) were tested. The coordinate origin for each set of holes was located at the midpoint of the hole breakout as shown. The internal crossflow feeding the axial holes was directed in the positive z-direction. For the compound angle holes, the crossflow was directed both in-line with and counter to the spanwise direction of injection as shown in the figure.

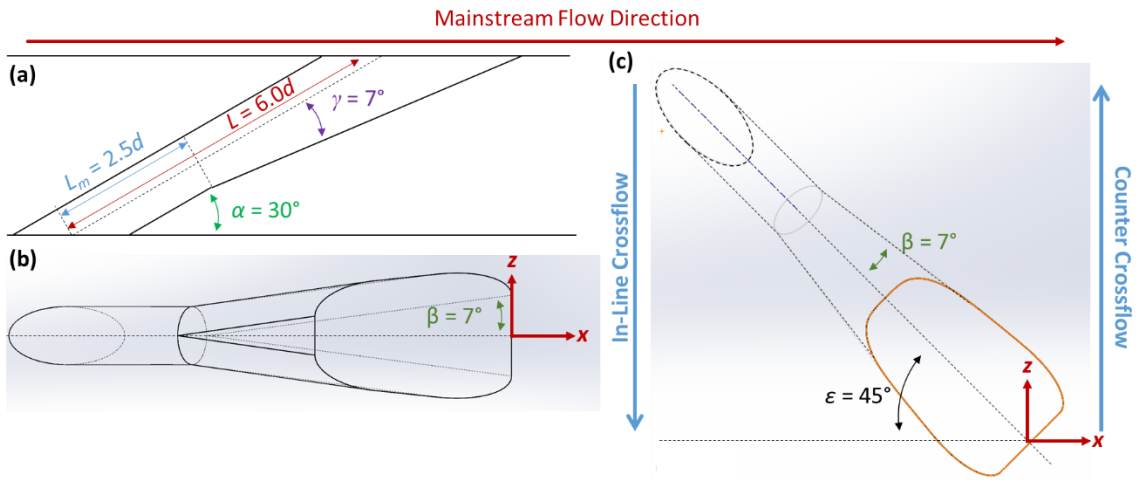

Figure 2.5: Diagram of 7-7-7 film cooling hole (a) side view, (b) top view of axial hole (c) top view of compound angle hole

2.2 EXPERIMENTAL CONDITIONS

2.2.1 Freestream Conditions

Table 2.1: Freestream parameters

Parameter	*Axial*	*Compound Angle*
Cooling Hole Diameter, d	4.0 mm	5.0 mm
Mainstream Temp, T_∞	310 K	310 K
Mainstream Velocity, U_∞	25 m/s	25 m/s
Mainstream Turbulence Intensity, Tu	4.8%	4.8%
Turbulence Integral Length Scale, Λ_x/d	2.5	2.0
Approach Boundary Layer Thickness, δ_{99}/d	2.9	2.3
Boundary Layer Displacement Thickness, δ^*/d	0.36	0.29
Boundary Layer Momentum Thickness, θ/d	0.27	0.22
Boundary Layer Shape Factor, H	1.33	1.33
Approach Reynolds Number, Re_d	6,000	7,500

The freestream conditions in Table 2.1 were held constant for all the experiments in this study. The highly turbulent mainstream and thick turbulent approach boundary layer were selected to simulate approach flow in the low curvature region of the suction side of a turbine blade. Upstream showerhead injection, as well as injection from other upstream film cooling rows is expected to thicken the boundary layer and increase the turbulence level therein. Note that there is a minor inconsistency introduced by the different film cooling hole diameters for the axial and compound angle holes. The mainstream velocity and boundary layer thickness were held constant, so the scaled parameters are somewhat different. These slight differences in relative boundary layer thickness and freestream Reynolds number are not expected to have a strong effect on the results based on a study by Anderson *et al* [45] who studied the effect of boundary layer thickness and mainstream Reynolds number for axial 7-7-7 holes. In that study, when the displacement thickness was doubled, the laterally averaged effectiveness increased by 0.05 at most for a turbulent mainstream, whereas the change in δ^*/d between geometries was only 19%. Furthermore, in Anderson *et al* [45], tripling the Reynolds number caused a similar magnitude change in

laterally averaged effectiveness, but the change in Reynolds number between conditions for this study was only 25%.

2.2.2 Coolant Conditions

Table 2.2: Coolant parameters

Parameter	***Axial, DR = 1.8***	***Axial, DR = 1.2***	***Compound Angle DR = 1.2***
Coolant Temp, T_c	172 K	258 K	258 K
$VR = U_j/U_\infty$	0.3 - 1.7	0.3 - 1.7	0.2 - 1.7
$VR_c = U_c/U_\infty$	0.2 - 0.5	0.2 - 0.6	0.2 - 0.6
$VR_i = U_c/U_j$	0.1 – 1.8	0.1 - 2.1	0.1 – 3.3
$M = \rho_\infty U_\infty/\rho_j U_j$	0.5 - 3.0	0.3 - 2.0	0.2 - 2.0
$Re_c = \rho_c U_c d_H/\mu_c$	31,000 - 78,000	15,000 - 45,000	15,000 - 45,000
r_x	3 - 48%	3 - 48%	2 - 48%

The coolant conditions in Table 2.2 are given in terms of the range over which those parameters were varied over the course of experimentation. The ranges of interest were chosen after consultation with the sponsors of this work and are believed to represent engine-relevant conditions. Three different coolant configurations are denoted in Table 2.2: axial holes at density ratio of DR = 1.2 and 1.8 and compound angle holes at DR = 1.2. DR = 1.8 approaches the range of engine realistic density ratios, which can exceed DR = 2.0. However, due to the difficulty of maintaining steady state conditions and combating the formation of frost at DR = 1.8, most of the experiments in this study were performed at DR = 1.2 once the observed trends at DR = 1.8 were replicated at DR = 1.2. Note that based on the results of Wilkes *et al.* [5], no attempt was made to hold the crossflow Reynolds number, Re_c, constant when varying VR_c or even to maintain a constant Re_c for the same VR_c when varying DR. Given that a number of important trends were maintained for the axial holes when DR was changed from 1.8 to 1.2, the assumption that Re_c has little effect on film cooling performance appears to be justified. Note that the extraction ratio, r_x, or the percentage of mass flow into the channel that was extracted as film cooling was held below

50%. For all conditions tested, even at the lowest injection rates, there was no evidence of a spanwise jet-to-jet trend to indicate that either static pressure drop through the channel or extraction of coolant affected the film cooling effectiveness.

2.3 Standard System Measurement Techniques

For all experiments conducted in this study, temperature, pressure, velocity, and flow rate measurements were essential to setting the correct experimental conditions. The following is an overview of the methods used to make these measurements and the accuracy of the techniques employed.

2.3.1 Gas Temperature Measurements

Bead type thermocouples were used to measure gas and water line temperatures throughout the system. Type T thermocouples were used for system monitoring to track the temperatures in the heat exchangers, cooling water loop, and chiller loop. These measurements were primarily used for system troubleshooting and were not directly incorporated into data processing. The reported accuracy of the NIST calibration for type T thermocouples is the greater of ± 1.0 K or ± 0.75% of the measured value, which was sufficient for these purposes.

Type E thermocouples were used to measure all temperatures that were used in calculating the mainstream and coolant conditions and flow rates. The NIST calibration for type E thermocouples has a reported accuracy that is the greater of ± 1.7 K or ± 0.5% of the measured value. To improve the accuracy of the specific thermocouples used in this system, they were calibrated against liquid nitrogen, a distilled water ice bath, and boiling water. The calibration yielded a linear function that was applied to the output of the NIST calibration. Once calibrated on a specific DAQ input channel, the thermocouple would only be used in that channel so that the calibration accounted for the resistance of the wire,

extension, and channel. The accuracy of these calibrations, established by evaluating the repeatability of the calibration, was on the order of ±0.2 K, a notable improvement from the accuracy of the NIST calibration.

The calibrated type E thermocouples were used to measure various temperatures in the system. The mainstream temperature, T_∞, was measured as the average of three thermocouples inserted through the floor of the test section near the inlet. The temperatures measured by the calibrated mainstream thermocouples were within ± 0.015 K of each other. The coolant temperature, T_c, was measured as the average of two thermocouples – one just upstream of the channel inlet and the other just downstream of the channel outlet. It was shown that the average coolant temperature and the temperature measured by inserting a thermocouple probe into the diffused section at the exit of the film cooling hole were within ±0.5 K. Type E thermocouples were also used to measure the temperatures in the inlet and outlet obstruction flow meters in order to compute the air properties at those locations.

2.3.2 Pressure Measurements

An array of pressure transducers was used to measure gauge pressures and pressure differences throughout the system. These transducers were all calibrated against a micro-manometer over their full range. Table 2.3 lists the pressure transducers used, their range and accuracy, and what they measured. Note that the channel inlet and outlet pressure transducers measured the static pressure in the channel near the location of the channel velocity profiles shown in Figure 2.3.

Table 2.3: Pressure transducers used in this study

Designation	*Used to Measure*	*Range (Pa)*	*Bias (Pa)*	*Precision (Pa)*
PT2	test section static pressure	0-500	± 0.65	± 0.38
PT4	outlet meter static pressure	± 6200	± 8.48	± 2.11
PT5	upstream pitot-static probe	0-2500	± 0.64	± 0.31
PT7	downstream pitot-static probe	0-250	± 0.54	± 0.34
PT8	outlet meter pressure drop	0-250	± 0.57	± 0.34
PT9	channel inlet static pressure	0-6200	± 5.69	± 1.59
PT10	channel outlet static pressure	0-2500	± 0.73	± 0.34
PT11	inlet meter static pressure	0-10000	± 8.62	± 0.65
PT12	inlet meter pressure drop	0-5200	± 4.60	± 1.05

2.3.3 Velocity Measurements

Pitot-static probes were used to measure the velocity of the mainstream flow in the test section both upstream and downstream of the suction plenum. The velocity was calculated as the difference in the total and static pressure of the flow using Equation 2.1:

$$U_\infty = \sqrt{\frac{2(p_{t,\infty} - p_\infty)}{\rho_\infty}} \tag{2.1}$$

The density, ρ, was calculated according to the ideal gas law using the measured static pressure and temperature of the test section, p_∞ and T_∞, and the ideal gas constant for nitrogen: R_{N2} = 296.8 J/(kg·K). The ideal gas constant for nitrogen was used in place of that of air because the injection of nitrogen into the system displaced the oxygen in the tunnel during the experiment. The estimation of uncertainty for the freestream velocity, U_∞ was calculated according to Equation 2.2:

$$U_\infty = \sqrt{\frac{2R_{N2}T_\infty(p_{t,\infty,g} - p_{\infty,g})}{p_{atm} + p_{\infty,g}}} \tag{2.2}$$

where the subscript g indicates the measured gauge pressure. The bias and precision uncertainties in p_{atm} were assumed to be $\delta p_{atm,b}$ = ± 500 Pa and $\delta p_{atm,p}$ = ± 200 Pa respectively. The sequential perturbation method of Moffat [46] was used to estimate the

bias and precision uncertainties in the freestream velocity to be $\delta U_{\infty,b}$ = ± 0.076 m/s and $\delta U_{\infty,p}$ = ± 0.029 m/s respectively. These uncertainties are smaller than the measured fluctuations of U_∞ over the course of an experiment, which were usually on the order of ± 0.1 m/s.

2.3.4 Flow Rate Measurements

Obstruction flow meters were used to measure the flow entering and exiting the channel such that the film cooling mass flow rate could be calculated as the difference between the two flow rates. Depending on the expected mass flow rate of coolant, different meters were used in order to have a sufficiently high pressure drop across the flow meter to allow for accurate measurement. The flow meters used over the course of this study are listed in Table 2.4 below along with their dimensions.

Table 2.4: Summary of obstruction flow rate meters

Designation	Throat Diameter (d_{th})	Pipe Diameter (d_p)	β	Calibration Standard
Inlet Orifice	27.9 mm	52.4 mm	0.53	ASME (Eqn. 2.3)
Outlet Venturi	36.8 mm	52.4 mm	0.70	Inlet Flow Meter
Outlet Orifice	24.9 mm	40.2 mm	0.62	Inlet Flow Meter

The inlet orifice was installed according to ASME standards so the standard ASME calibration, given in Equation 2.3, was used to determine its discharge coefficient. This correlation has a stated accuracy of ± 1%.

$$C_d = 0.5959 + 0.0312\beta^{2.1} - 0.184\beta^8 + 0.0029\beta^{2.5}\left(\frac{10^6}{Re_p}\right)^{0.75} \tag{2.3}$$

Two different outlet flow meters were used: a Venturi and an orifice meter. The Venturi meter was used for higher crossflow velocity ratios, $VR_c \geq 0.3$, because it had a lower pressure drop and a calibration that was insensitive to the pipe Reynolds number, Re_p, at higher flow rates. The outlet orifice plate was used for lower crossflow velocity ratios, $VR_c \leq 0.3$, because the pressure drop across the Venturi meter for these conditions was too low to measure accurately. $VR_c = 0.3$ was the overlap point for which film cooling effectiveness was measured using both the outlet Venturi and orifice meters to ensure test-to-test repeatability. The outlet meters were calibrated using the inlet orifice meter as the calibration standard. Calibrating them in this way ensured that the film cooling flow rate, which was calculated as the difference between the measured inlet and outlet flow rates, was not subject to bias errors from the flow meter calibrations. The calibration for the outlet flow meters was of the form:

$$C_d = a_0 + a_1\left(\frac{10^6}{Re_p}\right)^{0.75} + a_2\left(\frac{10^6}{Re_p}\right)^{1.5} \tag{2.4}$$

The mass flow rate through the flow meters was calculated iteratively using the following equations in conjunction with the appropriate calibration for C_d:

$$Re_p = \frac{4\dot{m}}{\pi\mu d_p} \tag{2.5}$$

$$\dot{m} = \frac{\pi}{4} d_{th}^2 \rho \frac{C_d}{\sqrt{1-\beta^4}} \sqrt{\frac{2\Delta p}{\rho}} \tag{2.6}$$

Because the mass flow rate was measured for the full row of holes, it is possible that there was some variation in the flow rate from hole-to-hole. Based on pressure

measurements in the channel upstream and downstream of the row of holes, it was estimated that the injection rate did not vary by more than 1.6% from the first to the last hole in the row of eight holes and for most conditions, that variation was less than 0.5%. A sequential perturbation analysis was used to estimate the bias and precision uncertainties in the important dimensionless coolant flow rate parameters: VR, VR_c, and VR_i. The measured values that were sequentially perturbed in this analysis included the pressure drop across the flow meters, the static pressures and temperatures used to determine fluid properties, the dimensions of the flow meters and film cooling geometry, and the freestream velocity. Additionally, the fossilized bias in the flow meter calibrations was taken into account when determining the uncertainty of the crossflow velocity, U_c. The following equations show how these dimensionless parameters were computed from the inlet and outlet mass flow rates:

$$VR = \frac{U_j}{U_\infty} = \frac{\dot{m}_{in} - \dot{m}_{out}}{N_h \frac{\pi}{4} d^2 \rho_c U_\infty} \tag{2.7}$$

$$VR_c = \frac{U_c}{U_\infty} = \frac{\dot{m}_{in}}{A_c \rho_c U_\infty} \tag{2.8}$$

$$VR_i = \frac{U_c}{U_j} = \frac{VR_c}{VR} = \left[\frac{A_c}{N_h \frac{\pi}{4} d^2} \left(1 - \frac{\dot{m}_{in}}{\dot{m}_{out}} \right) \right]^{-1} \tag{2.9}$$

Table 2.5 lists the bias and precision uncertainties for these dimensionless parameters at a selected condition: $VR = 1.11$, $VR_c = 0.5$, and $VR_i = 0.45$ for the 4 mm axial holes. Note that the precision uncertainties were at least an order of magnitude lower than the bias uncertainties. The uncertainty for VR_c was very small (< 1% of the calculated value) and can generally be considered negligible. The high bias uncertainty for VR was

driven primarily by the uncertainty in the film cooling hole diameter, which was measured to an accuracy of ± 0.1 mm. This bias therefore does not affect comparisons between experiments in this lab using different outlet flow meters because the same test coupon was used for all experiments. This bias uncertainty does however, affect comparisons between this work and that performed in other laboratories. A check of the zero-blowing condition was performed regularly throughout the course of the experiments. The holes would be taped over to force a velocity ratio of 0 and it was confirmed that the measured velocity ratio was within ± 0.05 of 0.

The precision uncertainty in VR was primarily driven by the precision in the measurement of the pressure drop across the outlet flow meter. The value of VR is more sensitive to Δp across the outlet meter than the inlet flow meter because the pressure drop was lower across the outlet meter. The uncertainty in VR_i is strongly dependent on the magnitude of VR ($VR_i = VR_c/VR$) so that as VR becomes small, any uncertainty in VR is magnified such that δVR_i increases as VR_i increases.

Table 2.5: Bias and Precision Uncertainties of Coolant Parameters for VR = 1.11, VR_c = 0.5, VR_i = 0.45

Parameter	Value	Bias Uncertainty	Precision Uncertainty
VR	1.11	0.108	0.0094
VR_c	0.50	0.005	0.0008
VR_i	0.45	0.042	0.0036

2.4 EXPERIMENT SPECIFIC TECHNIQUES

This section details the data acquisition and processing techniques used to make the primary measurements of interest to this study: film cooling discharge coefficients, adiabatic effectiveness, heat transfer coefficient augmentation, jet characteristic parameters, thermal fields, and in-hole velocity fields. Considerable effort was required to

ensure the accuracy and repeatability of these measurements not only to implement the experimental techniques, but also to ensure the proper corrections and processing techniques were applied.

2.4.1 Film Cooling Discharge Coefficients

The discharge coefficients of the film cooling holes were computed based on the measured coolant supply channel and test section static pressures and the film cooling mass flow rate. Pressure taps were machined into the top wall of the channel approximately 225 mm from the inlet and outlet of the channel. The pressure tubing connection to the pressure tap was carefully sealed with vacuum grease and tested for leaks along with the rest of the coolant system to confirm no leaks were present in the piping between the inlet and exit flow meters. The static pressure of the test section was monitored using the static pressure line from the downstream pitot-static probe used to measure the mainstream velocity. These pressure data were acquired during the course of running effectiveness experiments for all experiments performed at *DR* = 1.2. Concerns about frost forming on the channel pressure taps invalidated these data at *DR* = 1.8. The presence of frost produced discharge coefficient data that were not repeatable and changed suddenly in the early part of experiments.

The equation from Gritsch *et al.* was used to calculate C_d for the film cooling holes:

$$C_D = \frac{\dot{m}}{\frac{\pi}{4} d^2 p_{tc} \left(\frac{p_\infty}{p_{tc}}\right)^{(\gamma+1)/2\gamma} \sqrt{\frac{2\gamma}{(\gamma-1)RT_{tc}}\left(\left(\frac{p_{tc}}{p_\infty}\right)^{(\gamma-1)/\gamma} - 1\right)}} \tag{2.10}$$

The coolant pressure was calculated as the average of the channel inlet and outlet pressure, which were typically within 50 Pa of each other. Because these experiments were

performed at low speed ($Ma_\infty = 0.07$) the pressure ratio across the hole, $PR = p_{t,c}/p_\infty$ was low – less than $PR < 1.02$. A sequential perturbation analysis was used to determine the precision and bias uncertainties in the calculated discharge coefficients. The estimated precision uncertainty was $\delta C_{d,p} = \pm 0.01$ and was primarily influenced by how the precision uncertainty of the outlet flow meter influenced the measurement of $\dot{m}$. The estimated bias uncertainty was $\delta C_{d,b} = \pm 0.07$ due primarily to the bias uncertainty in the film cooling hole diameter.

2.4.2 Infrared Thermography

Infrared (IR) thermography was the primary measurement technique used in this study and was used to measure both film cooling effectiveness and heat transfer coefficient augmentation. A number of jet characteristic parameters were also derived from the effectiveness measurements and were useful in analysis of the data. Use of this technique required careful calibration of the camera and correction of the raw data to remove conduction errors.

2.4.2.1 Camera Use and Calibration

A FLIR model A655sc infrared camera was used to measure the temperature distribution on the test coupon and runout plate. The camera had a resolution of 640x480 pixels. A wide angle lens with a 13 mm focal length was used to view the surface over a region spanning from 20 mm upstream of the holes to 200 mm downstream of the hole and four hole pitches laterally. This viewing region roughly corresponded to 0.34 mm per pixel (0.07-0.08d). The actual resolution of the camera was somewhat greater as there was a small degree of smearing of temperature gradients between adjacent pixels that made the smallest area that could be resolved by the camera 0.68 mm square (0.17d). Optical access was provided through the ceiling of the test section through a zinc-selenide (ZnSe) window

with an anti-reflective coating. During operation, the camera was shrouded to ensure no outside sources of infrared light could reflect off the ZnSe window. The test coupon and runout plate were painted with a flat black paint to give the surface a uniform emissivity of $\varepsilon \approx 0.95$. A silver paint pen was used to make fiducial marks at the edges of the viewing area on the surface which were used in post processing to map each image to real space. During the course of an experiment, the coolant temperature and flow rate was allowed to reach steady state before images were captured. A set of five or more images was captured for each condition over a period of at least five minutes. In post-processing, a check was made to ensure that the laterally averaged effectiveness did not vary outside of precision uncertainty over the time in which images were captured. The images were captured and saved using software provided by FLIR. An in-house script written in Matlab was used to perform the spatial mapping and perform other post processing operations such as applying the camera calibration and producing contour plots.

The camera was calibrated against type E surface thermocouples placed on the surface of the test coupon and runout plate. The thermocouples were constructed by spot-welding strips of chromel and constantan to create a junction that could adhere flat to a surface to accurately measure surface temperature. The thermocouples were calibrated in the same manner as the mainstream and coolant thermocouples. To ensure that the thermocouples were measuring a region of uniform temperature, they were adhered to 1 mm thick copper tabs. The thermocouple assembly was then painted with the same flat black paint used to paint the test surface and were adhered to the test surface over and downstream of the film cooling holes. The IR camera was then calibrated *in situ* so as to remove most biases such as those from the window transmissivity and surface emissivity. The calibration was performed by turning the tunnel on and slowly reducing the coolant temperature from the mainstream temperature (310 K) to the minimum temperature that

the camera could measure (about 210 K) and then slowly warming the temperature back to ambient. The temperature measured by the IR camera at the thermocouple location was then correlated to the temperature measured by the thermocouple using a second order polynomial best-fit curve. The curve fit used data from multiple thermocouples and the calibration was consistent from thermocouple to thermocouple. The IR calibration used in this study is shown in Figure 2.6 below. The uncertainty from the calibration curve fit, using a 95% confidence interval, was estimated to be δT = 0.88 K. The camera calibration was found to repeatable to within this uncertainty.

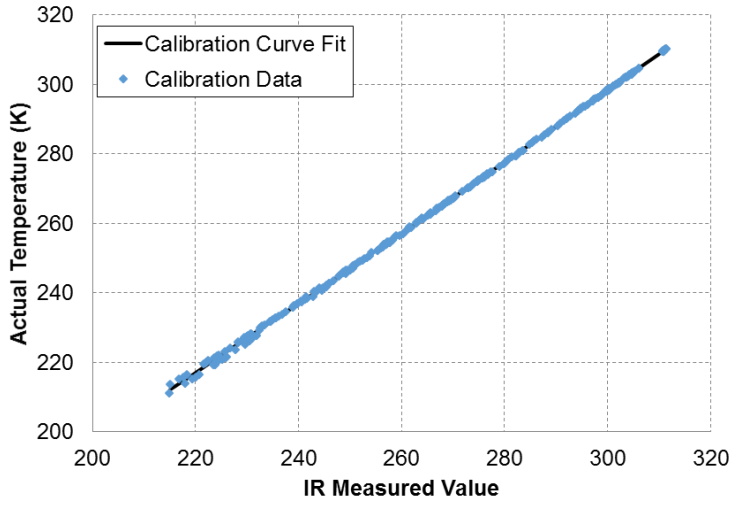

Figure 2.6: IR camera calibration used in this study

2.4.2.2 Conduction Correction for Adiabatic Effectiveness

Although the test coupon and runout plate were made of a low conductivity foam, conduction errors still affected the measured surface temperature distribution such that it was not equivalent to the adiabatic wall temperature. There were two modes of conduction that were of concern: through-wall conduction, caused by the cold aluminum channel underneath the test plate, and lateral conduction, which resulted from the lateral

temperature gradients imposed on the test surface by the film cooling jets. A three-dimensional finite element method was developed to use the measured surface temperature to predict the adiabatic wall temperature. This method was first implemented in McClintic *et al.* [21] and Klavetter *et al.* [47]. Assuming that the adiabatic wall temperature was the driving temperature for heat transfer into the test surface, it can be calculated as:

$$T_{aw} = T_{measured} - \frac{q''}{h_f} \tag{2.11}$$

This correction requires the calculation of a correction term: q''/h_f. The heat flux, q'', was computed from the measured surface temperature and model geometry using a commercially available finite element solver, Comsol Multiphysics®. Figure 2.7 shows a cross-sectional view of the finite element model along with the boundary conditions that were applied. The domain began at the downstream wall of the channel (x/d = 1.0) and did not include the film cooling holes due to the large uncertainty in the correct boundary conditions around the holes. The top surface boundary condition was the two-dimensional measured temperature of the test surface. The upstream wall of the channel was modeled as forced convection from an internal flow using Gnielinski's correlation for turbulent internal flow:

$$Nu_D = \frac{(f/8)(Re_D - 1000)Pr}{1 + 12.7(f/8)^{1/2}(Pr^{2/3} - 1)} \tag{2.12}$$

$$f = (0.79\ln(Re_c) - 1.64)^{-2} \tag{2.13}$$

The other upstream walls were assumed to be insulated based on the assumption that the lateral and through-wall conduction were much greater than streamwise conduction. A

natural convection boundary condition was applied to the bottom walls using an external room temperature of T_{amb} = 298 K. A thorough testing of the simulation showed that there was almost no sensitivity to the bottom wall boundary condition. An insulated boundary condition was assumed for far downstream and at the lateral edges of the model where temperature gradients were near-zero.

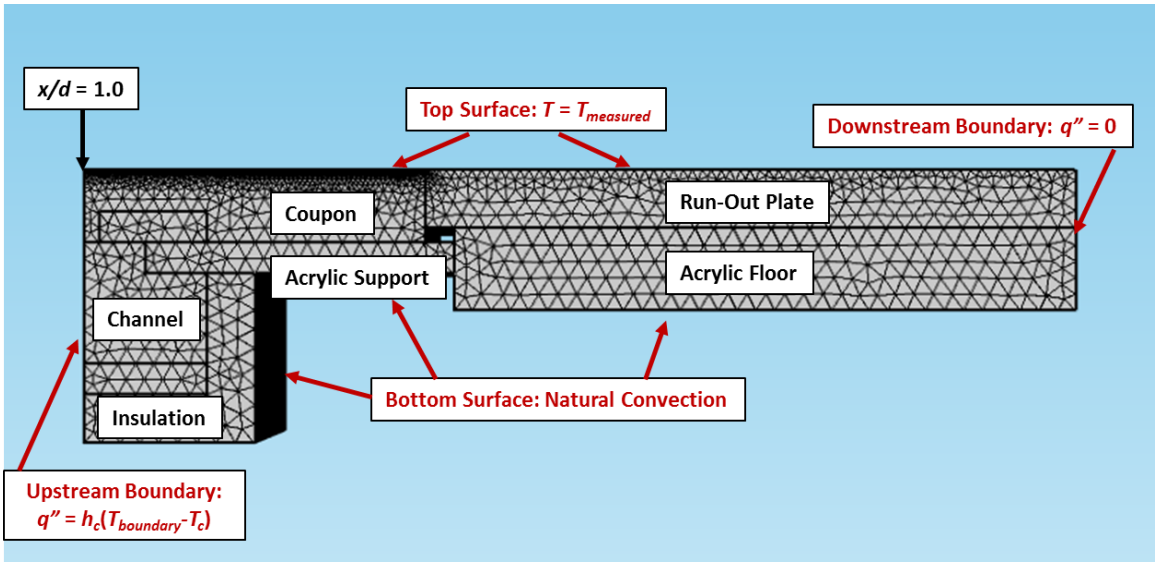

Figure 2.7 Finite element model and boundary conditions used for the conduction correction

The mesh used for the finite element solver is also shown in Figure 2.7. In the near-hole region (x/d = 1-19), a higher resolution mesh was used at the surface – with a max element size of 0.5 mm (0.125d). Further downstream, a lower resolution mash was used – max element size was 2.0 mm (0.5d). A coarser mesh with a maximum element size of 4 mm was used for regions away from the test surface. A grid independence test found that using a finer resolution in the near-hole region had no effect on the results beyond interpolation errors, which were on the order of $\delta\eta \approx 0.003$. This result was unsurprising because an element size of 0.5 mm is near the pixel resolution of the IR camera for these

experiments (0.34 mm) which governs the resolution of the top surface boundary condition. The solution was also shown to be insensitive to improved resolution in the downstream region and underneath the test surface because the temperature gradients in those regions were small.

The heat transfer coefficient with film cooling, h_f, was calculated using correlations for a turbulent boundary layer on a flat plate and with the assumption that $h_f/h_0 = 1.0$. The correlations used to predict h_0 from the measured boundary layer thickness and the flow properties were:

$$x_0 = \left(\frac{\delta_{99}}{0.37}\right)^{1.25} \left(\frac{\rho U_\infty}{\mu}\right)^{0.25} \tag{2.14}$$

$$Nu_x = \frac{h_0 x}{k} = 0.0296 Re_x^{4/5} Pr^{1/3} \tag{2.15}$$

where x_0 represents the distance that the approach boundary layer would have had to develop in order to have a thickness of δ_{99}. The calculation of x_0 was necessary because the boundary layer was tripped, so the distance from the leading edge was no longer an appropriate length scale to calculate Re_x. The value of x used to calculate Re_x in Eqn. 2.14 was equal to the sum of x_0 and the distance downstream of the approach boundary layer measurement. The assumption that $h_f/h_0 = 1.0$ was used initially as a simplification based on the results of Boyd *et al.* [48] which showed that for $VR < 2.0$ the heat transfer coefficient augmentation was close to unity. In this study, once heat transfer augmentation had been measured for the compound angle holes it was used to determine h_f in order to more accurately correct for conduction. However, it was found that there was little effect of using h_f instead of h_0 when correcting for conduction, even in regions of higher heat

transfer augmentation. Figure 2.8 shows the effect of applying the conduction correction for the compound angle film cooling holes with counter crossflow at VR_c = 0.4 and VR = 1.67. The conduction correction only affected laterally averaged effectiveness for x/d < 10, and had little effect further downstream. The correction was most prominent in the mid-pitch region between the jets – bringing the minimum effectiveness down from η = 0.07 to 0.02 in that region. More importantly, there was almost no difference between using the predicted value of h_0 and the measured h_f to determine the correction. Therefore, the data was corrected simply with h_0 because this was a simpler correction to implement.

There are limitations to applying this conduction correction method. In the near-hole region (x/d <2), it is expected that the upstream film holes caused streamwise conduction effects that were not modeled for all conditions. A simulation where cylindrical film holes were modeled instead of shaped holes (to reduce computational expense) showed that the effect of modeling the upstream film holes was not significant downstream of x/d = 2. Furthermore, the correction method did not account for the thermal boundary layer that developed as a result of the cold surface upstream of the holes due to conduction through the test coupon. As can be seen in Figure 2.8, the effectiveness in the mid-pitch region was η = 0.02, which is the result of that thermal boundary layer. This error only applies to the mid-pitch region, however, as the injection of coolant was previously shown in Stewart *et al.* [49] to force the approach thermal boundary layer to flow around the jet and not affect the centerline effectiveness. A correction to remove this thermal boundary layer has not yet been developed due to the difficulty of correcting out an error that varies in the spanwise direction by an unknown amount.

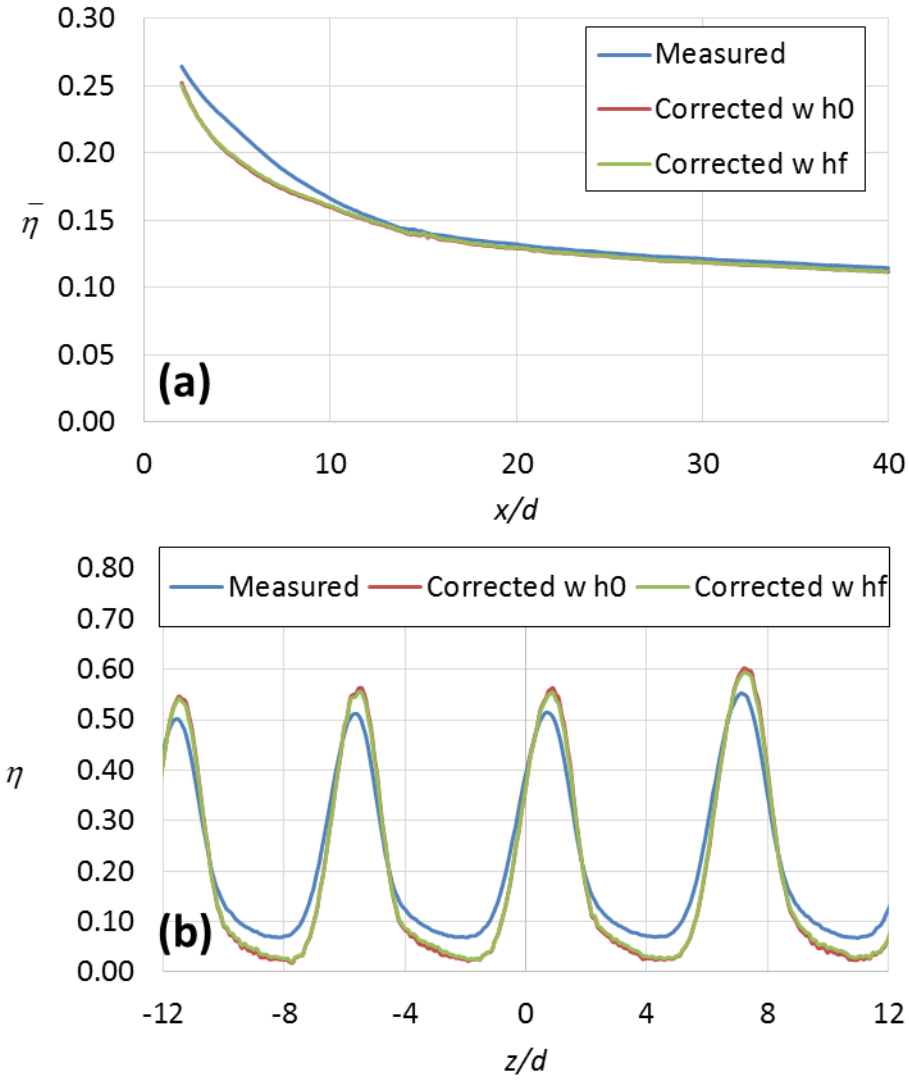

Figure 2.8: Effect of applying the conduction correction using h_0 and h_f on (a) laterally averaged η and (b) a lateral profile of η at $x/d = 5$

2.4.2.3 Repeatability and Uncertainty

The test-to-test repeatability of this method was confirmed by repeating several cases after disassembly and reassembly of the test coupon and channel. Figure 2.9 shows the test-to-test repeatability for axial holes at DR = 1.2 and VR_c = 0.3. Note that two different outlet flow meters were used for the two experiments (see Table 2.4) so this repeatability measurement is affected by the bias uncertainty from the outlet flow meter calibration. The laterally averaged effectiveness shown on Figure 2.9 were repeatable to within $\delta\,\eta = \pm 0.004$.

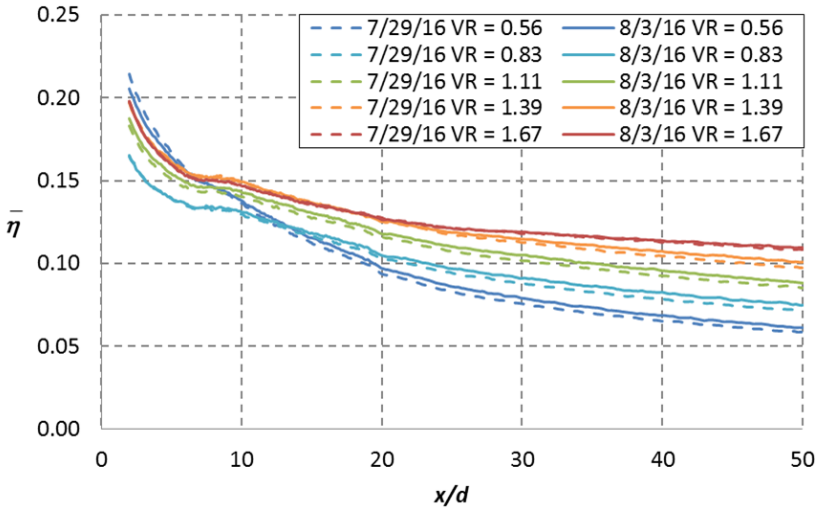

Figure 2.9: Test-to-test repeatability for laterally averaged effectiveness for axial shaped holes at DR = 1.2, VR_c = 0.3

The uncertainty in adiabatic effectiveness was estimated by sequentially perturbing the inputs to the calculation of η as well as the parameters and boundary conditions used for the finite element method. The estimate of local precision uncertainty of film cooling effectiveness is shown in Figure 2.10 (a) for axial holes at DR = 1.2, VR_c = 0.3, and VR = 1.11. The uncertainty was greatest in the near-hole region – as great as $\delta\eta_p = \pm 0.012$,

although typical precision uncertainties were closer to $\delta\eta_p = \pm 0.005$. The greatest contributor to the precision uncertainty was the precision of the IR camera from image to image as well as the interpolation errors. The precision of the camera itself was estimated by analyzing repeated images of the same condition with steady coolant and mainstream temperatures ($\delta T < 0.2$ K over 5 minutes). The interpolation error was estimated by making small changes to the mesh such that the nodes would have slightly different locations and quantifying the effect of doing so. The apparent step down in precision uncertainty at $x/d = 18$ was the result of a changing surface mesh density at that location, thus reducing the variance from image to image due to interpolation errors. Greater values of uncertainty were estimated for $DR = 1.8 - \delta\eta_p = \pm 0.011$ due to the increased jet-to-jet variation from the accumulation of frost on the test surface and in the film cooling holes. Great care was taken to inspect and defrost the holes during the course of an experiment. The holes were defrosted by forcing a negative injection rate until all visible traces of frost were gone – this process usually took only a few seconds. Only measurements where the jet-to-jet variation was within ± 0.01 in spatially averaged effectiveness were kept – the rest were assumed to be in error and discarded (note that this process only filtered out measurements at $DR = 1.8$ – measurements at $DR = 1.2$ were well within this limit). Local bias uncertainty for the same $DR = 1.2$, $VR_c = 0.3$, and $VR = 1.11$ condition is shown in Figure 2.10(b). The bias uncertainty was dominated by the IR camera calibration – as can be seen by the region of constant uncertainty $\delta\eta_b = \pm 0.014$ for $x/d > 10$. For $x/d < 10$, the higher uncertainties resulted from the combination of uncertainty due to the upstream boundary condition, model thermal conductivity, and the assumption that $h_f = h_0$ for axial holes. Bias uncertainty was estimated to be $\delta\eta_b = \pm 0.011$ for $DR = 1.8$ in the downstream region.

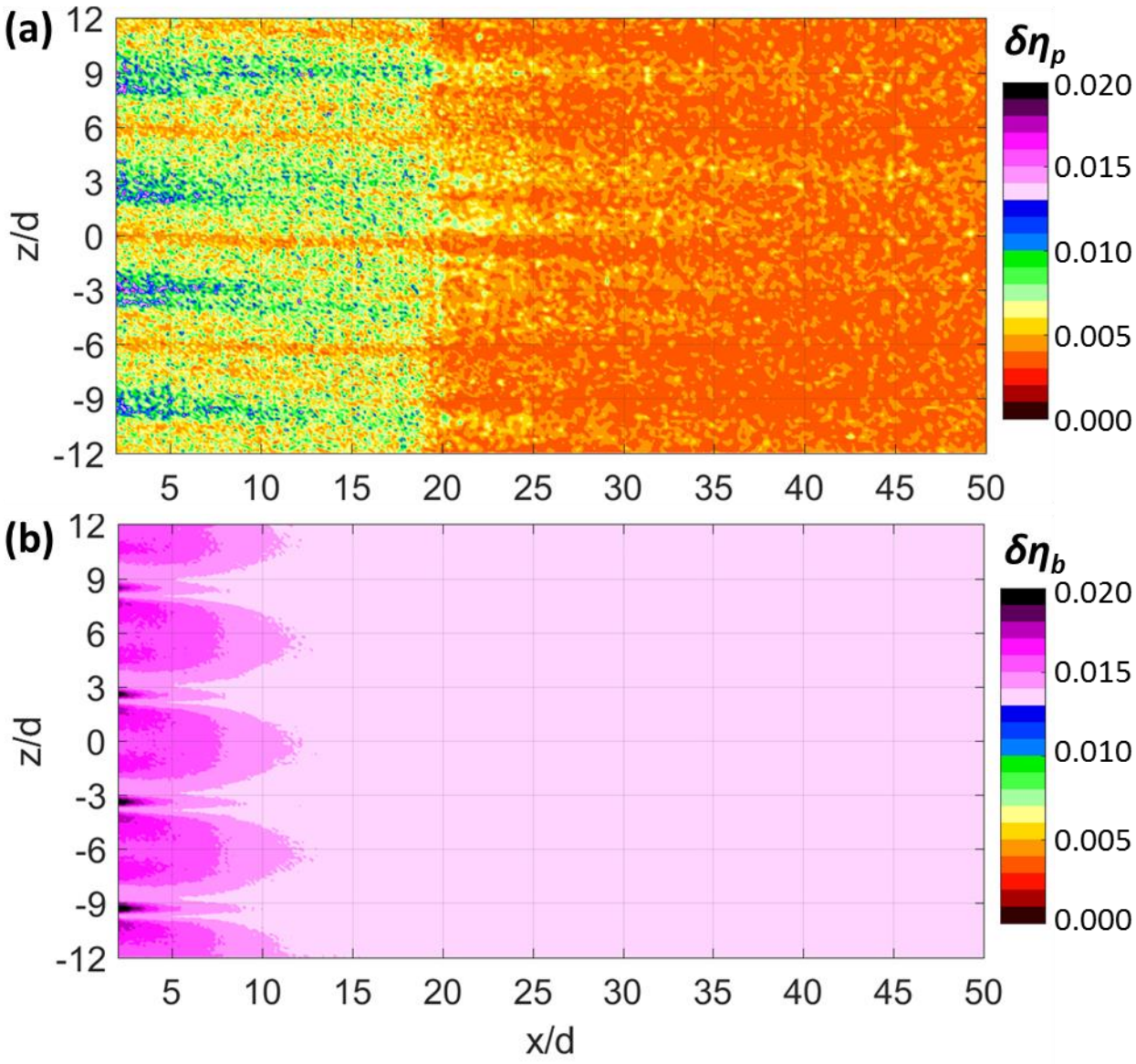

Figure 2.10: Local distribution of (a) precision and (b) bias uncertainty for axial holes at $DR = 1.2$, $VR_c = 0.3$, and $VR = 1.11$

2.4.2.4 Jet Characteristic Parameters

The analysis of adiabatic effectiveness was enhanced by considering a set of jet profile characteristic parameters. These parameters were used to quantify the effect of the internal crossflow feed on the shape and location of the film cooling effectiveness profiles. The characteristic parameters used were centerline effectiveness, η_{CL}, the location of the jet centerline, $(z/d)_{CL}$, the jet width, W, and the jet skew, S. Figure 2.11 shows how η_{CL}, $(z/d)_{CL}$, and W are defined. The centerline effectiveness, η_{CL}, refers to the peak effectiveness value at a given streamwise position, as opposed to its traditional definition as the effectiveness at the geometric centerline of the jet ($z/d = 0$). The centerline location, $(z/d)_{CL}$, was thus defined as the distance between the location of η_{CL} and the geometric centerline. Note that for axial holes, the crossflow was directed in the positive z/d direction so the jet in Figure 2.11 has a negative $(z/d)_{CL}$ value. For compound angle shaped holes, two different crossflow directions were used so the direction of the z/d axis was arbitrarily defined to be opposite the lateral direction of coolant injection, as shown in Figure 2.5. The jet width, W, was defined as the distance between the points on either side of η_{CL} where $\eta/\eta_{CL} = 0.5$. The jet skew was defined as a measure of jet asymmetry as follows:

$$S \equiv 1 - \frac{2\int_{(z/d)_{-1}}^{(z/d)_{CL}} \eta d(z/d)}{\int_{(z/d)_{-1}}^{(z/d)_{+1}} \eta d(z/d)} \tag{2.16}$$

A jet skew of $S = 0$ represents a symmetric jet. A positive skew, $S > 0$, indicates a jet where most of the cooling occurs on the positive side of $(z/d)_{CL}$, while the opposite is true if $S < 0$. The skew cannot exceed an absolute value of $|S| = 1$.

Figure 2.12 shows a sample test-to-test repeatability of the jet characteristic parameters for axial holes at $VR_c = 0.3$ and $VR = 0.83$. The repeatability was excellent for

η_{CL} and W/d – within $\delta\eta_{CL} = \pm 0.008$ and $\delta(W/d) = \pm 0.1$. Note that the maximum jet width shown was $W/d = 6.0$ which is equivalent to the pitch of the holes. Jet centerline location and skew were noisier parameters and consequently were less repeatable: $\delta(z/d)_{CL} = \pm 0.05$ and $\delta S = \pm 0.05$. The centerline location parameter became noisier going downstream due to the flattening out of the η profiles such that it became more difficult to accurately determine the location of the peak effectiveness level.

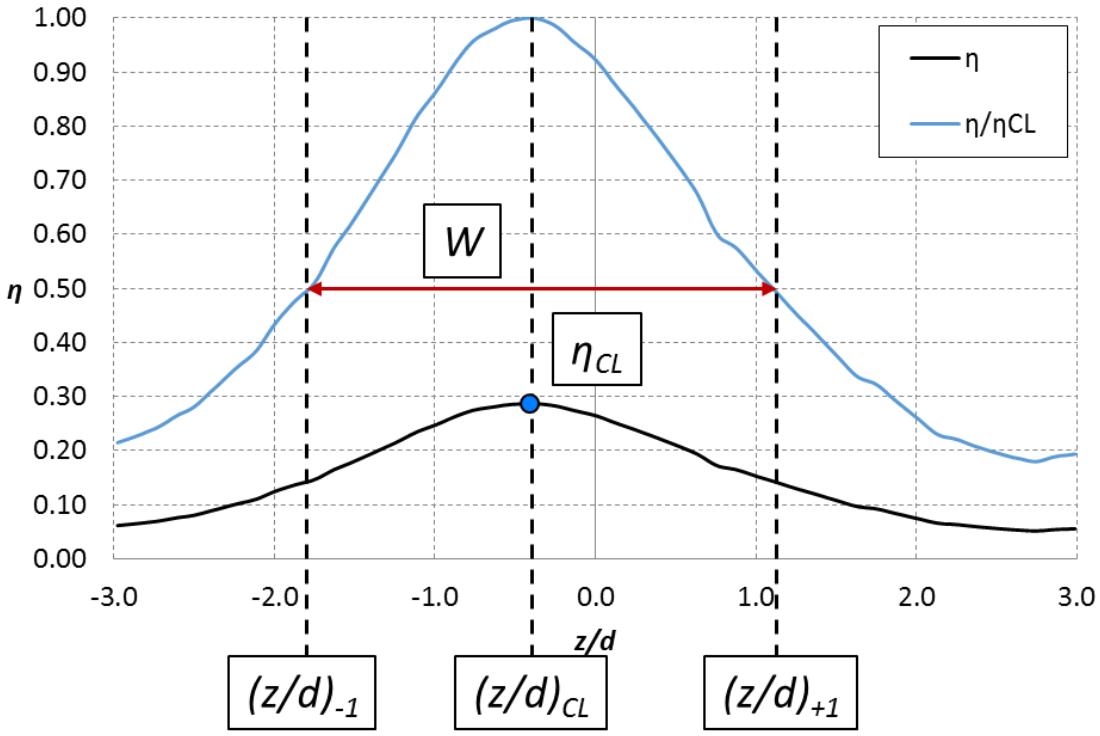

Figure 2.11: Jet characteristic parameters – sample η profile for axial holes at $x/d = 10$

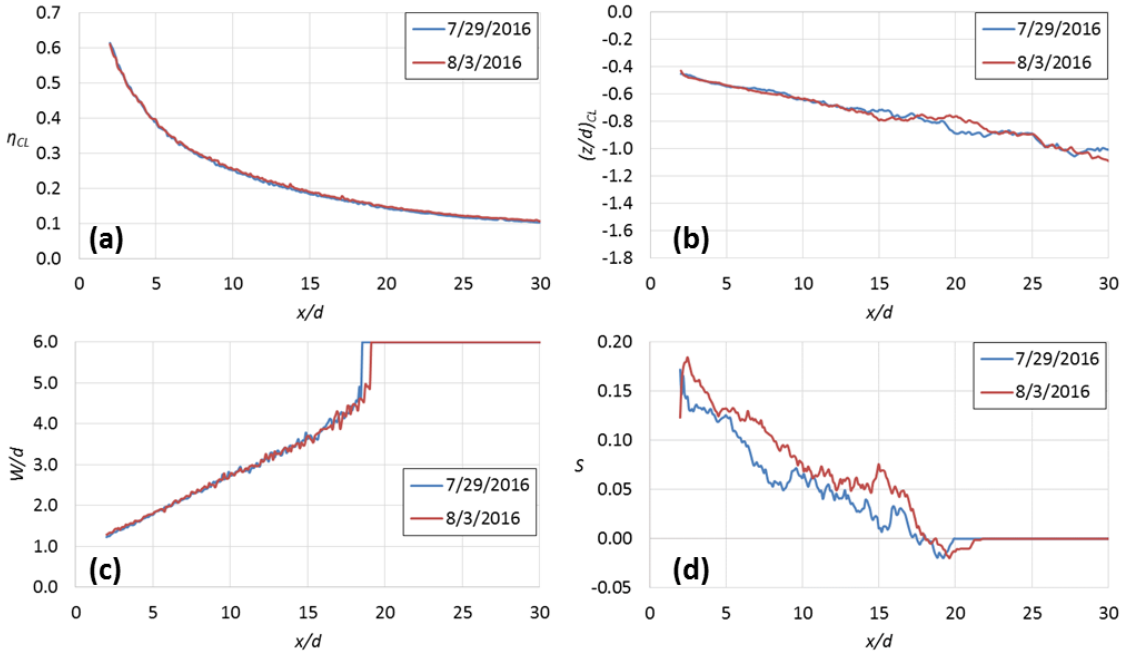

Figure 2.12: Test-to-test repeatability of (a) η_{CL}, (b) $(z/d)_{CL}$, (c) W/d, and (d) S, for axial holes at $VR_c = 0.3$ and $VR = 0.83$

2.4.2.5 Heat Transfer Coefficient Augmentation

Heat transfer coefficients in the presence of film cooling were measured by applying a constant heat flux to the test surface and measuring the resultant temperature profile on the surface. Two thin stainless steel foils were smoothly adhered to the test surface downstream of the holes and soldered to copper bus bars in order to provide the constant heat flux to the surface as shown in Figure 2.13. The use of two heat flux foils, while not ideal, was necessitated by the seam between the test coupon and the downstream runout plate at $x/d = 15$. The upstream foil mounted on the test coupon was 0.025 mm thick and covered a streamwise range of x/d = 0-14 and the downstream foil mounted on the runout plate was 0.013 mm thick and covered x/d = 16-40. The foils were connected to different power supplies that provided a constant heat flux of q''_{foil} = 1.7 kW/m^2. The current (by means of a shunt voltage) and voltage through each plate were measured to an

accuracy of ± 1.0% for the upstream plate and ± 0.01% for the downstream plate. Improved accuracy for the downstream foil was possible because it used a DC power supply, while the upstream foil used an AC power supply. The fact that AC voltage could not be measured as accurately as DC voltage was unfortunately not taken into account before acquisition of the power supply. The heat fluxes in the different foils were held to within 1% of each other during the course of the experiment.

Heat transfer coefficient augmentation was measured only for the compound angle holes at DR = 1.2 due to limited time. The compound angle holes were selected because the heat transfer augmentation was expected to be greater than for the axial holes. The technique for measuring heat transfer coefficients was very similar to that for measuring adiabatic effectiveness in terms of camera set up, calibration, and wind tunnel operation with some exceptions. Care was taken to never supply power to the heat flux foils if the mainstream fan was off so that the foils did not overheat. The conditions where the heat flux foils were turned on took longer to come to steady state, often requiring 30 minutes in between conditions. Measuring h_f also required repeating the adiabatic effectiveness measurements (a "foil off" condition) in the same experiment to determine the driving temperature for heat transfer. Computing heat transfer coefficient augmentation also required a measurement of h_0 with the film cooling holes taped over. Similar to the h_f measurements, the h_0 measurement was accompanied by a "foil off" condition to account for the effects of an upstream thermal boundary layer.

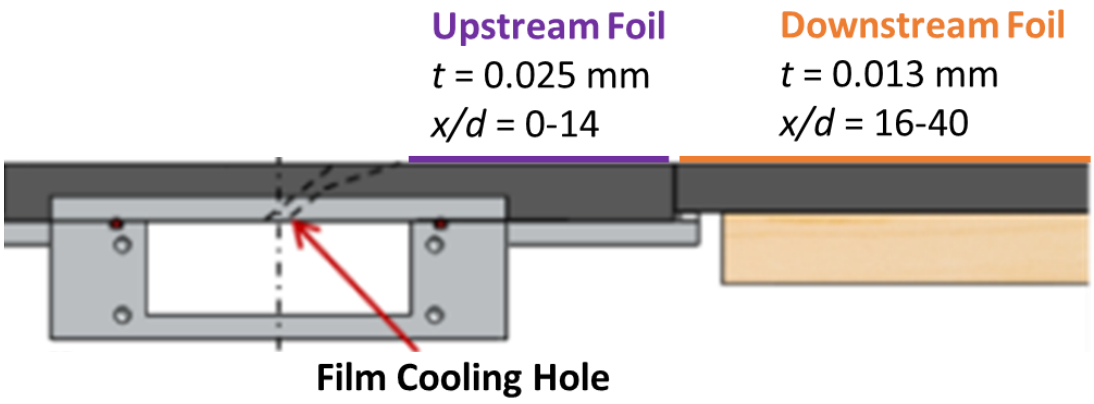

Figure 2.13: Installation of the two heat flux foils

A similar conduction correction procedure was implemented to compute h_f and h_0 as was used to compute η. The predicted $q''_{conduction}$ from the finite element simulation was used to remove the conductive heat flux from q''_{foil}. Additionally, a radiation correction was applied assuming black box radiation with the surrounding test section walls at the mainstream temperature, T_∞. The heat flux correction is shown in the equations below:

$$q''_{convection} = q''_{foil} - q''_{conduction} - q''_{radiation} \tag{2.17}$$

$$q''_{radiation} = \varepsilon\sigma(T_\infty^4 - T_{surface}^4) \tag{2.18}$$

The convective heat flux was then used to compute the heat transfer coefficients using the corrected adiabatic wall temperature:

$$h_f = \frac{q''_{convection}}{T_{measured} - T_{aw}} \tag{2.19}$$

As a first step, T_{aw} was calculated as described in the previous section using h_0 in Equation 2.11 in place of h_f with the intent of using h_f to produce a more accurately

corrected T_{aw} once h_f had been calculated. The process to compute T_{aw} and h_f is therefore iterative, however, as was shown by Figure 2.7, assuming $h_f/h_0 = 1.0$ when correcting T_{aw} was an appropriate assumption and therefore, no iteration was required. The heat transfer augmentation was then simply calculated as the ratio of h_f and h_0.

The heat transfer coefficient without film cooling was measured three times: for VR_c = 0.2, 0.4, and 0.6 to ensure consistency in the measurement technique. Figure 2.14 (a) shows the test-to-test repeatability of h_0. The repeatability was within ± 2 W/(m^2·K) for most of the streamwise distance or ± 2% of the measured value. The in-test repeatability for the normalized heat transfer coefficient with film cooling is shown in Figure 2.14 (b). The heat transfer coefficient with film cooling was normalized as follows:

$$h_{f,norm} = \frac{h_f - h_0}{h_{f,peak} - h_0} \tag{2.20}$$

where $h_{f,peak}$ is the maximum local heat transfer coefficient. The repeat point was not a true in-test repeat in that it used the same heat flux on image as the first point but a different heat flux off image. The two heat flux off images were within $\delta\eta$ = ± 0.003 of each other, resulting in a repeatability of $h_{f,norm}$ of ± 0.03.

Similar to the measurements of adiabatic effectiveness, the uncertainty in h_f/h_0 was estimated by sequentially perturbing the primary measurements and the parameters of the various correction processes. The precision uncertainty in heat transfer coefficient augmentation was estimated as $\delta h_{f,norm}$ = ± 0.031 and was primarily a result of the precision uncertainty of the IR camera. The estimated bias uncertainty was of similar magnitude – $\delta h_{f,norm}$ = ± 0.028. It primarily came from the boundary conditions used for the conduction correction.

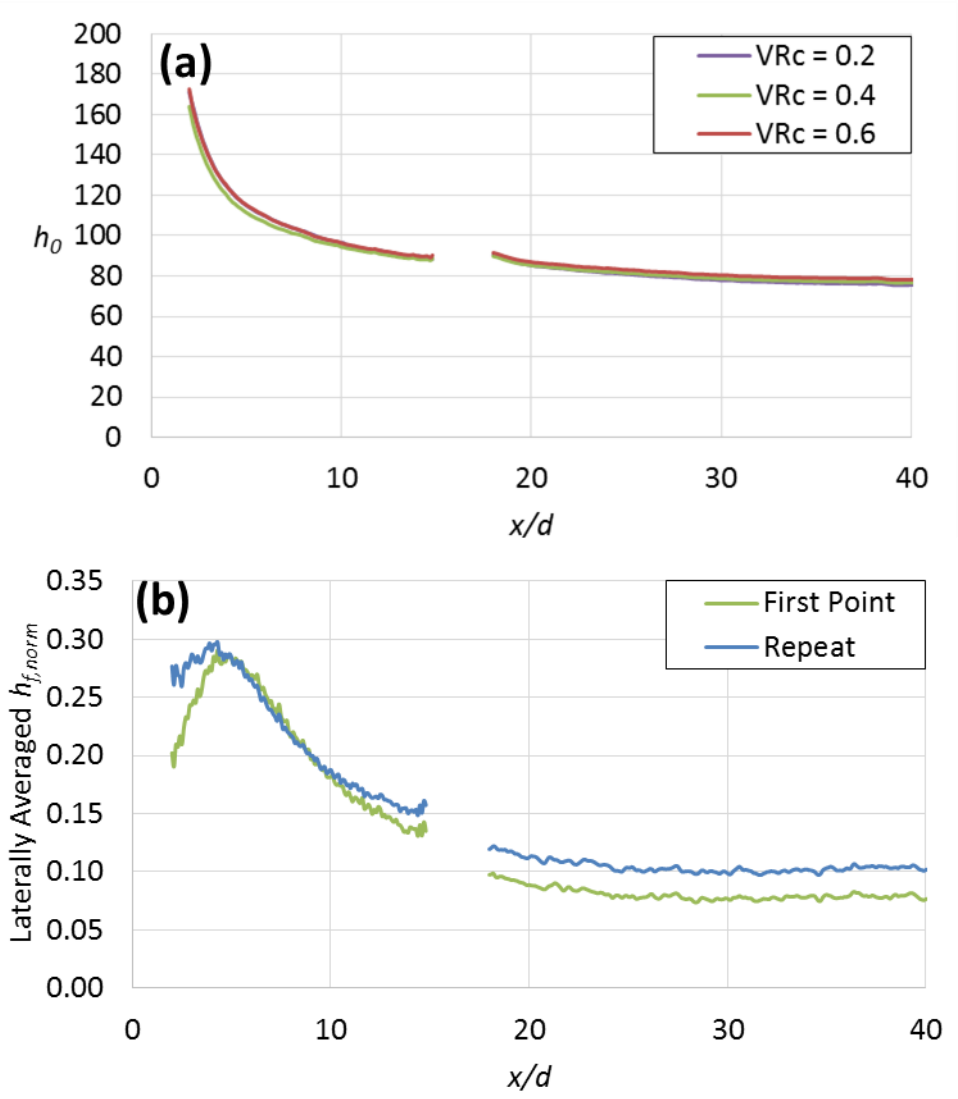

Figure 2.14: (a) test-to-test repeatability of h_0 and (b) in-test repeatability of $h_{f,norm}$

2.4.2.6 Prediction of Overall Effectiveness

As discussed in Section 1.2.2, a one-dimensional analysis can be performed to predict the overall effectiveness, φ, from the measured adiabatic effectiveness, η, and heat transfer coefficient with film cooling, h_f, using the equation:

$$\varphi = \frac{1 - \chi\eta}{1 + Bi + h_f/h_c} + \chi\eta \tag{2.21}$$

The analysis from Dyson *et al.* [50] suggested that a range of $0.1 < Bi < 1.0$ was appropriate for a typical airfoil. Given that the freestream parameters selected for this study are intended to simulate film cooling in the low curvature section on the suction side of a film cooled blade, $Bi_0 = (h_0 \cdot t)/k = 0.8$ was selected because the heat transfer coefficients are typically high in that region relative to the rest of the airfoil. The Biot number with film cooling was higher in cases of $h_f/h_0 > 1.0$. For axial shaped holes, where h_f/h_0 was not measured, it was assumed that $h_f = h_0$ for the purposes of implementing this model.

Internal cooling was assumed to produce a constant crossflow channel heat transfer coefficient, h_c, under the downstream surface. The internal heat transfer coefficient was predicted using Gnielinski's formula for turbulent internal flow, given in Equations 2.12 and 2.13. The coolant warming factor was assumed to be $\chi = 0.9$ and takes into account the expected warming of the coolant as it passes through the holes. The assumed value was based on previous experience in measuring overall effectiveness from a thermally scaled film cooling model.

This model was useful to demonstrate that changing the internal crossflow affects both the internal cooling and the external film cooling effectiveness. It is not expected to produce an accurate prediction of φ under engine conditions. The precision uncertainty in the adiabatic effectiveness and heat transfer coefficient propagate through this model to produce an estimated precision uncertainty in the model of $\delta\varphi_p = \pm 0.004$ when comparing conditions to one another. The bias uncertainty in the model was greater due to the assumptions made regarding the remaining parameters. Conservatively assuming a 25% uncertainty for the internal heat transfer model and the assumed Biot number as well as a

0.05 uncertainty in χ, the bias uncertainty was estimated to be $\delta\varphi_b = \pm 0.035$. The greatest contributor to that uncertainty was the model used to predict the internal heat transfer coefficient, h_c.

2.4.3 Thermal Field Measurements

Thermal fields were measured above the wall and in the diffuser section of the film cooling hole by use of a microthermocouple probe for the axial holes. The probe was a type E thermocouple with a wire diameter of $d_{probe} = 50\ \mu m = 0.013d$. A picture of the probe is shown in Figure 2.15. The microthermocouple wire was secured to a 0.254 mm diameter stainless steel rod by means of shrink wrap tubing, taking care to keep the wires insulated from the rod and each other. The thin stainless steel rod was secured by shrink wrap to a 3.175 mm diameter tungsten-carbide rod which was the primary support for the probe. The microthermocouple leads were then soldered to larger diameter type E thermocouple wire which was connected to the data acquisition system. The junction of the microthermocouple wire was set at an angle such that it would be parallel to the laidback floor of the diffuser of the film cooling hole.

Because all thermal field measurements were made at $DR = 1.2$, the probe could be calibrated over a smaller range of temperatures – from 254-313K. The probe, as well as the mainstream and coolant thermocouples were all calibrated in a bath containing a mixture of water and propylene glycol. The bath had a reported accuracy of ± 0.1K. Calibrating the probe, mainstream, and coolant thermocouples together in the bath served to remove any bias present in the calibration from affecting the normalized temperature measured by the probe. A linear best fit calibration correlation was applied to each thermocouple. The calibrations were only considered valid for the channel with which each thermocouple was calibrated so care was taken to ensure that the thermocouples were connected to same DAQ

channel each time. The uncertainty of calibrating the thermocouples using this method was estimated to be δT_{probe} = ± 0.21 K based on the calibration repeatability. This estimation was borne out in the agreement between the probe and the mainstream and coolant thermocouples during the course of experimentation. When the probe was brought far from the wall into the mainstream it agreed with the average of the mainstream thermocouples to within ± 0.25 K and when the probe was lowered into the diffused section of the hole and into a region of constant temperature it agreed with the average of the coolant thermocouples to within ± 0.22 K.

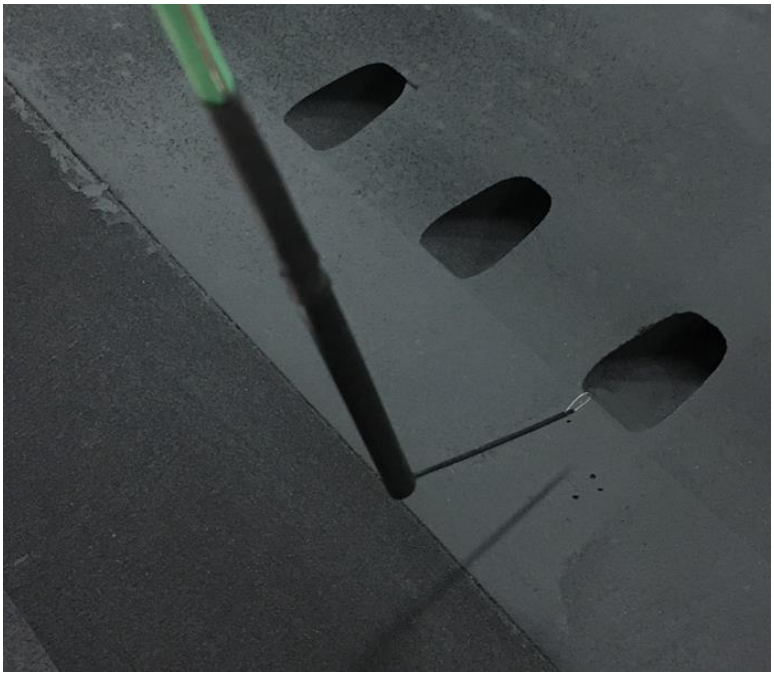

Figure 2.15 Image of the microthermocouple probe used in this study

The probe was held and traversed through the test section by an assembly of three Zaber model T-LSR traverses which had a stated accuracy of ± 15 μm. Access into the test section was provided by a 31.75 mm wide slot cut into the top window of the test section.

This enabled the probe to be traversed almost a full pitch – a slight misalignment between the slot in the ceiling and the film cooling hole limited the lateral movement of the probe to between z/d = -2 and 3. The slot was taped over to reduce the leakage into the top of the tunnel while still allowing the probe to pass through. The probe was moved in three y-z planes at three different span-wise locations: x/d = -2, 0, and 5. At the start of each experiment, the probe was located relative to a mark drawn at the centerline of the hole at x/d = 0. The wall was located by carefully observing the vibrations in the probe – the junction would vibrate slightly when inserted into the turbulent film cooling jet but the vibrations would stop when the probe was brought into contact with the wall. The degree of this vibration was estimated to be on the order of the width of the microthermocouple wire based on visible observation. The resolution of what the probe could measure was therefore about 100 μm in the wall normal and 50 μm laterally. It was estimated that the probe was located accurately to within ± 0.05d in the lateral and stream-wise directions and ± 0.025d in the wall-normal direction. Once the probe was located relative to the film cooling geometry, it was moved automatically according to a set of points input to LabVIEW. It took approximately 45 minutes for each profile to be measured. During that time, the mainstream and coolant flows were held steady. For each probe location the traverse was allowed 2 s to steady out before a data point was saved. The data was recoded at a rate of 250 Hz over a period of 3 s for a total of 750 data points. Figure 2.16 shows a contour plot of the thermal fields for VR_c = 0.4, VR = 1.11 at x/d = -2 and 0 with "x" marks showing the discrete locations (about 320 per profile) where the probe was used to measure the temperature field. Note that at x/d = -2, the probe was traversed down into the diffuser of the hole (y/d < 0).

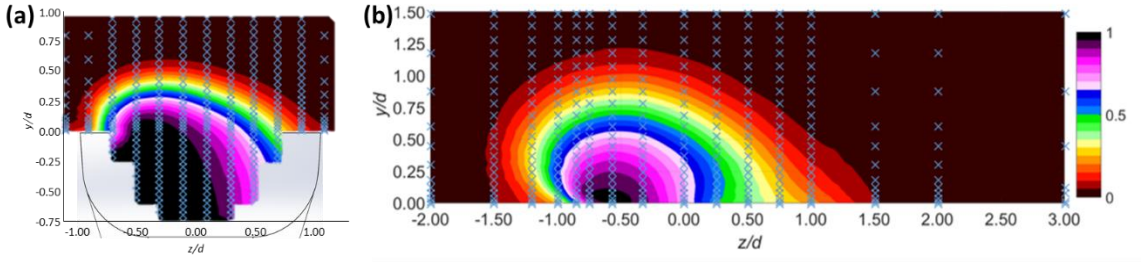

Figure 2.16: Location of measurement points for thermal fields for VR_c = 0.4, VR = 1.11 at (a) x/d = -2 and (b) x/d = 0

The gas temperatures measured by the thermal field probe were normalized in a similar manner as adiabatic effectiveness:

$$\theta = \frac{T_\infty - T_{gas}}{T_\infty - T_j} \tag{2.22}$$

The test-to-test repeatability was evaluated for VR_c = 0.2, VR = 0.83 at x/d = 0, as shown in Figure 2.17. The figure compares effectiveness along the centerline, z/d = -0.33, which had a repeatability that was characteristic of the full profile. Note that due to an error in locating the wall for the repeat point, the two profiles were not measured at the same set of y locations. The repeatability of the measurement was estimated to be ± 0.01. The major contributing factor to the precision uncertainty of the measurement was the steep thermal gradient and unsteady of flow in the shear layer between the coolant jet and the mainstream flow. An analysis of repeat measurements at selected regions estimated that in the shear region, the precision uncertainty was as high as $\delta\theta_p$ = ± 0.05, while in the core of the jet and in the mainstream flow, the precision uncertainty was $\delta\theta_p$ = ± 0.005. The precision uncertainty could have been reduced had a longer sampling time been used. The bias uncertainty in the measurement was driven by the calibration of the thermocouple probe and was estimated to be $\delta\theta_b$ = ± 0.004.

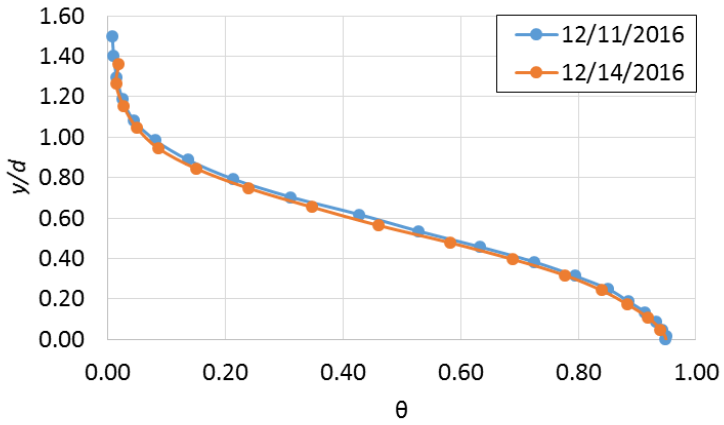

Figure 2.17: Thermal fields repeatability for $VR_c = 0.2$, $VR = 0.83$, $x/d = 0$, $z/d = -0.33$

2.4.4 Particle Image Velocimetry

2.4.4.1 System Setup and Operation

A particle image velocimetry (PIV) system was used to measure flow fields in the diffuser section of the axial 7-7-7 hole. The system works by imaging an illuminated flow field that is seeded with small particles or droplets. The movement of the particles is determined by comparing two successive images to track the movement of groups of particles. A schematic showing the setup of the system is shown in Figure 2.18 and corresponding photographs are shown in Figure 2.19. A Litron Lasers Model No. NANO L135-15PIV dual ND:YAG laser with a maximum energy output of 800 mJ and a pulse duration of 4 ns was mounted on top of the test section. Optical access into the tunnel for the laser was provided by a mirror angled such that the laser sheet was nearly normal to the injected coolant. The laser sheet was five degrees off normal due the need to avoid interference with a port in the ceiling of the test section. A TSI Powerview Plus CCD camera with a pixel resolution of 1600x1200 capable of operating at 32 frames per second was used to capture images of the seeded flow. A telephoto lens with a focal length of 180

mm and a maximum aperture of f/3.5 was used to view the measurement plane. The camera-lens assembly was mounted above the test section on a traverse supported by a tripod. This setup isolated the camera from vibrations caused by the wind tunnel. Optical access for the camera was enabled by mounting a small mirror just inside the ceiling of the test section. This placement of the mirror allowed the camera to be oriented normal to the thick acrylic ceiling, preventing internal reflections in the acrylic from distorting the view of the hole. An experiment ran prior to introducing this setup showed that mounting the mirror this way inside the test section had no measurable effect on the film cooling effectiveness. Unfortunately, the construction of the test section prohibited a view directly down the axis of the film cooling holes. The maximum attainable angle to the surface was 15°, which meant that at the desired measurement plane, shown in Figure 2.18 (b), only 2/3 of the hole cross-section was visible.

Measuring flows near a surface is difficult for PIV systems due to the reflection of the laser at the surface overflowing the camera's detector and obscuring the near-wall particles. To combat this difficulty, the surface of the hole diffuser as well as the surface around the film holes was coated with a paint infused with rhodamine 6G. Rhodamine 6G is a dye that absorbs light at the wavelength of the laser, 532 nm, and has a peak re-emission at 566 nm. To create the paint, rhodamine 6G powder was dissolved in methanol and the solution was mixed into a water-based clear coat paint. This was a challenging process that took a number of iterations to develop a paint that would effectively absorb and re-emit the incident laser. Of note, it was helpful to leave the mixture in a sealed container overnight to allow it to settle and fully dissolve. In order to better remove the reflections, a bandpass optical filter was purchased for the camera with a bandpass range of 500-555 nm that permitted passage of the laser light but not the re-emission from the rhodamine dye. However, use of this filter proved to be unnecessary. The angle of the diffuser reflected the

laser away from the camera and out of the measurement plane. Also, because the camera could not see the bottom of the diffuser due to the viewing angle, the laser sheet reflection at the bottom of the diffuser was not visible. Furthermore, it was found that reflections in the measurement plane were most effectively reduced by running the laser at low power and that the filter made it more difficult to see the seed when the laser was at low power.

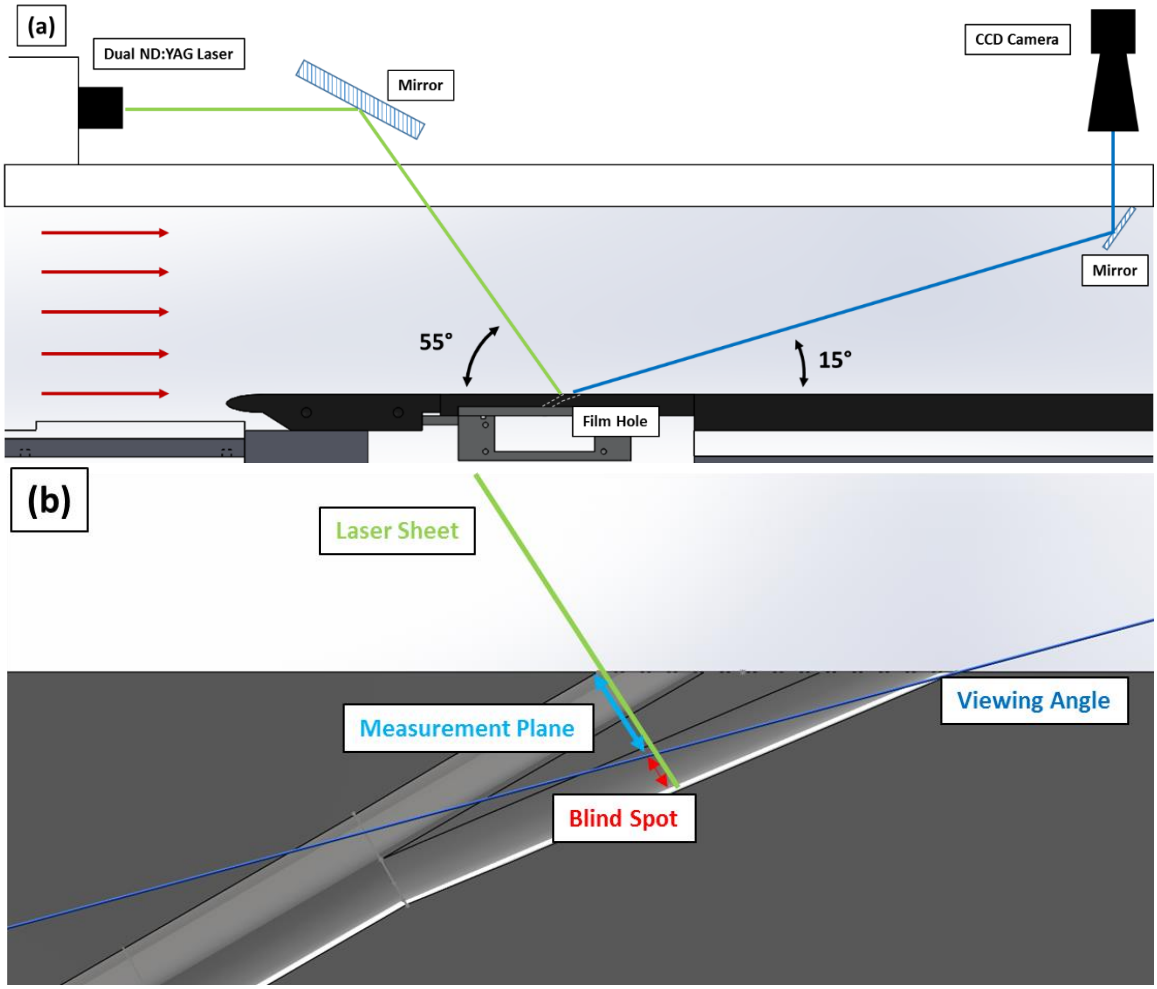

Figure 2.18: Schematic of PIV setup to measure in-hole flow fields (a) overall configuration and (b) in-hole detail

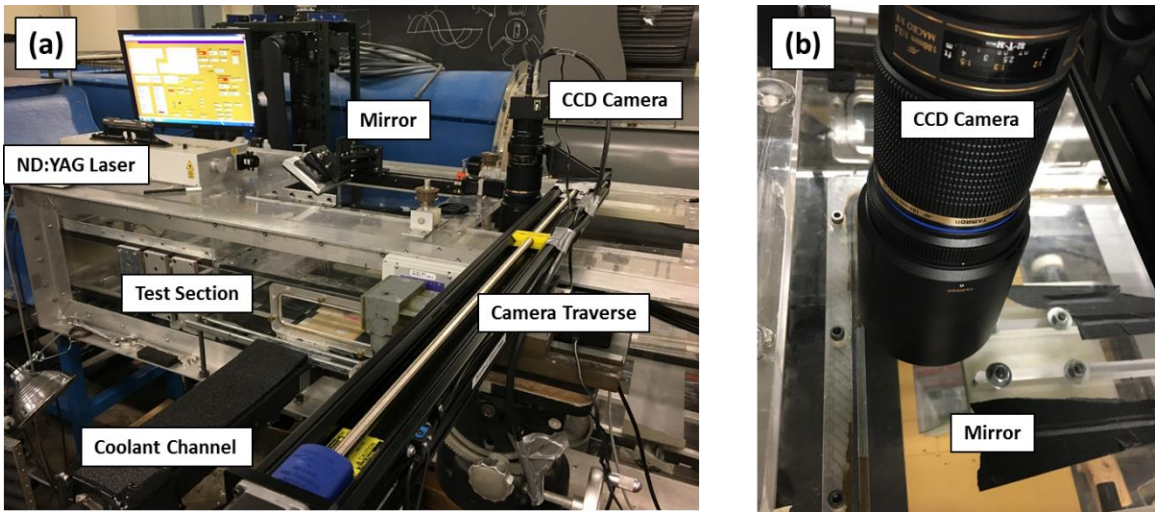

Figure 2.19: Photographs of the PIV system used to make in-hole measurements (a) overall configuration and (b) close-up view of the camera and mirror

An oil droplet generator was used to introduce atomized olive oil to seed the flow. The oil droplets had a mean diameter ranging from 0.5 to 1.0 μm, which corresponded to a Stokes number of up to 0.008 for the maximum injection rate. For Stokes number < 0.01, the seed is expected to resolve turbulent frequencies of at least 10 kHz based on the analysis in [51]. The seed was introduced into the coolant loop upstream of the coolant heat exchanger. Because the aim of these experiments was to visualize coolant flow within the film hole, no attempt was made to balance the seed density between the coolant and mainstream loops, although because the system was a closed loop, the mainstream was effectively seeded during the course of the experiment.

The selection of the time difference, Δt, between laser pulses is critical to the operation of PIV systems. If Δt is too short, the particles in successive images will not move enough to measure accurately and if Δt is too long, it will be impossible to track the particles between frames. A common rule of thumb is that the particles should move about a quarter the width of the interrogation region (typically 16 or 32 pixels) between frames.

Therefore, an appropriate Δt can be estimated from the camera resolution and expected fluid velocity. Because there are no measurements of velocity fields within the diffuser of a shaped film cooling hole in the literature, the appropriate maximum velocity for determining Δt was unknown. Based on the observed bias in the hole and an assumed swirling flow in the hole, the rotational distance in the hole required to produce that bias was used to estimate an average swirling velocity through the hole on the order of U_{swirl} = 6 m/s. Combined with the camera resolution of 1 pixel = 20 μm an appropriate time difference was estimated to be $\Delta t \approx 13$ μs. Another factor to consider in selecting Δt is the time the particles are expected to take to pass through the laser sheet. This consideration was especially important for this measurement because the largest component of velocity was expected to be orthogonal to the measurement plane. The laser sheet thickness was 1.1 mm, thus flow though the sheet at the mainstream velocity, $U_\infty = 25$ m/s would pass through the measurement plane in 40 μs. While there were certainly some particles that appeared or disappeared between frames, $\Delta t = 13$ μs resulted in a measurable vector field.

The conditions for which in-hole velocity fields were measured corresponded to those for which in-hole thermal fields were measured. Unlike the other experiments in this study, these experiments were conducted at unit density ratio, $DR = 1.0$. Testing at elevated density ratios in this facility required the use of molecular sieve desiccant to dry the air and prevent formation of frost, but the olive oil used as seed is detrimental to the performance and long term usefulness of this desiccant. However, because the measurement plane was located right at the upstream edge of the hole, the effect of the density ratio on the flow field was expected to be small due to minimal interaction between the mainstream and the jet upstream of this location. During the course of testing, the mainstream and coolant flow were held steady at $T_\infty = T_c = 295$ K. Before acquiring data, the laser was pulsed for 10-15s to allow it to warm up and the seed was turned on to ensure it was sufficiently dense

for measurements. 1,000 image pairs were acquired for each condition at a rate of about 5 Hz, which was the maximum rate the system could capture and save the images. An in-test repeat point was measured for $VR_c = 0.4$ and $VR = 1.11$.

2.4.4.1 PIV Data Processing

The velocity field data was processed using PIVlab, an open-source Matlab application developed for performing PIV calculations. Prior to processing a number of preprocessing steps were undertaken. Figure 2.20 compares a raw image of the hole to a pre-processed image. The area of interest was selected and the region of reflection was masked off (the masked region is shaded red). Within the area of interest, a high pass filter was used to remove much of the background noise due to reflection in the hole and the particle intensity was capped to reduce the influence of very bright particles. A fast Fourier transform window deformation algorithm was used to process the image pairs to determine instantaneous velocities. Four interrogation passes were used: the first pass used an interrogation region of 64 pixels, the second 32 pixels, and the final two steps used interrogation regions of 16 pixels. An overlap of 50% was used for each pass. The resultant vectors from the processing are shown in Figure 2.21 (a) and compared to the post-processed image in Figure 2.21 (b). Three post-processing steps were performed: a velocity limit filter, a standard deviation filter, and a local median filter. The velocity limit filter removed all vectors that exceeded a defined limit. A number of different velocity filters were used to test their effect on the final result, the effect of which is discussed in the results section. Most of the data presented was filtered such that all vectors exceeding 10 m/s were removed. The standard deviation and local median filter were used to remove vectors that were considerably different from their neighbors. The program replaced the filtered vectors with interpolated vectors, which are shown in orange in the post-processed data. 85% of

the calculated vectors were preserved by the filtering, while the other 15% were interpolated.

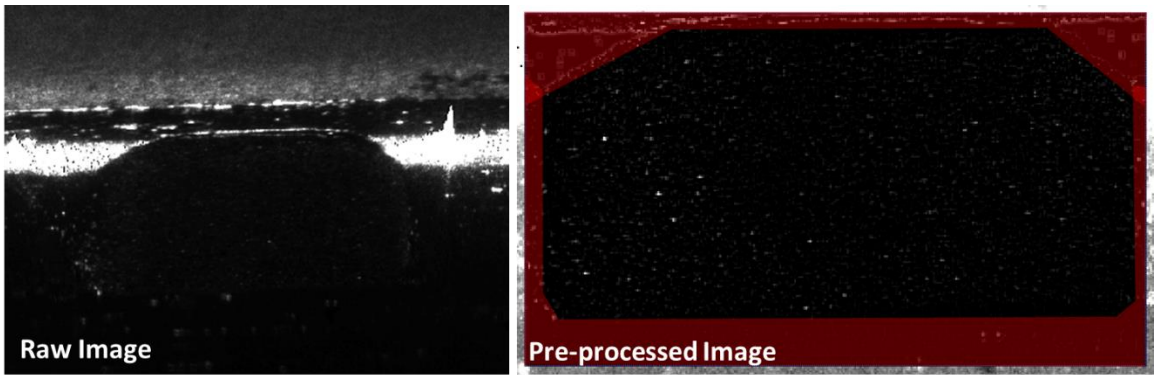

Figure 2.20: Comparison of a sample raw and pre-processed image

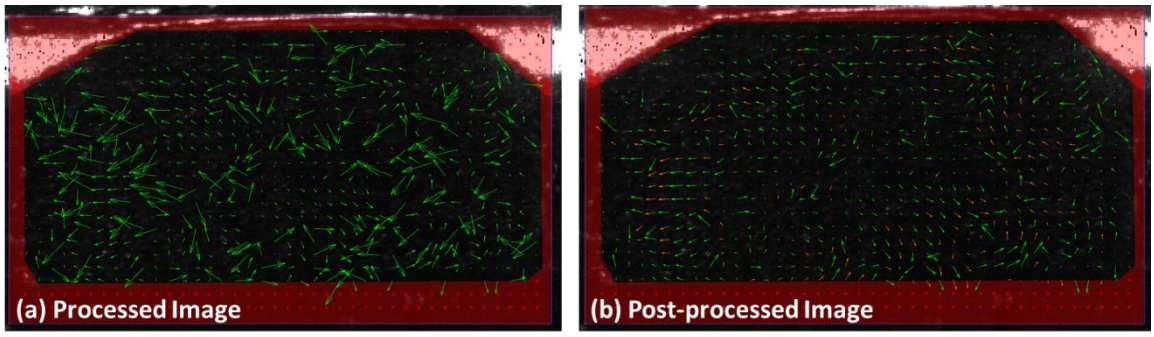

Figure 2.21: Comparison of (a) processed and (b) post processed data. Green vectors are processed data and orange vectors are interpolated

It is evident from the images in Figure 2.21 that there was considerable variation in local velocity within the film cooling hole. This result is unsurprising given that the flow through film cooling holes is unsteady, highly turbulent, and often features regions of separation and recirculation. The difficulty of post-processing the data was determining which vectors were noise and which resulted from turbulence in the flow. It is desirable to

filter out the former while preserving the latter and to that end, a considerable amount of attention was paid to selecting the appropriate filtering velocity. Given that no previous measurements of secondary flow within the diffuser of a film hole fed by internal crossflow exist in the literature, there was no clear limit to set for the instantaneous velocities, so a trial-and-error approach was used to determine an appropriate velocity filter setting. Figure 2.22 shows the mean vector fields resulting from filtering a pair of flow conditions with different filtering velocities, U_f. For VR_c = 0.4, VR = 1.11, reducing the filtering velocity from V_f = 10 to 5 m/s increased the mean velocity in all but the top right of the plot. At U_f = 5 m/s, there was no longer a downward flow in that top right corner – indicating that the filtering velocity was set too low because it removed a flow feature that relied on instantaneous velocities greater than 5 m/s. For VR_c = 0.6 and VR = 0.83, increasing U_f from 10 to 20 m/s greatly obscured a vortical feature in the right of the plot, suggesting that the more relaxed filter permitted too much noise to be counted as actual velocities. Therefore, a filtering velocity of U_f = 10 m/s was chosen to process the data presented in this study. It is certainly possible that this filter removed some turbulent fluctuations and thus increases the uncertainty in the mean and fluctuating velocity measurements. However, removing high velocity random fluctuations, whether from turbulence or noise, allows the important flow structures to be observed more clearly, which is the primary goal of performing these in-hole velocity measurements.

It is likely that much of the noise in the data was caused by the main component of velocity being normal to the measurement plane, introducing erroneous vectors into the measurement. The setup of the timing, Δt = 13 μs, was such that a particle traveling at the mainstream velocity, U_∞ = 25 m/s would pass through about a third of the thickness of the laser sheet, which was 1.1 mm thick. Therefore, most particles visible in the first frame would be visible in the second, but particles would still appear or disappear between

frames, introducing errors. It is likely that most of these instances were removed by the post-processing filters, but potentially at the cost of filtering out actual fluctuating velocities. The other error introduced by the primary velocity component was caused by the seed particles that remained within the laser sheet between frames. The viewing angle was 20° away from being normal to the measurement plane, so a particle that moved purely normal to the plane would still appear to move in the y^* direction – the movement would be in the positive y^* direction for flow in the direction of injection. This is a difficult error to account for because the magnitude of the through-plane velocity is expected to vary across the plane. The maximum average through plane velocity was 16.7 m/s. At that through plane velocity, a particle traveling normal to the measurement plane would have an apparent velocity of 5.7 m/s. However, given the similarity of profiles at matched VR_i at different injection velocity ratios, it was not apparent that this error substantially affected the measured flow structure given that this error would be expected to scale with injection rate.

The spatial calibration used to calculate distances in the image is had an uncertainty of ± 0.003d based on the reading of the ruler imaged in the calibration image. The precise location of the hole in the image had a greater uncertainty of about ± 0.03d in each direction. That uncertainty represents an error that is consistent for all conditions tested. The spatial resolution from the 16x16 pixel interrogation windows with 50% overlap was 0.044d in both direction.

The in-test repeatability of the mean velocity field is shown in Figure 2.23 for VR_c = 0.4 and VR = 1.11. These two points were measured at the start and end of the experiment and represent the average of 1,000 image pairs. The flow structure was well-maintained between the two different points. The velocity magnitude varied by ± 30% and the direction varied by ± 8°. The variance in velocity magnitude was large relative to the overall

magnitude of the measured secondary flow velocity and was likely the result of an insufficient number of images to produce mean flow data. However, the similar flow structures between repeat points is an encouraging indication that a larger data set would produce better repeatability and would be more useful for validation of computational predictions.

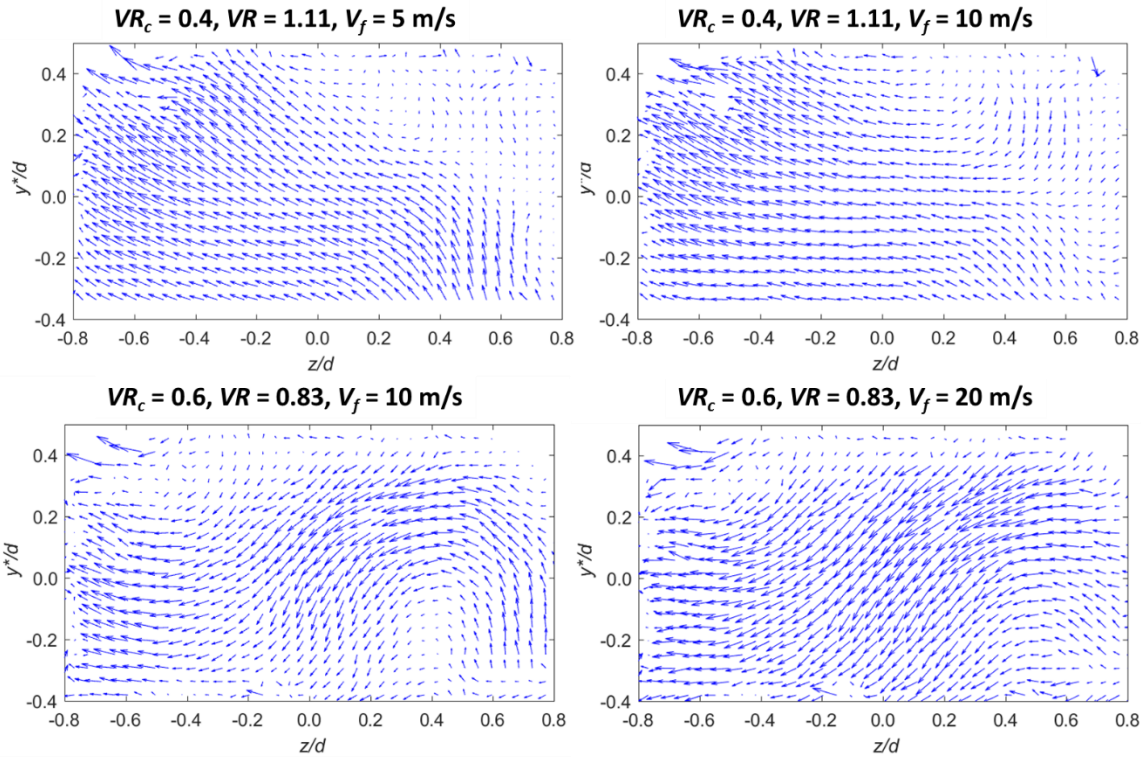

Figure 2.22: Effect of applying different filtering velocities, U_f, to two different conditions on the mean velocity field

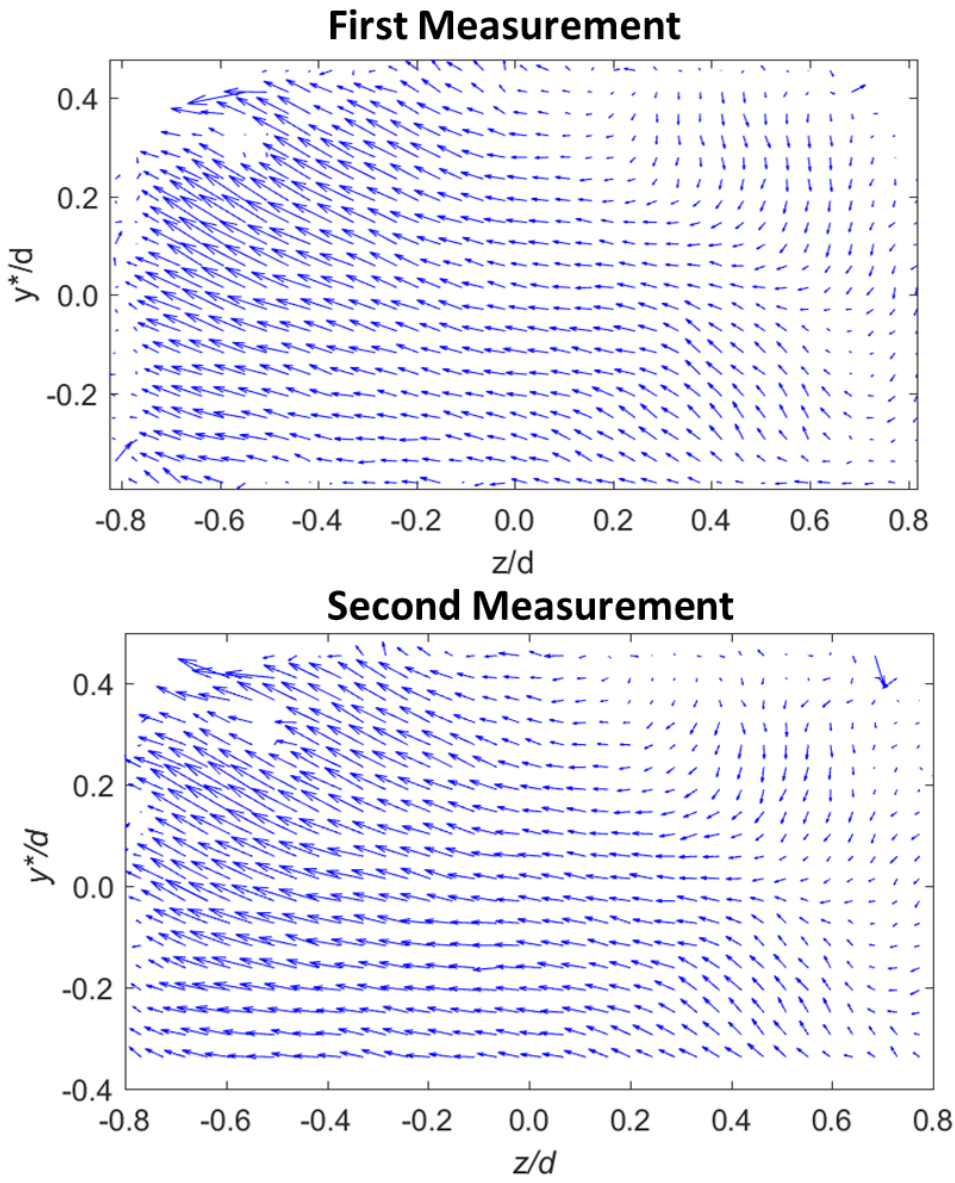

Figure 2.23: In-test repeatability for $VR_c = 0.4$, $VR = 1.11$ of mean velocity fields based on the average of 1,000 image pairs

Chapter 3: Effect of Crossflow on Axial Shaped Holes

An experimental study was performed to investigate the effect of internal crossflow feed on a single row of axial shaped holes. Previous studies have found that internal crossflow caused a degradation in film cooling effectiveness. Discharge coefficients, adiabatic effectiveness, near-hole thermal fields and in-hole velocity fields were measured for a single row of axial 7-7-7 laidback fan-shaped film cooling holes. The holes were fed by an internal crossflow oriented perpendicular to the mainstream flow over a range of crossflow-to-mainstream velocity ratios of VR_c = 0.2-0.6 and for a range of coolant jet-to-mainstream velocity ratios of VR = 0.2-1.7. While most of these measurements were made at a low density ratio of DR = 1.2, the sensitivity to density ratio was studied by repeating a large number of these conditions at an engine relevant DR = 1.8. The goal of these experiments was to determine the factors that influence the previously observed degradation in effectiveness due to internal crossflow.

3.1 Density Ratio

The density ratio at engine conditions, resulting from the temperature ratio between the coolant and mainstream air, is approximately DR = 2.0. While it is desirable to simulate this density ratio in a laboratory setting, to do so is often difficult and time consuming, and therefore many studies, including this one, test at lower density ratios. In order to account for these differences, many studies have endeavored to determine the appropriate injection parameter (i.e. blowing ratio, velocity ratio or momentum flux ratio) that best scales low density ratio film cooling performance to engine conditions. While no single injection parameter has been consistently shown to best predict film effectiveness, often one of the three works better than the others. For plenum-fed 7-7-7 holes, a study by Anderson *et al.* [52] showed that velocity ratio best scaled laterally averaged effectiveness for a range of

density ratios from DR = 1.2-1.6. The scaling with velocity ratio implies that matching the shear layer interaction between the mainstream and the issuing coolant jet was the most important factor to matching film effectiveness.

In this study, two density ratios were tested: DR = 1.2 and DR = 1.8. A comparison of spatially averaged effectiveness from x/d = 5-50 as a function of (a) velocity ratio, (b) blowing ratio, and (c) momentum flux ratio is shown in Figure 3.1 for VR_c = 0.3-0.5. Due to difficulties with frost forming in the hole, complete data sets were not obtained for VR_c = 0.2 and 0.6 at DR = 1.8. Unlike the results of Anderson *et al*. [52] for plenum-fed 7-7-7 holes, the velocity ratio was not clearly the best scaling parameter for all conditions. For VR_c = 0.3, the blowing ratio appears to work well for M = 1.0-2.0, although it did not do well for M < 1.0. For VR_c = 0.5, the velocity ratio was the better scaling parameter: spatially averaged effectiveness scaled very well for VR = 0.3 and for VR > 1.0. The peak values of spatially averaged effectiveness was greater for DR = 1.8 but the peaks both occurred at VR = 0.83. And while blowing ratio fails completely to scale VR_c = 0.5, the velocity ratio at least captured the trend of increasing effectiveness with increasing VR for VR_c = 0.3. The velocity ratio also best captured the trend of reduced effectiveness with increasing VR_c for VR > 1.0. The momentum flux ratio, on the other hand, did not appear to scale the data well for any condition.

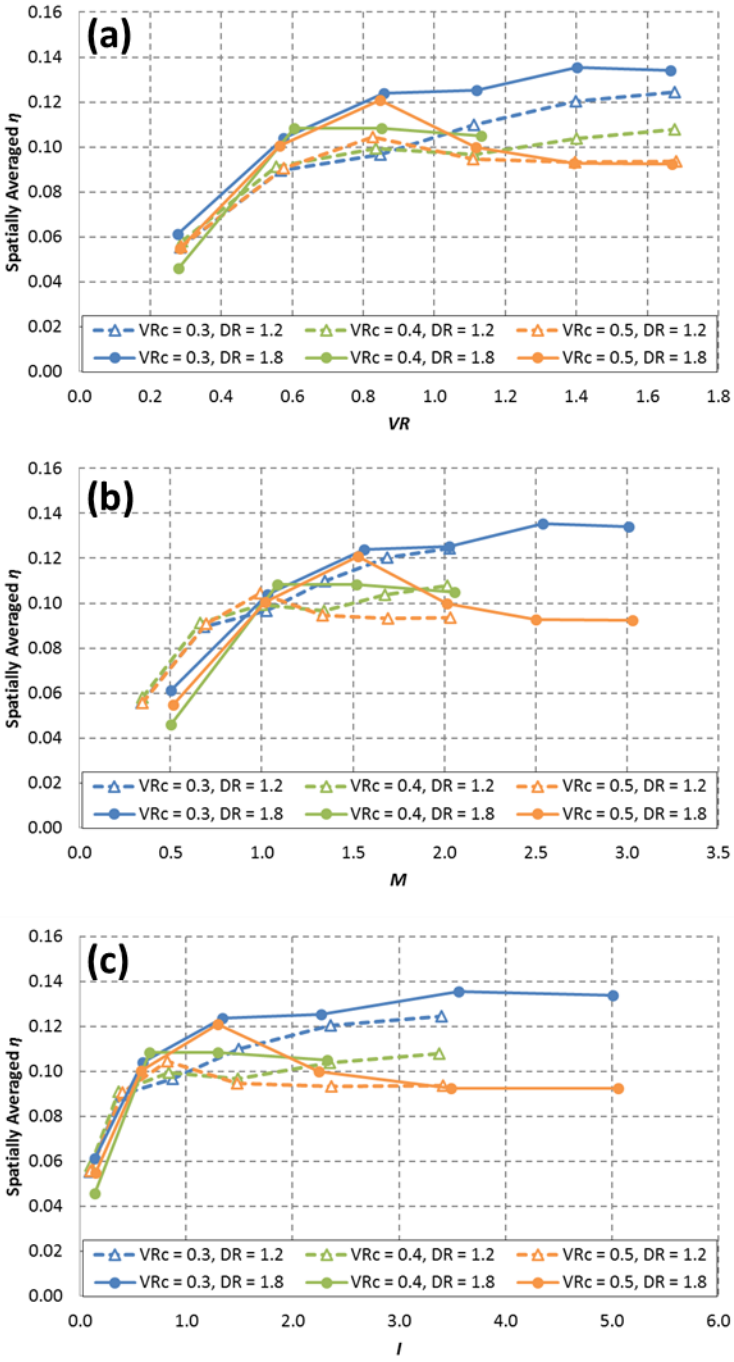

Figure 3.1: Spatially averaged η scaled with (a) VR, (b) M, and (c) I at DR = 1.2 and 1.8. Data was averaged over four pitches from x/d = 5-50.

Contours of local film effectiveness are displayed in Figure 3.2 for $VR_c = 0.3$, which did not scale well with VR in terms of spatially averaged effectiveness. Note that the discontinuity at $x/d = 2$ is due to using a simple one-dimensional correction detailed in [9] to correct for conduction in the near-hole region. This was done to show how the coolant biased within the holes, not to accurately correct out conduction effects, hence the mismatch with the more accurate three-dimensional conduction correction for $x/d > 2$. Also, note that for $DR = 1.8$, the infrared camera was unable to measure the peak effectiveness level in the near-hole region, hence the uniform effectiveness level in the hole of about $\eta \approx 0.7$. For all conditions and at both density ratios, the coolant was biased toward the windward side of the hole. At the lower injection ratio, the $DR = 1.2$, $VR = 0.83$, $M = 1.0$ case compared better to the $DR = 1.8$ case at matched blowing ratio, at least in terms of centerline effectiveness. The jet broadened when density ratio increased, explaining the higher spatially averaged effectiveness for $DR = 1.8$. The matched velocity ratio conditions did not compare well at different density ratios – the $DR = 1.8$ condition had better lateral spreading and higher centerline effectiveness than at $DR = 1.2$. At the higher injection rate shown in Figure 3.2 (b), the effectiveness in the near-hole region ($x/d < 15$) scaled slightly better with velocity ratio than with blowing ratio. Further downstream, the higher density ratio condition had higher effectiveness, likely due to the greater mass flow rate of coolant.

The laterally averaged data presented in Figure 3.3 shows that VR and M scaled the data well in certain ranges. In the near-hole region at $x/d = 10$, the data collapsed within uncertainty when scaled with VR for $VR_c = 0.5$. It also collapsed well at that location for $VR_c = 0.3$ for $VR > 1.0$. On the other hand, the data did not scale well with M at this location. Further downstream, at $x/d = 40$, both $VR_c = 0.3$ and 0.5 scaled with M to within uncertainty for all injection rates. It could also be argued that $VR_c = 0.5$ also scaled with VR at $x/d = 40$. It makes sense that the effectiveness would scale better with VR in the near-hole region

because the shear-layer interactions are more dominant in that region. The better scaling with M further downstream likely occurred due to the dispersal of coolant downstream such that the mass of coolant injected was the more important contributor to effectiveness than any near-hole jet-mainstream interactions.

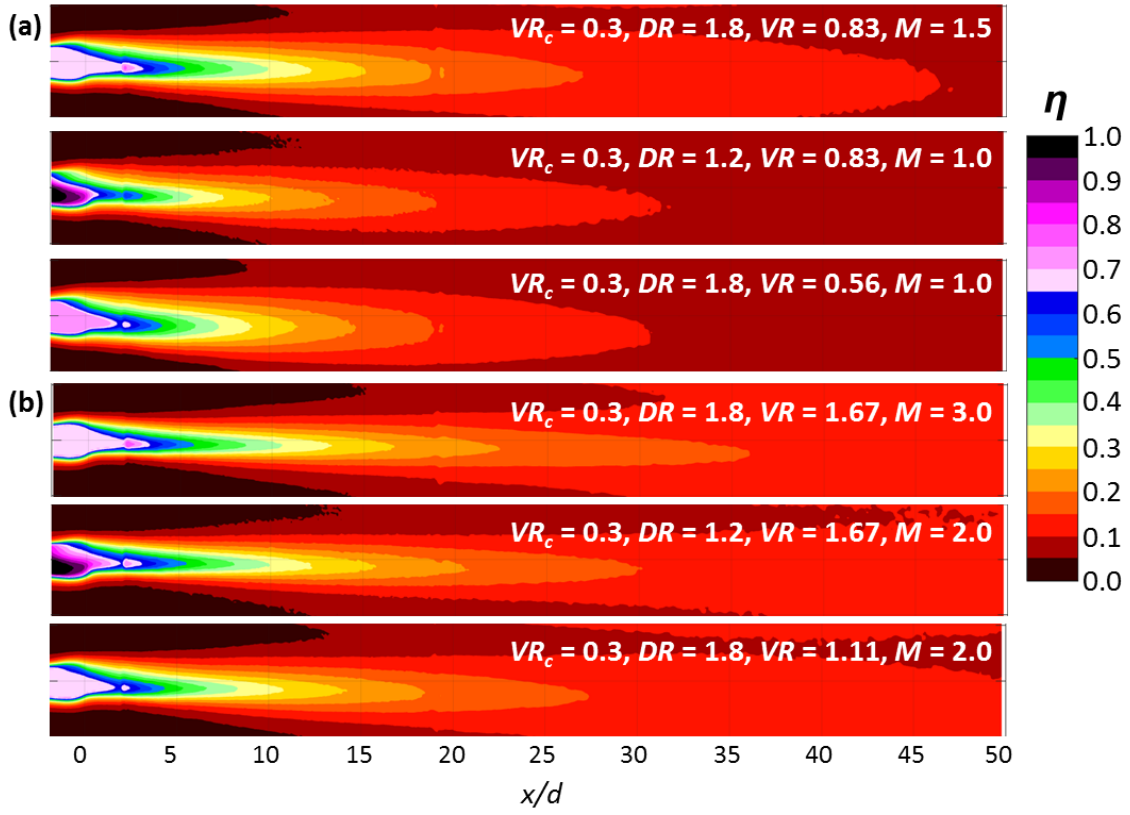

Figure 3.2: Local distributions of effectiveness for $VR_c = 0.3$ to compare scaling with velocity ratio and blowing ratio at (a) a lower injection rate and (b) a higher injection rate

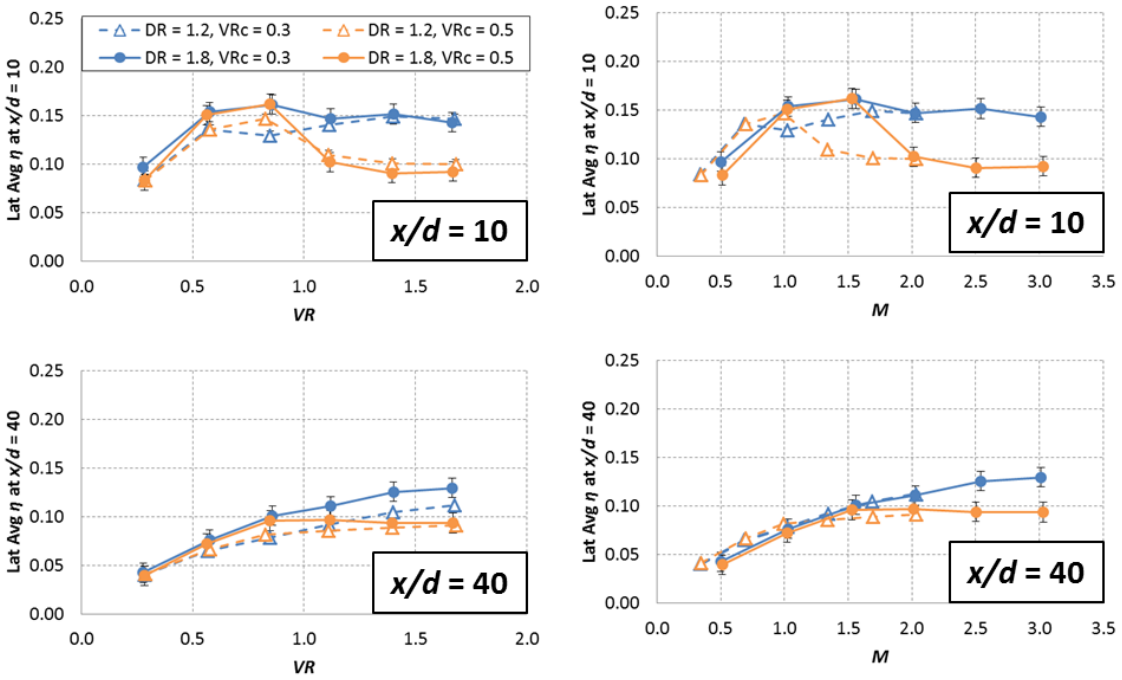

Figure 3.3: Laterally averaged effectiveness for selected streamwise locations scaled with *VR* and *M*

To further investigate scaling with velocity ratio and blowing ratio, lateral profiles of effectiveness at x/d = 10 are shown in Figure 3.4 for selected conditions at lower injection rates. For VR_c = 0.3, the scaling with blowing ratio at M = 1.00 was clearly better than the scaling with velocity ratio at VR = 0.83, where DR = 1.8 had much greater peak effectiveness. At M = 1.00, DR = 1.8 had slightly greater effectiveness at all lateral locations, but the shape of the profiles were very similar, despite having different laterally averaged effectiveness. However, at VR_c = 0.5, the profiles scaled better with velocity ratio. With the exception of the far right jet, the jet profiles were fairly close when velocity ratio was matched, but at matched M = 1.00, DR = 1.2 had greater peak effectiveness. These results more clearly show that VR_c = 0.3 scaled better with M while VR_c = 0.5 scaled better with VR.

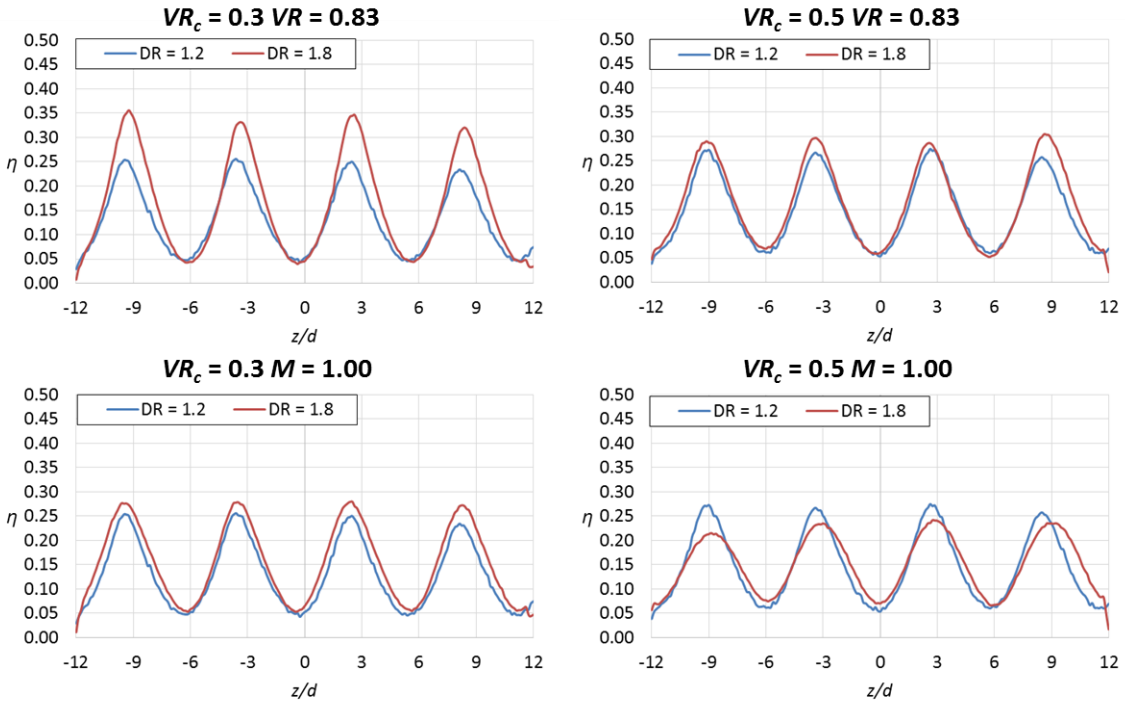

Figure 3.4: Lateral profiles of effectiveness at $x/d = 10$ for lesser injection rates

Lateral profiles of effectiveness at $x/d = 10$ are similarly shown for greater injection rates in Figure 3.5. For both $VR_c = 0.3$ and 0.5 the data scaled well with velocity ratio at $VR = 1.67$ and with blowing ratio at $M = 2.00$. This result corresponded with the agreement in laterally averaged effectiveness in Figure 3.3. The agreement at $M = 2.00$ is somewhat misleading for $VR_c = 0.5$ because the laterally averaged effectiveness for both density ratios happened to converge at this point after being quite different at lower blowing ratios. It is unclear whether this agreement would continue at higher M. Also, for both crossflow-to-mainstream velocity ratios, the laterally averaged effectiveness was somewhat insensitive to velocity ratio for $VR = 1.11$-1.67.

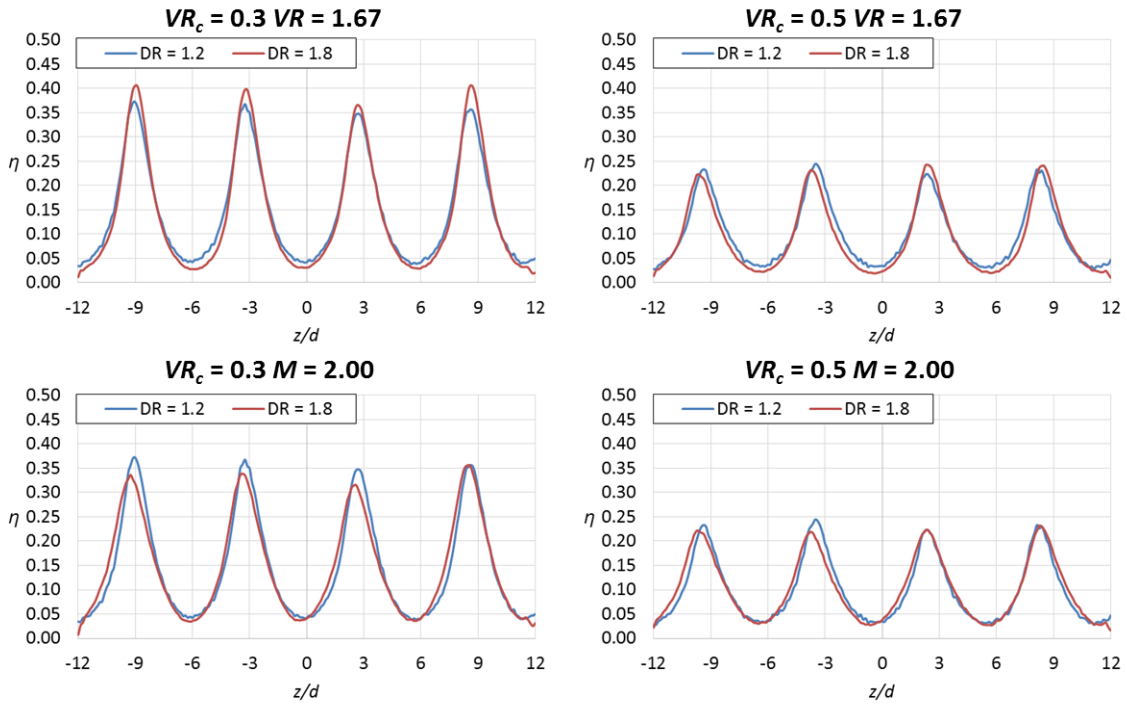

Figure 3.5: Lateral profiles of effectiveness at x/d = 10 for greater injection rates

To further investigate the density ratio effect, the laterally averaged effectiveness was scaled with x/Ms, a commonly used parameter in film cooling effectiveness correlations. This scaling takes into account both downstream distance and the blowing ratio such that a location further downstream at a greater blowing ratio is equivalent to a location closer to the hole at a lesser blowing ratio. In theory, laterally averaged effectiveness for well-attached jets from the same film-hole geometry should collapse on a single curve when scaled with x/Ms and any conditions that fall below that curve indicate a jet that has reduced effectiveness due to detachment from the surface. Figure 3.6 shows laterally averaged effectiveness for selected blowing conditions at DR = 1.2 and 1.8. Interestingly, when velocity ratio is matched, the laterally averaged effectiveness was similar for the two density ratios, even though scaling with x/Ms includes blowing ratio.

The importance of both scaling parameters suggests that M best scales the downstream performance of the jets while VR best scales the near-hole effects that cause detachment. For $VR_c = 0.3$, there was a slight reduction in effectiveness going from $VR = 0.56$ to $VR = 1.11$, likely indicating jet separation. At $VR_c = 0.5$, the effectiveness was also reduced going from $VR = 0.56$ to 1.11, but the reduction in effectiveness was much more extreme than for $VR_c = 0.3$. This suggests that the increased crossflow velocity increased jet separation or caused a reduction in effectiveness by some other means.

The density ratio had a measurable but small effect on film cooling effectiveness for crossflow-fed axial shaped holes. More importantly, several important trends were preserved when density ratio was reduced to $DR = 1.2$ from 1.8. For both density ratios the coolant biased toward the same side of the hole and the reduction in effectiveness with increasing crossflow velocity was consistent as well. These similarities suggest that important flow physics was maintained between the two conditions and therefore results at $DR = 1.2$ are expected to be useful to understanding how internal crossflow affects film cooling at engine conditions. Therefore, the majority of the results in this chapter are presented for $DR = 1.2$. When necessary, results at $DR = 1.8$ will be reported to confirm that important trends remained consistent.

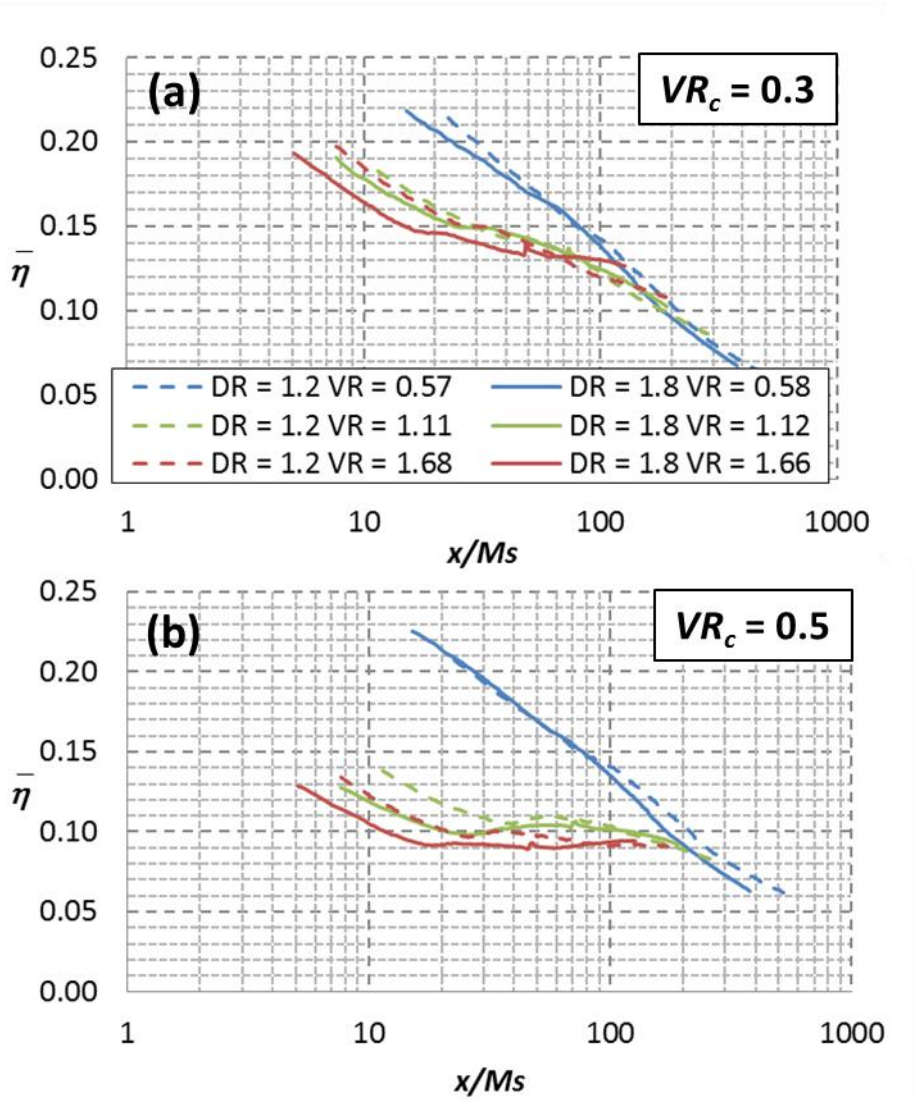

Figure 3.6: Laterally averaged effectiveness scaled with *x/Ms* for (a) $VR_c = 0.3$ and (b) $VR_c = 0.5$

3.2 DISCHARGE COEFFICIENTS

The discharge coefficient through a film cooling hole represents the losses through the hole, which occur at the inlet due to separation, in the hole due to interaction with the wall, and at the outlet due to mixing with the mainstream. A number of studies have shown that internal crossflow reduces the discharge coefficient for axial round and shaped film cooling hole. Notably, Gritsch *et al.* [24] showed that for wide-angle, axial, laidback fan-shaped holes, the discharge coefficient was primarily a function of the blowing ratio and the internal crossflow velocity. That study showed that the data collapsed somewhat when the discharge coefficient, C_d, was normalized by the plenum discharge coefficient at the same pressure ratio, $C_{d,plenum}$, and scaled with the jet-to-crossflow momentum flux ratio.

In this study, discharge coefficients were measured for all blowing conditions for $DR = 1.2$ (an attempt was made to measure C_d at $DR = 1.8$ but was aborted due to concerns about frost forming around the pressure tap). Figure 3.7 (a) shows the measured discharge coefficients for all conditions tested plotted against the pressure ratio across the holes. The discharge coefficients decreased with increasing VR_c, except between $VR_c = 0.2$ and 0.3. This trend is in agreement with the literature, which shows C_d decreasing with increasing internal crossflow velocity. A similar, albeit simpler, scaling to that of Gritsch *et al.* [24] is shown in Figure 3.7 (b), which scales C_d with the coolant-jet-to-crossflow velocity ratio, U_j/U_c. With the exception of $VR_c = 0.2$, all of the data collapses to a single curve within uncertainty. The exception to the rule, $VR_c = 0.2$ occurs because the scaling with U_j/U_c would not hold for plenum-fed holes, so there must be some VR_c at which this scaling no longer collapses the data. The steep drop-off in C_d at low U_j/U_c corresponded to low injection rates where the coolant likely failed to diffuse effectively and the mainstream blockage of the coolant was more severe. The scaling with U_j/U_c was maintained at even low injection rates, suggesting that the losses at the inlet of the hole were still the most

important factor. This result demonstrates that the losses and likely the flow structures through the holes were driven by flow at the hole inlet. It is likely that the size of the separation region at the inlet is driven by the jet-to-crossflow velocity ratio and that losses at the hole inlet were very large compared to the other losses going through the hole.

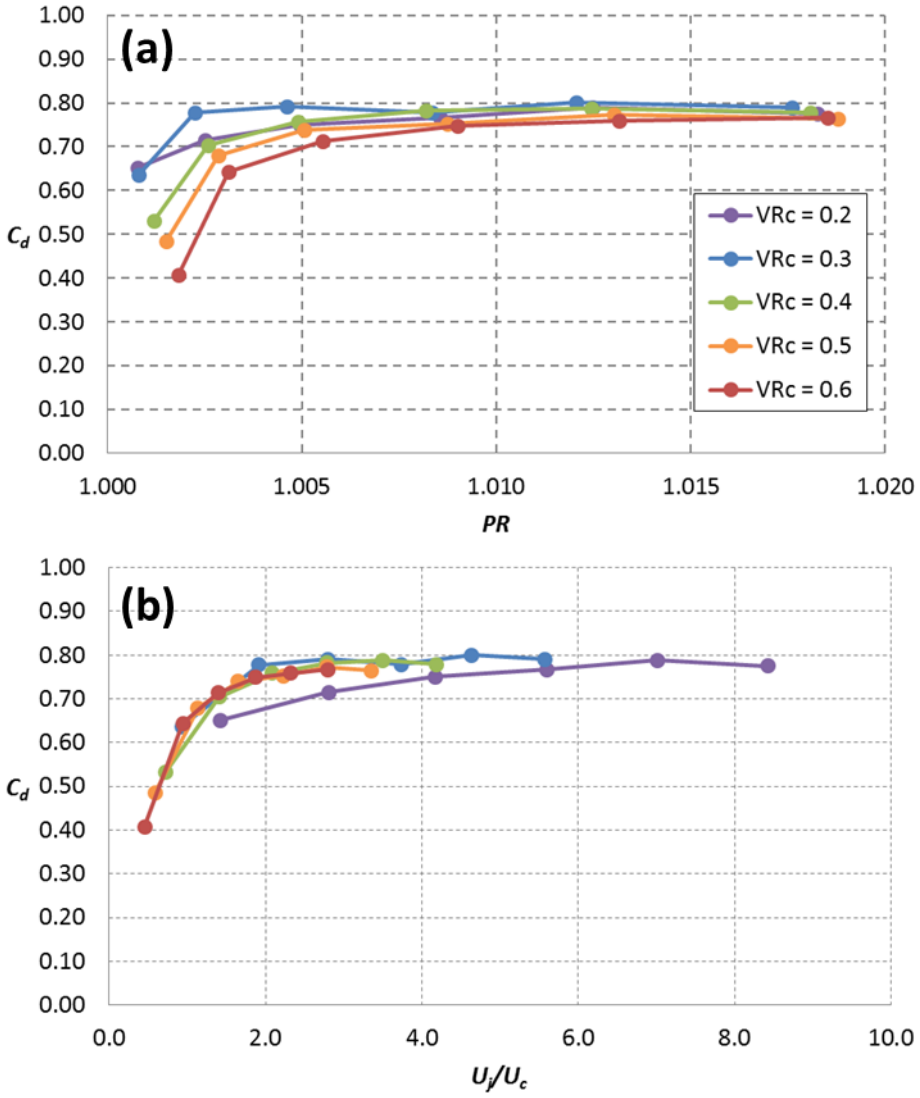

Figure 3.7: Discharge coefficients at *DR* = 1.2 for all flow conditions (a) scaled with pressure ratio and (b) scaled with jet-to-crossflow velocity ratio

3.3 ADIABATIC EFFECTIVENESS

Internal crossflow has been shown to reduce film cooling effectiveness relative to a plenum-fed condition for a few axial shaped hole geometries, including the one in this study. Very few studies have examined the effect of the crossflow velocity magnitude and none have done so over the wide range of flow parameters tested in this study. Figure 3.8 shows a plot of spatially averaged effectiveness for all flow conditions at a density ratio of $DR = 1.2$. The effectiveness was averaged over four pitches from $x/d = 5$-20 and compared to data for plenum-fed 7-7-7 holes from Anderson *et al.* [52]. For the plenum-fed holes, η increased with increasing injection rate until about $VR = 0.8$, after which jet separation reduced the effectiveness. For $VR = 0.4$-1.0, the plenum-fed holes greatly outperformed the crossflow-fed holes, but at $VR = 1.5$, the plenum-fed holes were within uncertainty of the $VR_c = 0.2$ crossflow condition. While no study in the literature has shown this effect before, no study in the literature has tested $VR_c < 0.35$. Increasing VR_c reduced the effectiveness at higher injection rates. Howerev, at lower injection rates, such as $VR = 0.83$, increasing VR_c from 0.3 to 0.6 increased effectiveness. The sharp decrease in effectiveness between $VR_c = 0.2$ and 0.3 at this injection rate was surprising and occurred due to biasing in the diffuser, which is discussed later. This trend was reversed as the velocity ratio increased to $VR = 1.67$, for which effectiveness decreased with increasing VR_c. For $VR \leq 0.56$, the spatially averaged effectiveness had very little sensitivity to crossflow magnitude.

The reduction in effectiveness relative to the plenum condition was the result of the coolant biasing in the diffuser. Figure 3.9 compares local distributions of effectiveness for the plenum-fed ($VR_c = 0$) and lowest crossflow velocity condition ($VR_c = 0.2$). Arrows to the left of the $VR_c = 0.2$ plots indicate the direction of internal crossflow. Unlike the symmetric plenum-fed jets, the jet profile for $VR_c = 0.2$ was skewed as a result of biasing in the diffuser, which can be observed relative to the outline of the hole exit shown in the

figure. Bias in the diffuser resulted in reduced centerline effectiveness relative to the plenum condition for both VR = 0.83 and 1.67. The coolant jets shown in this figure were biased toward the windward side of the diffuser relative to the internal flow direction, which is consistent with the wider-angle laidback fan-shaped holes of Gritsch *et al.* [12]. Unlike the wider-angle holes, these holes did not have a forked effectiveness profile. At both injection rates shown, the crossflow resulted in improved lateral spreading of the coolant jets relative to the plenum-fed condition, likely due to increased turbulence in the jet. Recall that at VR = 1.67, the plenum and VR_c = 0.2 conditions were within uncertainty of each other in terms of spatially averaged effectiveness. The improved lateral spreading of the crossflow-fed holes made up for the reduction in centerline effectiveness relative to the plenum-fed holes.

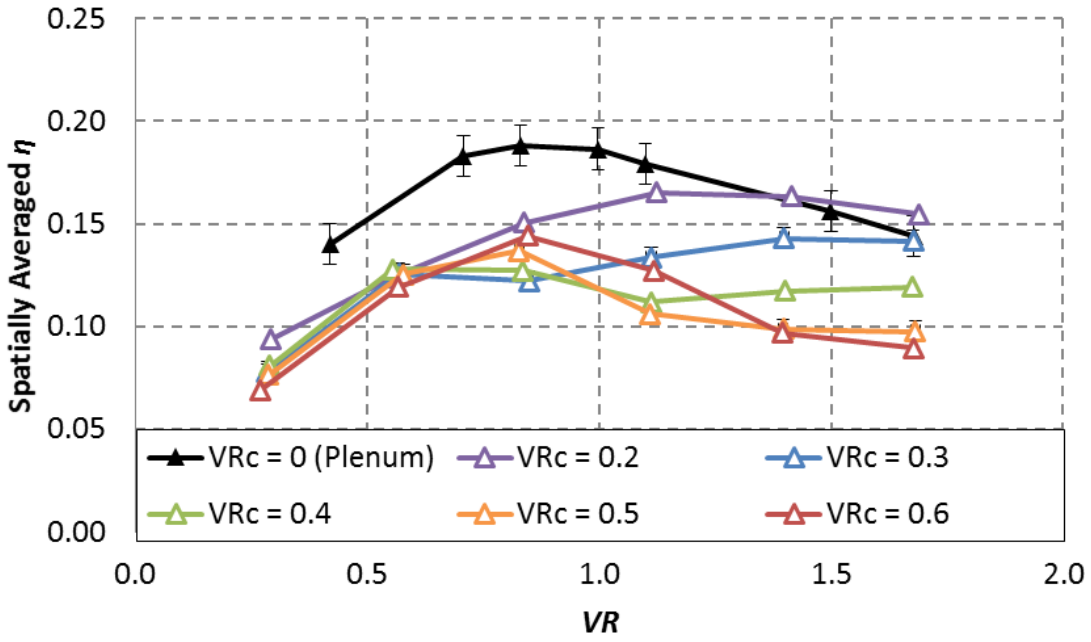

Figure 3.8: Spatially Averaged η over 4 pitches from x/d = 5-20 at DR = 1.2. Plenum-fed data is from [52]

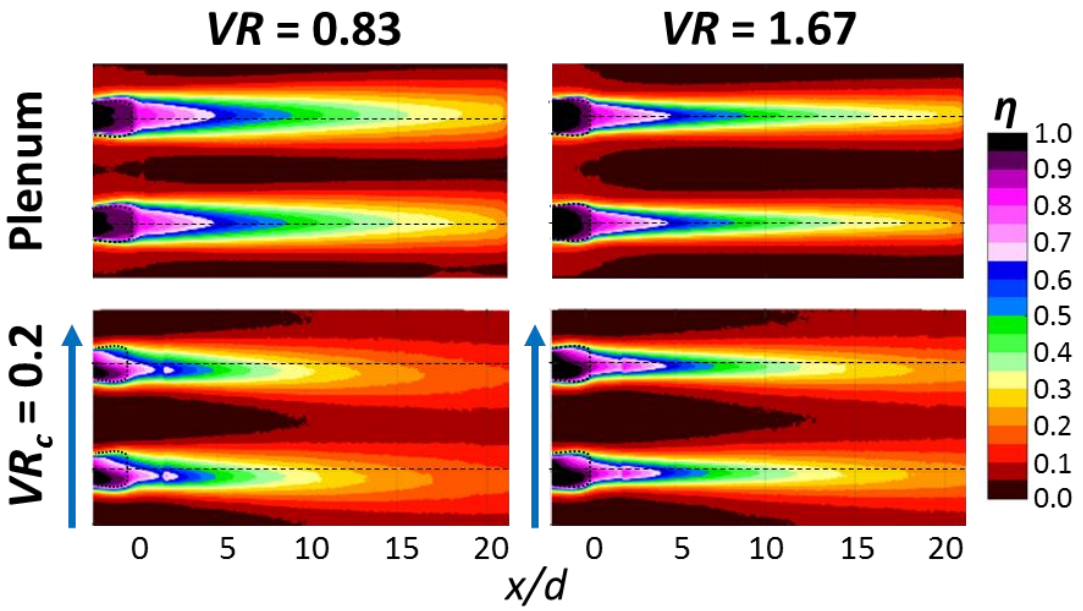

Figure 3.9: Comparison of local effectiveness for the plenum and VR_c = 0.2 conditions. Plenum data is from Anderson *et al.* [52]

The effect of increasing VR_c varied considerably depending on the injection rate. Figure 3.10 shows contours of effectiveness for the full range of VR_c tested in this study for three selected injection rates: VR = 0.56, 1.11, and 1.67. At VR = 0.56, the spatially averaged effectiveness had very little sensitivity to VR_c, which can be observed in the left column of the figure. The contours are not all identical, however. VR_c = 0.2 had slightly higher centerline effectiveness than the other conditions while the centerline effectiveness was slightly lower for VR_c = 0.6. More interestingly, the degree of biasing was reduced with increasing crossflow velocity, such that a forked jet can be observed in the diffuser for VR_c = 0.5 and 0.6 (and can be seen more clearly in the thermal field results in Figure 3.18 later in this chapter). A different trend can be observed for VR = 1.11. While VR_c = 0.2 was clearly the most effective condition at this injection rate, the centerline effectiveness did not necessarily decrease with increasing VR_c, but was a minimum at VR_c

= 0.4. That condition also appeared to experience the most extreme biasing in the diffuser. At VR = 1.67, the centerline effectiveness and the degree of biasing increased with increasing VR_c over the full range of tested crossflow velocities. These results suggest a connection between the centerline effectiveness and the degree of bias in the diffuser. These factors appear to be a function of both injection rate and crossflow velocity.

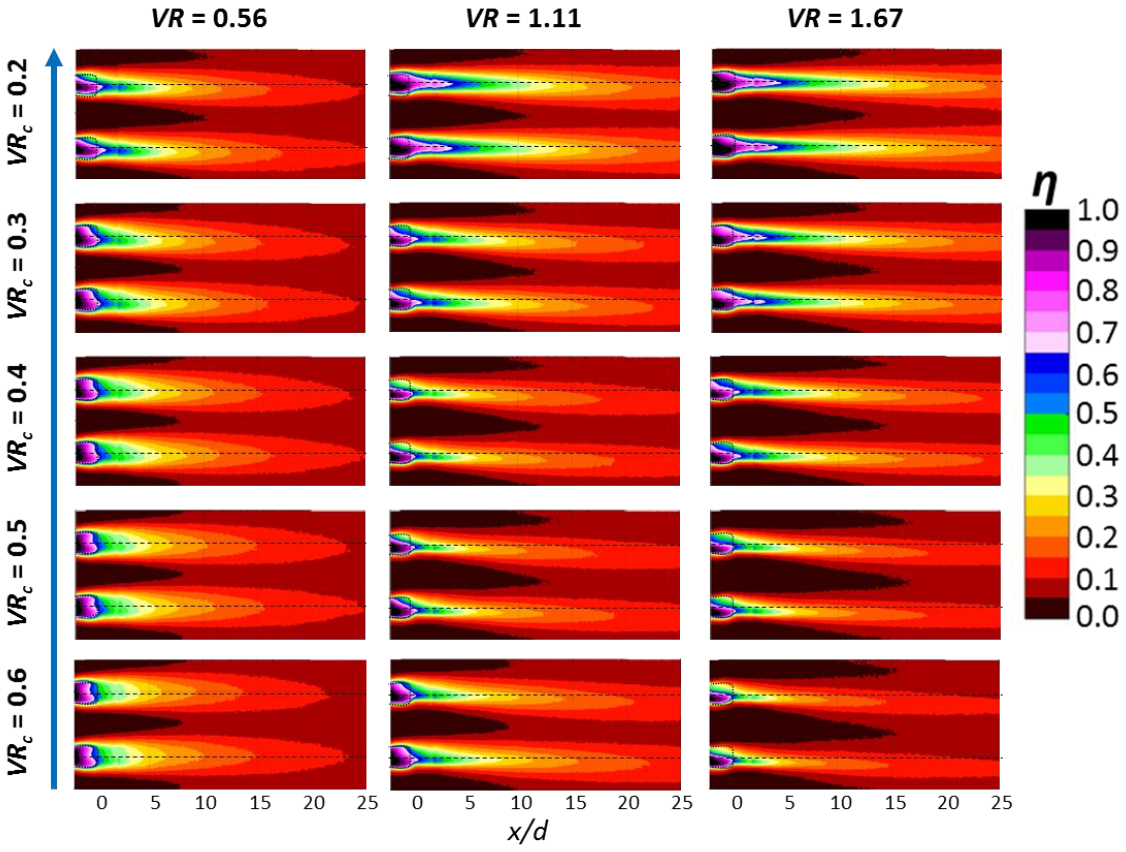

Figure 3.10: Contours of local film cooling effectiveness for selected conditions

Figure 3.11 shows a zoomed in view of the hole for selected conditions to better show the biasing within the diffuser. Note that the 1D conduction correction used to calculate the effectiveness in this region was not as accurate as the 3D correction used

downstream. For VR = 0.56, the jet exiting the hole had a forked effectiveness profile within the diffuser that disappeared shortly downstream. As noted previously, the peak biasing in the diffuser occurred at VR_c = 0.4 for VR = 1.11 and at VR_c = 0.6 for VR = 1.67.

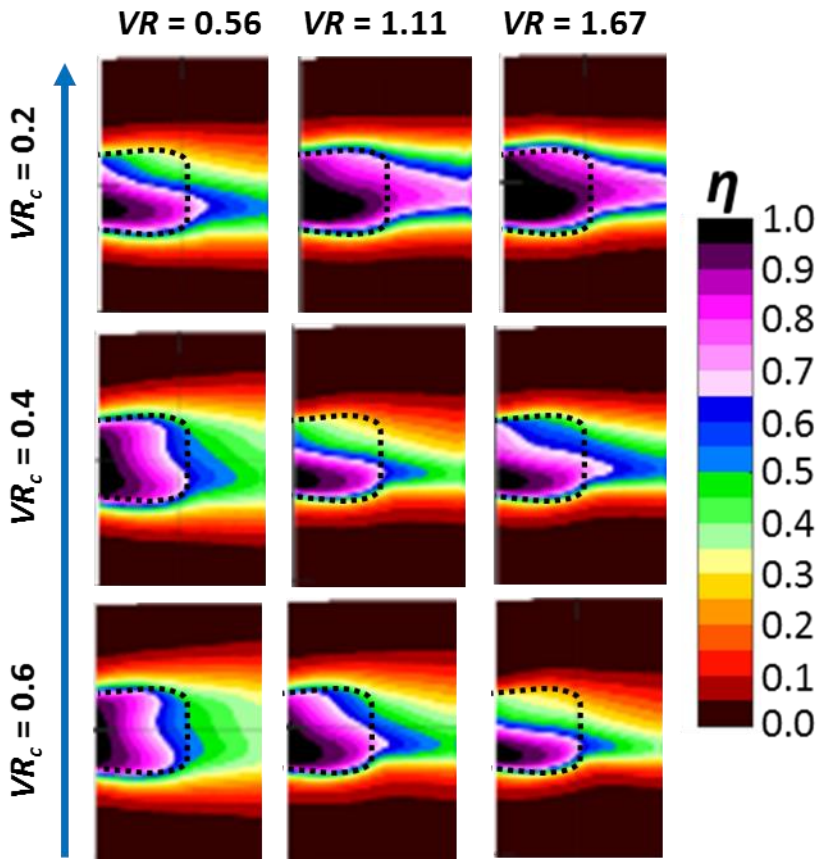

Figure 3.11: Contours of 1D conduction corrected η in the near-hole region

3.4 Jet Characteristic Parameters

Because jet biasing appeared to be correlated with a reduction in film cooling effectiveness, an effort was made to quantify how the internal crossflow velocity influenced the shape and location of the jet. To that end, four jet characteristic parameters were defined: jet centerline effectiveness, η_{CL}, jet centerline location, $(z/d)_{CL}$, jet width, W,

and jet skew, S. These parameters allow for a quantitative comparison of what can be observed from the distributions of local effectiveness. For details on how these parameters were defined and calculated, please refer to Section 2.4.2.4.

These jet characteristic parameters can be used to analyze the contours of effectiveness as shown for $VR = 1.11$ in Figure 3.12. The contours in Figure 3.10 showed that the centerline effectiveness was at a minimum for $VR_c = 0.4$ and 0.5, which is confirmed by the plot of centerline effectiveness. The centerline location moved further from the geometric centerline ($z/d = 0$) as VR_c was increased from 0.2 to 0.4, then reversed direction to move back toward the geometric centerline as VR_c increased to 0.6. Thus, Figure 3.12 (a) and (b) clearly show a connection between the degree of bias in the diffuser and the centerline effectiveness. Interestingly, the jet centerline continued to move further from the geometric centerline as the jet moved downstream. This result is unexpected given that the mainstream flow would be expected to turn the jet into the streamwise direction. However, by 30d downstream, the jets showed no sign of being turned by the mainstream. This result suggests that some secondary flow was responsible for moving the jet laterally as it moved downstream. Given that computational predictions such as the one performed by Saumweber and Schulz [14] suggest the existence of an asymmetric counter-rotating vortex pair for crossflow-fed fan-shaped holes, this explanation seems plausible. The jet width, shown in Figure 3.12 (c) was relatively insensitive to VR_c for $VR_c \geq 0.4$, but narrowed when reduced to $VR_c = 0.2$. This results suggests that increased crossflow velocity caused increased lateral spreading of the coolant jets up to a point. The increased lateral spread was possibly a result of increased turbulence intensity in the hole or a stronger asymmetric counter-rotating vortex pair. Note that the jet width cannot exceed the width of the pitch, $p/d = 6$, which is the maximum possible value of W/d. Once the jet becomes as wide as the pitch, the jets are considered to be merged, after which point neither

jet width nor skew is defined. The jet skew, shown in Figure 3.12 (d), was the noisiest of the four parameters as it was dependent on $(z/d)_{CL}$, which was noisy as well. The skew for all VR_c started out positive and quickly declined to zero going downstream, where the jet became symmetric. The sign of the skew was opposite the sign of the centerline location, which is expected to be caused by the jet's lateral movement. Near the hole, $VR_c = 0.6$ had the greatest skew while $VR_c = 0.2$ was the least skewed.

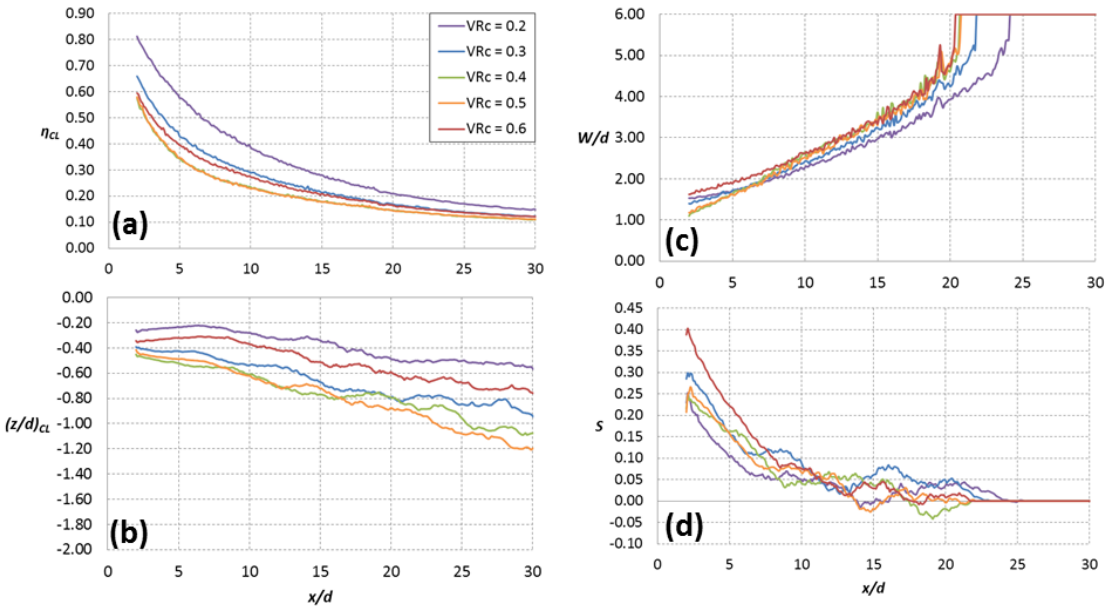

Figure 3.12: Jet characteristic parameters for $VR = 1.11$ (a) centerline effectiveness, (b) centerline location, (c) jet width, and (d) jet skew

Given the large range of flow parameters tested in this study, the jet characteristic parameters were averaged in order to better understand how they were affected by injection rate and crossflow velocity. It was found that the data collapsed when scaled with the film hole inlet velocity ratio, $VR_i = U_c/U_j$. Figure 3.13 shows the scaling of the four jet characteristic parameters, averaged from x/d = 5-20, scaled with the inlet velocity ratio. The averaged η_{CL}, $(z/d)_{CL}$, and S all collapsed to within uncertainty. Given that the

discharge coefficients also scaled with this ratio (scaling with its inverse is shown in Figure 3.7), this result confirms the importance of separation at the hole inlet. More interestingly, there existed a critical inlet velocity ratio, $VR_{i,cr}$ = 0.36, at which there was a local minimum in η_{CL}, a maximum in $|(z/d)_{CL}|$, and a local minimum in S. This critical inlet velocity ratio thus represents a maximum bias condition where the film hole diffuser was the least effective. The existence of this $VR_{i,cr}$ explains why the η_{CL} declined with increasing VR_c for VR = 1.67, but not for VR = 1.11. It also suggests that if VR_c were increased further at VR = 1.67, the effectiveness would increase and the bias in the diffuser would be reduced. The corresponding local minimum in the jet skew at $VR_{i,cr}$ is an interesting result, as increased jet bias would be expected to result in increased skew. It is possible, that as VR_i approached 0.36, the coolant was forced more and more toward the windward side of the diffuser, resulting in a jet that was more akin to that of a cylindrical hole with a compound angle of 7°. There would therefore be less coolant available to cool the surface on the leeward side of the jet, resulting in a less skewed jet.

There are a number of other interesting observations that can be made regarding Figure 3.13. Disregarding the local minimum around VR_i = 0.36, the centerline effectiveness tended to decrease as a result of increasing VR_i. This occurred because VR decreases and VR_c increases as VR_i increases. Because the 7-7-7 holes tend to separate at high injection rates, it is likely that this trend would fail at sufficiently high injection ratio, but it is unclear at which point this would happen for each VR_c. For VR_c = 0.3-0.5, the centerline effectiveness increased as VR increased from 1.39 to 1.67, suggesting that the effectiveness could continue to increase with increasing VR up to a point. On the other hand, VR = 0.28 was sufficiently low to cause the averaged η_{CL} to deviate from the curve – all points in Figure 3.13(a) with averaged $\eta_{CL} < 0.15$ were at VR = 0.28. For these conditions, there was poor performance due to low VR.

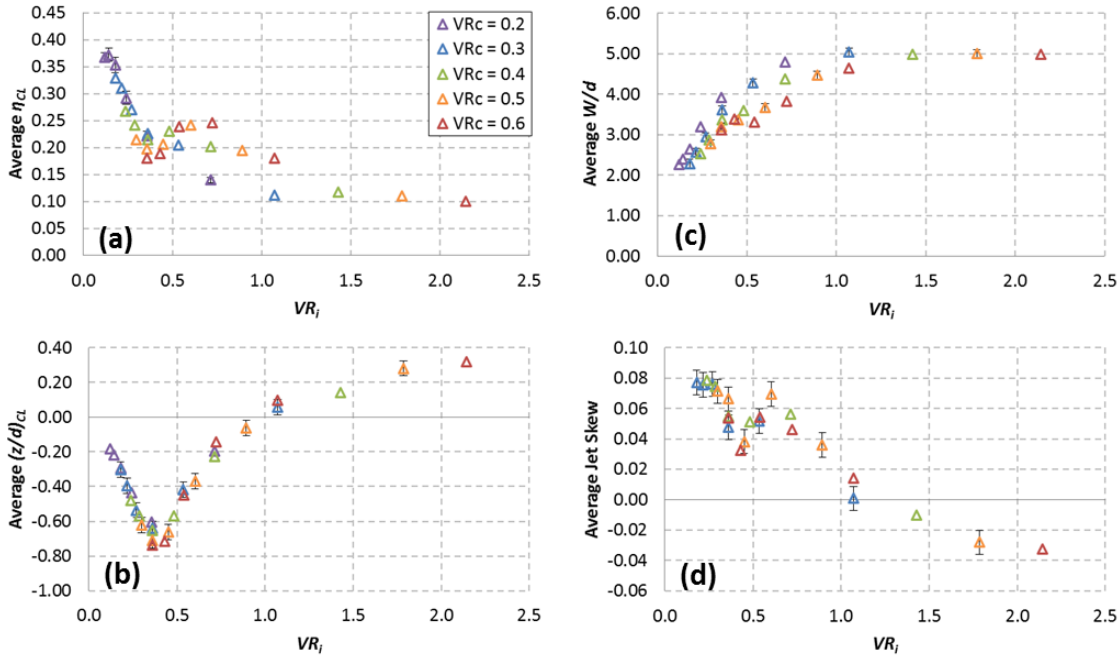

Figure 3.13: Jet characteristic parameters averaged over x/d = 5-20, scaled with VR_i (a) centerline effectiveness, (b) centerline location, (c) jet width, and (d) jet skew

At VR_i = 1.0, the centerline location and jet skew reversed directions. At this VR_i, the jet switched from biasing toward the windward to the leeward side of the diffuser and from skewing toward the leeward to the windward side of the jet. This result is compatible with the computational studies of Saumweber and Schulz [14] and Kohli and Thole [37], who both predicted that a strong swirl formed in film cooling holes fed by crossflow that determines how the coolant biases within the diffuser. If that indeed is the case, this result shows that, for a fixed film hole geometry, the inlet velocity ratio drives the strength of the swirl relative to the jet velocity in the hole. The larger the inlet velocity ratio, the more revolutions the swirling coolant made as it passed through the hole. Due to the expected separation at the hole inlet, the coolant jet would have entered the hole biased toward the

leeward side of the hole, requiring it to make at least a half rotation at $VR_i = 0.36$. At $VR_i = 1.0$, the coolant would have made at least ¾ of a rotation such that it exited the diffuser without biasing toward either side.

Unlike the other jet parameters, the jet width did not collapse to within uncertainty when scaled with inlet velocity ratio, nor did the data collapse when scaled with VR or VR_c. The jet width increased with increasing VR_i, although this could have also been a result of lower VR resulting in flatter jet profiles with lower centerline effectiveness. For the jet skew, the scaling with VR_i, did not hold for $VR_c = 0.2$, which is not plotted on Figure 3.13 for the sake of clarity. Similar to the scaling of the discharge coefficients breaking down for $VR_c = 0.2$, this scaling is expected to fail as plenum conditions are approached ($VR_i = 0$) as the plenum-fed jet nominally has a skew of $S = 0$.

Given the importance of this scaling analysis to understanding how internal crossflow affects film cooling, the scaling with VR_i was also performed at $DR = 1.8$, which is a more engine-realistic density ratio. Figure 3.14 compares the scaling of η_{CL} and $(z/d)_{CL}$ at $DR = 1.2$ and 1.8. While the data at $DR = 1.8$ was more scattered due to jet-to-jet variation, the trends observed at $DR = 1.2$ were indeed preserved at $DR = 1.8$. These trends include the correspondence of the local minimum in centerline effectiveness and the maximum biasing at $VR_i = 0.36$, the direction of bias switching at $VR_i = 1.0$, and the breakdown in the scaling of the centerline effectiveness at $VR < 0.3$.

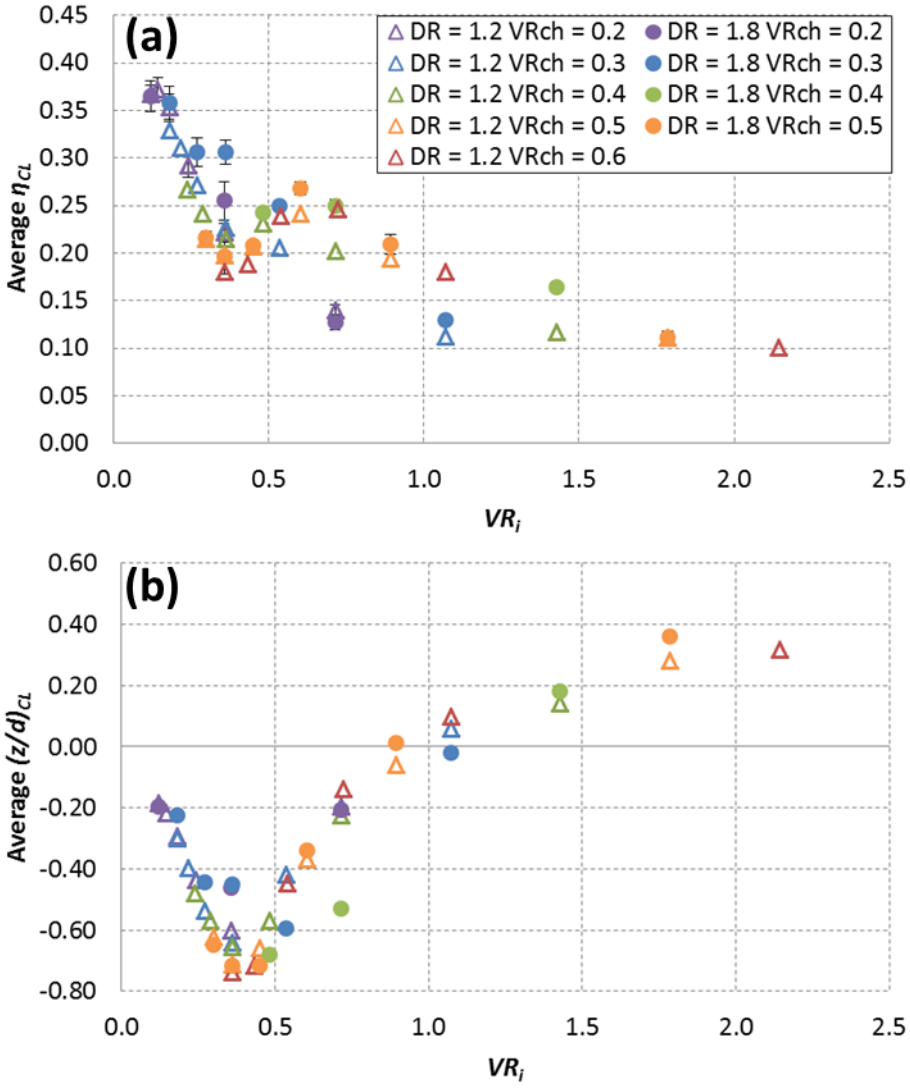

Figure 3.14 Effect of density ratio on (a) η_{CL} and (b) $(z/d)_{CL}$ averaged over x/d = 5-20 and scaled with VR_i

3.5 Near-Hole Thermal Fields

In order to better understand the mechanisms behind coolant biasing and its effect on film effectiveness, thermal fields were measured in the near-hole region both above the surface and within the diffuser of the film hole. These thermal fields were measured in the y-z plane at three streamwise locations: x/d = -2, 0, and 5. At x/d = -2, the probe was lowered

into the diffused section of the hole to measure the temperatures within the diffuser. These measurements were performed for six flow conditions, selected to show the relative importance of VR_i, VR, and VR_c. These conditions are given in Table 3.1 below. These parameters were chosen to ensure that there were at least two different values of each parameter that were matched.

Table 3.1: Flow conditions used for thermal field measurements

VR_c	VR	VR_i
0.20	0.83	0.24
0.40	1.67	0.24
0.40	1.11	0.36
0.60	1.67	0.36
0.40	0.56	0.71
0.60	0.83	0.71

Biasing in the diffuser resulted in mainstream air ingestion into the opposite side of the diffuser, an effect that was driven by the inlet velocity ratio. Figure 3.15 shows thermal field plots for all conditions listed in Table 3.1 at x/d = -2. The contours of θ are overlaid on a cutaway view of the diffuser at that x/d location. Each row in the figure is at a different inlet velocity ratio, and VR_i increases from top to bottom. A plenum-fed condition is shown at the top. Internal crossflow was directed from left to right and the contour plots show the jet as viewed from downstream looking back toward the holes. The temperature profiles in the holes show how the jets biased in the diffuser at different inlet velocity ratios. These plots are in agreement with the plots of local effectiveness and jet characteristic parameters in that they show that the biasing was the most extreme at the critical inlet velocity ratio of VR_i = 0.36. At that condition, the coolant in the diffuser clearly favored the windward side of the diffuser and allowed considerable ingestion into the leeward side of the diffuser. This result was consistent at both conditions at this inlet velocity ratio, regardless of

differences in VR and VR_c. The ingestion of mainstream flow into the diffuser is problematic for film cooling in two ways: it warms the coolant before it ever exits the holes, thus reducing film cooling downstream, and it leaves part of the film hole itself unprotected from the high temperature mainstream.

The degree and manner of ingestion varied with inlet velocity ratio. The plenum condition, shown at the top, had a roughly symmetric profile with some evidence of ingestion at the side of the hole. This ingestion shows that the flow failed to fully diffuse laterally and that the mainstream flow was able to partially penetrate down into the diffuser. These measurements are unable to distinguish between ingestion and turbulent transport of heat, but the location of the region of reduced θ implies there was some degree of ingestion. At VR_i = 0.24, ingestion increased on the leeward side of the hole relative to the direction of internal crossflow, and was similar to that of the plenum-fed case on the windward side of the hole. The location of ingestion into the windward side of the hole corresponded with the effectiveness measurements which show the jet biasing toward the windward side of the diffuser. Unsurprisingly, ingestion occurs away from where the core of the jet was located. The jet served to block the mainstream from entering the diffuser, but in the absence of the jet, the mainstream flow was able to ingest. As previously discussed, at VR_i = 0.36, there was considerable ingestion on the leeward side of the film hole due to the jet biasing toward the windward side. Interestingly, at VR_i = 0.71, there was ingestion down into the center of the diffuser. Recall that the direction of biasing switched at VR_i = 1.0, so at this condition, the jet was nearly symmetric. However, the coolant flowed along the bottom wall of the diffuser unlike the plenum-fed or VR_i = 0.24 conditions. This result seemingly confirms that the bias in the diffuser was indeed driven by a swirling flow initiated at the inlet of the hole. The plenum condition was simulated by Oliver *et al.* [31] using an implicit LES scheme and was shown to have good agreement to experimental

thermal fields at x/d = 5. That simulation also predicted strong jetting of coolant on the upstream side of the hole relative to the mainstream as it accelerated around a large separation region in the diffuser. This jetting coolant was likely responsible for blocking the mainstream from ingesting into the diffuser, except at the edges. The coolant at VR_i = 0.24, though slightly biased, acted similarly to the plenum condition, preventing ingestion into the center and windward side of the diffuser. As VR_i increased, the rotation of the jet increases and the coolant jetted toward the windward side of the diffuser at VR_i = 0.36, failing to prevent ingestion down into the leeward side of the diffuser. At VR_i = 0.71, the coolant jet now favored the bottom of the diffuser, and no longer blocked the mainstream from ingesting down into the top of the diffuser. This condition therefore had improved effectiveness relative to VR_i = 0.36, but performed poorly relative to the plenum due to the ingestion into the center of the diffuser.

While the inlet velocity ratio clearly governed biasing and injection in the diffuser, there were differences between plots in the left and right hand columns of Figure 3.15 due to the injection rate. Figure 3.16 shows plots of θ at x/d = -2 for (a) z/d = -0.11 and (b) y/d = 0. At z/d = -0.11, the curves all go to θ = 1.0 as they go down into the hole. There are differences between the matched VR_i curves going out of the hole, likely caused by differences in injection rate. For all three matched VR_i pairs, higher VR corresponded with greater y/d for a given value of θ. Because the mainstream ingested down in to the diffuser at this lateral location for VR_i = 0.71, that pair of curves started to diverge within the diffuser itself. This effect can also be observed at y/d = 0. For VR_i = 0.71, the two curves were most different at the peak θ values (z/d = -0.5 and 0.9). These differences were likely the result of the location of the shear layer between the mainstream and the coolant, which would be sensitive to the injection rate. At z/d = 0.1-0.3, the two curves were similar probably because the shear layer for both of these injection rates was located well below

y/d = 0. The shape of this profile is also in agreement with the forked effectiveness distribution observed in the adiabatic effectiveness distributions.

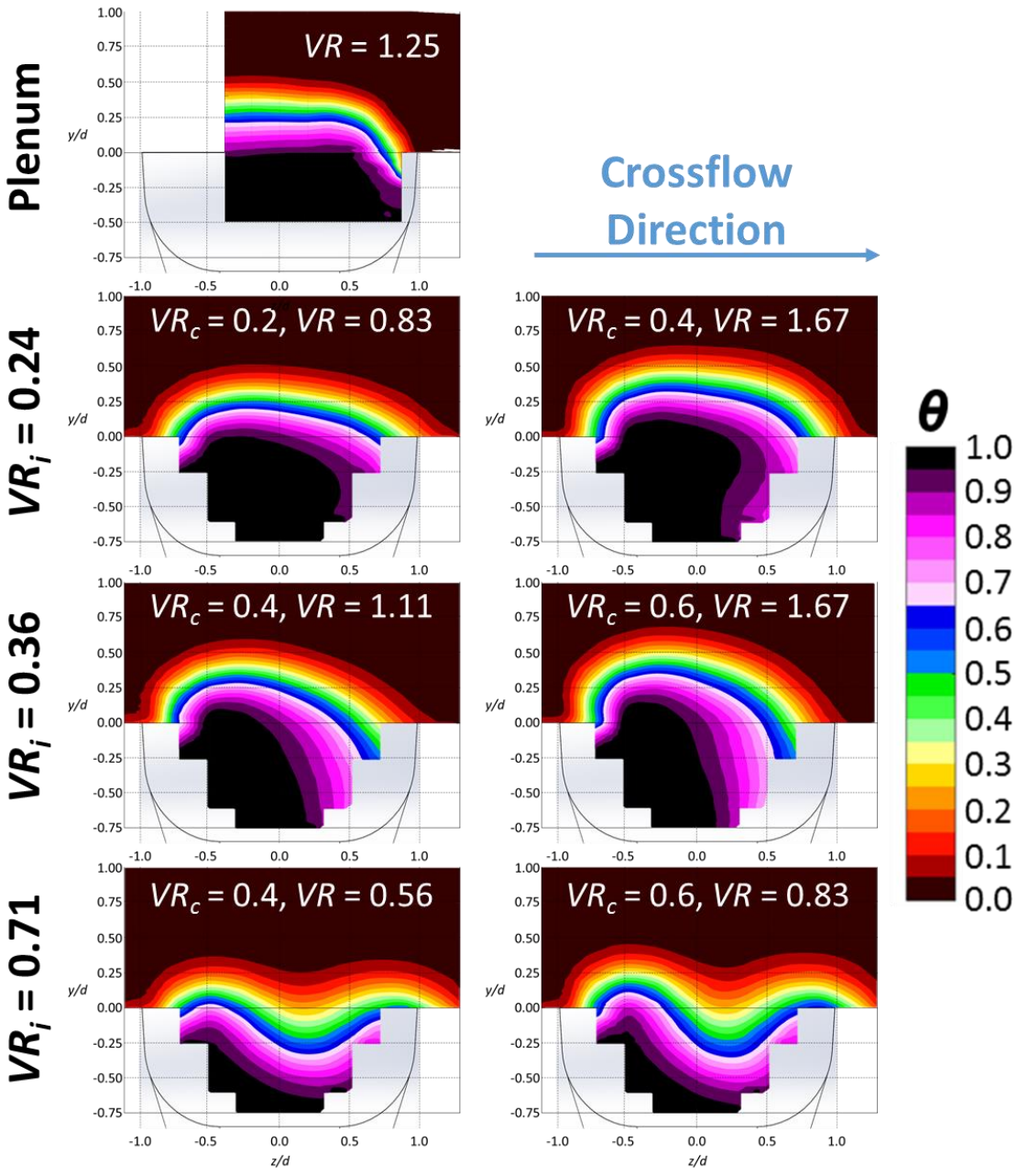

Figure 3.15: Thermal fields in the *y-z* plane at *x/d* = -2

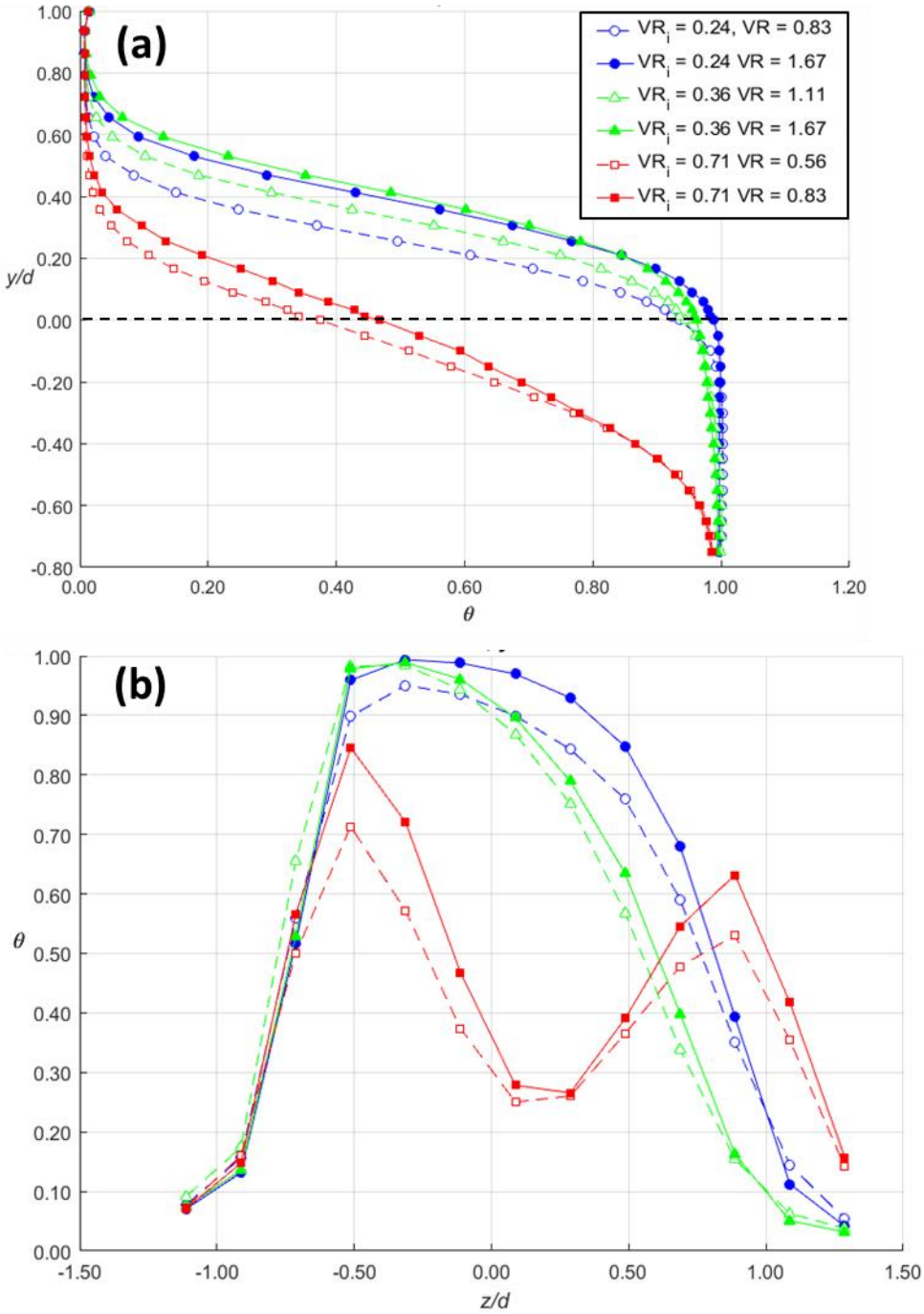

Figure 3.16: Line plots of θ at x/d = -2 and (a) z/d = -0.11 and (b) y/d = 0

The effect of injection rate can be observed in the thermal field profiles further downstream. That effect can be clearly observed in Figure 3.17 for VR_i = 0.24. At VR = 0.83, the jet remained well-attached to the surface at x/d = 5, while for VR = 1.67, the jet core had lifted off the wall. However, the centerline effectiveness and location were similar between the two conditions, corresponding with the scaling of those parameters with VR_i. Similarly, at VR_i = 0.71, the jet-to-mainstream velocity ratio had a notable effect on the downstream thermal filed profile, as shown in Figure 3.18. Unlike VR_i = 0.24, the two-pronged jet at VR_i = 0.71 resulted in a flatter downstream jet that remained better attached to the wall, albeit at lower VR. The difference in VR was not as pronounced for the two cases at VR_i = 0.71, but the higher injection rate of VR = 0.83 clearly resulted in the spread of coolant further away from the wall and maintained faint traces of the forked profile in the hole at x/d = 5 (if only in the slanted jet shape), while that profile was non-existent at that location for VR = 0.56. There was a slight difference in centerline effectiveness between the two conditions at x/d = 5, but the centerline location was nearly identical.

The degree of biasing also had an effect on jet separation. Figure 3.19 shows thermal field contours for VR = 1.67 at VR_i = 0.24 and 0.36. The jet core separated from the surface at both inlet velocity ratios, but at VR_i = 0.36 the increased biasing in the diffuser resulted in a jet that separated further from the surface and had reduced effectiveness. While the profiles at x/d = 0 were not very different for the two conditions, the jet at VR_i = 0.36 had a more compact jet core compared to VR_i = 0.24 due to increased bias at VR_i = 0.36. The more compact core at VR_i = 0.36 thus had an increased effective momentum and separated more readily

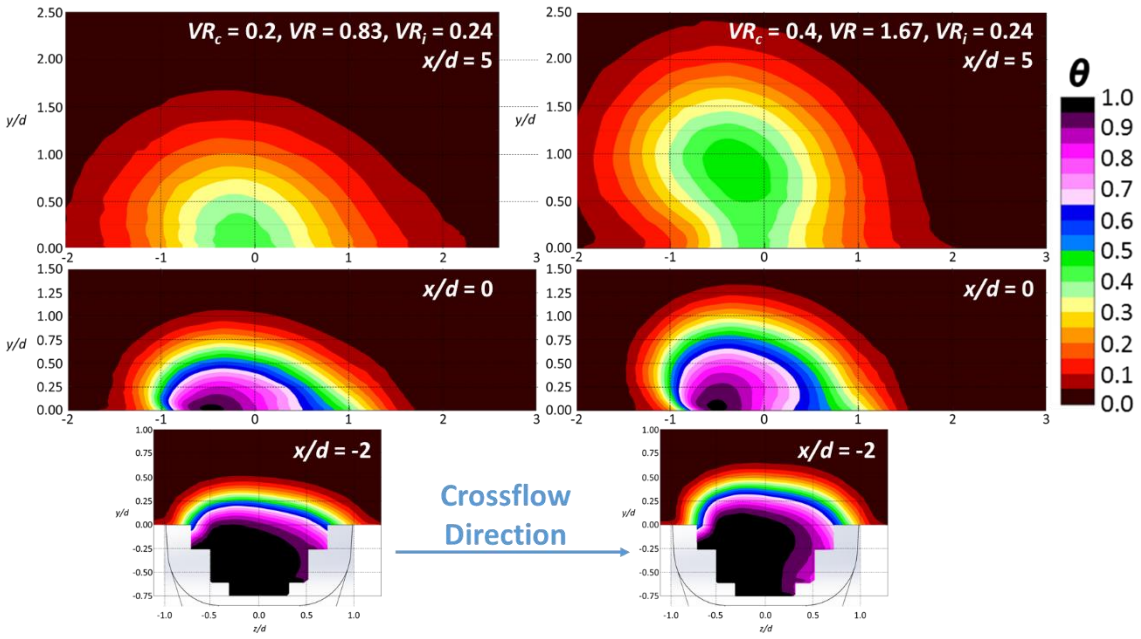

Figure 3.17: Thermal fields at x/d = -2, 0, and 5 for VR_i = 0.24

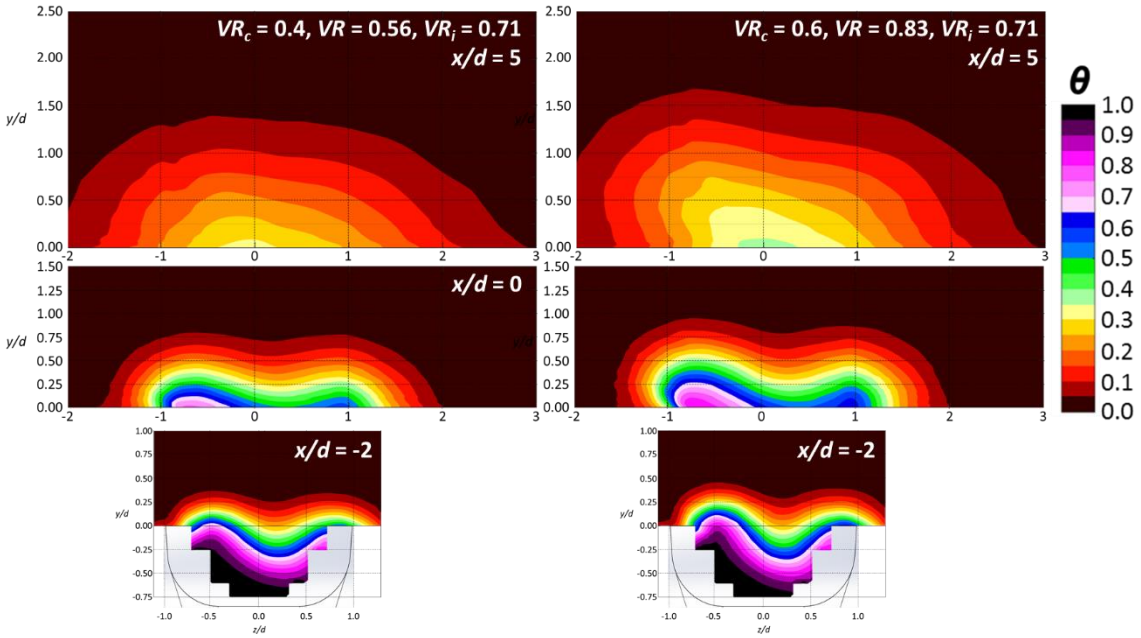

Figure 3.18: Thermal fields at x/d = -2, 0, and 5 for VR_i = 0.71

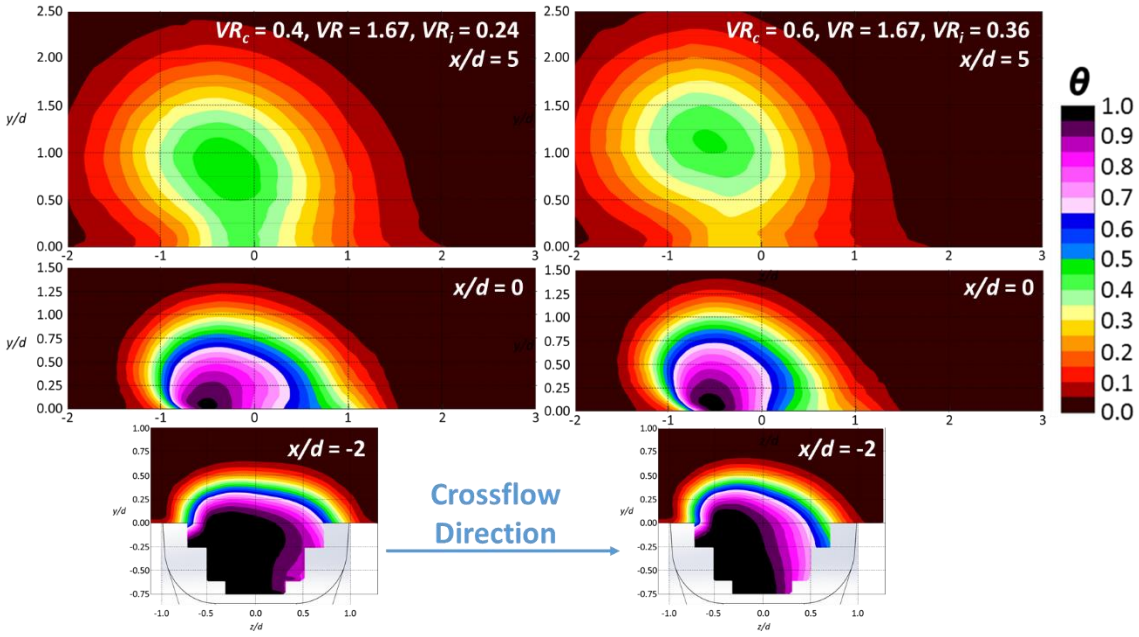

Figure 3.19: Thermal fields at x/d = -2, 0, and 5 for VR = 1.67

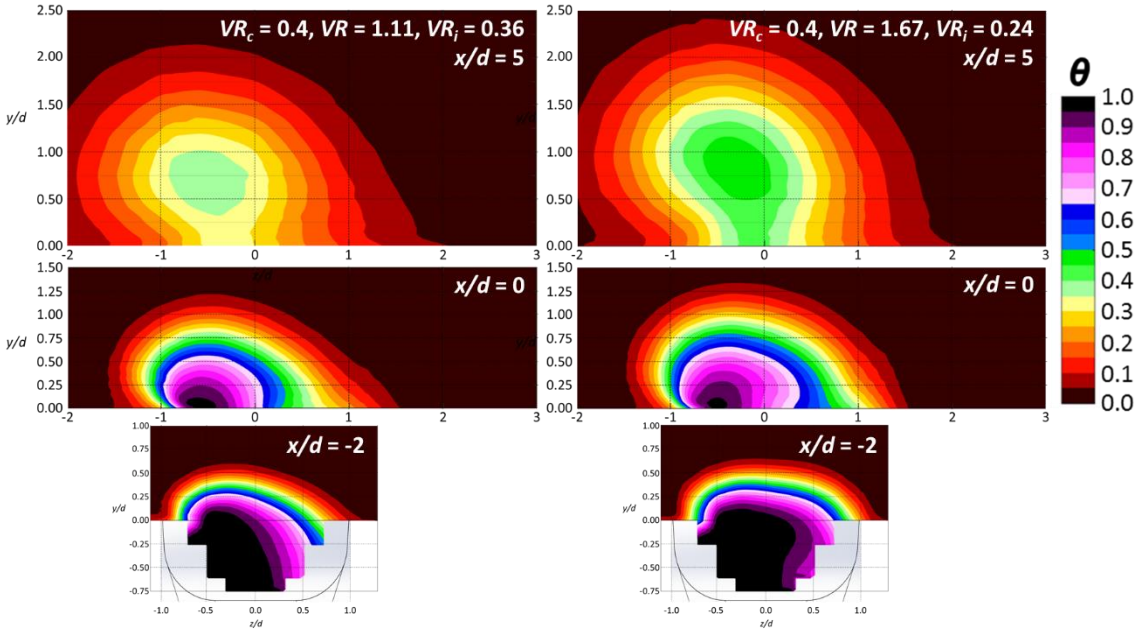

Figure 3.20: Thermal fields at x/d = -2, 0, and 5 for VR_c = 0.4, VR = 1.11 and 1.67

Because of the critical inlet velocity ratio causing a maximum jet bias at $VR_i = 0.36$, the effectiveness increased from VR = 1.11 to 1.67 for VR_c = 0.4. It is unusual for effectiveness to increase with increasing injection rate after decreasing (as it did from VR = 0.83 to 1.11), but this unusual result can be explained by the crossflow effect. Figure 3.20 shows thermal fields for VR_c = 0.4 at VR = 1.11 and 1.67. The increase in effectiveness when VR was increased from 1.11 to 1.67 was the result of a colder jet core with more coolant injected. Both profiles had a similar extent of detachment from the wall at x/d = 5, because the biasing was more severe at VR_i = 0.36, which increased the effective momentum of the jet.

3.6 IN-HOLE VELOCITY FIELDS

Flow fields were measured within the diffuser right at the upstream edge of the hole. The measurement plane was oriented nearly normal to the axis of the metering section of the hole in order to observe the secondary flow structures causing the bias in the diffuser. Please refer to Section 2.4.4 for detail on the setup of the PIV system used to make these measurements. The conditions tested were the same as those for the thermal fields, with the exception of the mainstream-to-coolant density ratio, which was set to DR = 1.0 for the flow field measurements. The flow fields in this location are not expected to be very sensitive to density ratio – this is the first location where the coolant flow field can be influenced by the overflowing mainstream. Also, recall that the degree of biasing was similar between DR = 1.2 and 1.8, indicating similar in-hole flow physics. Previous computational studies have predicted that a swirling flow within the film hole was responsible for the biasing of coolant in the diffuser for holes fed by an internal crossflow [14, 37]. Furthermore, the experimental effectiveness and thermal field data shown thus far, such as the scaling of jet location with the inlet velocity ratio, the maximum bias that

occurs at VR_i = 0.36, and the apparent rotation of the core of the jet within the diffuser as shown by thermal field measurements, strongly suggests the existence of this swirling flow structure. The primary aim of these in-hole velocity field measurements was to observe the secondary flow within the holes to confirm that this swirling flow was indeed responsible for the biasing within the diffuser. Furthermore, measurements of the secondary flow within the diffuser of shaped film cooling holes have yet to be presented in the literature.

A mean swirling flow was observed in the diffuser at an inlet velocity ratio of VR_i = 0.71. Figures 3.21-23 show the mean in-hole velocity fields at the upstream edge of the outlet (5.13 hole diameters from the inlet) at a plane that was 5° off of normal to the injection direction at different VR_i. The velocity vectors are overlaid on contours of in-plane fluctuating velocity normalized by the mainstream velocity. The shape of the hole at that location is superimposed on the figure and the internal crossflow was directed from left to right. Figure 3.21 shows two cases, each at VR_i = 0.71, one at VR_c = 0.4, VR = 0.56 and the other at VR_c = 0.6, VR = 0.83. There was a swirling flow for both conditions on the leeward side of the hole relative to the direction of internal crossflow. The existence of this vortex seemingly confirms that the bias in the hole was the result of an asymmetric swirl that formed due to inlet flow effects. The vortex was better defined for VR_c = 0.4, VR = 0.56. It is possible that the bottom of the diffuser blocked the view of the bottom of the vortex for VR_c = 0.6, VR = 0.83. Otherwise, the mean flow for each condition was remarkably similar, with the vortex on the leeward side of the hole and the flow on the windward side moving in the windward direction, confirming that the inlet velocity ratio was the important scaling parameter for both in-hole thermal and velocity fields. The fluctuating velocity was nearly constant throughout the measurement plane for each condition. VR_c = 0.6, VR = 0.83 had a slightly greater fluctuating velocity than VR_c = 0.4, VR = 0.56. These results are furthermore, consistent with the effectiveness and thermal

field measurements. At $VR_i = 0.71$, the jet was still biased toward the windward side of the hole, as can be seen in the flow moving toward the windward side and filling out that side of the diffuser. Furthermore, at this inlet velocity ratio, the thermal fields showed ingestion down into the center of the diffuser, corresponding to the downward flow in the center of the diffuser due to the vortex on the leeward side. Moreover, the thermal fields suggest that the rotation in the hole should be counter-clockwise relative to a view down the hole in order to move the center of the jet from top-left to the left side to bottom-left with increasing VR_i, and the vortex in Figure 3.21 is oriented in the counter-clockwise direction. The velocity of the swirling flow is also of interest. At its strongest, the swirling velocity in this plane is on the order of $0.1U_\infty$. Based on the length of the hole to this point, L, the average perimeter of the hole, P_{avg}, the velocity of the jet, U_j, and the expected number of rotations within the hole, N_r, the average swirling velocity in the hole, $U_{s,avg}$, can be estimated as:

$$U_{s,avg} = \frac{N_r P_{avg}}{L} U_j \tag{3.1}$$

The average swirling velocity was estimated at $U_{s,avg} \approx 0.2\ U_\infty$ and $0.3\ U_\infty$ for conditions (a) and (b) in Figure 3.21 respectively based on an estimated $N_r = 0.63$. The estimated average swirl velocities are greater than the observed maximum swirling velocity in the measurement plane, meaning that the swirl velocities in the cylindrical section of the hole would have had to be greater than the average estimated swirl velocities in order to produce the measured bias. This result is unsurprising because the expansion into the diffuser is expected to attenuate the strength of the in-hole vortices.

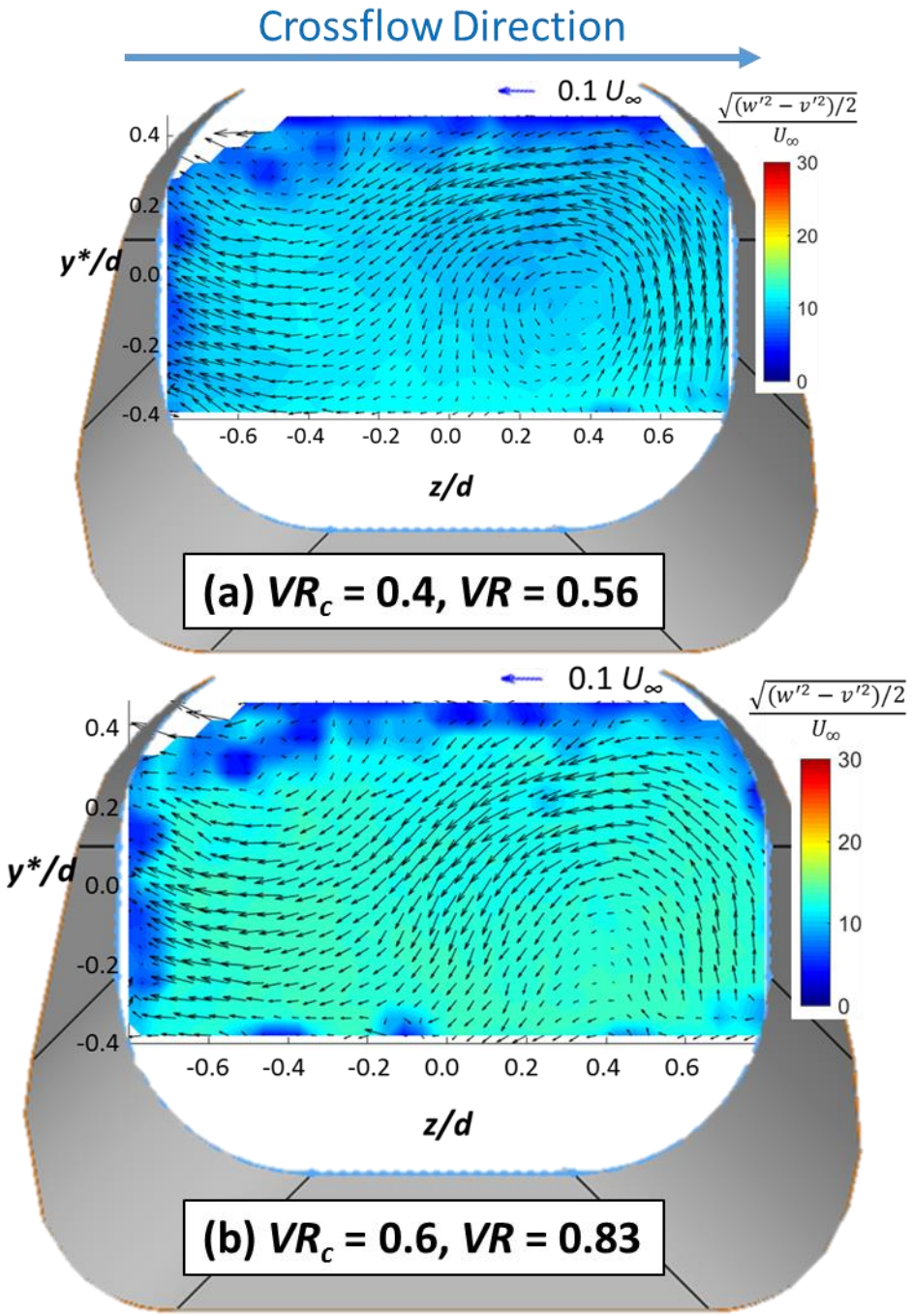

Figure 3.21: Mean in-hole velocity fields at the upstream edge of the outlet for VR_i = 0.71

In-hole velocity fields corresponding to conditions with maximum biasing, VR_i = 0.36, did not have any mean vortical pattern. Figure 3.22 shows in-hole velocity fields for VR_i = 0.36 at two flow conditions: VR_c = 0.4, VR = 1.11 and VR_c = 0.6, VR = 1.67. While it is possible that a vortical pattern did indeed exist but was not visible due to the viewing angle used for these measurements, the in-hole vortices would have been weaker for this inlet velocity ratio and may have been too weak or intermittent to measure after attenuation in the diffuser. If indeed that is the case, the metering hole length is likely an important geometric parameter for determining the effect of internal crossflow on film cooling. As for VR_i = 0.71, the fluctuating velocities were nearly uniform across the measurement plane. These velocity fields also correspond well to the effectiveness and thermal field measurements. At VR_i = 0.36 the biasing toward the windward side of the diffuser was the most extreme, as can be seen in how the flow in the measurement plane is predominantly directed toward the windward side. The thermal fields show a considerable amount of ingestion into the leeward side of the diffuser which corresponds with the downward flow on the leeward side of the hole. This downward flow appears to be a residual part of a vortical flow as can be seen in how the flow moves downward on the leeward side of the diffuser and upward on the windward side of the hole. It is possible that this vortex was part of a counter-rotating vortex pair and that its counterpart existed in the bottom part of the hole. Like at VR_i = 0.71, there is considerable similarity between the two flow conditions shown in Figure 3.22 for VR_i = 0.36.

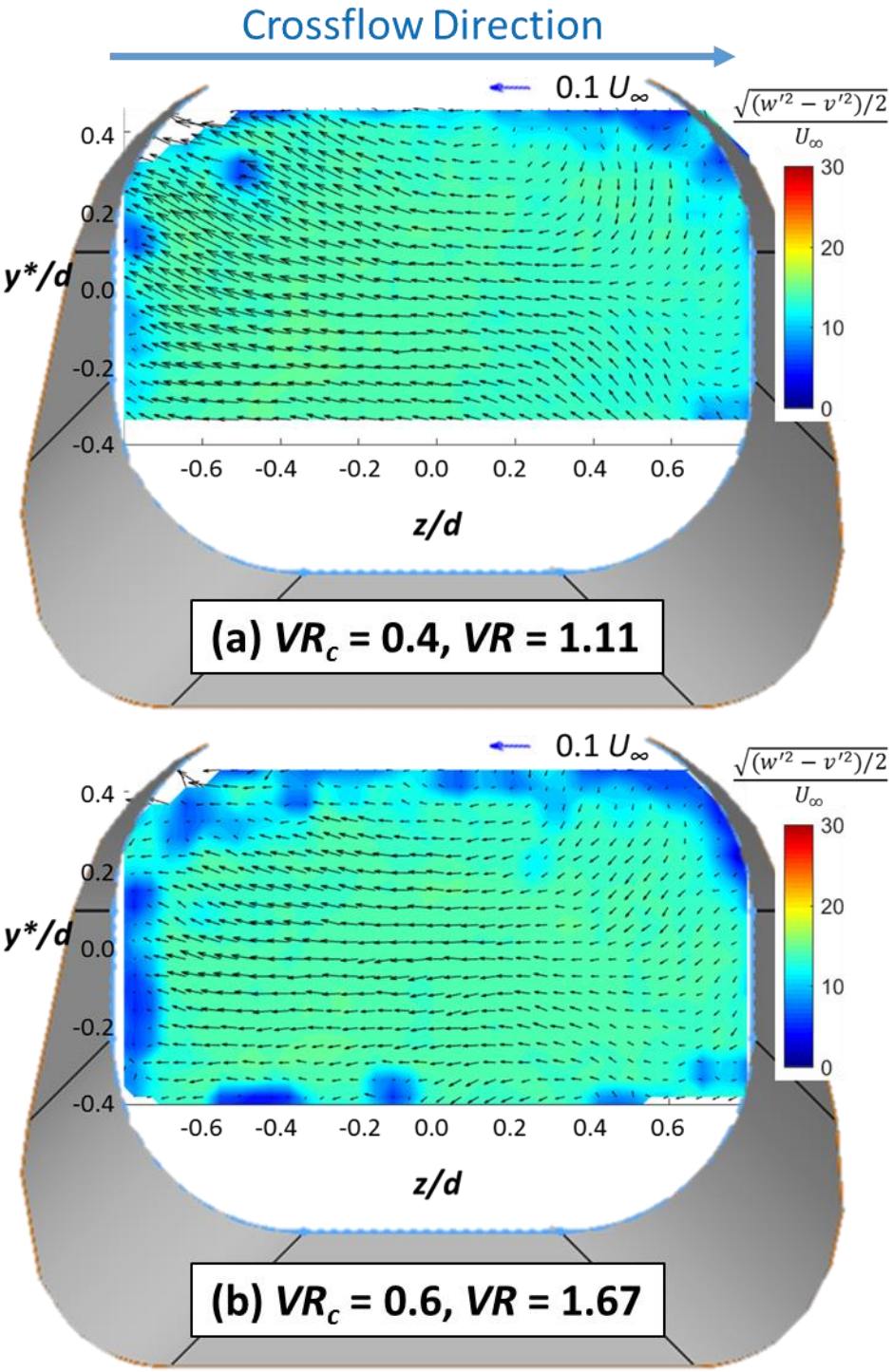

Figure 3.22: Mean in-hole velocity fields at the upstream edge of the outlet for VR_i = 0.36

The flow field for VR_i = 0.24 was very similar to that of VR_i = 0.36, as can be seen in Figure 3.23. Only one condition was tested for VR_i = 0.24. Like at VR_i = 0.36, the flow predominantly moved toward the windward side of the diffuser, corresponding to the direction of biasing observed in the effectiveness and thermal field measurements. The downward flow along the leeward edge of the hole likely contributed to the ingestion of mainstream flow observed in that region in the thermal field measurements. Like at VR_i = 0.36, no mean vortical structures were observed in the diffuser and the fluctuating velocity was nearly uniform within the measurement plane.

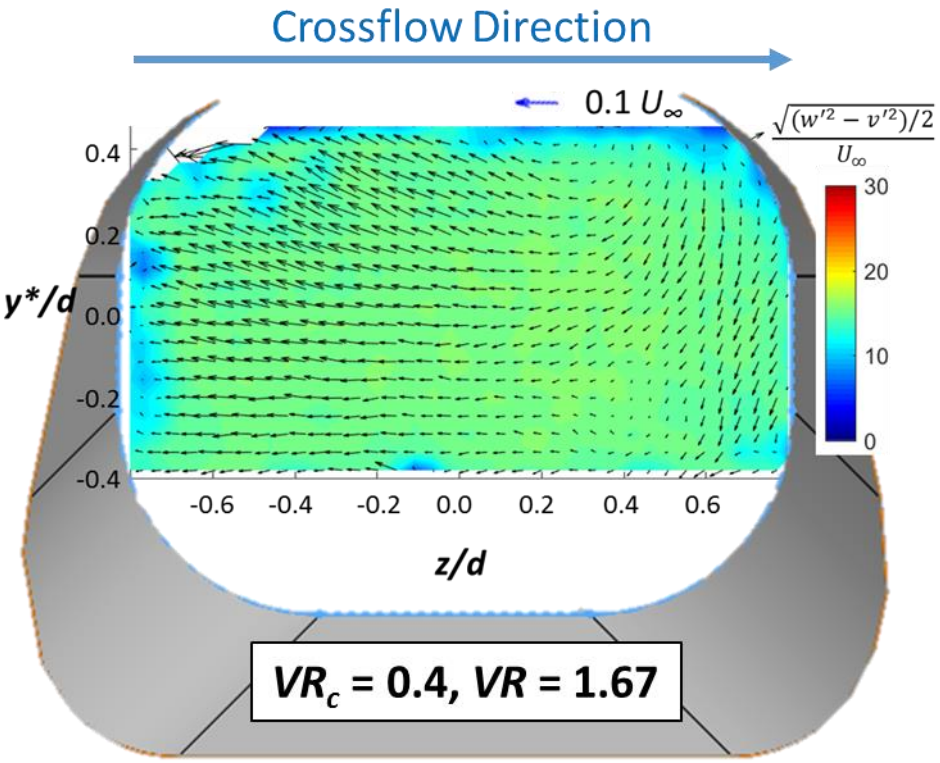

Figure 3.23: Mean in-hole velocity fields at the upstream edge of the outlet for VR_i = 0.24

Flow within the hole was highly turbulent and unsteady. The fluctuating velocities in Figures 3.21-23 show fluctuating velocities on the order of 15-20% of the mainstream velocity. The fluctuating component of velocity was therefore similar or even greater in magnitude to the mean secondary flow velocity. This can be observed in part by the instantaneous flow fields shown in Figure 3.24 for $VR_i = 0.71$, $VR_c = 0.4$, $VR = 0.56$ for three successive image pairs taken 0.2s apart. Compared to the mean velocity plots, the instantaneous velocity had considerably more randomness and less structure. There are also some indications of smaller vortices that did not exist in the mean flow. These images give a sense of the unsteady and highly turbulent flow that exists in the film hole. Unfortunately, the frequency that these images were captured at was not sufficient to resolve some of the smaller, more intermittent flow structures.

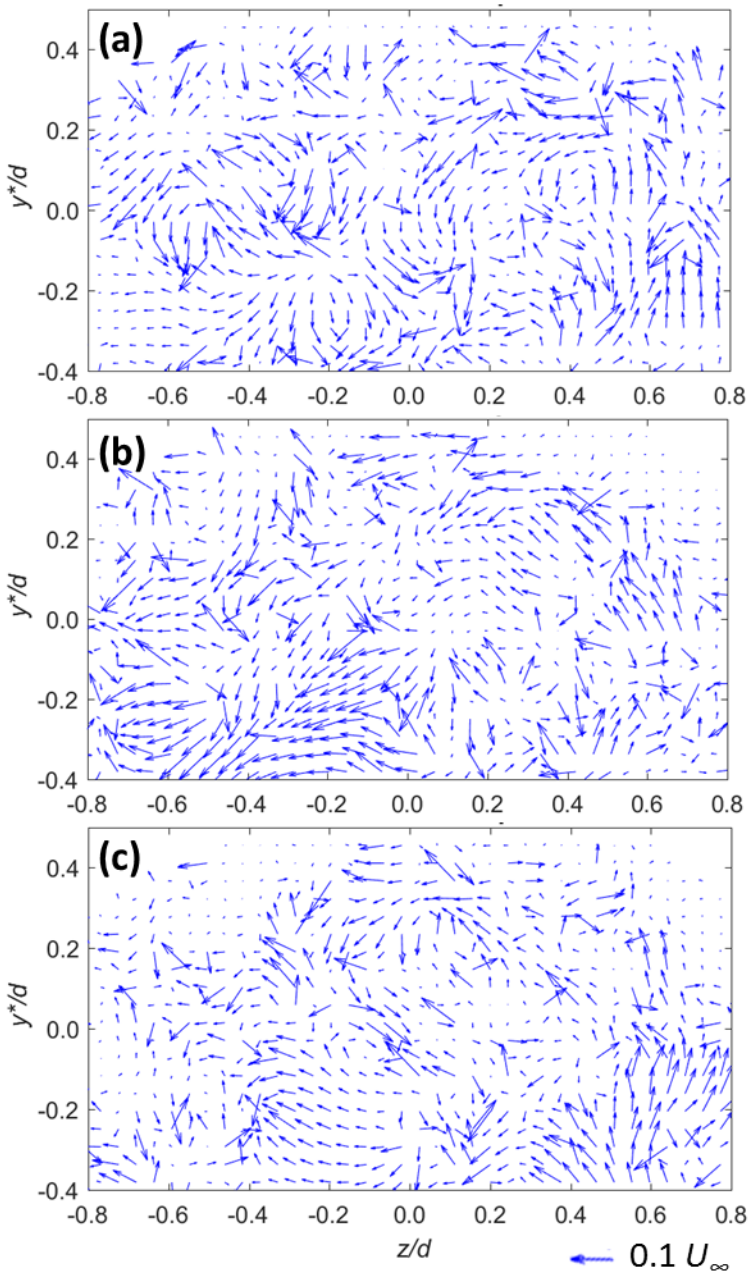

Figure 3.24: Instantaneous velocity fields for $VR_i = 0.71$, $VR_c = 0.4$, $VR = 0.56$ for three images captured at (a) $t = t_0$, (b) $t = t_0 + 0.2$s, and (c) $t = t_0 + 0.4$s

3.7 PREDICTION OF OVERALL EFFECTIVENESS

While internal crossflow has been shown to reduce film cooling effectiveness, increased internal crossflow can also increase the internal heat transfer coefficient. The two effects are competing. A one-dimensional model was used to predict the overall effectiveness from the measured adiabatic effectiveness to determine the net effect of varying the internal crossflow velocity. Because heat transfer coefficient augmentation was not measured for the axial holes, it was assumed that $h_f/h_0 = 1$, an assumption justified somewhat by the results of Boyd *et al*. [48] who found that laterally averaged $h_f/h_0 \approx 1$ for plenum-fed 7-7-7 holes. Because this model is one-dimensional, it is not expected to accurately predict local values of φ; instead, it was applied to spatially averaged data to aid in the understanding of the net impact of internal crossflow. Figure 3.25 plots spatially averaged adiabatic effectiveness and predicted overall effectiveness for the range of flow conditions tested in this study. The predicted overall effectiveness is of course, greater than the adiabatic effectiveness due to the introduction of internal cooling. For the conditions tested, the internal cooling dominated and the predicted overall effectiveness increased with increasing VR_c despite the reduction in adiabatic effectiveness with increasing VR_c. Note that the size of the precision uncertainty bars for the predicted overall effectiveness are about the same size as the markers. Table 3.2 gives the ratio of heat transfer coefficients, h_f/h_c, and the overall film cooling effectiveness without film cooling, φ_0, where η is assumed to be 0. The values of these parameters are also given for the case of perfect internal cooling where h_c goes to infinity. Note that φ_0 has a finite upper limit due to conduction. The value of φ_0 acts as a baseline level of overall effectiveness which is improved by the introduction of film cooling. $VR_c = 0.6$ started with an advantage of 0.11 in φ_0, which the improved effectiveness at $VR_c = 0.2$ was not able to overcome. The

degradation in adiabatic effectiveness due to crossflow did result in diminishing returns in terms of the increase in φ with increased crossflow velocity.

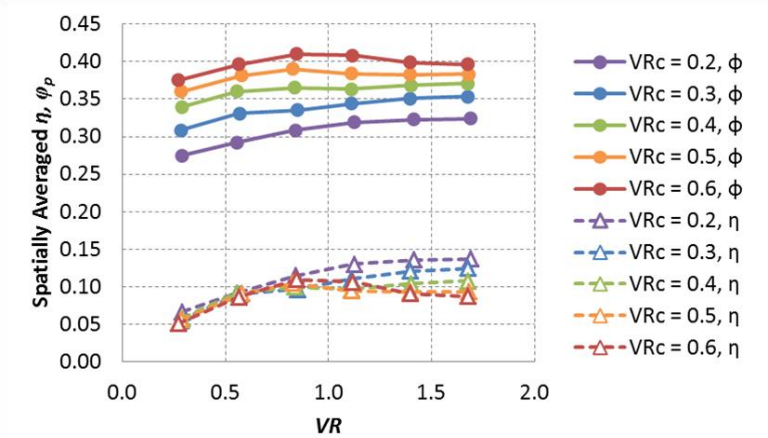

Figure 3.25: Spatially averaged η and φ_p from x/d = 5-20

Table 3.2: Heat transfer coefficient ratio and overall effectiveness without film cooling for a range of crossflow-to-mainstream velocity ratios

VR_c	h_f/h_c	φ_0
0.2	2.58	0.23
0.3	1.88	0.27
0.4	1.51	0.30
0.5	1.27	0.33
0.6	1.10	0.34
∞	0.00	0.56

The application of the model as shown in Figure 3.25 is perhaps, too simplistic. For instance, it assumes that the underside of the surface is uniformly cooled by a constant internal crossflow velocity, while in an actual engine, the coolant temperature warms as it passes through serpentine channels that wind beneath the surface. Furthermore, the coolant exiting the film holes is no longer available for internal cooling. To account for these effects, the model was altered to simulate a realistic geometry, as shown in Figure 3.26.

The mass flow rate in, $\dot{m}_{in}$, was used to determine the crossflow velocity ratio that affected adiabatic effectiveness. The coolant available to cool the surface 40 hole diameters downstream of the row of holes was calculated as the difference between the inlet mass flow rate and the mass flow through the film holes. Additionally, the temperature rise in the channel was calculated using an energy balance. To simplify the calculation, an average temperature was used for the internal crossflow temperature downstream.

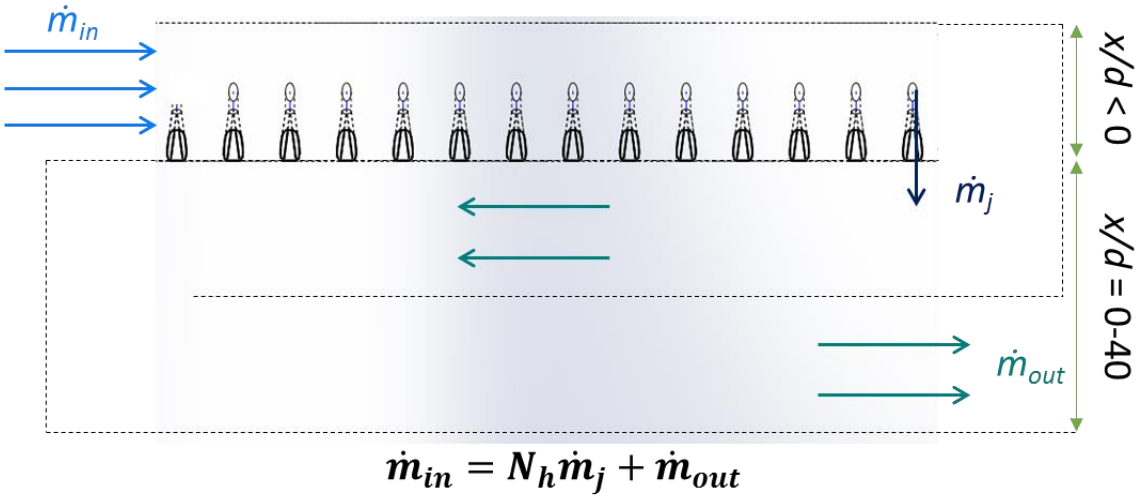

Figure 3.26: Diagram of assumed model geometry

The result of applying these changes is shown in Figure 3.27. Note that the conclusion remained unchanged: VR_c = 0.6 had the highest predicted overall effectiveness and internal cooling dominated. Due to coolant warming and film ejection, the predicted effectiveness was lower than in the original formulation, especially for the higher injection rates. Using this new assumed geometry also allows for a calculation of how effectively the coolant was used on a mass flow rate basis: $\varphi/\dot{m}_{in}$, as shown in Figure 3.27 (b). Unsurprisingly, VR_c = 0.2 made the most effective use of coolant due to its higher adiabatic effectiveness. Note that the mass flow rate of coolant was not normalized, so the units of

$\varphi/\dot{m}_{in}$ are (s/kg) and the experimental mass flow rate was used rather than trying to estimate an engine-scale mass flow rate. While the values of $\varphi/\dot{m}_{in}$ do not therefore translate to engine scale, the comparison from condition to condition is still useful – recall that coolant in a gas turbine engine is pulled from the working fluid so it is desirable to utilize it as efficiently as possible.

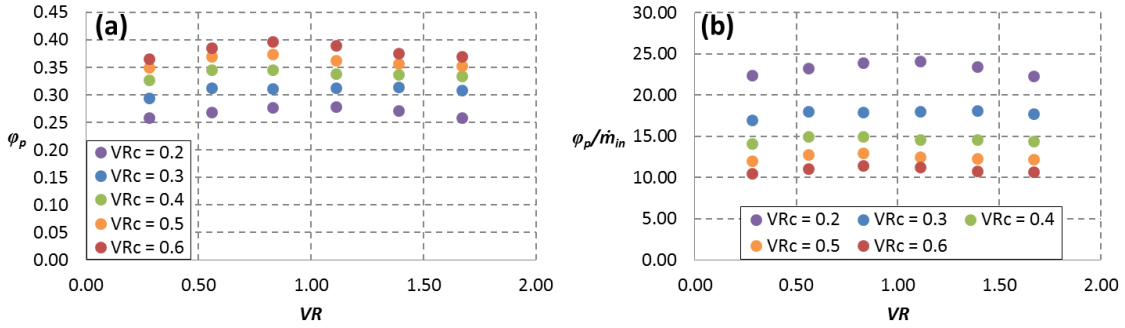

Figure 3.27: Spatially averaged (a) φ_p and (b) $\varphi_p/\dot{m}_{in}$ averaged over x/d = 5-40 for the assumed model geometry of Figure 3.26

The use of this model thus far has considered the constant channel geometry used in the experiments. However, by assuming that the adiabatic effectiveness is independent of the height of the crossflow channel, and instead dependent only on the crossflow velocity and injection rate, a number of different analyses can be performed. For example, $\dot{m}_{in}$ can be held constant while the height of the channel can be changed to vary VR_c, as shown in Figure 3.28 (a). VR_c = 0.6, which had the smallest channel height, had the highest overall effectiveness as the heat transfer was driven primarily by the velocity in the channel. This result shows that given a constant mass flow rate, the best overall effectiveness was achieved by reducing the height of the channel to increase internal heat transfer. A similar analysis was performed by holding VR_c constant and varying channel height, as shown in Figure 3.28 (b). There was a slight sensitivity to channel height at the highest injection

rates, where the increased mass flow rate due to the increased height resulted in improved heat transfer due to more coolant being available to cool the downstream plate. However, this slight improvement likely would not justify the increased coolant mass flow rate required.

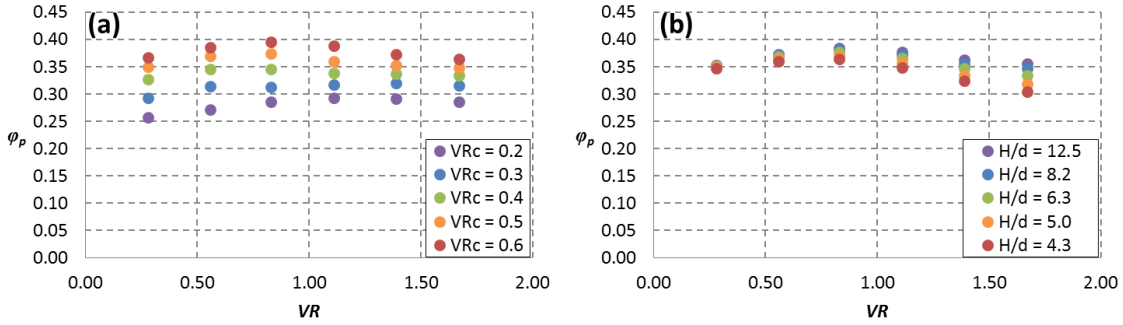

Figure 3.28: Spatially averaged φ_p from x/d = 5-40 for (a) constant mass flow rate and (b) constant $VR_c = 0.6$

Another analysis made possible by this model is to consider the number of holes that should be used to cool the model. If the airfoil is assumed to have a set radial length (for this case, a length of $L_{r,blade} = 96d$ was assumed) with holes evenly spaced across the blade, varying the number of holes varies the hole pitch. A smaller pitch with more holes would increase the film effectiveness at the expense of reduced internal cooling downstream. The adiabatic effectiveness was adjusted with the changing pitch as follows:

$$\eta_2 = \eta_1 \frac{p_1}{p_2} \tag{3.2}$$

Recall that the pitch for the experimental data was $p/d = 6.0$. For a constant $VR_c = 6.0$ and channel height of $H/d = 4.3$ (and thus a constant mass flow rate), the effect of changing p/d on the predicted overall effectiveness is shown in Figure 3.29. The effect of changing p/d

was not strong, but at low injection rates, higher φ_p was obtained for reduced p/d and a greater number of film holes. This trend reversed with increasing injection rate, which starved the downstream channels, such that at VR = 1.67, there was a significant reduction in φ_p when going to p/d = 3.

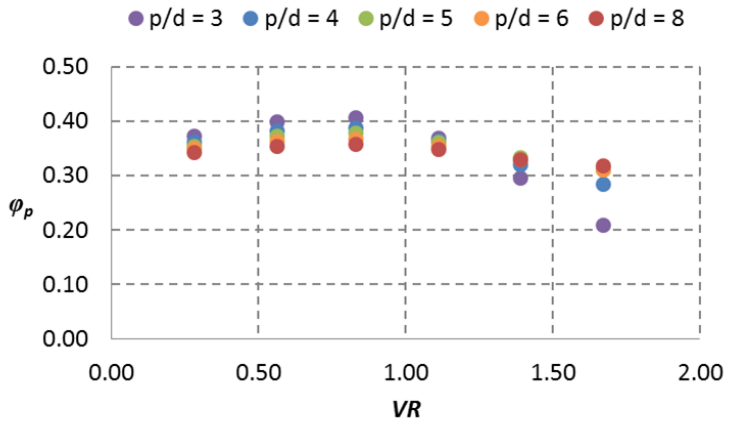

Figure 3.29: Effect of changing p/d on spatially averaged φ_p for x/d = 5-40, VR_c = 0.6, H/d = 4.3.

While this analysis does not precisely predict the overall effectiveness at engine conditions, there are a number of uses for it in evaluating different design parameters for gas turbine heat transfer because it approximates the contributions of both external and internal cooling. And as has been shown, it allows engine designers, within reasonable limits, to expand the use of a given data set beyond the original experimental parameters.

3.8 Implications for Film Cooling Design

The results presented in this chapter confirm that crossflow indeed degrades film cooling effectiveness for 7-7-7 axial holes. Given that previous studies that tested other shaped hole geometries also found a degradation in effectiveness due to internal crossflow, even though no attempt was made to determine the important factors behind this

degradation, it seems advisable for engine designers to avoid feeding axial shaped film cooling holes with internal crossflow altogether. However, a radical redesign of internal cooling passages in gas turbine airfoils seems unlikely, so in this section a number of design considerations regarding the effect of internal crossflow on film cooling are discussed.

A local minimum in centerline effectiveness was observed at a critical inlet velocity ratio of $VR_i = 0.36$ for the 7-7-7 geometry of this study which corresponded to a maximum bias in the diffuser of the hole. Clearly, this inlet velocity ratio should be avoided as the biasing greatly reduced film cooling effectiveness. Running at a low velocity ratio, $VR_c = 0.2$, would be ideal for improving film effectiveness, but could be compromise the internal cooling by reducing the internal velocity and potentially starving downstream channels of coolant. The overall effectiveness predictions showed that maximizing the internal crossflow velocity produced the coldest wall temperature, but at the cost of diminishing returns for using more coolant. While it is possible to argue from these results that the internal cooling should be maximized at the expense of film cooling, it is still desirable to maximize the film effectiveness as much as possible for a given internal flow in order to best protect hot gas engine components.

The critical inlet velocity ratio of $VR_i = 0.36$ is almost certainly a function of film hole geometry. The in-hole thermal and velocity fields measured in this study show, or at least strongly imply, the existence of an asymmetrical vortical structure in the film hole due to hole inlet separation. This structure is still visible at the exit of the diffuser for higher inlet velocity ratios, $VR_i \geq 0.71$, but for lesser inlet velocity ratios, this structure has largely devolved into lateral movement toward the windward side of the diffuser and downward movement on the leeward side permitting ingestion into the hole. This result suggests that the swirling flow is strongest in the cylindrical portion of the hole near the inlet. Interestingly, the critical velocity ratio, $VR_i = 0.36$ is roughly equivalent to the ratio

between the hole diameter and the length of this cylindrical section: $d/L_m = 0.40$. While this ratio equality may not hold for all geometries, it makes sense that there would be more jet rotation for a longer metering hole length because the diffuser would likely impede further rotation. If indeed these ratios are related, reducing L_m would increase $VR_{i,cr}$ and should result in a hole that is less sensitive to crossflow effects. Increasing $VR_{i,cr}$ would reduce sensitivity to crossflow effects by moving the point of maximum bias away from the higher operational injection rates. The relationship between $VR_{i,cr}$ and hole geometry should be addressed in future studies of internal crossflow.

Beyond changing flow conditions and geometry parameters, reducing the effect of internal crossflow may call for more fundamental changes to film hole design. Two such designs will be discussed here and are shown in Figure 3.30. The first proposed design is a 14-0-7 hole with an asymmetric diffuser. Because the majority of conditions tested in this study biased toward the windward side of the hole, a hole that only diffuses in one direction may prove advantageous. The measured in-hole thermal and velocity fields showed ingestion on the leeward side of the diffuser, which should be reduced by not diffusing away from the biased jet. Furthermore, the velocity fields showed that the windward side of the diffuser was clearly working effectively as much of the coolant was moving toward that side of the diffuser. A 14° lateral expansion angle is proposed instead of a 7° angle because the lateral movement in the diffuser suggests that the flow could fill out a large angle diffuser without separating.

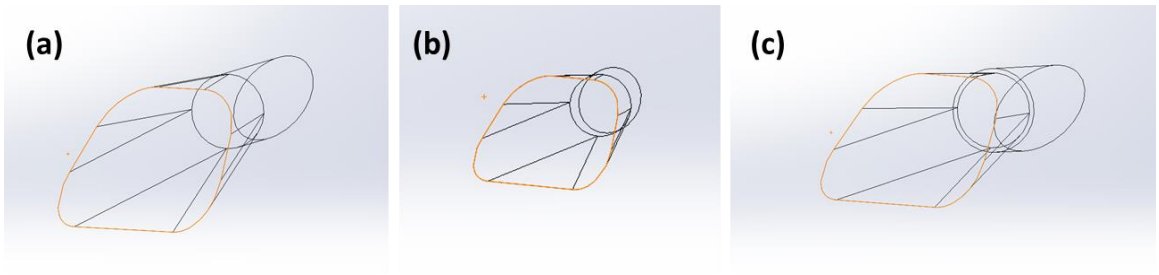

Figure 3.30: Proposed film hole design changes (a) baseline 7-7-7 axial hole, (b) 14-0-7 hole with asymmetric diffuser, and (c) 7-7-7 hole with undersized diffuser

The second proposed geometry shown in Figure 3.30 (c) requires machining an undersized diffuser such that the flow entering the diffuser encounters a backward facing step. This design is intended to disrupt the flow structure in the hole and to reduce bias in the diffuser. The genesis for this idea came from the difficulty of keeping frost from forming within the film cooling holes during testing at higher density ratios. During the course of one failed experiment, it was observed that the film cooling jets became more effective when a ring of frost formed within the hole near the beginning of the hole diffuser. Figure 3.31 shows uncorrected contours of effectiveness for a condition with (a) frost forming in the holes and (b) immediately after the frost was removed. The effectiveness for the frosted holes was considerably greater than that for the defrosted holes. These images were not measured at steady state and at slightly different injection rates, so the comparison is not ideal. Further testing of both this geometry and the asymmetrically diffused hole is required to determine their efficacy at mitigating the crossflow effect.

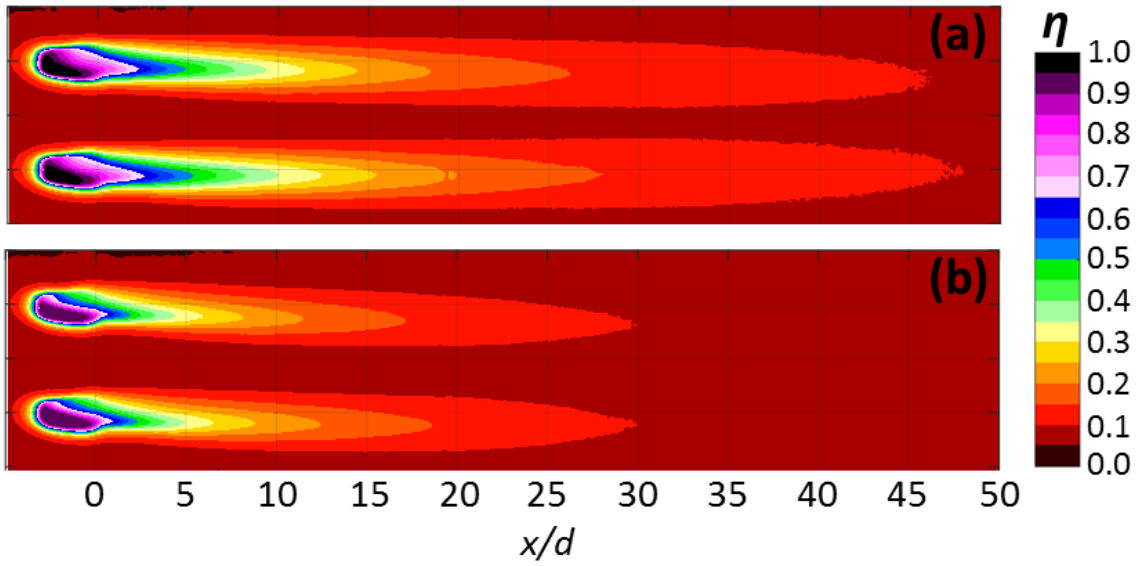

Figure 3.31: Uncorrected contours of adiabatic effectiveness at DR = 1.5, VR_c = 0.37 for (a) VR = 1.10 with frost in the holes and (b) VR = 1.20 without frost

Chapter 4: Effect of Crossflow on Compound Angle Shaped Holes

Because film cooling holes often have a compound angle, the effect of internal crossflow was also studied for compound angle 7-7-7 laidback fan-shaped holes. As for the axial hasped holes, the effect of crossflow velocity ratio, VR_c, and injection rate, VR, on the film cooling effectiveness, η, and the discharge coefficient, C_d, was studied. In addition to discharge coefficients and film cooling effectiveness, the heat transfer coefficient augmentation was measured downstream of the compound angle holes. Up to this point, no previous studies have tested the effect of varying the crossflow velocity for compound angle shaped holes. Nor have discharge coefficients for crossflow-fed compound angle holes been measured before. A range of crossflow-to-mainstream velocity ratios, VR_c = 0.2 - 0.6, was tested for a range of jet-to-mainstream velocity ratios, VR = 0.2 - 1.7. Because important trends were shown to be consistent between DR = 1.2 and 1.8 for the axial shaped holes, all experiments were conducted at DR = 1.2 for the compound angle shaped holes. The spanwise component of film injection required that the sensitivity to crossflow direction also be investigated. The two crossflow directions were denoted "in-line" for crossflow in-line with the lateral direction of injection and "counter" for internal crossflow directed counter to that direction. See Figure 2.5 for a diagram of the film hole geometry and crossflow directions. The results presented in this chapter for compound angle holes will be compared to those for axial shaped holes to show the impact of compound angle injection for film holes fed by an internal crossflow.

4.1 Discharge Coefficients

The discharge coefficients for axial shaped holes collapsed when scaled with the jet-to-crossflow velocity ratio, with the exception of VR_c = 0.2. The same trend was observed for both in-line and counter crossflow for the compound angle holes, as shown in

Figure 4.1. Unsurprisingly, the in-line crossflow had higher discharge coefficients than counter crossflow because it had a more favorable turning angle at the hole inlet. At high U_j/U_c, the in-line holes approached $C_d = 0.81$, which was 9.5% higher than $C_d = 0.74$ for the counter crossflow condition. Interestingly, the in-line crossflow had a peak discharge coefficient at $U_j/U_c = 1.5$. It is likely that at this condition, the diffuser was behaving more effectively due to the manner in which the jet biased in the hole. As mentioned in the discussion of the discharge coefficients for the axial holes, the scaling with U_j/U_c broke down for VR_c due to the low crossflow velocity ratio approaching a plenum condition where this scaling would not be expected to hold.

The discharge coefficients for the axial holes fell between those for the counter and in-line crossflow-fed compound angle holes, as shown in Figure 4.2 for $VR_c = 0.3$-0.6. At higher U_j/U_c, the axial discharge coefficients approached those of the in-line compound angle shaped holes. The similarity in the shape of the curves and the scaling with U_j/U_c suggests that the crossflow affected flow in the holes for all conditions in a similar manner. This result therefore suggests that the compound angle holes were affected by similar in-hole secondary flow as the axial holes. Recall that for the axial holes, an in-hole swirling flow caused coolant biasing and mainstream ingestion into the diffuser, both of which contributed to reduced film cooling effectiveness. The compound angle of the hole, likely had an effect on the strength of these secondary flows as indicated by the different values of discharge coefficient for different flow geometries and crossflow directions.

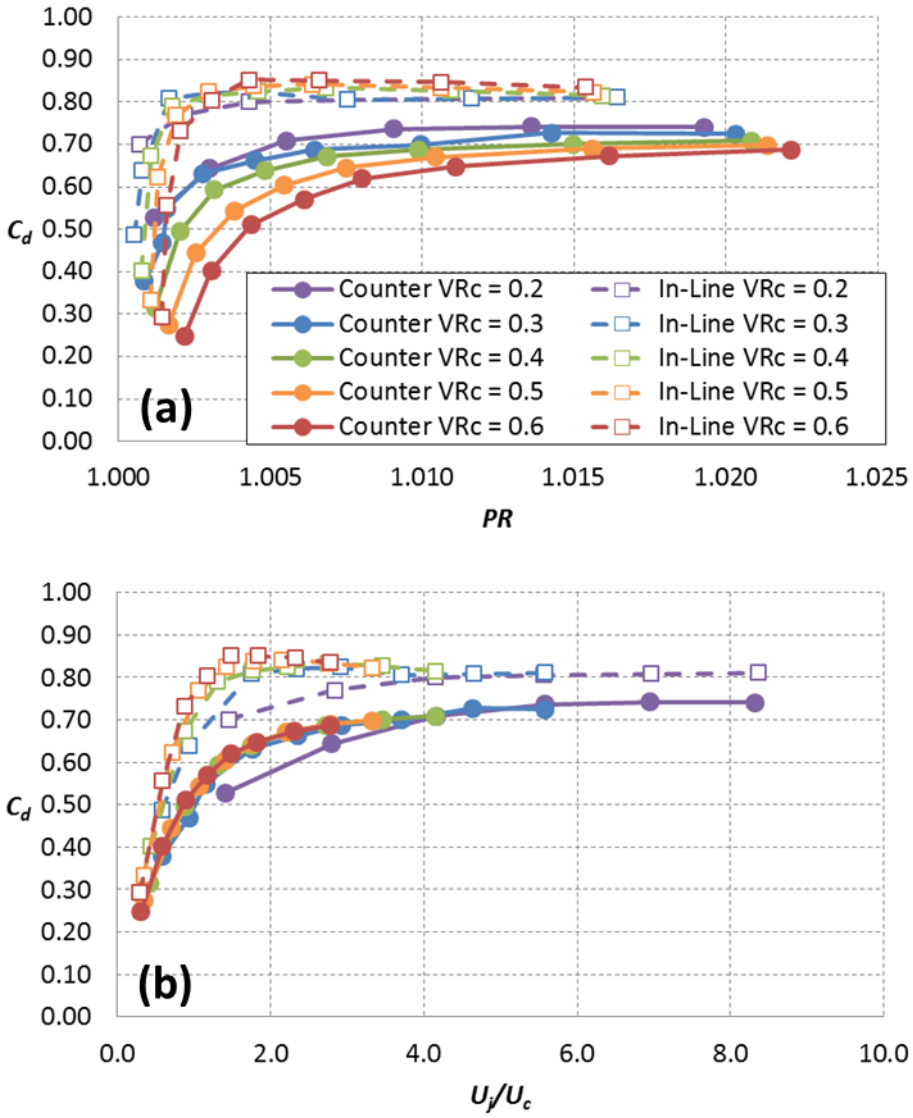

Figure 4.1: Discharge coefficients for compound angle shaped holes scaled with (a) pressure ratio and (b) jet-to-crossflow velocity ratio

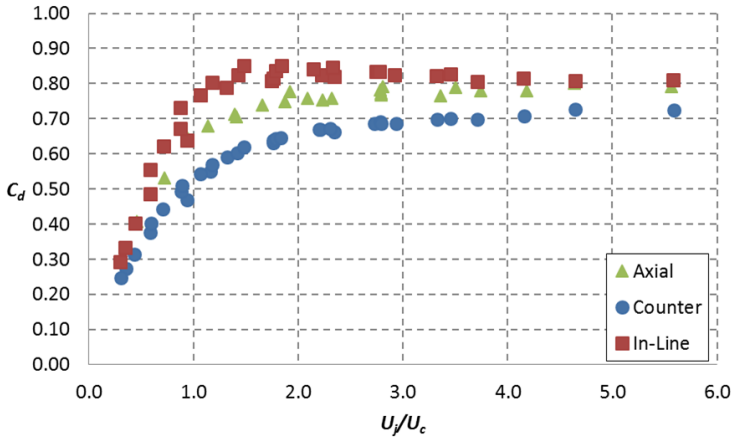

Figure 4.2: Comparison of discharge coefficients for axial and compound angle film holes for VR_c = 0.3-0.6

4.2 Adiabatic Effectiveness

Internal crossflow was shown to reduce the effectiveness of axial 7-7-7 holes relative to a plenum condition. This reduction in effectiveness occurred primarily at higher injection rates. The only study in the literature to test the effect of internal crossflow on compound angle, shaped holes, Dittmar *et al.* [20], found that for wide-angle fan-shaped holes, in-line crossflow resulted in up to 50% higher laterally averaged effectiveness than counter crossflow. Few conclusions can be drawn from that study, however, as the crossflow velocity was neither varied nor reported.

For the compound angle holes of this study, counter crossflow resulted in higher spatially averaged effectiveness than in-line crossflow, as shown in Figure 4.3 (a). The difference between the two crossflow directions was most pronounced at greater injection rates, $VR > 0.7$ and greater crossflow velocities, $VR_c \geq 0.4$. This result is seemingly at odds with the results of Dittmar *et al* [20], although that study used a very different geometry so differences such as this are not entirely unexpected.

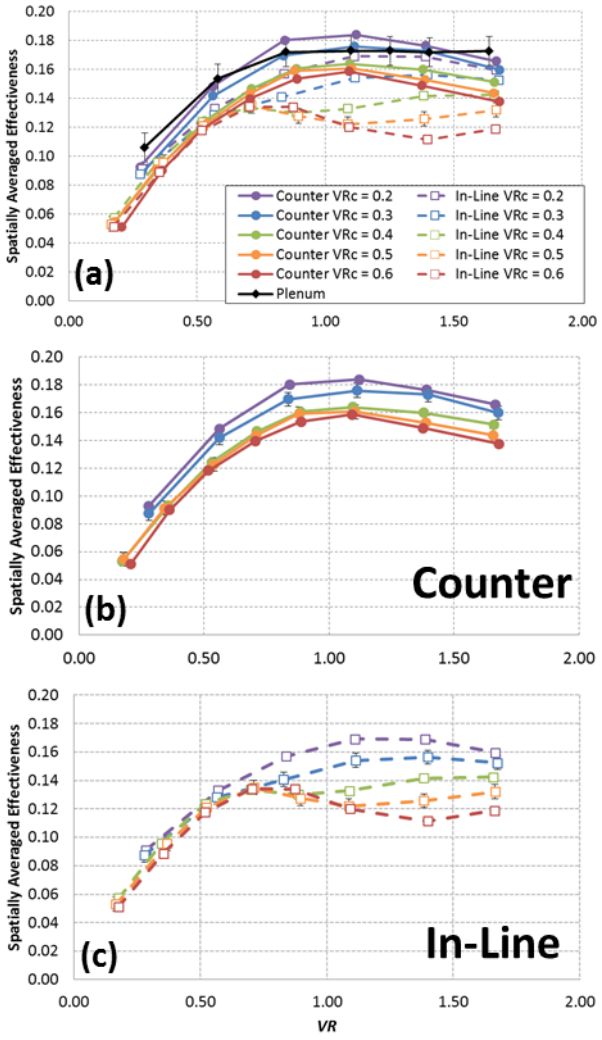

Figure 4.3: Spatially averaged effectiveness, x/d = 5-20, for compound angle shaped holes (a) for all conditions, (b) counter crossflow, (c) in-line crossflow Plenum data from [53]

Spatially averaged effectiveness is plotted separately for counter and in-line crossflow in Figure 4.3 (b) and (c) respectively. For each crossflow direction, the spatially averaged effectiveness was reduced with increasing VR_c. For counter crossflow, most of the reduction in effectiveness due to crossflow occurred from VR_c = 0.2-0.4, after which, crossflow did not have a strong effect on spatially averaged effectiveness. The shape of the

spatially averaged curves for counter crossflow did not change much with increasing VR_c – all counter crossflow velocities tested resulted in a peak effectiveness at $VR \approx 1.1$. The spatially averaged effectiveness for in-line crossflow had a similar trend to that of the axial shaped holes. There was little sensitivity to VR_c at low injection rates, but for $VR > 0.7$, the effect of crossflow became more pronounced. The shapes of the spatially averaged curves were also impacted by in-line crossflow. Like counter crossflow, in-line crossflow had a peak effectiveness at $VR = 1.1$ for $VR_c = 0.2$, but the injection rate corresponding to the peak effectiveness was reduced at the higher crossflow-to-mainstream velocity ratios. Therefore, in-line and counter crossflow likely resulted in different flow physics in the film holes.

There was little sensitivity to crossflow direction at $VR_c = 0.2$ and similarly little difference between the $VR_c = 0.2$ conditions and the plenum-fed case. Figure 4.4 compares contours of effectiveness at selected conditions between the plenum-fed case and both crossflow directions. The step change in effectiveness at $x/d = 2$ for the crossflow-fed holes is the result of processing the data before $x/d = 2$ with a one-dimensional conduction correction. The 1D correction was not as accurate as the three-dimensional correction described in Section 2.4.2.2 and produced lower centerline effectiveness. The plenum-fed data was taken from Anderson *et al* [53]. On the whole, the jets shown in the figure had similar effectiveness. The jets all had similar trajectories and there was a narrowing of the jets and increased lateral movement when VR was increased from 0.83 to 1.67. At both injection rates, counter crossflow had the highest centerline effectiveness of all the conditions, although the difference was only slight at $VR = 1.67$. For $VR = 1.67$, both crossflow-fed conditions had better lateral spreading than the plenum-fed case. This result is similar to what was observed for the axial holes. The improved lateral spreading for the crossflow-fed holes is likely due to increased intensity of secondary flows within the jet.

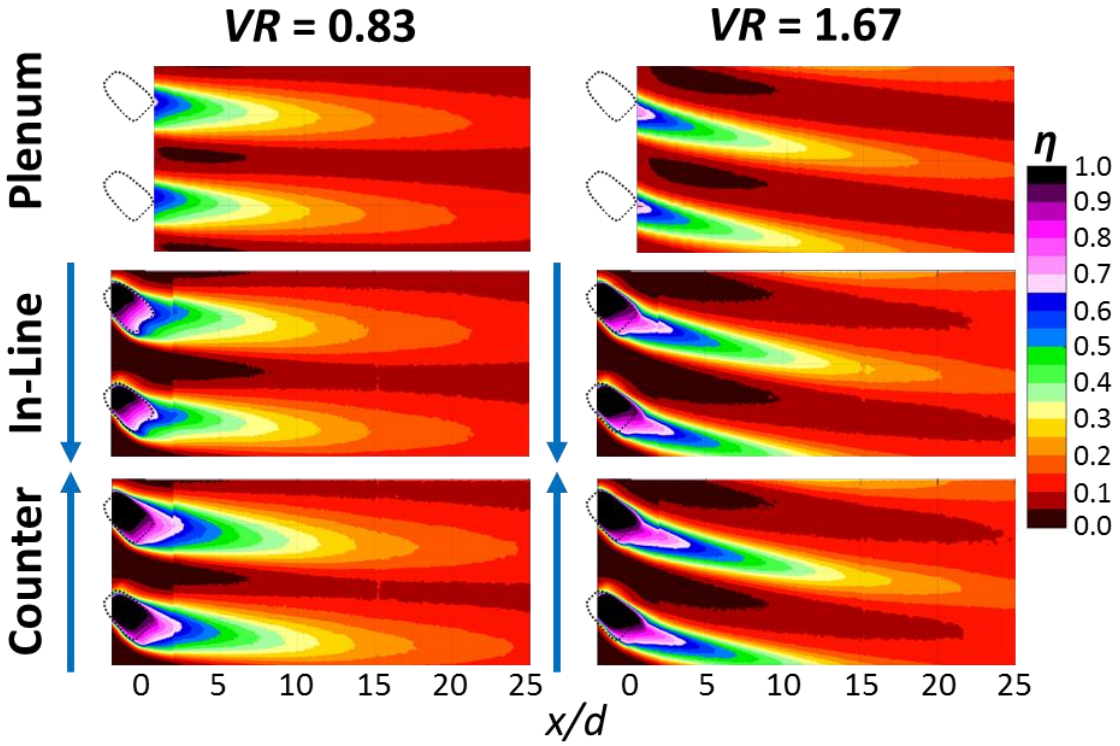

Figure 4.4: Contours of η comparing the plenum condition from [53] to counter and in-line crossflow at $VR_c = 0.2$

Like the crossflow-fed axial holes, counter crossflow caused biasing in the diffuser, primarily toward the windward side relative to the crossflow direction. Figure 4.5 shows contours of local effectiveness for counter crossflow. As shown by the spatially averaged effectiveness, the reduction in effectiveness due to increasing internal crossflow velocity occurred between $VR_c = 0.2$ and 0.4. For $VR_c > 0.4$, there was little sensitivity to the magnitude of crossflow velocity. The reduction in effectiveness from $VR_c = 0.2$ - 0.4 appears to occur due to biasing in the diffuser, which biased more strongly toward the windward side of the diffuser, relative to the direction of internal crossflow, with increasing crossflow velocity. While the direction of biasing in the diffuser was similar to that of the

axial holes, the reduction in effectiveness due to crossflow was not as severe. This relative insensitivity to crossflow direction was likely due to a reduction in ingestion of mainstream air into the diffuser. For the axial holes it was shown that regions of reduced effectiveness in the film holes corresponded to mainstream ingestion into the diffuser. Because of the compound angle injection, the jet biased toward the upstream side of the diffuser relative to the mainstream flow, and likely blocked the mainstream air from ingesting into the downstream side of the diffuser. This resulted in improved effectiveness and less jet dispersion further downstream. The axial holes had reduced effectiveness due to internal crossflow due to three possible reasons: ingestion due to biasing and secondary flow in the diffuser, failure of the diffuser to slow down the jet, and increased turbulence generation in the film hole. The counter crossflow condition appeared to greatly reduce the effect of mainstream ingestion and thus was less sensitive to crossflow.

In-line crossflow was considerably more sensitive to internal crossflow velocity than counter crossflow, as shown in Figure 4.6. Like the counter crossflow and axial holes, the coolant tended to bias toward the windward side of the diffuser relative to the direction of internal crossflow. Because the crossflow direction was reversed relative to counter crossflow, the coolant biased toward the downstream side of the hole relative to the mainstream. At $VR = 0.56$, this effect was not very pronounced and the coolant jets all had similar effectiveness. Note that while the velocity ratio was nominally $VR = 0.56$ for this condition, in actuality there was some variation: $VR_c = 0.2$ and 0.3 were at $VR = 0.56 \pm 0.01$ and $VR_c = 0.4$-0.6 were at $VR = 0.53 \pm 0.01$, making it difficult to determine whether these slight differences were the result of increased VR_c or reduced VR. At $VR = 1.11$, however, there was a notable difference in jet behavior going from $VR_c = 0.3$ to 0.4. At $VR_c = 0.4$, the biasing in the diffuser appeared to result in significant mainstream ingestion. Because the jet was on the downstream side of the hole, the mainstream was allowed to

ingest into the upstream side of the hole unopposed. This resulted in reduced effectiveness and reduced lateral movement of the jet going downstream with increasing VR_c. The reduction in effectiveness with increasing VR_c was more gradual for VR = 1.67, but it can be observed that the effectiveness of the jet was reduced as the biasing of the coolant became more severe.

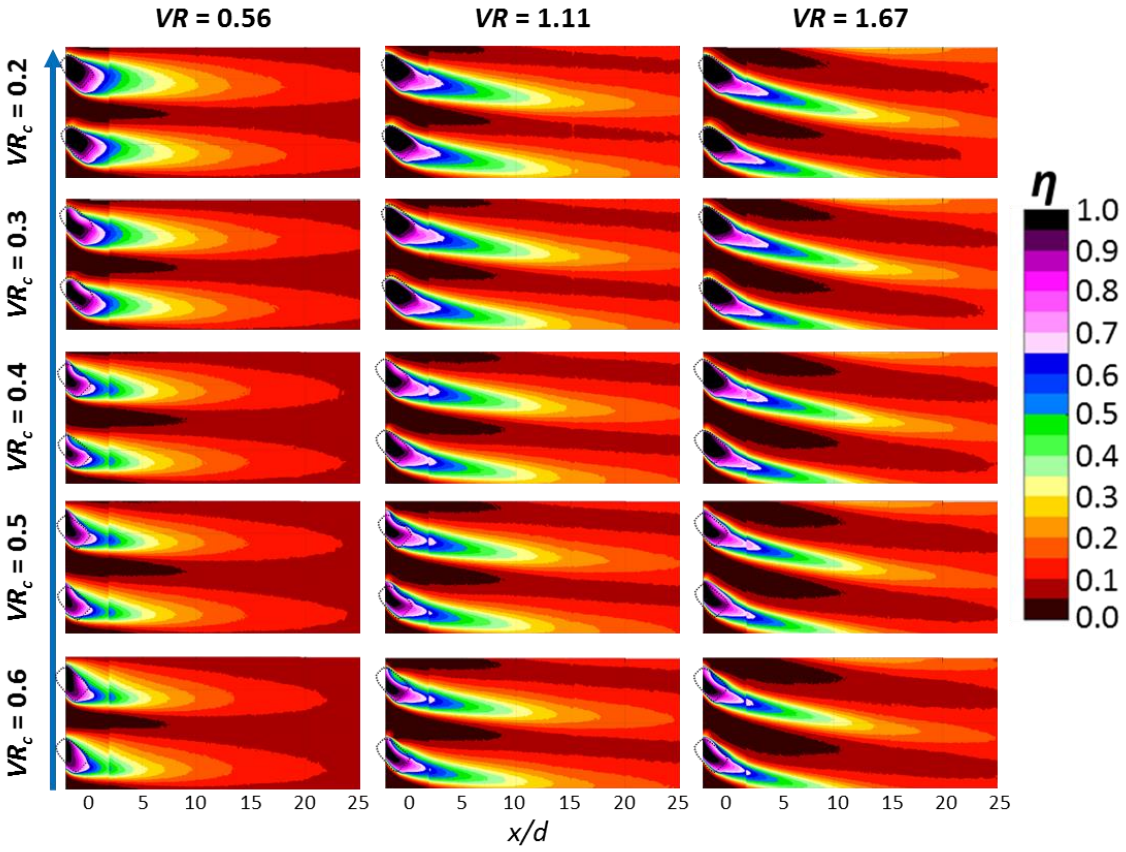

Figure 4.5: Contours of η for counter crossflow

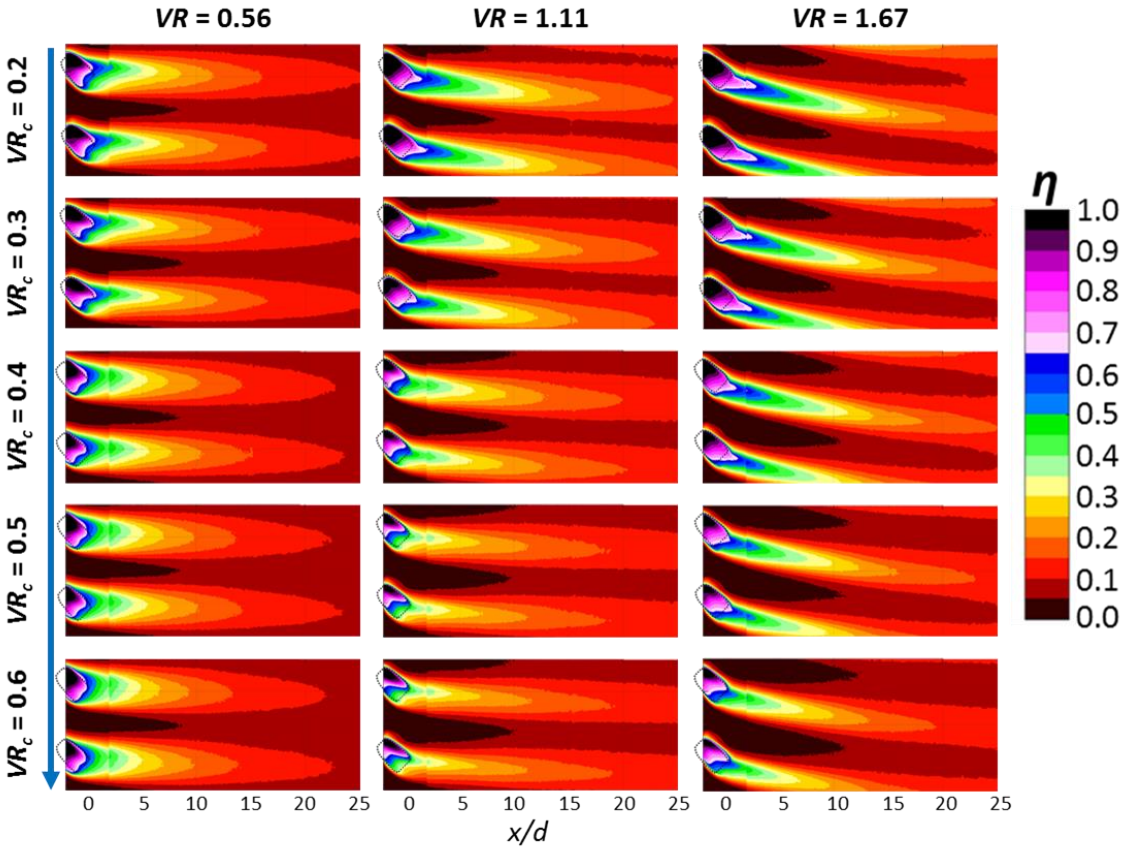

Figure 4.6: Contours of η for in-line crossflow

The biasing in the diffuser is more clearly shown in Figure 4.7 for VR = 1.11 in plots of effectiveness corrected using the aforementioned one-dimensional conduction correction. For counter crossflow, the exiting coolant was slightly biased toward the leeward side of the hole relative to the direction of internal crossflow at VR_c = 0.2. In-line flow exited the hole with almost no bias. The different extent in bias is likely the result of different strength swirling flow in the hole for each crossflow direction. As VR_c increased to 0.4 and 0.6 the biasing favored the windward side of the hole more strongly for both counter and in-line crossflow. The larger region of low effectiveness within the diffuser for in-line crossflow implies that the ingestion was more significant than for counter crossflow.

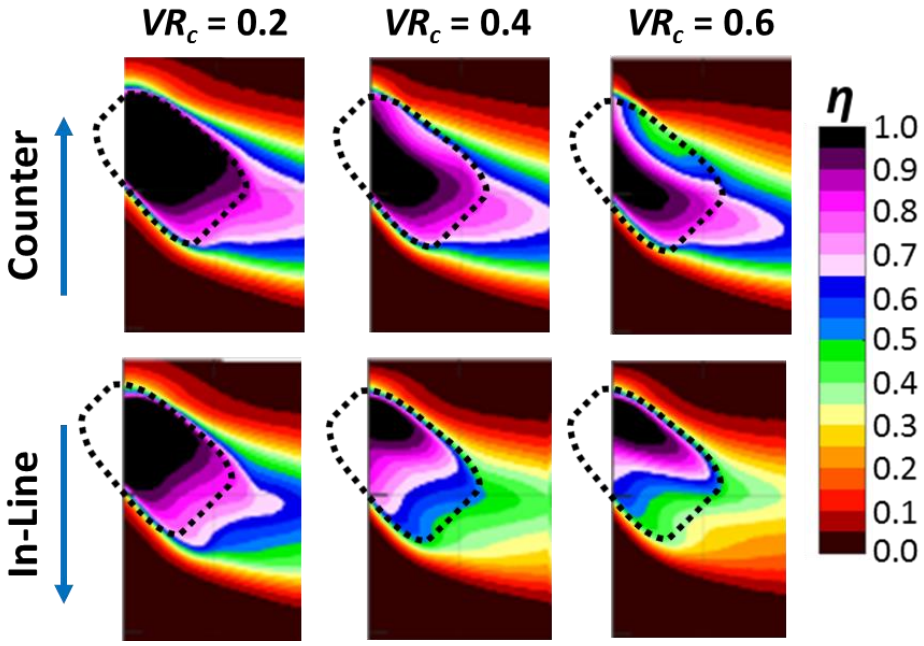

Figure 4.7: Contours of 1D conduction corrected η in the near-hole region for $VR = 1.11$

The compound angle holes had greater spatially averaged effectiveness than the axial holes, as shown in Figure 4.8. For both $VR_c = 0.2$ and 0.5, the counter crossflow outperformed the in-line crossflow and both outperformed the axial holes. At $VR_c = 0.2$, the effectiveness for compound angle injection was consistently greater than for axial injection for $VR > 0.5$. Interestingly, the shape of all three spatially averaged curves was similar for the three conditions. At $VR_c = 0.5$, all configurations had similar performance for $VR < 0.5$ but diverged at greater injection rates. The shape of the axial curve was most similar to in-line crossflow, although the two diverged for $VR > 1.0$, with the compound angle condition having greater effectiveness at higher injection rates.

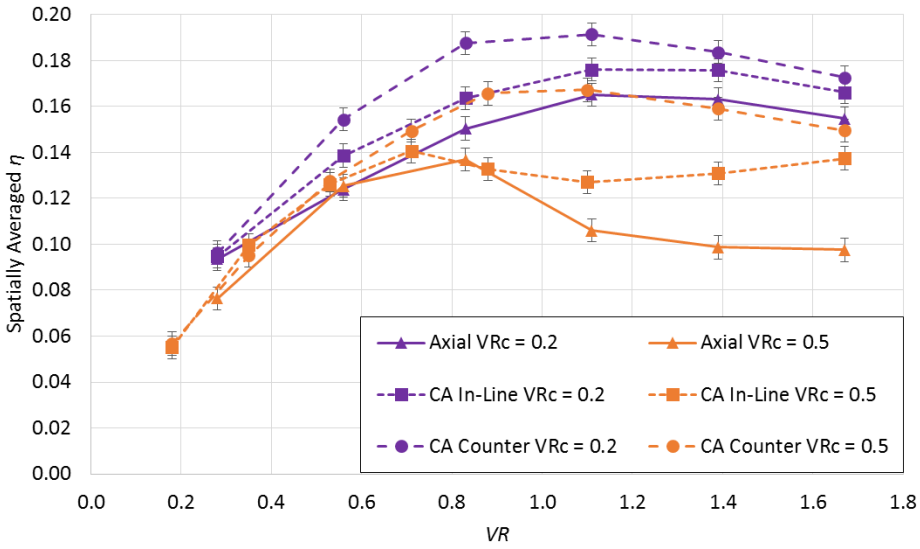

Figure 4.8: Spatially averaged η for all hole geometries and crossflow directions averaged over x/d = 5-20

Contours comparing the axial and compound angle holes at VR = 1.11 are shown in Figure 4.9. The counter crossflow compound angle holes had higher centerline effectiveness and improved lateral spreading than the axial holes for all crossflow velocities, especially for elevated VR_c. The exception to that rule occurred at VR_c = 0.2 where the axial holes had comparable centerline effectiveness but reduced lateral spreading. The in-line crossflow compound angle holes had similar or even reduced centerline effectiveness than the axial holes for all conditions tested. However, the compound angle injection resulted in greater lateral spreading of coolant and overall greater average effectiveness for the compound angle holes. This result is consistent with the few studies in the literature that have compared the effectiveness of axial and compound angle shaped holes. The common explanation for this behavior is that the compound angle hole presents a larger profile to the incoming mainstream flow, which enables the mainstream to force the jet down to the surface of the part more effectively. This effect is

likely more important the more biased the jet is because a biased jet does not fill out the diffuser and would be more likely to separate from the wall at high injection rates. Therefore, the compound angle holes have greater effectiveness than the axial holes, especially at high VR_c and VR.

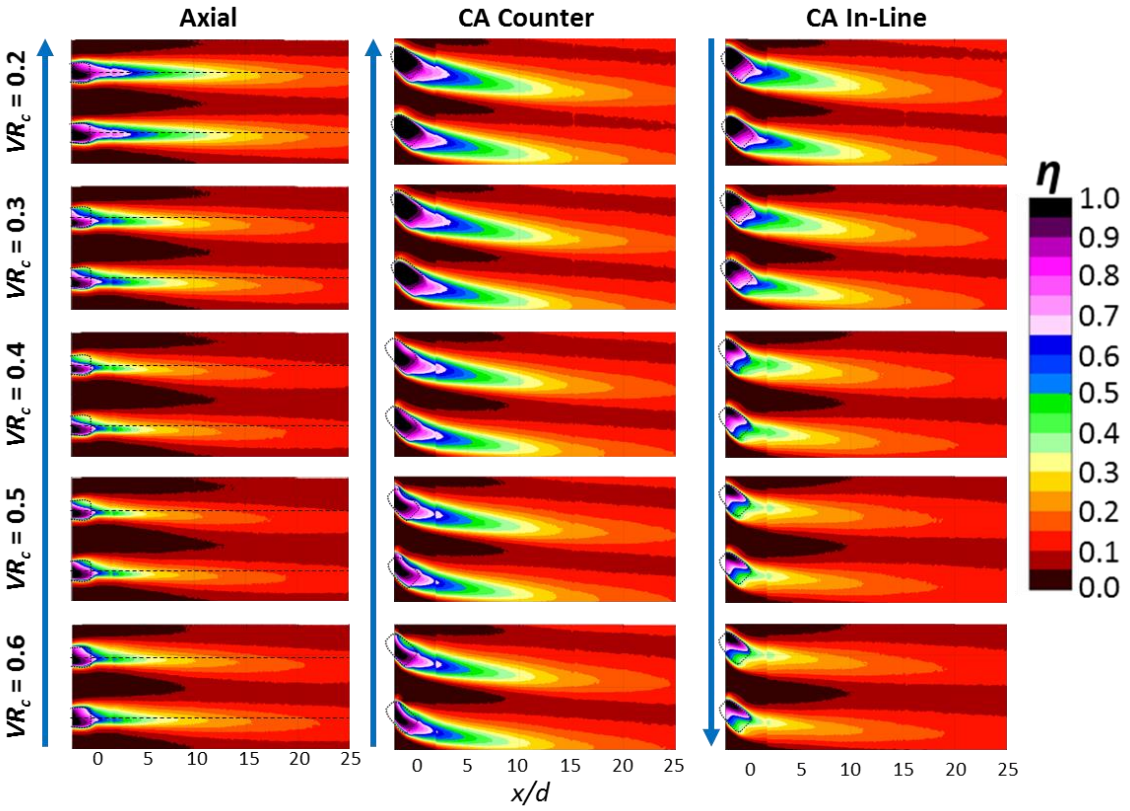

Figure 4.9: Contours of η for axial and compound angle holes at VR = 1.11

4.3 Jet Characteristic Parameters

The same four jet characteristic parameters that were investigated for the axial holes: centerline effectiveness, centerline location, jet width, and jet skew, were also investigated for the compound angle shaped holes. For details on how these parameters were defined and calculated, please refer to Section 2.4.2.4. For axial holes, the averaged

centerline effectiveness, centerline location, and jet skew all collapsed with the inlet velocity ratio, $VR_i = U_c/U_j$. Furthermore, the centerline effectiveness and skew had a local minimum at $VR_i = 0.36$ which corresponded to the maximum jet movement due to biasing. This section details a similar effort to find appropriate scaling parameters for the jet parameters in the case of compound angle injection.

The centerline effectiveness for the compound angle holes collapsed with VR_i for in-line crossflow, but not for counter crossflow, as shown in Figure 4.10. While η_{CL} tended to decrease with increasing VR_i for counter crossflow, it did so at different rates for different crossflow velocities. Centerline effectiveness for in-line crossflow, on the other hand, collapsed in a similar manner to that of the axial holes when scaled with VR_i, with a local minimum at $VR_i = 0.36$. This is likely the result of the two different biasing mechanisms in the diffuser for each crossflow direction. For counter crossflow, ingestion was minimized by the jet exiting on the upstream side of the hole relative to the mainstream. For in-line crossflow and axial holes, the biasing in the diffuser resulted in mainstream ingestion. The fact that η_{CL} did not scale with VR_i for counter crossflow and the counter crossflow cases had reduced mainstream ingestion suggests that mainstream ingestion was a primary contributor to reduced effectiveness due to internal crossflow.

Figure 4.11 compares the centerline effectiveness curves as a function of VR_i for compound angle holes with in-line crossflow and axial holes. The two curves fall nearly on top of each other. Even the point at $VR_i = 0.71$ that was separate from the other points ($VR_c = 0.2$, $VR = 0.28$) was matched between the two geometries. This result indicates that the effect of ingestion due to biasing was very similar for the axial and in-line crossflow cases and strongly suggests that the swirling flow within the hole was very similar for both cases. If indeed the swirling flow within the holes was similar between the two conditions,

it therefore must not be strongly influenced by the compound angle of the hole – at least not for ε = 0-45°.

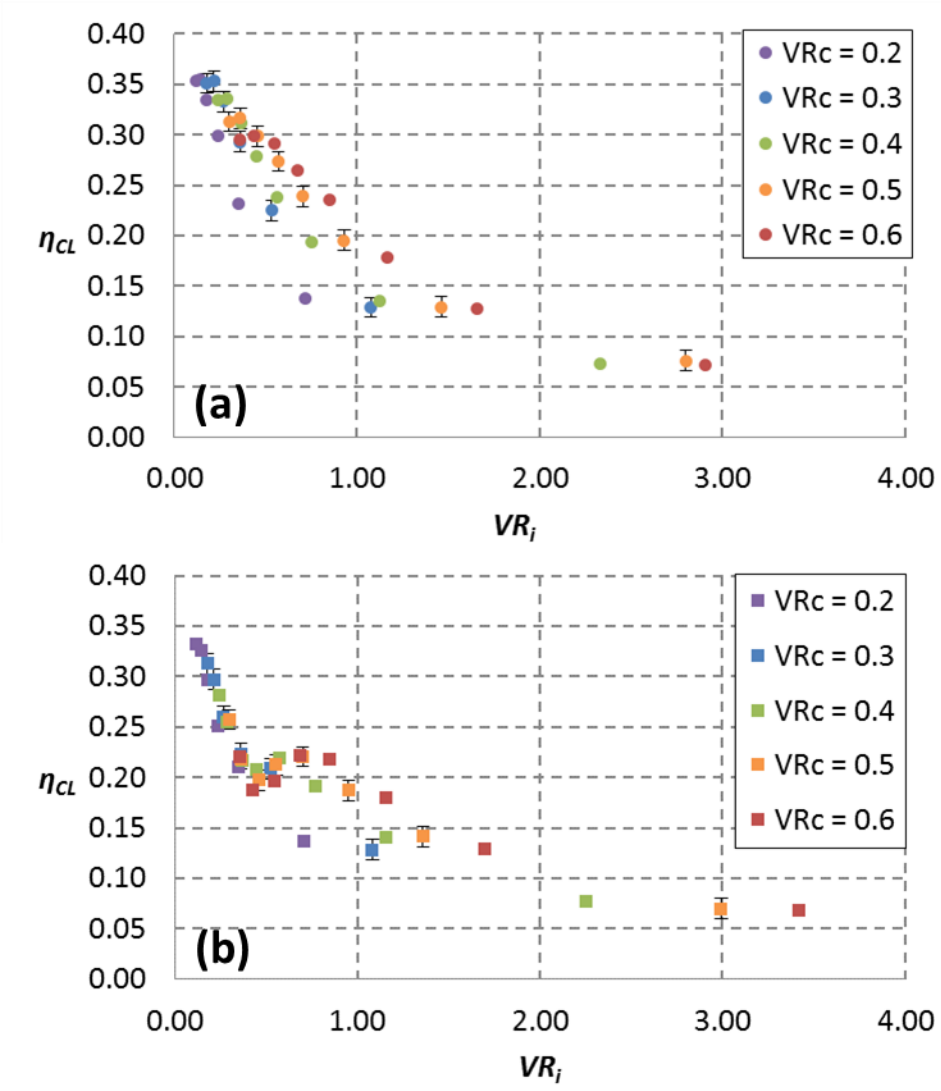

Figure 4.10: Scaling of averaged η_{CL} over x/d = 5-20 with VR_i for (a) counter crossflow and (b) in-line crossflow

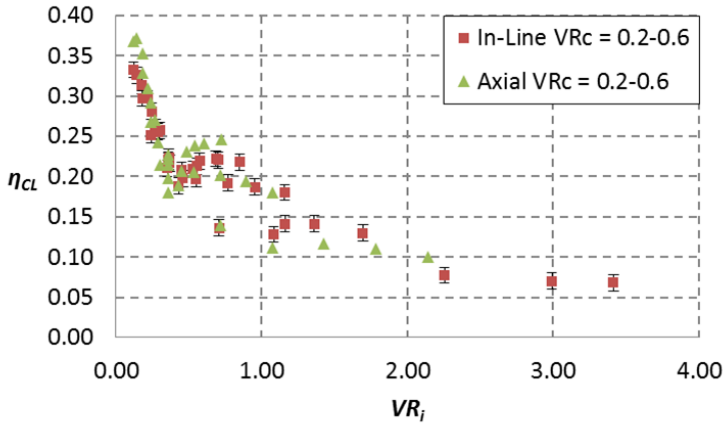

Figure 4.11: Comparing averaged η_{CL} from x/d = 5-20 for CA holes with in-line crossflow and axial hole

A number of other scaling parameters were investigated for the average centerline effectiveness of counter crossflow-fed compound angle holes. As shown in Figure 4.12(a), the jet-to-mainstream velocity ratio was a better scaling parameter than the inlet velocity ratio, although η_{CL} decreased with increasing VR_c, similar to spatially averaged η. Because the centerline effectiveness curves had a similar shape at all VR_c, a dependence on VR_c^n was investigated. Figure 4.12 (b) shows the result of that scaling attempt: $\eta_{CL}VR_c^{0.15}$ collapsed to within uncertainty when scaled with VR. While the exponent $n = 0.15$ does not relate to any as-yet-tested physical phenomenon, it indicates the degree to which the internal crossflow velocity caused a degradation in effectiveness for the counter crossflow condition. Because ingestion was not a major factor for counter crossflow, the scaling with $VR_c^{0.15}$ likely characterizes how either the reduced efficacy of the diffuser or enhanced turbulence generation within the hole reduced the film cooling effectiveness.

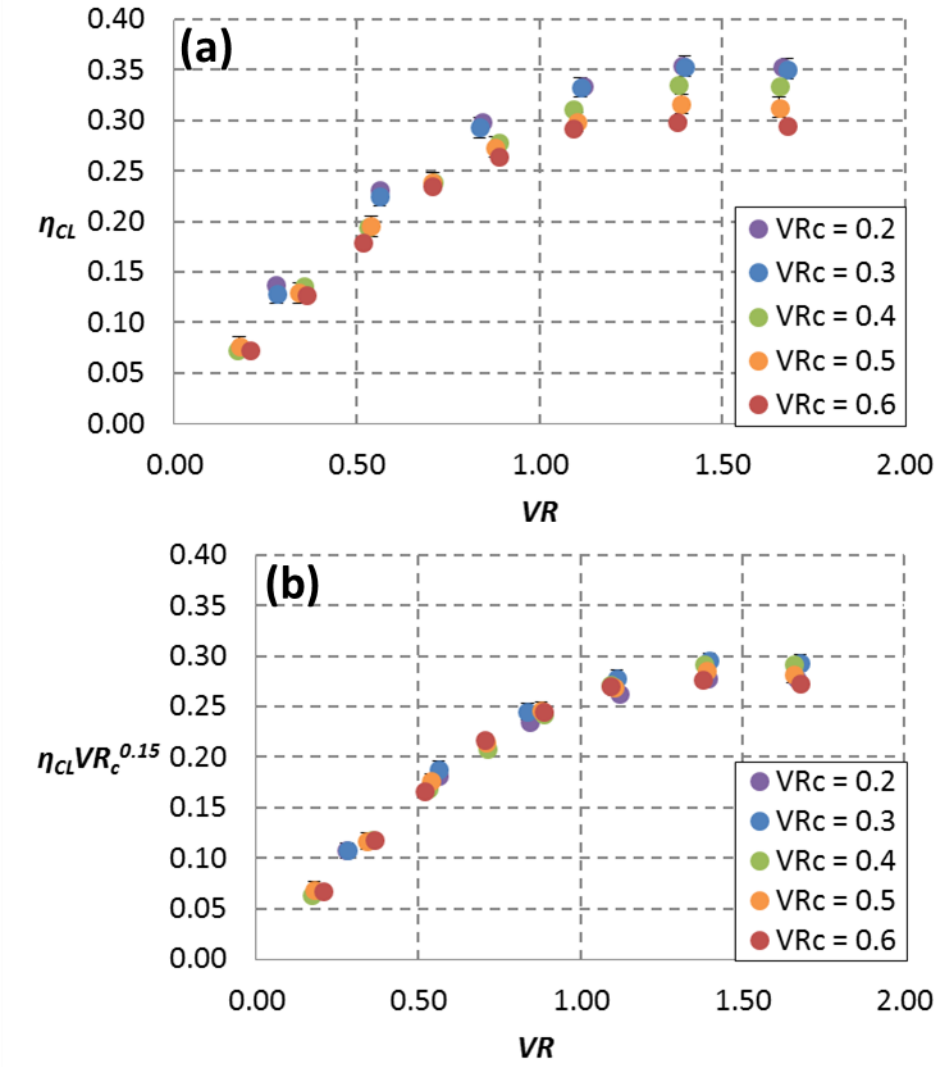

Figure 4.12: Scaling averaged (x/d = 5-20) (a) η_{CL} and (b) $\eta_{CL}VR_c^{0.15}$ for counter crossflow-fed compound angle holes

The other averaged jet characteristic parameters for compound angle holes predominantly scaled with injection rate. Figure 4.13 plots the average centerline location, jet width, and jet skew for both counter and in-line crossflow. For counter crossflow, both $(z/d)_{CL}$ and W/d collapsed when scaled with VR, showing that these parameters were insensitive to crossflow velocity. It makes sense that the jet trajectory would collapse with

VR for compound angle holes, as the lateral component of injection dominated over any effect the bias in the diffuser had. The collapse of *W/d* with *VR* also indicates the importance of velocity ratio in determining the lateral spreading of the coolant. The location and width of the jets for the in-line case did not collapse as cleanly as for counter crossflow. The in-line jets had less movement with increasing VR_c, especially at greater injection ratios. This same effect can be observed in the contour plots. Because the mainstream flow ingested into the diffuser, it was more effective at influencing the direction of the film cooling jets than for the counter crossflow condition. A similar trend was seen for the width of the in-line jets for $VR > 1$. Increased crossflow velocity resulted in increased biasing and mainstream ingestion, which increased the dispersal of the jet in the lateral direction. For $VR < 1$, on the other hand, there was very little difference between the jet width of the counter and in-line conditions. The jet skew did not collapse particularly well with any of the flow parameters investigated, although it did have a semblance of a trend when scaled with *VR* for counter crossflow. The jets had a maximum skew at around $VR = 0.85$. The in-line jets had very little skew relative to the counter jets.

The difference in the scaling of the jet characteristic parameters between the axial and compound angle holes is not wholly unexpected. For the most part, the compound angle injection dominated how the jet interacted with the mainstream and spread over the surface. In the case of in-line crossflow, the biasing in the diffuser as a result of crossflow had a small effect, but not as pronounced as the effect it had for the axial holes. However, the averaged centerline effectiveness for the inline holes showed that similar flow physics governed the effectiveness as for the axial holes.

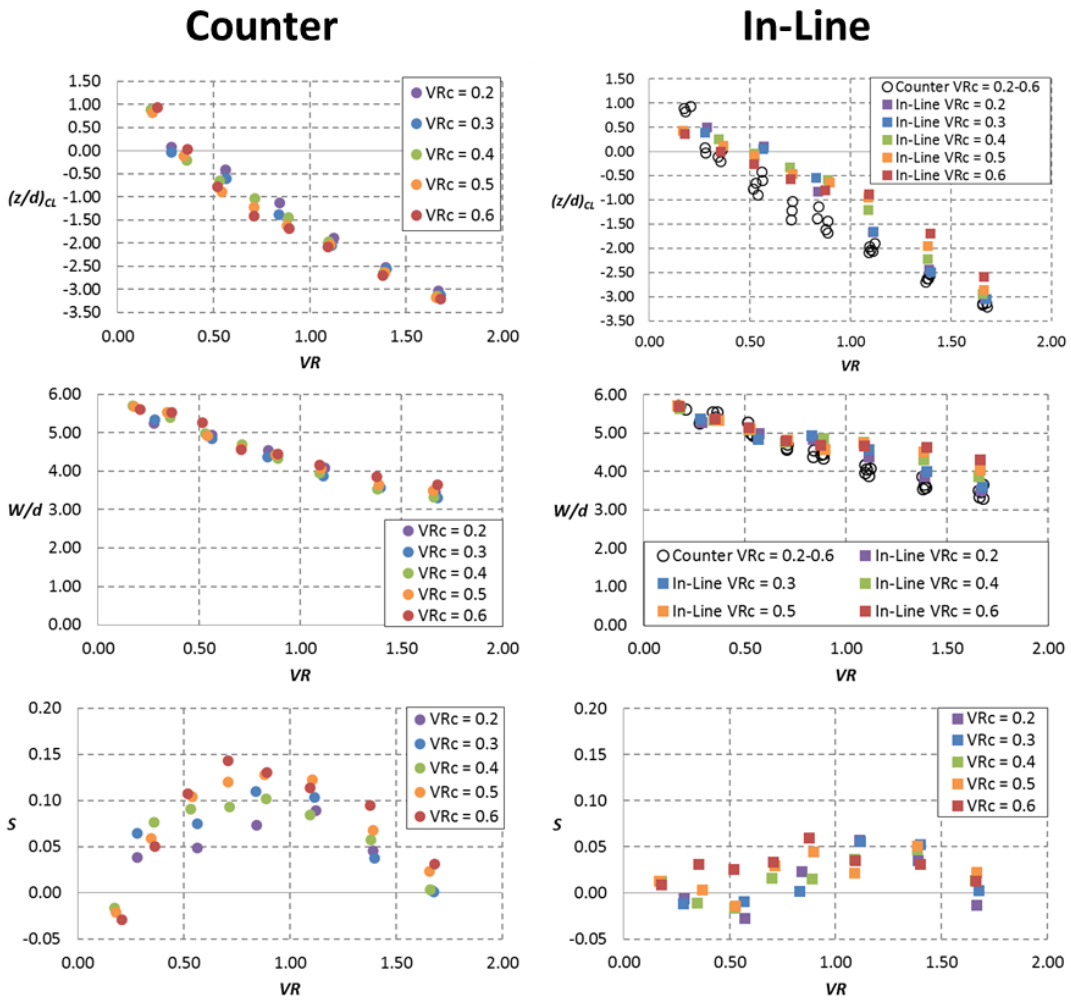

Figure 4.13: Jet characteristic parameters averaged over *x/d* = 5-20 for compound angle holes fed by counter and in-line crossflow

4.4 HEAT TRANSFER COEFFICIENT AUGMENTATION

Heat transfer coefficient augmentation, h_f/h_0, was measured downstream of the compound angle shaped holes to study the effect of internal crossflow on the heat transfer to the external surface. The compound angle geometry was chosen for these measurements instead of the axial geometry because the compound angle holes were expected to have higher heat transfer coefficient augmentation due to increased blockage of the mainstream. Previous studies have found that plenum-fed compound angle shaped holes had increased heat transfer augmentation relative to axial shaped holes [18, 19]. Dittmar *et al* [20] found that compound angle shaped holes fed by an internal crossflow had 60% greater h_f/h_0 for in-line crossflow at a lower injection rate but similar augmentation at a higher injection rate. As mentioned previously, that study only tested a single unspecified internal crossflow velocity.

The heat transfer coefficient augmentation data presented in this section is normalized as $h_{f,norm}$ as follows:

$$h_{f,norm} = \frac{h_f - h_0}{h_{f,peak} - h_0} \tag{4.1}$$

where $h_{f,peak}$ is a representative peak heat transfer coefficient. This scaling can be useful in that it primarily varies from 0 to 1 in the same manner as adiabatic effectiveness and $h_{f,norm}$ = 0 corresponds to h_f/h_0 = 1.0, or no heat transfer coefficient augmentation.

Internal crossflow resulted in higher spatially averaged $h_{f,norm}$ than the baseline plenum condition [53], as shown in Figure 4.14. The data was averaged over two pitches for x/d = 5-40, excluding x/d = 15-18 due to the effect of the gap between heat flux plates. The increase in heat transfer coefficient relative to the plenum case was most pronounced at VR = 1.67. For all conditions, the heat transfer coefficient augmentation increased with

increasing injection rate, as expected. Interestingly, the in-line and crossflow conditions had similar average $h_{f,norm}$ for VR_c = 0.4 and 0.6, but not for VR_c = 0.2, where counter crossflow had significantly greater spatially averaged $h_{f,norm}$. Therefore, the average augmentation decreased with increasing VR_c for the counter crossflow condition, while the in-line crossflow had peak average augmentation for VR_c = 0.4.

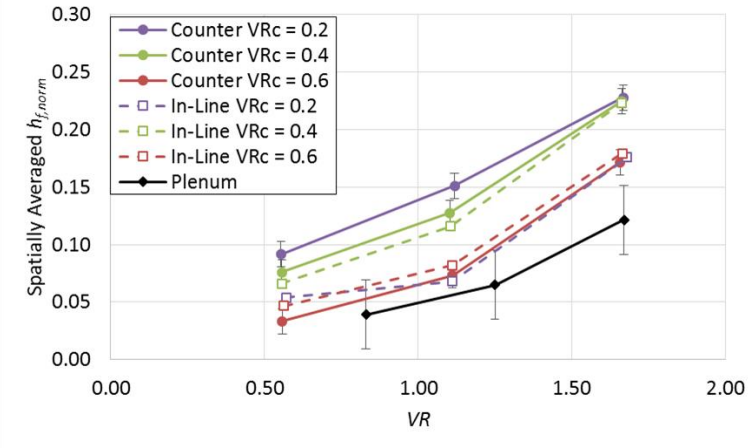

Figure 4.14: Spatially averaged $h_{f,norm}$ for x/d = 5-40 compared to plenum data from [53]

The laterally averaged $h_{f,norm}$ plotted in Figure 4.15 shows how it varied in the streamwise direction. For counter crossflow, spatially averaged $h_{f,norm}$ at VR_c = 0.2 increased due to increased laterally averaged $h_{f,norm}$ in the downstream region. The laterally averaged $h_{f,norm}$ actually increased going downstream for VR_c = 0.2, while it leveled out or decreased for the higher crossflow velocities. The peak $h_{f,norm}$ in the near-hole region occurred at VR_c = 0.4 for all three injection rates and for both counter and in-line crossflow. Similar to counter crossflow, laterally averaged $h_{f,norm}$ for VR_c = 0.2 increased going downstream for in-line crossflow, but was lower in the near-hole region. The interaction between the mainstream and the issuing jet likely resulted in increased mixing and turbulence generation for counter crossflow relative to in-line crossflow.

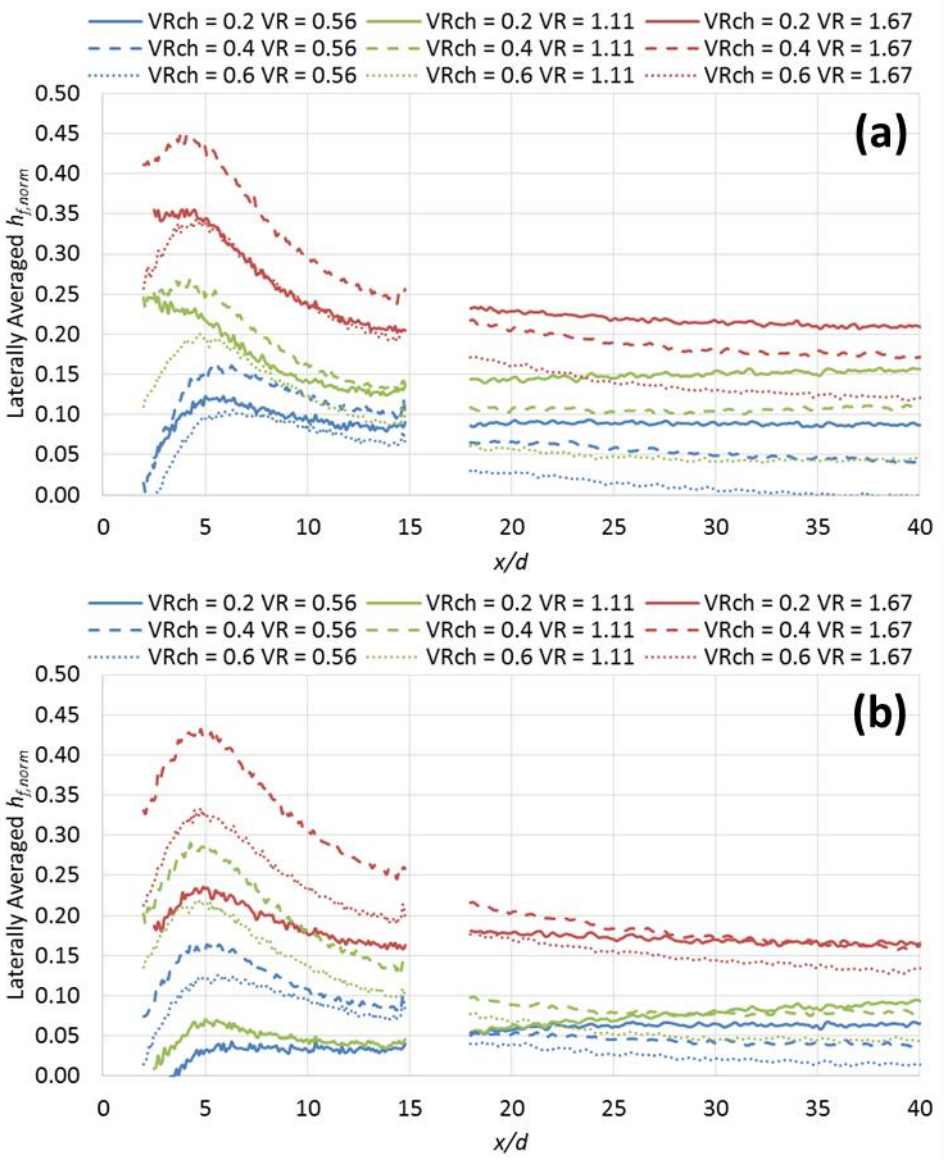

Figure 4.15: Laterally averaged $h_{f,norm}$ for (a) counter crossflow and (b) in-line crossflow

The increased $h_{f,norm}$ for the crossflow conditions relative to the plenum-fed case can be seen in the contour plots of Figure 4.16 for $VR_c = 0.2$ and $VR = 1.67$. All conditions had two distinct streaks of increased $h_{f,norm}$: one in the flow path of the film cooling jet that disappeared by $x/d = 10$ and another that formed on the positive spanwise side of the jet

and propagated far downstream. The streak of increased augmentation under the jet was likely the result of increased turbulence generation within the film hole. The streak of increased augmentation that formed beside the jet was likely the result of a vortical structure that formed as the mainstream rolled over the jet and is particularly undesirable because it increases heat transfer in a region of low film cooling effectiveness. The jet-centerline augmentation was more pronounced for the plenum case than for the crossflow conditions, while the augmentation due to the downstream vortex was greater for the crossflow conditions, especially for counter crossflow. Counter crossflow had higher augmentation than in-line crossflow at all measured streamwise locations, possibly due to increased turbulence production at the inlet of the hole.

Contours of local $h_{f,norm}$ show the effects of crossflow velocity and injection rate on heat transfer coefficient augmentation for counter crossflow in Figure 4.17. The dashed lines on the figure indicate the location of the jet centerline defined by the distribution of film cooling effectiveness and clearly show the downstream streak of increased augmentation was located next to rather than under the jet. It is clear from the contours as well as the previously shown averaged data that the injection rate had the strongest effect on the augmentation, while the effect of VR_c was measurable, but weak. Increasing the injection rate resulted in increased $h_{f,norm}$ in both the jet center and in the streak adjacent to the jet. This result is not surprising given that increased coolant injection is expected to increase the turbulence in the jet as well as the blockage of the mainstream. The contours do show that there was increased augmentation with decreasing VR_c in the downstream region. In the near-hole region, $VR_c = 0.4$ had the highest laterally averaged $h_{f,norm}$ because the region of increased augmentation was broader.

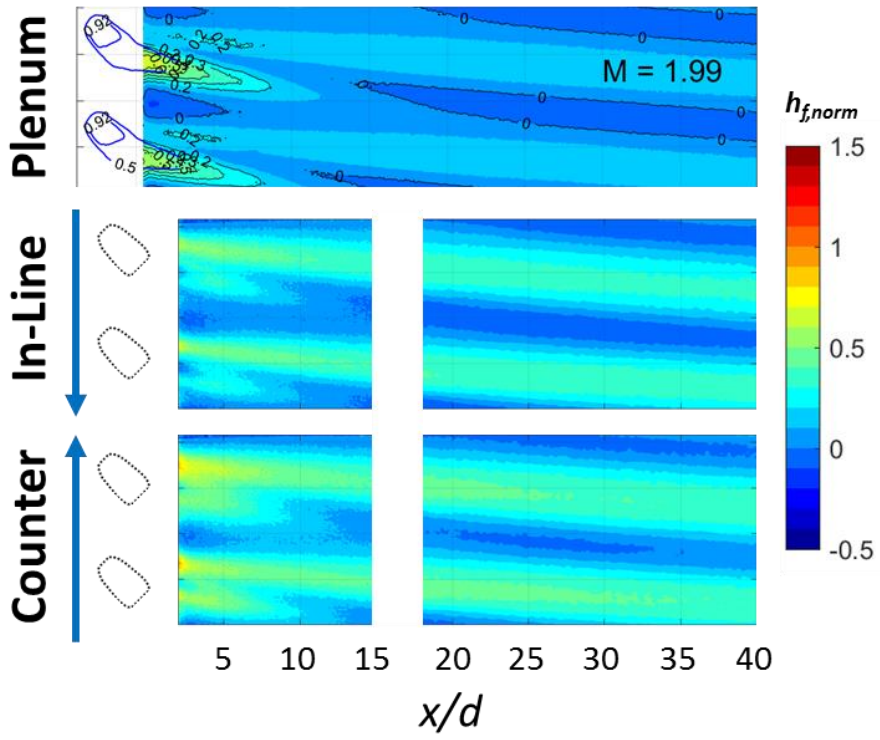

Figure 4.16: Contours of $h_{f,norm}$ at VR = 1.67 for the plenum configuration of [53] and for VR_c = 0.2

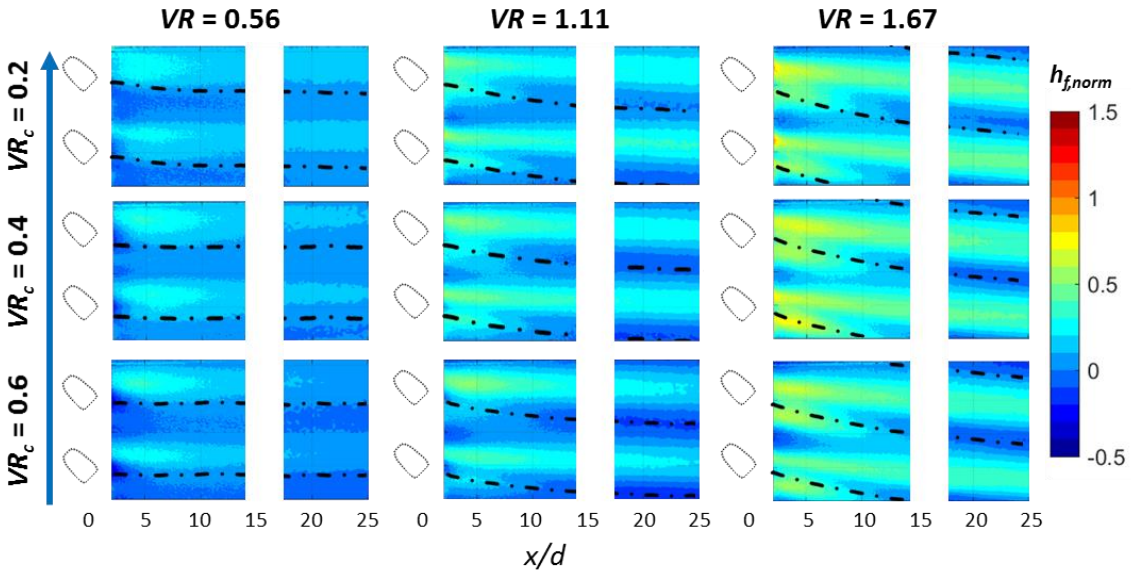

Figure 4.17: Contours of $h_{f,norm}$ for counter crossflow

The local distributions of $h_{f,norm}$ for in-line crossflow are shown in Figure 4.18. Unlike counter crossflow, the peak augmentation occurred at VR_c = 0.4 for in-line crossflow. It is unclear why the augmentation was highest for this condition. It is possible that the biasing within the diffuser at this condition resulted in enhanced mixing with the mainstream flow. The augmentation for VR_c = 0.2 was notably lower than for the higher crossflow velocities. Note that the increased augmentation for in-line crossflow is correlated with reduced effectiveness for these conditions, especially at higher injection rates. It appears that for in-line crossflow, the increased biasing toward the downstream side of the hole relative to the mainstream flow resulted in increased mainstream blockage and turbulence production such that heat transfer augmentation was increased.

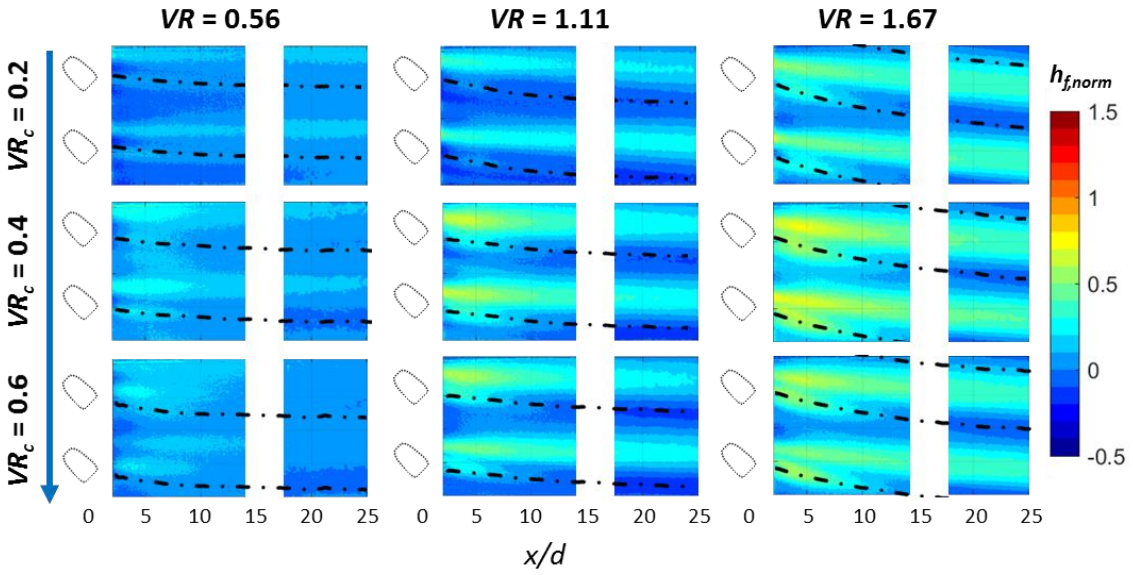

Figure 4.18: Contours of $h_{f,norm}$ for in-line crossflow

The relative strength of the two streaks of heat transfer coefficient augmentation varied with injection rate and crossflow direction. Figure 4.19 shows plots of normalized

heat transfer coefficient augmentation and adiabatic effectiveness at x/d = 5. Note that to produce these plots the value of $h_{f,peak}$ used to normalize the profiles of heat transfer coefficient augmentation used the peak value of h_f at x/d = 5.0. The two peaks in $h_{f,norm}$ can be observed for all conditions shown, although the peak under the jet was less pronounced for in-line crossflow at VR = 1.11. Furthermore, the peak under the jet was not aligned with the jet centerline, but favored the positive z/d side of the jet. The magnitudes of the two peaks also varied relative to each other. The peaks tended to be of similar magnitude for VR = 1.67, while at VR = 1.11, the peak to the side of the jet was consistently larger. Also, the peak under the jet was larger relative to the peak adjacent to the jet for counter crossflow than it was for in-line crossflow. This result suggests that the counter crossflow jets had higher turbulence intensity than the in-line crossflow jets. Also, for most of the conditions, VR_c = 0.4 and VR_c = 0.6 had a larger relative peak under the jet than VR_c = 0.2, which is also indicative of higher turbulence intensities in the jet due to increased internal crossflow.

Similar to the analysis performed for film cooling effectiveness, the location of the peak heat transfer coefficient augmentation was tracked for the different conditions tested. Figure 4.20 plots the averaged location of peak h_f/h_0, $(z/d)_{peak}$, for x/d = 10-30. That streamwise range was chosen because in the near-hole region, the region of peak augmentation moved back and forth between the two streaks of increased augmentation. The data presented is therefore a measure of peak location for the streak located to the positive z/d side of the jet. The streak of increased augmentation moved further in the negative lateral direction with increasing injection rate. For in-line crossflow, the peak location was purely a function of injection rate and was insensitive to VR_c. Counter crossflow had more negative lateral movement than in-line crossflow and had increased negative lateral movement with increasing VR_c.

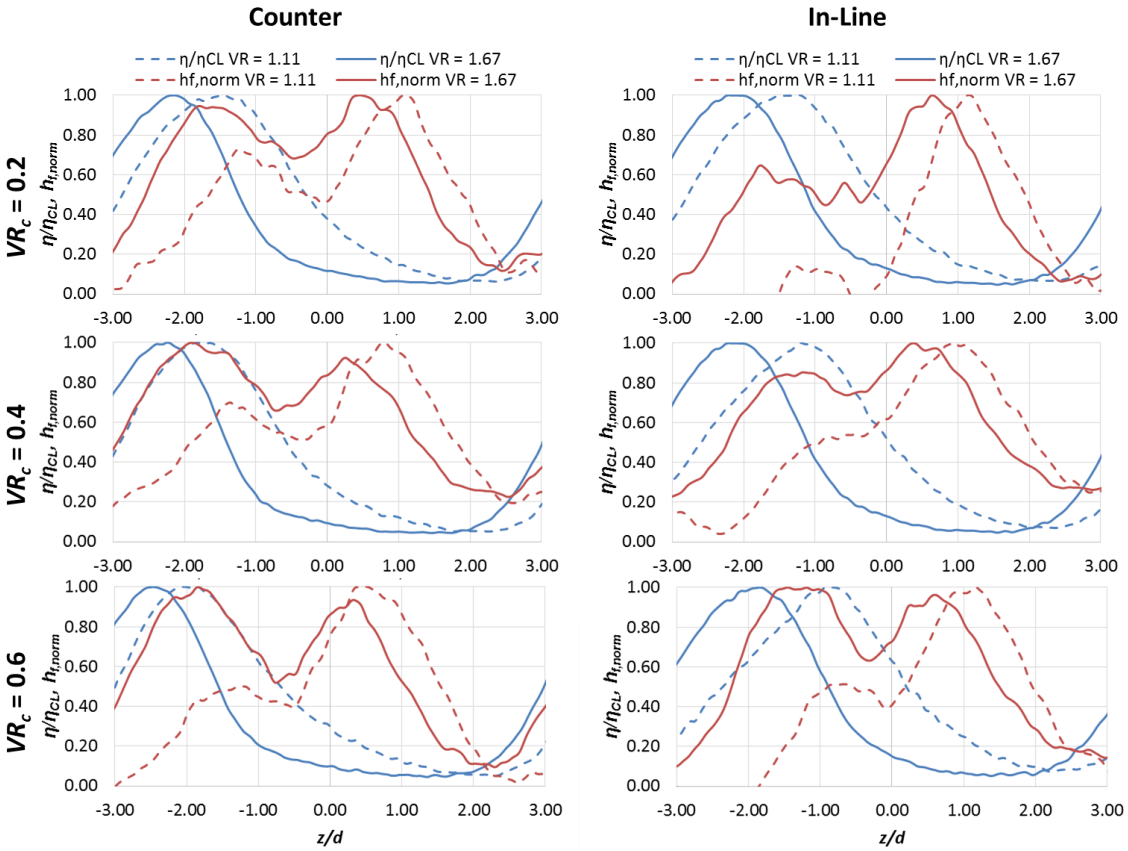

Figure 4.19: Normalized lateral profiles of η/η_{CL} and $h_{f,norm}$ at x/d = 5.0

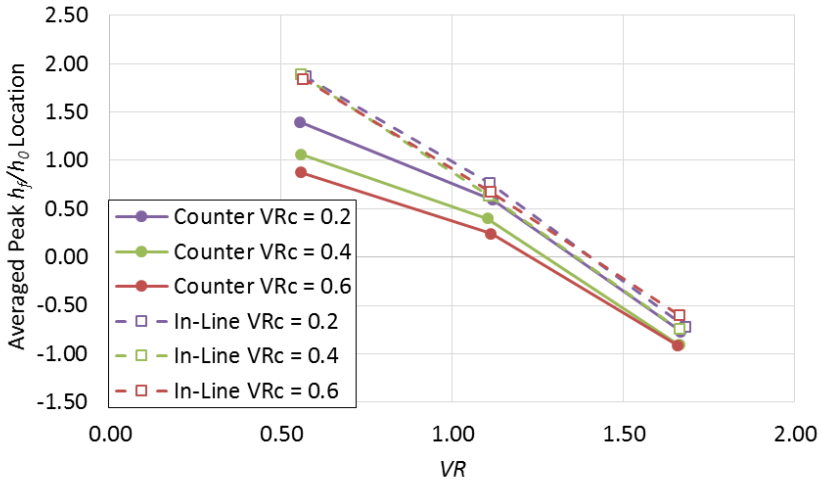

Figure 4.20: Average location of peak h_f/h_0 over x/d = 10-30

The location of peak h_f/h_0, $(z/d)_{hf}$, was not aligned with the location of peak adiabatic effectiveness, $(z/d)_{CL}$, due to the compound angle injection Figure 4.21 (a) compares the locations of peak effectiveness and heat transfer coefficient augmentation for in-line crossflow at $VR_c = 0.4$. As shown previously, increasing the injection rate resulted in increased lateral movement of $(z/d)_{hf}$. Interestingly, there was a slight lateral movement of $(z/d)_{hf}$ in the positive z/d direction for $VR = 0.56$ despite $(z/d)_{CL}$ moving in the negative lateral direction. For $VR = 1.11$ and 1.67 $(z/d)_{hf}$ moved in the negative lateral direction at different rates, indicating that there was some connection between the lateral movement of the jet and the lateral movement of the adjacent vortex. This result indicates that the vortex formed by the blockage of the mainstream did not simply propagate downstream parallel to the mainstream flow, but was influenced by the direction of the coolant jet. The difference between $(z/d)_{hf}$ and $(z/d)_{CL}$ is shown in Figure 4.21 (b). The difference between the two locations increased going downstream for all injection rates and the difference was greatest for $VR = 1.67$.

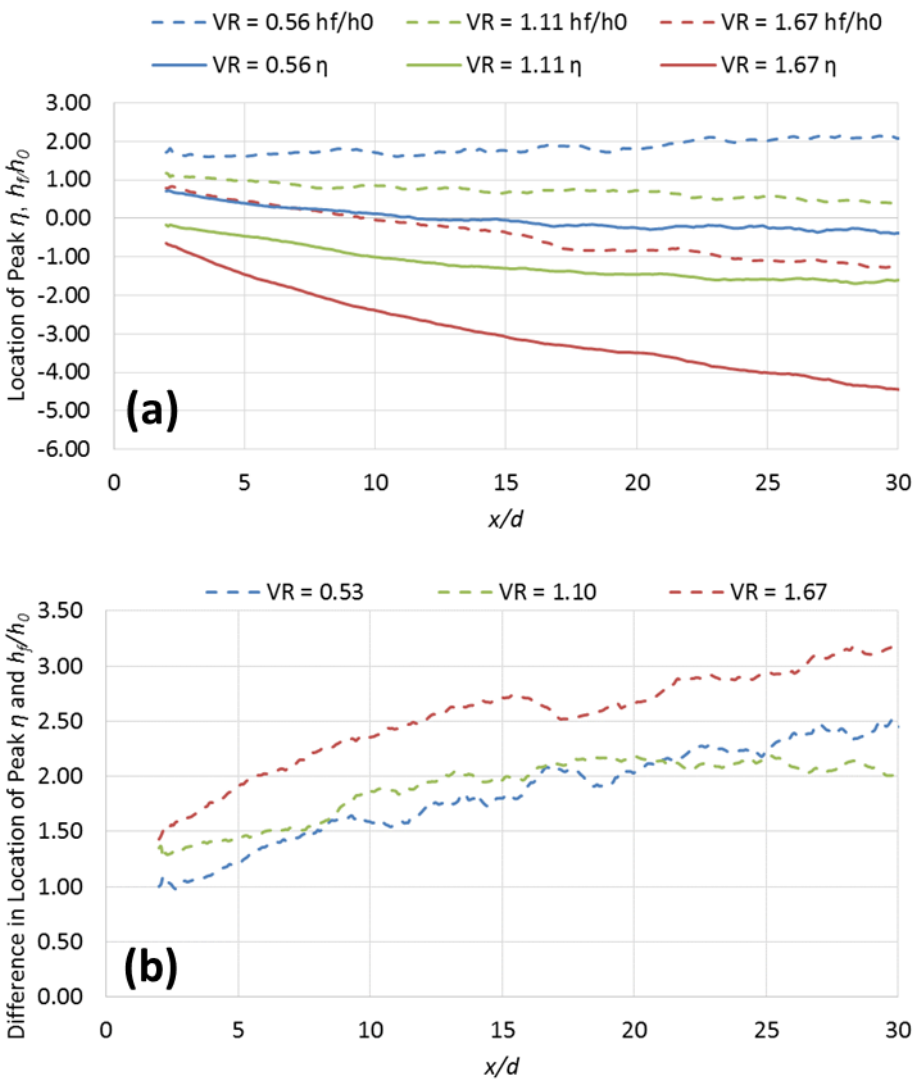

Figure 4.21: (a) Locations of peak η and h_f/h_0 for in-line crossflow at $VR_c = 0.4$ and (b) difference between the locations of peak η and h_f/h_0

4.5 PREDICTION OF OVERALL EFFECTIVENESS

The one-dimensional model used to predict overall effectiveness for the axial holes was also applied to the compound angle holes for the conditions where both adiabatic effectiveness and heat transfer coefficient augmentation had been measured. Unlike the axial holes, where heat transfer augmentation was not measured and assumed to be h_f/h_0 = 1.0, the measured values of h_f/h_0 were incorporated into the prediction for the compound angle holes. The result of performing this analysis in the near-hole region (x/d = 5-15) is shown in Figure 4.22 for both compound angle and axial holes. For all three geometries, the overall effectiveness increased with increasing VR_c due to the resultant increase in the internal heat transfer coefficient, h_c. This increase in φ with increasing VR_c occurred despite decreasing η with increasing VR_c for most conditions. The compound angle holes had greater overall effectiveness than the axial holes at greater injection rates, consistent with the greater adiabatic effectiveness measured for compound angle injection. This result shows that including the heat transfer augmentation for the compound angle holes did not increase heat transfer into the surface enough to overcome the increase in adiabatic effectiveness. At VR_c = 0.4 and 0.6 and VR = 1.11 and 1.67 the counter crossflow outperformed the in-line crossflow, a result that was again, consistent with the effectiveness measurements.

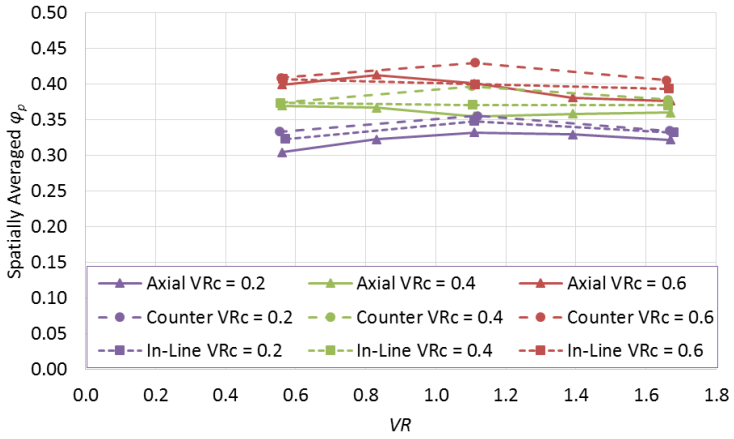

Figure 4.22: Spatially averaged φ_p for axial and compound angle film cooling holes. Data was averaged from x/d = 5-15

The individual contributions of the adiabatic effectiveness and heat transfer coefficient augmentation are shown in Figure 4.23 (a) and (b) respectively. To remove the influence of internal cooling, the internal heat transfer coefficient was assumed to be the same for all three crossflow velocities in part (a) of the figure. The observed differences in overall effectiveness were therefore the result of differences in η. The overall effectiveness with $\eta = 0$ is also plotted to show how the introduction of film cooling increases the overall effectiveness over the bassline condition without film cooling. The differences between conditions are smaller for φ than they are for η, showing that a large increase in η results in a smaller increase in φ. Figure 4.23 (b) shows the effect of assuming $h_f/h_0 = 1.0$ while holding everything else constant. The increase in h_f due to film cooling injection caused up to a 5.7% decrease in overall effectiveness, which is a significant reduction in overall effectiveness. This decrease in performance shows the negative aspect of film injection – namely that it can increase the heat transfer coefficient into the surface.

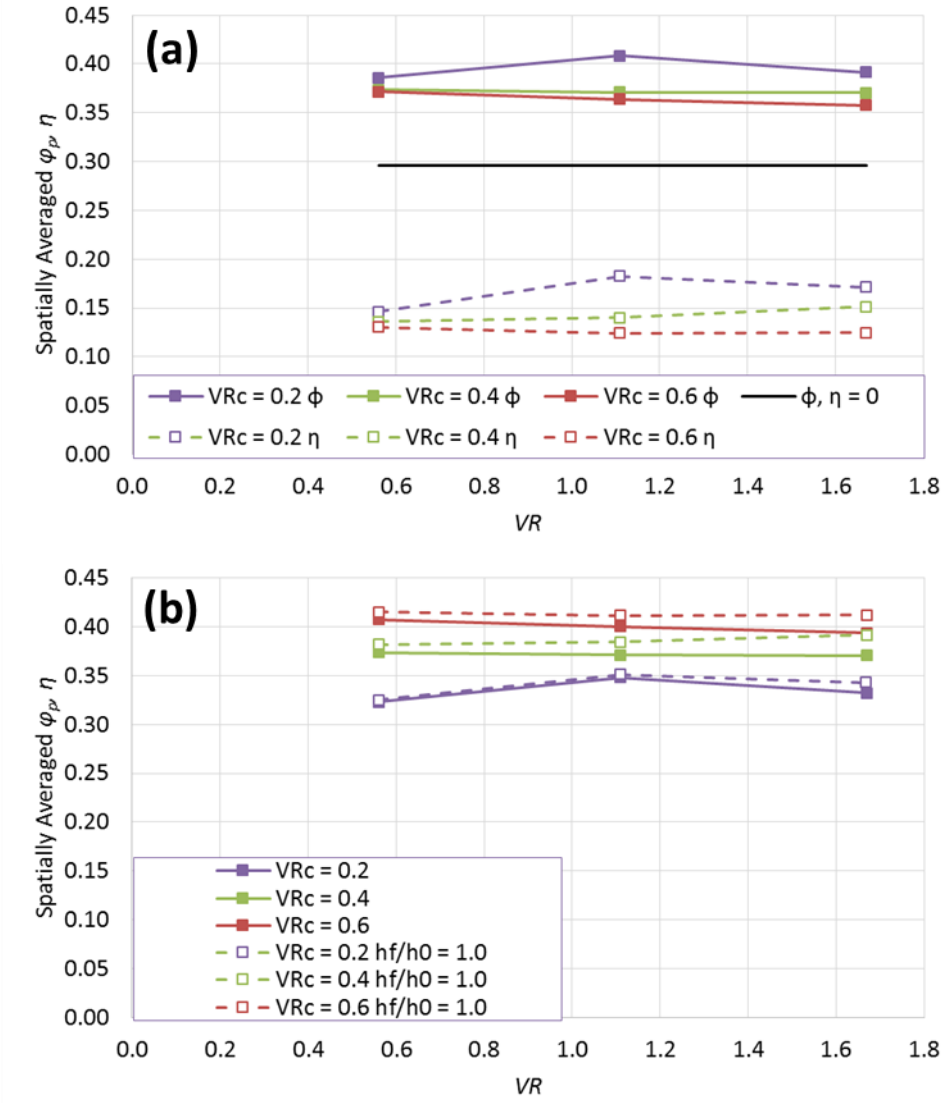

Figure 4.23: Spatially averaged (a) η and predicted φ with constant h_c and (b) predicted φ with and without considering h_f/h_0 for in-line crossflow, x/d = 5-15

Unlike heat transfer augmentation for axial holes, which previous studies have shown is greatest underneath the film cooling jet, the peak h_f/h_0 for the compound angle holes of this study was typically located away from the centerline of the jet. The high heat transfer coefficient augmentation along the pitch-line where the adiabatic effectiveness was

low is undesirable as it enhances heat transfer in a region where the driving temperature is high. The simple one-dimensional analysis used thus far is unable to accurately predict local overall effectiveness because it does not account for lateral conduction. Therefore, a three-dimensional finite element analysis similar to the process used to correct for conduction (described in Section 2.4.2.2) was used to predict local distributions of φ using the measured adiabatic effectiveness and heat transfer coefficient augmentation as boundary conditions for the top surface and the measured coolant temperature and modeled internal heat transfer coefficient as boundary conditions for the bottom surface. Contours of overall effectiveness are shown in Figure 4.24 for $VR_c = 0.4$ and $VR = 1.67$ for both film hole geometries and crossflow directions. The thermal gradients on the surface are small compared to the gradients in the contours of adiabatic effectiveness due to conduction within the wall. Unsurprisingly, the counter crossflow condition had the greatest overall effectiveness on an area and laterally averaged basis. However, the critical design parameters when evaluating overall effectiveness are the minimum effectiveness and maximum thermal gradient in the surface. The minimum effectiveness in a part represents the hottest point that experiences the most severe temperature and thermal cycling while thermal gradients can cause increased stress due to uneven thermal expansion. The lowest predicted effectiveness was φ_{min} = 0.33, 0.32, and 0.30 for the axial, compound angle counter, and compound angle in-line conditions respectively. Despite the greater adiabatic effectiveness for the compound angle holes relative to axial holes, the high heat transfer coefficient augmentation between the compound angle jets resulted in slightly reduced minimum overall effectiveness relative to the axial holes. Granted, this condition was chosen for this analysis because it had the maximum heat transfer augmentation in the near-hole region in order to make this point and it is therefore expected that the compound angle holes would perform more favorably at other conditions, especially at lower injection rates.

And while the axial holes were assumed to have $h_f/h_0 = 1.0$, it is not expected that taking the heat transfer coefficient augmentation into account for the axial holes would alter the minimum overall effectiveness because the peak h_f/h_0 is expected to occur near the jet centerline. The thermal gradients were also greater for compound angle injection than for the axial holes. The maximum change in φ from centerline to mid-pitch was $\Delta\varphi = 0.10$, 0.26, and 0.23 for the axial, compound angle counter, and compound angle in-line conditions respectively. Having over twice the local temperature difference could result in reduction in part life for compound angle holes.

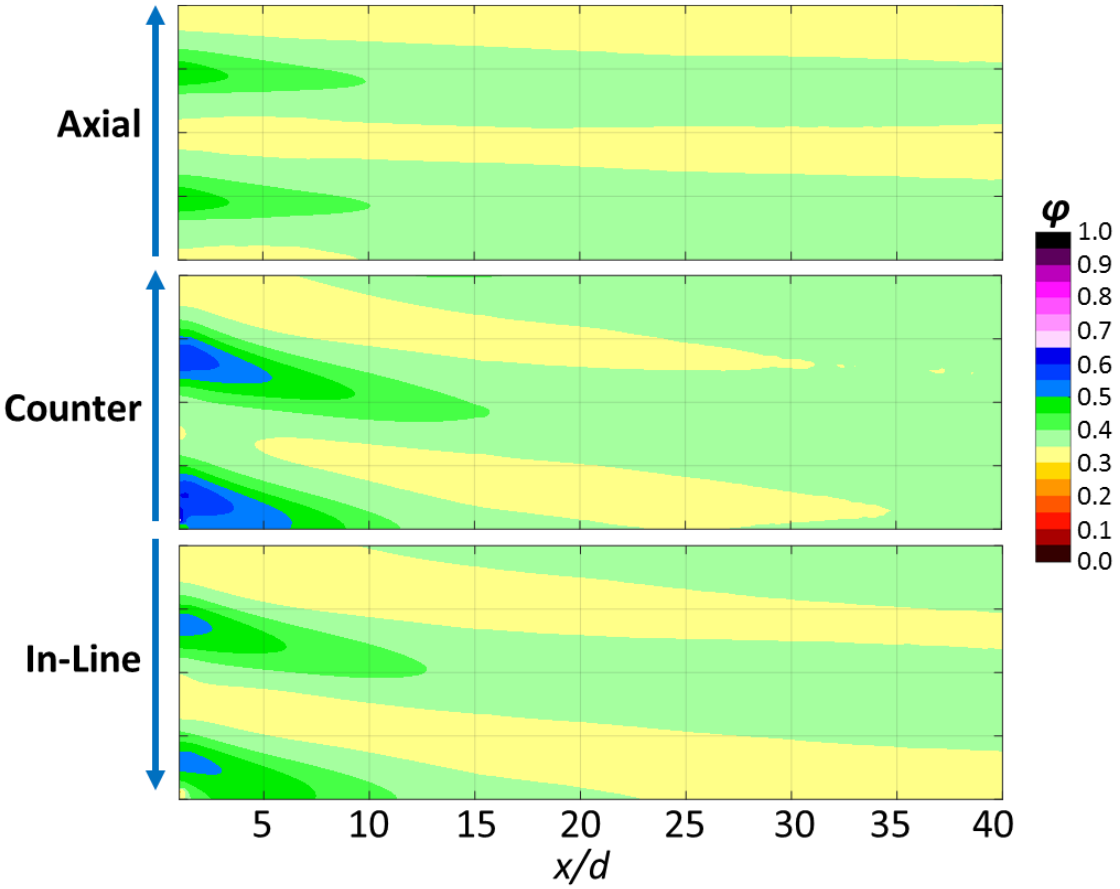

Figure 4.24: Contours of predicted overall effectiveness for $VR_c = 0.4$ and $VR = 1.67$

4.6 Implications for Film Cooling Design

The results presented in this chapter emphasize the importance of considering crossflow direction when feeding compound angle holes with an internal crossflow. For this 7-7-7 laidback fan-shaped hole geometry, feeding the holes with counter crossflow had two distinct advantages: greater effectiveness and a relative insensitivity to the magnitude of internal crossflow velocity. The important flow feature to producing these valuable characteristics was the coolant biasing toward the upstream side of the diffuser relative to the mainstream approach flow. This direction of bias served to prevent ingestion into the diffuser, which proved to be a considerable concern for axial holes and compound angle holes fed with an in-line crossflow. The effectiveness of the compound angle holes was also aided by the increased lateral spreading due to the lateral component of injection. While it may be tempting to claim that counter crossflow is preferred to in-line crossflow, this result is likely geometry dependent. For example, Dittmar *et al* [20] found that in-line crossflow outperformed counter crossflow for a wider angle 14-14-0 fan-shaped hole. The difference between the two geometries is almost certainly governed by the swirling flow observed for the axial holes in this study. For the 7-7-7 holes of this study, the hole geometry likely permitted a greater degree of rotation than the 14-14-0 holes. Therefore, it is important for engine designers to know how a particular geometry will bias before determining its orientation relative to internal crossflow. If possible within other constraints, it would be preferable to select a film hole geometry that had better performance when fed with in-line crossflow because of the greater discharge coefficients and corresponding reduced pressure drop across in-line crossflow-fed holes.

While the improved lateral spreading of compound angle holes provided increased film cooling effectiveness, the heat transfer coefficient augmentation between jets was shown to be cause for concern. Increasing the heat transfer coefficient in that region

resulted in hotter maximum metal temperatures and steeper thermal gradients in the surface temperature. Therefore, compound angle film cooling holes should be installed with careful attention given to where enhanced augmentation can cause part failure. This problem might be avoided by reducing pitch spacing or using staggered rows of compound angle holes so that there are fewer regions of low effectiveness where the mid-pitch regions of augmented heat transfer coefficients would be of less concern.

Chapter 5: Conclusions

The effect of internal crossflow was investigated for a row of axial and compound angle 7-7-7 laidback fan-shaped holes in order to better quantify the important flow parameters governing how internal crossflow affects film cooling performance and to examine the root cause of that effect. To that end, measurements of film cooling effectiveness, heat transfer coefficient augmentation, near-hole thermal fields, and in-hole velocity fields were performed for a wide range of film injection and internal crossflow parameters. The experimental facility was a low speed, low temperature, closed loop wind tunnel set up to produce flow over a flat plate at engine-relevant mainstream conditions. Jet-to-mainstream velocity ratios from VR = 0.2-1.7 and crossflow-to-mainstream velocity ratios from VR_c = 0.2 to 0.6 were tested. Additionally, for axial shaped holes, coolant-to-mainstream density ratios of DR = 1.2 and 1.8 were tested to study the effect of density ratio on crossflow-fed film cooling and to determine the coolant injection parameter that best scaled the film cooling effectiveness. The measurements of film effectiveness were further enhanced by analyzing them in terms of jet characteristic parameters – centerline effectiveness, location, width, and skew – and in terms of a predicted overall effectiveness to account for changes in internal cooling in determining the overall effect of varying the internal crossflow velocity.

5.1: Summary of Important Results

The four driving questions guiding this research that are enumerated at the end of Chapter 1 have been investigated and answered by the efforts of this study as follows.

How does internal crossflow velocity and injection rate affect film cooling?

This study, like previous studies found that, for the most part, introducing an internal crossflow reduced the film cooling effectiveness relative to that of plenum-fed shaped holes. Unlike previous studies, this study investigated a sufficiently wide range of crossflow velocities and injection rates and observed trends that the smaller data sets of previous studies missed.

For axial holes, the most important observed trend in this study was the scaling of discharge coefficients, centerline effectiveness, centerline location, and jet skew with the inlet velocity ratio, or the ratio between the internal crossflow velocity and the mean velocity in the cylindrical inlet section of the film cooling hole. The inlet velocity ratio also scaled the biasing within the diffuser such that the maximum diffuser bias corresponded to a local minimum centerline effectiveness at $VR_i = 0.36$. Due to the scaling with VR_i, the effectiveness was greatest at the lowest crossflow-to-mainstream velocity ratio, $VR_c = 0.2$ because most injection rates for that condition were at $VR_i < 0.36$ and thus avoided much of the degradation due to internal crossflow. The measured degradation due to crossflow was significant – up to a 47% reduction in spatially averaged effectiveness when VR_c was increased from 0.2 to 0.6 for $VR = 1.67$.

The compound angle holes had greater film cooling effectiveness than the axial holes due to improved lateral spreading – up to 70% greater spatially averaged effectiveness at $VR_c = 0.5$. Furthermore, the results for compound angle holes showed the importance of internal crossflow direction. Similar to the axial holes, the internal crossflow caused bias within the diffuser, but because of the compound angle of the holes, the side of the diffuser that the coolant favored was critical to the downstream effectiveness. Counter crossflow (directed counter to the lateral direction of coolant injection) had greater effectiveness and less sensitivity to internal crossflow than in-line crossflow because the

flow in the diffuser biased toward the upstream side of the diffuser relative to the incoming mainstream and blocked the mainstream flow from ingesting into the hole. In-line crossflow, on the other hand, biased the coolant toward the downstream side of the diffuser such that the mainstream flow was able to ingest into the diffuser and reduce the downstream effectiveness. Because counter crossflow was less sensitive to internal crossflow, its jet characteristics did not scale well with the inlet velocity ratio and instead scaled better with the injection rate. In-line crossflow, being more sensitive to internal crossflow, had centerline effectiveness that scaled with the inlet velocity ratio in a manner very similar to that of axial holes.

Heat transfer coefficient augmentation for the compound angle holes was predominantly a function of the injection ratio, although there was a measured influence of internal crossflow. The crossflow-fed holes had greater augmentation than plenum-fed holes with the same geometry. Except for VR_c = 0.2 where counter crossflow had much greater augmentation than in-line crossflow, there was little influence of internal crossflow direction. The heat transfer augmentation was characterized by two features: a region of increased augmentation that was roughly located under the film cooling jet that went away by x/d = 10, and a region of increased augmentation on the positive lateral side of the jet that propagated far downstream. This second region was likely the result of the mainstream flow being blocked by the issuing compound angle jet, resulting in a swirling flow to the side of the jet.

What impact does density ratio have on the crossflow effect?

The axial holes were tested at a laboratory-friendly density ratio of DR = 1.2 and an engine relevant density ratio of DR = 1.8 in order to understand how the experiments performed at laboratory conditions would translate to engine conditions. Unlike axial 7-7-

7 holes, which had previously been shown to scale best with jet-to-mainstream velocity ratio, there was no one single scaling parameter that best scaled all conditions tested. The velocity ratio was indeed the best injection parameter to characterize the film effectiveness for VR_c = 0.5, with most conditions within the experimental uncertainty and a peak effectiveness levels that were within 16% of each other. However, at VR_c = 0.3, the jet-to-mainstream mass flux ratio, or blowing ratio, best scaled the effectiveness with most conditions agreeing to within experimental uncertainty. More importantly, important trends were maintained at both density ratios. The coolant biased toward the same side of the diffuser for both cases and corresponded to a reduction in effectiveness. Also, centerline effectiveness and location scaled similarly with VR_i for both density ratios. This result demonstrates that the important flow physics governing how internal crossflow affects film cooling performance were largely insensitive to density ratio and that the important conclusions of this study are indeed relevant to engine design.

What is the root cause behind the behavior of crossflow-fed holes?

The in-hole thermal and velocity fields also scaled well with inlet velocity ratio, showing that the inlet velocity ratio was the most important scaling parameter for the development of flow within a crossflow-fed film cooling hole. Based on the in-hole measurements performed by this study, much of the essential in-hole flow physics for crossflow-fed holes has been observed or can be inferred. At the inlet of the hole the internal crossflow feed formed a separation region on the windward side of the hole due to the inability of the flow to navigate a sharp 90° turn, and caused most of the coolant to accelerate around the separation region, entering the hole on the leeward side. The size of this separation region and the acceleration of the flow around it have not been measured, but both were almost certainly driven by the inlet velocity ratio. The mean swirling flow

that was observed at the upstream edge of the hole outlet for $VR_i = 0.71$ was oriented in the clockwise direction when looking down into the hole. The direction of the swirl corresponded with how the core of the jet in the measured thermal fields appeared to rotate with increasing VR_i. Furthermore, the magnitude of the swirling velocity was on the order of the estimated swirling velocity required for the coolant jet, starting at the leeward side of the hole inlet, to complete over a half rotation through the hole to bias the jet on the bottom-windward side of the diffuser outlet at $VR_i = 0.71$. These results strongly indicate that a strong swirling flow developed at the inlet of the hole and was ultimately what caused the jets to bias in the hole and degrade the effectiveness. The swirling flow, however, was not observed in the in-hole velocity fields at lower inlet velocity ratios of $VR_i = 0.36$ and 0.24, suggesting that the swirling flow was largely attenuated by the lateral and forward expansion in the diffuser.

The swirling secondary flow did more than just cause the jet to bias in the diffuser. The in-hole thermal fields showed a substantial amount of mainstream ingestion into the diffuser that scaled with the inlet velocity ratio. At $VR_i = 0.36$, where the jet was fully biased toward the windward side of the diffuser, there was considerable ingestion into the leeward side of the hole. At $VR_i = 0.71$, where the jet was biased toward the bottom-windward side of the diffuser, most of the ingestion was into the top of the diffuser. Ingestion into the diffuser was likely the primary cause of reduced effectiveness for crossflow-fed holes, as evidenced by the counter crossflow compound angle holes, which appeared from the effectiveness measurements to experience very little ingestion and were thus less sensitive to the internal crossflow velocity. The ingestion locations in the thermal fields corresponded with a downward velocity in the in-hole velocity fields, indicating that the swirling secondary flow in the hole was a primary contributor to the ingestion.

How do these results influence film cooling design?

The results of this study should help inform better design practices. For the 7-7-7 geometry considered in this study, there were certainly conditions to avoid, such as feeding the compound angle holes with an in-line crossflow or having an inlet velocity ratio close to VR_i = 0.4 for axial holes. However, the adiabatic effectiveness is only a boundary condition and does not represent the metal temperature, which is the primary design parameter for turbine cooling. The metal temperature is dependent on both external heat transfer, characterized by the adiabatic effectiveness and heat transfer coefficient augmentation, and by the internal heat transfer, characterized by the coolant temperature and the internal heat transfer coefficient. A one-dimensional analysis was used to predict the normalized metal temperature, or overall effectiveness, by taking both the external and internal heat transfer into account. The result of this analysis showed that increasing the crossflow velocity increased the overall effectiveness for both the axial and compound angle geometries. The increase in overall effectiveness occurred despite decreasing film effectiveness for increasing VR_c. While the overall effectiveness was predominantly determined by the internal cooling, the overall effectiveness without film cooling was considerably lower than with film cooling. A similar three dimensional finite element analysis predicted overall effectiveness for a selected condition from the surface distributions of film cooling effectiveness and heat transfer coefficient augmentation for both axial and compound angle holes. That analysis showed that despite having greater spatially averaged overall effectiveness, the compound angle holes had lower minimum overall effectiveness and greater thermal gradients due to increased heat transfer augmentation between jets. These analyses suggest that engine designers should first prioritize maximizing the internal cooling and then design film cooling holes that produce

the best distribution of coolant across the surface in combination with the selected internal cooling design.

The geometry of the film cooling holes was not varied in this study. Different film cooling geometries could produce better overall effectiveness in the presence of internal crossflow. The in-hole velocity fields suggest that the expansion in the diffuser attenuated the swirling flow that caused ingestion into the diffuser. A shorter metering length could reduce the swirl and may be less sensitive to crossflow. Two new axial hole designs were also proposed in Section 3.8, including a hole with asymmetric diffusion that takes advantage of a known direction of bias, or a hole with an undersized diffuser that could disrupt the secondary flow within the hole and reduce ingestion.

5.2: Recommendations for Future Work

The results of this study provide critical insight into the behavior of axial and compound angle shaped film cooling holes fed by an internal crossflow, but they also raise a number of further questions that should be addressed by future research. These questions include:

- *How does the film hole geometry impact these results?* Certainly different shaped hole geometries will perform differently when fed by an internal crossflow. There are a great number of geometric parameters used to define a shaped hole, but the results of this study suggest that the length of the cylindrical portion of the hole may be critical to how many in-hole rotations the coolant jet will make – longer cylindrical inlet sections should correspond to increased rotation. The ratio between the average hole perimeter to the length of the hole may also be important (see Equation 3.1 in Section 3.6). Assuming an average swirl velocity in the hole, this parameter would affect the number of rotations the jet makes in the hole. Geometry

modifications such as an asymmetrically diffusing hole or a diffuser mismatch to disrupt the in-hole secondary flow may also be worth investigating.

- *How do internal features such as rib turbulators impact these results?* Internal channels in gas turbine airfoils feature rib turbulators to increase the internal heat transfer coefficient. These structures could also impact the film cooling effectiveness by changing the internal flow. This effect was shown by Klavetter *et al* [47] for cylindrical compound angle holes, but only for a single crossflow-to-mainstream velocity ratio. It would be interesting to see if any of the trends observed for a smooth-walled channel held up for a turbulated channel.
- *Does in-hole secondary flow enhance convection in the hole?* A study by Davidson *et al* [54] used a matched-Biot number model to measure overall effectiveness on a simulated turbine vane and found that in-hole convection had a substantial contribution to the measured overall effectiveness. It is possible that the increased swirl velocity in the crossflow-fed holes may increase the in-hole convective heat transfer. A matched-Biot number model could be used to determine this effect and to verify the usefulness of the one-dimensional model used to predict overall effectiveness in this study.
- *How do mainstream parameters impact these results?* All conditions tested in this study were measured for the same mainstream conditions, which featured a thick turbulent approach boundary layer, high mainstream turbulence, and an external Reynolds number of Re_d = 6,000 or 7,500. These parameters all vary considerably at engine conditions. It would be interesting to see how crossflow-fed holes perform at higher mainstream Reynolds numbers or a thinner approach boundary layer. It is likely that many of the trends would be preserved but that the effectiveness would change considerably.

- *Can any of these results be replicated computationally?* Given the importance of the inlet velocity ratio to determining ingestion and biasing within the diffuser, it would be valuable to know what level of computational complexity would be required to replicate the in-hole velocity or thermal fields, if indeed these results can be replicated computationally. While RANS solvers consistently struggle to accurately predict film cooling effectiveness, if they were able to predict where the maximum biasing or ingestion would occur, these tools would be useful to select optimal film cooling injection rates and to evaluate the sensitivity of new geometries to internal crossflow.

Appendix: Finite Element Conduction Correction Technique

A.1 Development and Motivation

In the course of this study, a three dimensional, finite element was developed to correct for conduction errors in the measurements of adiabatic effectiveness and heat transfer coefficient augmentation. The technique and its implementation were first discussed in McClintic *et al* [21], which implemented the technique for compound angle cylindrical holes. It was developed initially to account for a more complicated backing geometry than was used for previous experiments in this laboratory. Figure A.1 shows a cross-sectional schematic of the test facility as it was during that study. Because the cold aluminum channel sat directly under the tunnel and the supporting structure beneath the plate up to x/d = 18 was made from aluminum, there were considerable conduction errors. The high thermal conductivity of the aluminum made it such that the backing temperature for the test coupon was essentially equivalent to the coolant temperature for that range of streamwise positions. The normalized temperature of the foam with the film holes blocked off was η_0 = 0.05-0.07 – for a perfectly adiabatic wall, η_0 = 0.

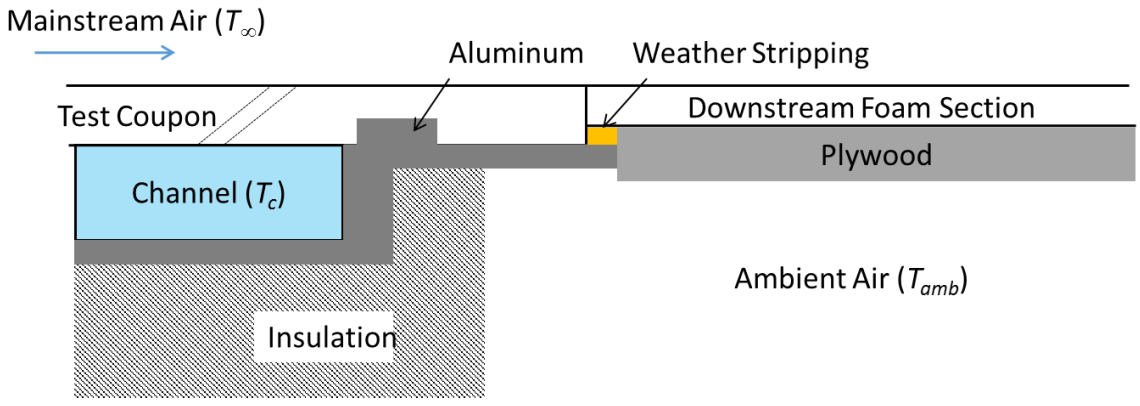

Figure A.1: Cross-section of the flat plate channel assembly as originally designed

The accepted technique for correcting these conduction errors at that time was to use a one-dimensional conduction correction of the form:

$$\eta = \frac{\eta_m - \eta_0}{1 - \eta_0} \tag{A.1}$$

where η_m is the normalized measured temperature distribution. This one-dimensional technique had the advantage of being tied to a measured η_0 distribution in the laboratory such that no conduction calculations were required. Equation A.1 above was developed from a one-dimensional heat transfer analysis with the assumption that the driving temperature on the backside of the model was the coolant temperature. That assumption was appropriate for locations where the cold aluminum plate ran underneath much of the viewing area and it worked reasonable well further downstream where η_0 was near zero and the correction was negligible anyway.

In order to better investigate the conduction effects within the flat plate, a three dimensional analysis was performed to predict the conductive heat flux at the surface required to produce the measured surface temperature. Comsol Multiphysics®, a commercially available solver was used to implement a steady-state conduction analysis of the test geometry. The three-dimensional technique, used the measured surface temperature as a boundary layer to predict the heat flux at the surface. The correction for conduction was implemented according to a heat balance at the wall:

$$q" = -k \left.\frac{\partial T}{\partial y}\right|_{y=0} = h_f (T_{aw} - T_m) \tag{A.2}$$

With the heat flux normal to the wall, q'', calculated by the finite element solver, the measured wall temperature, T_m, measured during the experiment, and the heat transfer coefficient with film cooling present, h_f, either measured or predicted with a standard flat plate correlation, the adiabatic wall temperature, T_{aw}, can be calculated. Were the wall truly adiabatic ($q'' = 0$), the adiabatic wall temperature would be equivalent to the measured temperature. Unfortunately, adiabatic surfaces were unavailable at the time of this study. Details regarding the assumptions, implementation, and limitations of this method are discussed later. Figure A.2 demonstrates its usefulness relative to the 1D conduction correction method traditionally used in this and other laboratories. Figure A.2 (a) shows that the 1D and 3D corrections did not differ appreciably when calculating laterally averaged effectiveness. The magnitude of the correction was large, up to 0.05, due to the aluminum plate underneath the model. This result was encouraging as this laboratory has produced a significant amount of laterally averaged effectiveness data using the 1D correction. Figure A.2 (b) shows that the 1D model failed to predict local values of η near the holes. The plot shows the difference between the 1D and 3D models was as great as 0.05 in η. This difference is well outside the uncertainty of the measurement and would be an error of considerable significance if comparing to computational results. The difference results from the 3D correction taking lateral conduction into account, which, by definition, is ignored by the 1D model. The 3D correction had greater centerline effectiveness as it accounts for the warming of the jet centerline by lateral conduction. The lateral conduction was only of concern for $x/d < 20$ for the condition shown in the figure, which was for compound angle cylindrical holes. For shaped holes, which produce coolant jets that remain better attached further downstream, lateral conduction can be significant further downstream.

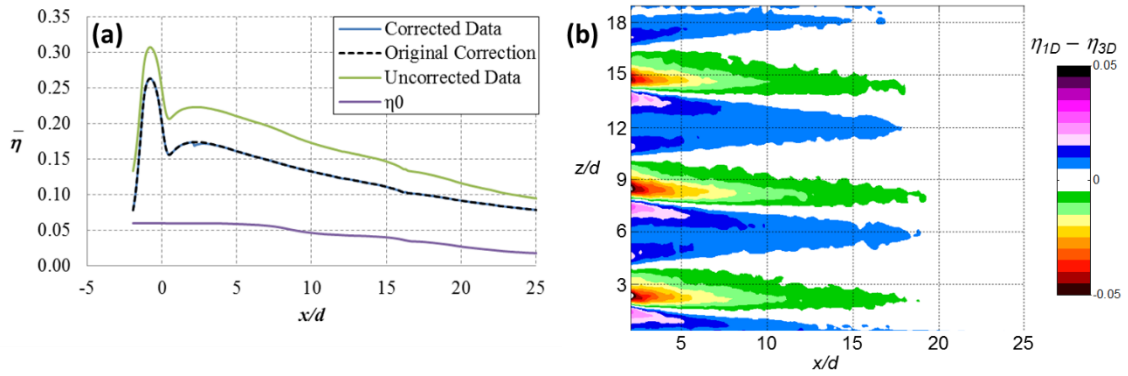

Figure A.2: Comparison of (a) laterally averaged η and (b) spatial distribution of the difference between the 1D and 3D conduction correction

A.2 CURRENT IMPLEMENTATION

The current implementation of the method is described in detail in this section. Much of this information is repeated from Chapter 2 which describes the experimental methods used in this study. Starting with a data set containing the surface temperature mapped to x and z coordinates on the surface of the model, this section details how the adiabatic wall temperature was calculated. A three dimensional model of the test plate was created in Comsol. Figure A.3, a repeat of Figure 2.7, shows an x-y view of the model used for the axial 7-7-7 holes in this study. A key difference between this model and the one used in [21] was the replacement of the cold aluminum bar underneath the test surface with a lower conductivity acrylic bar, which reduced the magnitude of the correction considerably. Note that the channel was still made from aluminum. The thermal conductivities of all modeled materials were input to the models –Table A.1 lists the values of thermal conductivity used. The important thermal conductivity was that of the closed cell polyurethane foam (General Plastics Last-a-Foam R-3315) which the test coupon and run-out plate were constructed from. The value reported in Table A.1 is the same as given in the data sheet supplied by General Plastics. Perturbing $k_{polyurethane}$ by ± 0.004 (10%)

resulted in change in laterally averaged effectiveness of less than $\delta\eta = 0.002$, which is negligible relative to the bias uncertainty in adiabatic effectiveness. The same perturbation of thermal conductivity similarly had a negligible effect on heat transfer coefficient augmentation.

Table A.1: Thermal conductivities of modeled materials

Material	***Component Used For***	***Thermal Conductivity W/(m·K)***
Polyurethane Foam	Coupon, Run-Out Plate	0.044
Aluminum	Channel	238
Acrylic	Acrylic Support and Floor	0.20
Insulation	Insulation	0.11

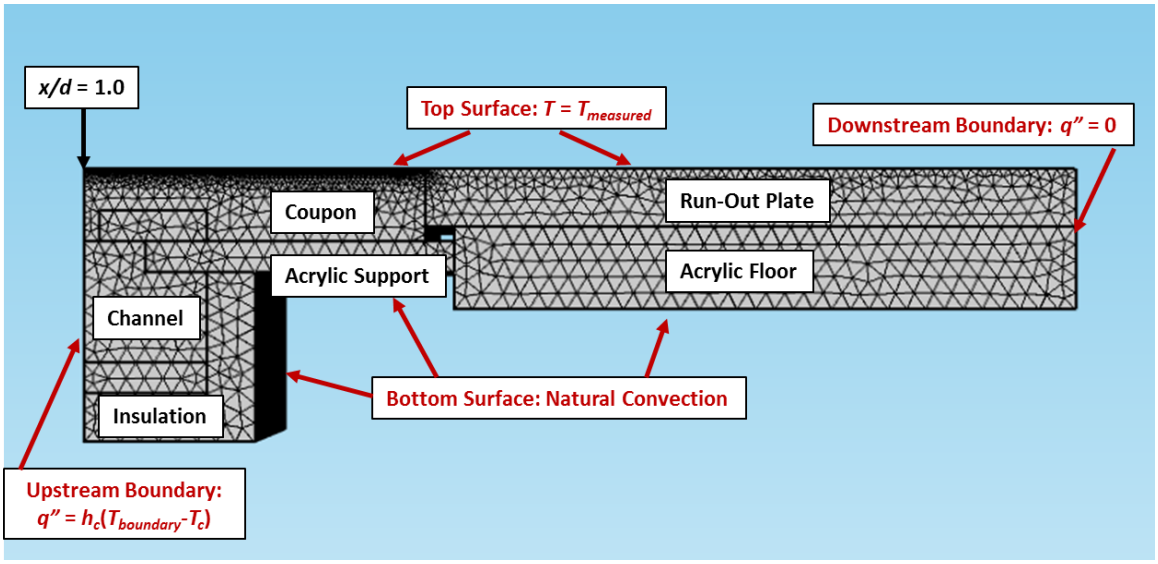

Figure A.3: Finite element model, boundary conditions, and mesh

The boundaries of the model were selected both to reduce the number of unknown boundary conditions and to reduce computational complexity. The downstream boundary was simply set as the limit of the IR camera's viewing region, which worked well because for the conditions tested, there was little lateral or streamwise variation in adiabatic

effectiveness, thus the thermal gradients in that region were vanishingly small. Therefore, an insulated boundary condition was used at the downstream edge ($q''_x = 0$). The lateral edges of the model were mid pitch lines in between the film cooling jets. It was clearly appropriate to also set insulated boundary conditions ($q''_z = 0$) at these edges for axial film holes as that boundary condition also doubles as a periodic boundary condition. The same insulated boundary condition was also used for the compound angle film holes with the rationale that by the time the compound angle jet crosses the pitch line, the lateral conduction would be very small. The top and bottom boundaries were defined by the solid-air interfaces at the top and bottom of the flat plate model. The temperature of the top boundary was set to the measured two-dimensional temperature distribution ($T = T_{measured}$), which was imported into Comsol and interpolated onto the model grid points. A natural convection boundary condition was applied to the bottom surfaces using the built-in models in Comsol for natural convection. These models required different characteristic geometries, depending on whether the surface was vertical or horizontal as well as the ambient driving temperature, which was assumed to be T_{amb} = 298K. A study of the sensitivity to the bottom surface boundary condition found that the solution was effectively insensitive to the exact specified condition. The upstream boundary was the most difficult to define. For the purpose of this study, it was set to be at x/d = 1, which corresponded to the downstream wall of the channel relative to the mainstream direction. Applying a boundary at this location avoided the considerable complication of modeling the film cooling holes and making appropriate assumptions regarding the in-hole boundary conditions (for which no experimental correlations exist). A convective heat flux boundary condition ($q''_x = h\Delta T$) was applied to the upstream channel wall using the coolant temperature, T_c, as the driving temperature and an internal heat transfer coefficient was predicted using Gnielinski's formula for turbulent internal flow:

$$Nu_D = \frac{(f/8)(Re_D - 1000)Pr}{1 + 12.7(f/8)^{1/2}(Pr^{2/3} - 1)} \quad \text{(A.3)}$$

$$f = (0.79\ln(Re_c) - 1.64)^{-2} \quad \text{(A.4)}$$

An insulated boundary condition ($q''_x = 0$) was applied to the remaining upstream edges, that is, to the upstream edge of the test coupon and insulation. It was assumed that the streamwise conduction at this location was much lower than the lateral and through wall conduction. Because that assumption required further justification, a separate model was made with cylindrical holes modeled upstream. A constant temperature boundary condition of $T = T_c$ was applied to the internal surface of the holes (which assumes the maximum possible heat transfer to the internal surface of the holes). The difference between the conditions with and without the film holes was a maximum of $\delta\eta = 0.003$ near the hole. Because this difference was small, the assumed boundary conditions were appropriate for this condition.

The solution was solved using the mesh shown in Figure A.3. Two different density free triangular meshes were applied to the top surface. A fine mesh with a maximum element size of 0.5 mm was generated for the top of the test coupon. A coarser mesh with a maximum element size of 2 mm was generated for the top of the run-out plate. The rest of the domain was meshed with an unstructured tetrahedral mesh with a maximum element size of 4 mm. The mesh was comprised of 1.15 million elements. A grid independence study was performed independently for the different regions of the model. Figure A.4 shows the results of refining the grid for the test coupon for a selected lateral effectiveness profile ($x/d = 5$). The different curves are different mesh settings. The "Original" setting was an unstructured tetrahedral mesh with a maximum element size of 4mm and no

refinement near the top surface. The remaining meshes represent a number of cases with the mesh refined to 0.34-0.50 mm at the top surface and are all within ± 0.005 in η near the peak. This variation represents the error from interpolation. Any refinement of the mesh beyond 0.34 mm is impractical given that this is the pixel resolution of the IR camera.

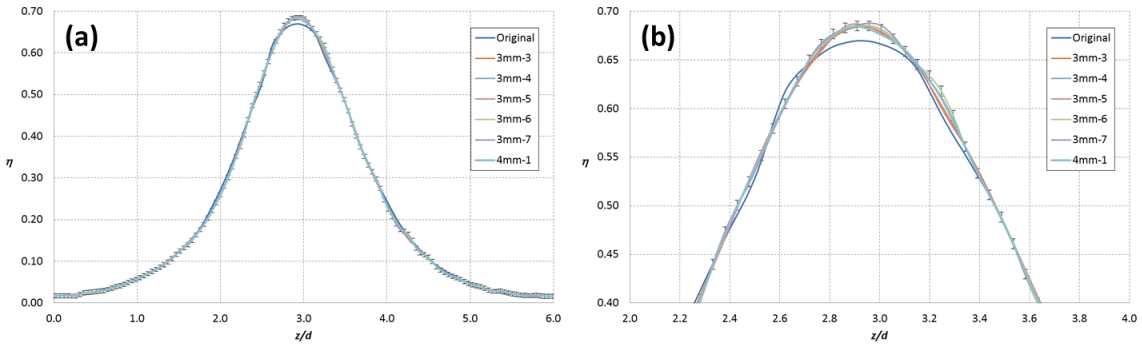

Figure A.4 Effect of varying the mesh on a profile of η for a selected condition. (b) is a zoomed in view of the peak of (a)

The finite element solver took about 3 minutes to process each point and was called by a Matlab script written to interface with Comsol. The script told Comsol where to find the surface temperature data to use for the top boundary condition and the values of h_c and T_c to used. The interpolated top surface temperature distribution and heat flux were output in a text file for each condition. A separate Matlab script was used to compute the conduction correction and to produce contour plots and laterally averaged data.

The calculation of the adiabatic wall temperature was complicated considerably by the selection of an appropriate h_f to use in Equation A.1. A number of options have been explored over the course of the past four years, each with their benefits and shortcomings:

Use η_0 to calculate h_0

This was the initial method used to calculate h_0 for the compound angle round holes study of [21]. In principle, the measured temperature of the plate with the film holes blocked off can be used to calculate the heat transfer coefficient without film cooling, h_0, using the finite element solver to predict q'' and the measured mainstream temperature, T_∞, as the driving temperature for heat transfer. The crucial failing of that method was that a thermal boundary layer develops over the plate due to the mainstream interaction with the cold test coupon upstream of the holes. The thermal boundary layer invalidated the assumption that T_∞ was the driving temperature for heat transfer.

Use h_0 from a correlation

This was the technique used to process the axial 7-7-7 hole data in this study. The correlation predicted the heat transfer coefficient based on the boundary layer thickness by the following equations:

$$x_0 = \left(\frac{\delta_{99}}{0.37}\right)^{1.25}\left(\frac{\rho U_\infty}{\mu}\right)^{0.25} \tag{A.5}$$

$$Nu_x = \frac{h_0 x}{k} = 0.0296 Re_x^{4/5} Pr^{1/3} \tag{A.6}$$

The first equation predicts the effective start length, x_0, from the boundary layer thickness, δ_{99}. Because the approach flow was tripped to produce a thick turbulent boundary layer, the correct value of x to use in Equation A.5 was no longer the distance from the leading edge over which the boundary layer had developed, so x represents the development distance necessary to produce the approach boundary layer.

Of course, the heat transfer coefficient with film cooling, h_f, should be used to determine the conduction correction, and not the heat transfer coefficient without film cooling h_0. However, absent any measurement of h_f, the substitution of h_0 made sense for the axial holes, particularly since Boyd *et al* [48] measured $h_f/h_0 \approx 1.0$ for axial plenum-fed 7-7-7 holes.

For the conditions where h_f/h_0 was measured for the compound angle holes, the heat transfer augmentation was used to calculate h_f by multiplying h_f/h_0 by the value of h_0 from the correlation. The assumption for that method was that the h_0 from the correlation was more accurate in the near-hole region than the measured h_0 value from the experiment. The reason for this assumption was that because the heat flux plate started at $x/d = 0$, h_0 would too high due to the starting of the thermal boundary layer – recall that the h_0 is used to correct the condition where the heat flux plate is off. The inaccuracy introduced by using h_0 from a correlation would be primarily confined to the jet centerline region in the near-hole region (x/d <10) because the issuing jet displaces the upstream thermal boundary layer, resulting in greater heat transfer coefficient immediately downstream of the hole. It is estimated that the error introduced by use of this correlation could be as great as $\delta\eta = 0.03$ in the centerline upstream of $x/d = 5$ but becomes vanishingly small further downstream and in between coolant jets.

Use a measured value of h_f

Using a measured value has the potential to be much more accurate than using a correlation. However, it is also important to use an appropriate measured value. A method that uses a heat flux plate to produce a thermal boundary layer that starts appropriately far

upstream of the holes would be much better suited to produce h_f for this conduction correction. That type of data was not measured for this study.

For conditions where a measured h_f/h_0 was used to determine the appropriate value of h_f, an iterative process was needed to calculate both η and h_f. Because each parameter is required to calculate the other, an initial value of h_0 was assumed to first correct the effectiveness of the compound angle film holes and then the corrected effectiveness was used to calculate h_f, which could then be used to recalculate η. Fortunately, only one iterative pass was needed, as there was very little sensitivity of the conduction correction to the difference between h_0 and h_f. Figure A.5 shows this difference for a profile of effectiveness at x/d = 5. The conduction correction clearly had a significant effect, increasing effectiveness in the centerline and reducing it along the pitch line. However, there was very little difference between using h_f and h_0 to correct the data.

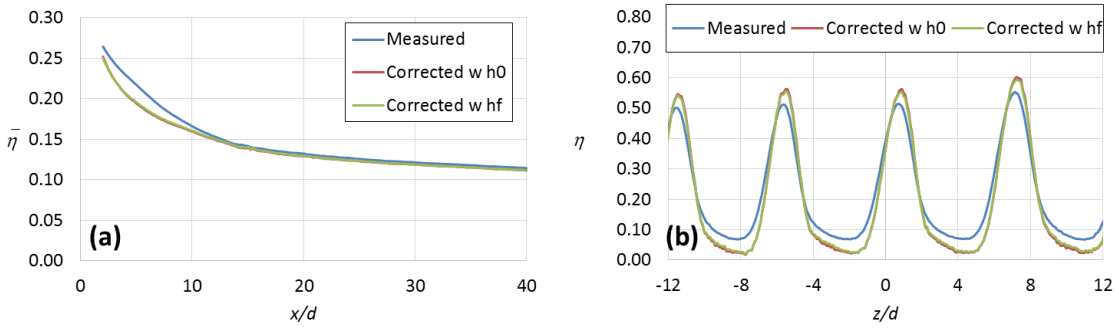

Figure A.5: Effect of applying the conduction correction using h_0 and h_f on (a) laterally averaged η and (b) a lateral profile of η at x/d = 5

A.3 Instructions for Processing Data Using this Technique

The following is a step-by-step tutorial for using Comsol and Matlab to correct for conduction. The instructions in this section walk through how to build the Comsol model from scratch and how to set it up for use with the Matlab script that interfaces with the model. It also describes how to run that script and produce outputs. The scripts that perform the final correction step are only briefly discussed as there are a number of different calculations that can be performed depending on the desired output.

A.3.1 Walkthrough for Building a Simple Model for Conduction Corrections

This guide will walk you through the steps of creating a simple flat plate model for use in performing a conduction correction.

Using the Model Wizard

1. Open Comsol
2. The screen should give you the option between creating a blank model or selecting the model wizard. Select the Model Wizard
3. Select 3D
4. In the "Select Physics" screen select "Heat Transfer in Solids" and click "Add". "Heat Transfer in Solids (ht)" should appear in the "Added Physics" box below. Click the green arrow labeled "Study"
5. In the Select Study" screen, click on "Stationary". When you do so, it should appear in the box labeled "Added study". Once you have confirmed that, click "Done" at the bottom of the screen to go to your model.

Comsol User Interface

The user interface screen that you will see when you exit the Model Wizard is shown in Figure A.6. Everything you will need to do can be done through the "Model Builder" menu on the far left of the screen. Currently "Geometry 1" is selected on the Model Builder menu so it shows up in the middle of the screen in the "Geometry" menu, allowing you to make changes to the selected feature. The "Graphics" box on the right of the screen will show the model geometry once the model is built.

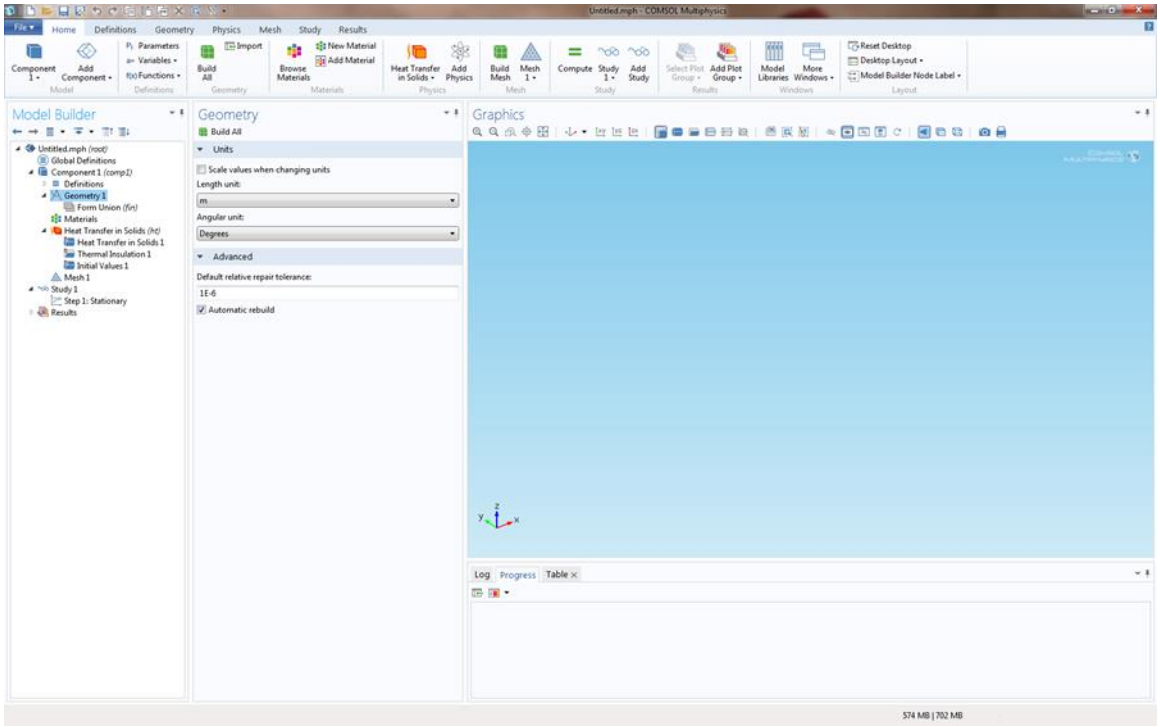

Figure A.6: Screenshot of Comsol for a blank model

Creating the Model Geometry

This section describes how to create the model geometry. This will be a simplified version of the geometry created for this study. This geometry will be designed for the 4 mm axial shaped holes. It will start at x/d = 1.0 and end at x/d = 50. It will be four pitches

wide where p/d = 6. A foam test surface of thickness t = 3d will be assumed with an acrylic baseplate that is 15 mm thick.

1. First create global parameters. Right click on “Global Definitions” in the Model Builder menu and select “Parameters”. This will bring up the “Parameters” menu in the middle box on the screen.
2. Fill out the Parameters menu as shown in Figure A.7. Make sure to use brackets around the units as shown. The description column is for reference purposes only.
3. Create a work plane by right clicking “Geometry 1” and select “Work Plane.” This will bring up the “Work Plane” menu in the middle box
4. In the Work Plane menu, make sure the plane is an *xy* plane (should be set by default). In the “z-coordinate” box enter the equation “zd_start*d” to put the plane at z/d = -12 (z = -48 mm). Figure A.8 shows how this screen should be filled out
5. Create the test coupon. Right click on “Plane Geometry” and selecting “Rectangle”. Fill out the Rectangle menu in the center box as shown in Figure A.9 (a). Click “Build Selected” at the top of the Rectangle menu to create the rectangle. Right click on “Rectangle 1” and select “Properties” to rename it.
6. Repeat step 6 to create another rectangle for the acrylic plate by entering the geometry specifications shown in Figure A.9 (b).
7. Right click on “Work Plane 1” and select “Extrude”. Under “Distances from Plane” enter “zd_width*d”. Then click “Build All Objects: on the top of the Extrude menu. This should build a three-dimensional geometry of two rectangular prisms stacked

on top of each other as desired. You can rotate the view by clicking and dragging in the Graphics box.

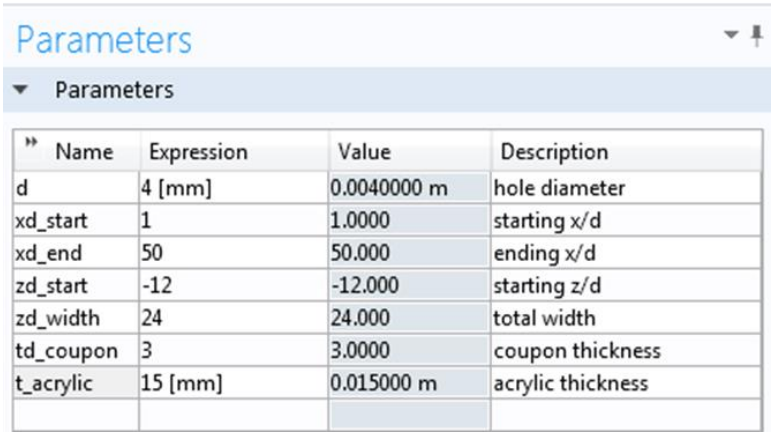

Name	Expression	Value	Description
d	4 [mm]	0.0040000 m	hole diameter
xd_start	1	1.0000	starting x/d
xd_end	50	50.000	ending x/d
zd_start	-12	-12.000	starting z/d
zd_width	24	24.000	total width
td_coupon	3	3.0000	coupon thickness
t_acrylic	15 [mm]	0.015000 m	acrylic thickness

Figure A.7: Global parameters to use for model building

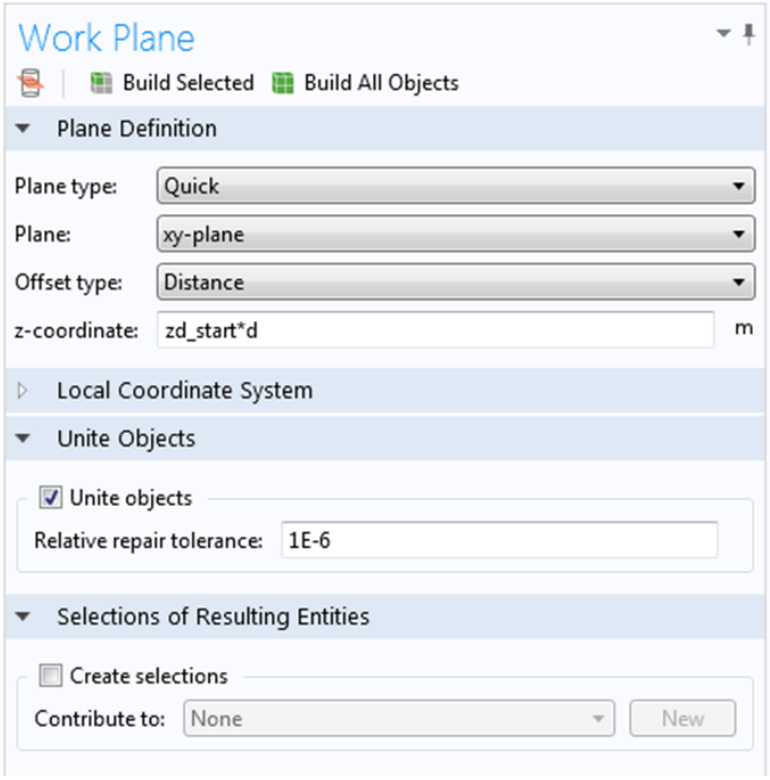

Figure A.8: Create an *x*-*y* work plane at *z*/*d* = -12

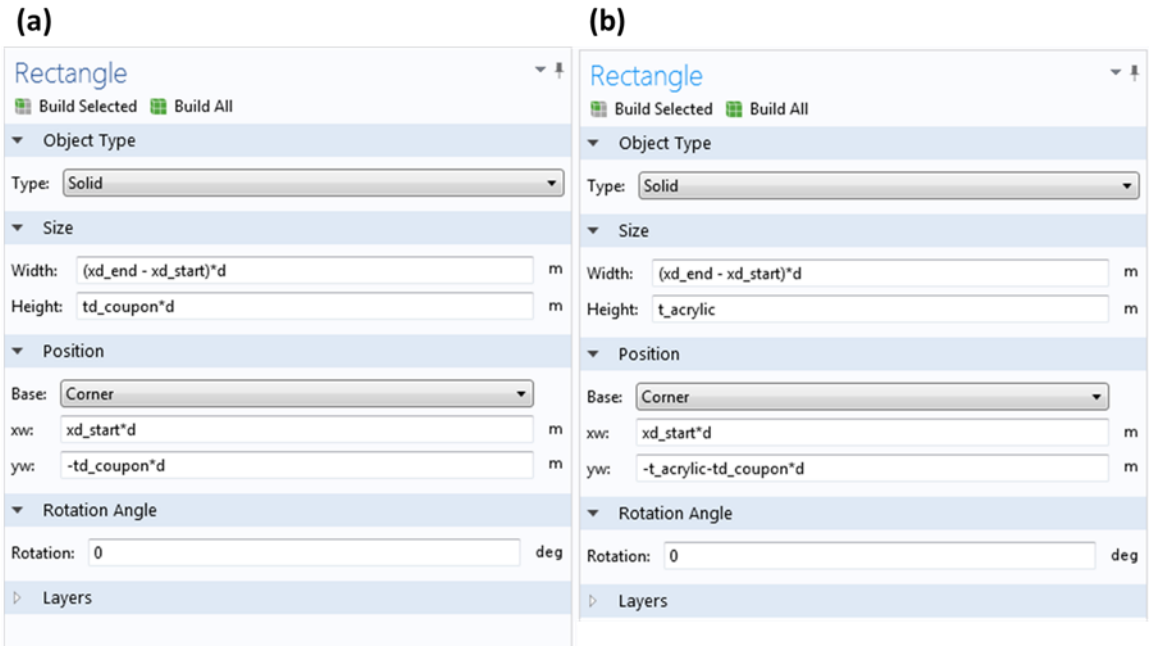

Figure A.9: Settings for creating rectangles to define (a) the test coupon and (b) the acrylic plate

Defining Material Properties

You will need to define new materials for each layer. Comsol will ask for the thermal conductivity, density, and constant pressure specific heat of each material. The materials used for this example have thermal conductivity as shown previously in Table A.1. The density and specific heat will not affect the solution because this is a steady state solver but Comsol still requires them.

1. To create a new material, right click on "Materials" in the Model Builder menu and select "New Material" which will create a new material, "Material 1" and open the Material menu in the middle box.
2. Enter in the property data for the polyurethane foam as shown in Figure A.10. I used ρ = 240 kg/m^3 and c_p = 4730 J/(kg·K). The first material you create is

automatically assigned to the whole model. This is indicated by the whole geometry being highlighted in purple.

3. Create a second material. First click on the bottom section of the geometry in the Graphics window. This will override the initial assignment of the foam to that region. You should see only the bottom part of the model highlighted.
4. Enter the properties for acrylic. I used ρ = 1190 kg/m^3 and c_p = 1470 J/(kg·K).
5. Once you have assigned acrylic to the bottom part of the model, if you select the foam you will see only the top of the model highlighted and a note in the "Selection" box that this material was overridden.

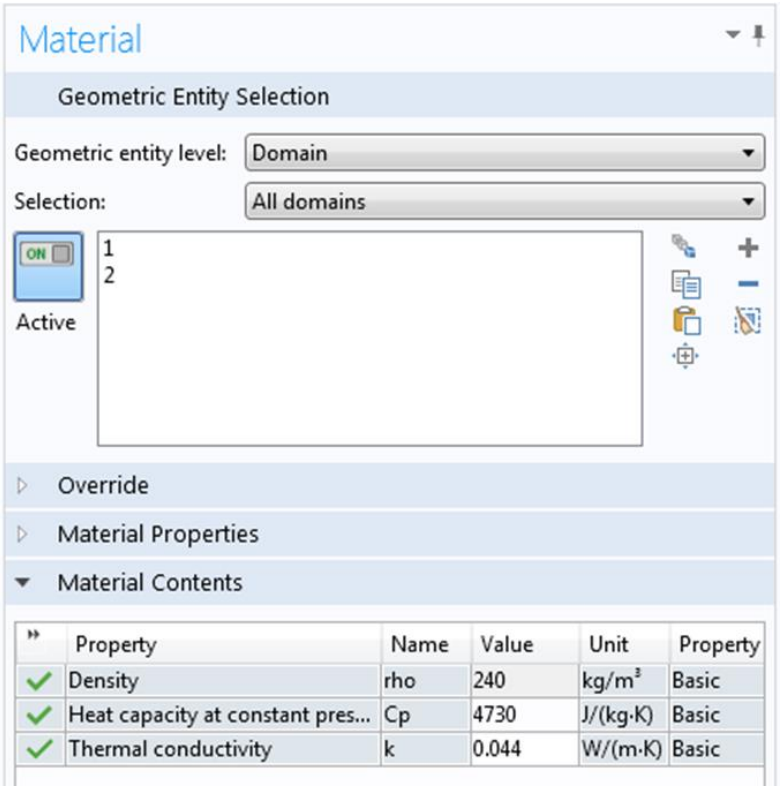

Figure A.10: Defining material properties for the closed-cell polyurethane foam

Importing Surface Temperature Data

You will need to import the measured surface temperature distribution to perform the conduction correction. To do so, you will need to have a tab-delimited text file with data in three columns – the x and z locations in meters in the first two columns and the corresponding temperature data in the third column. It is easier if all location data is in meters and all temperature data is in Kelvins. If you import data in terms of x/d, z/d, and η, you will have to use equations to convert to quantities that have units. This guide will discuss how to import the data in meters and Kelvins. Note that this process is demonstrated here to familiarize you with how the data is imported into Comsol and so you can run the solver manually. A Matlab script, described later, written to call Comsol automates this process.

1. Right click on "Global Definitions", move the mouse over "Functions", and select "Interpolation". This will open the Interpolation window in the middle box.
2. Change the "Data source" to "File".
3. Click "Browse" and select the text file to import. Comsol should automatically recognize that the number of arguments is 2. Set the "Data format" to "Spreadsheet"
4. Click "Import" to import the data file.
5. Under "Units" enter "m" and "K" for "Arguments" and "Function" respectively.
6. Figure A.11 shows how the Interpolation window should look when you have done this correctly

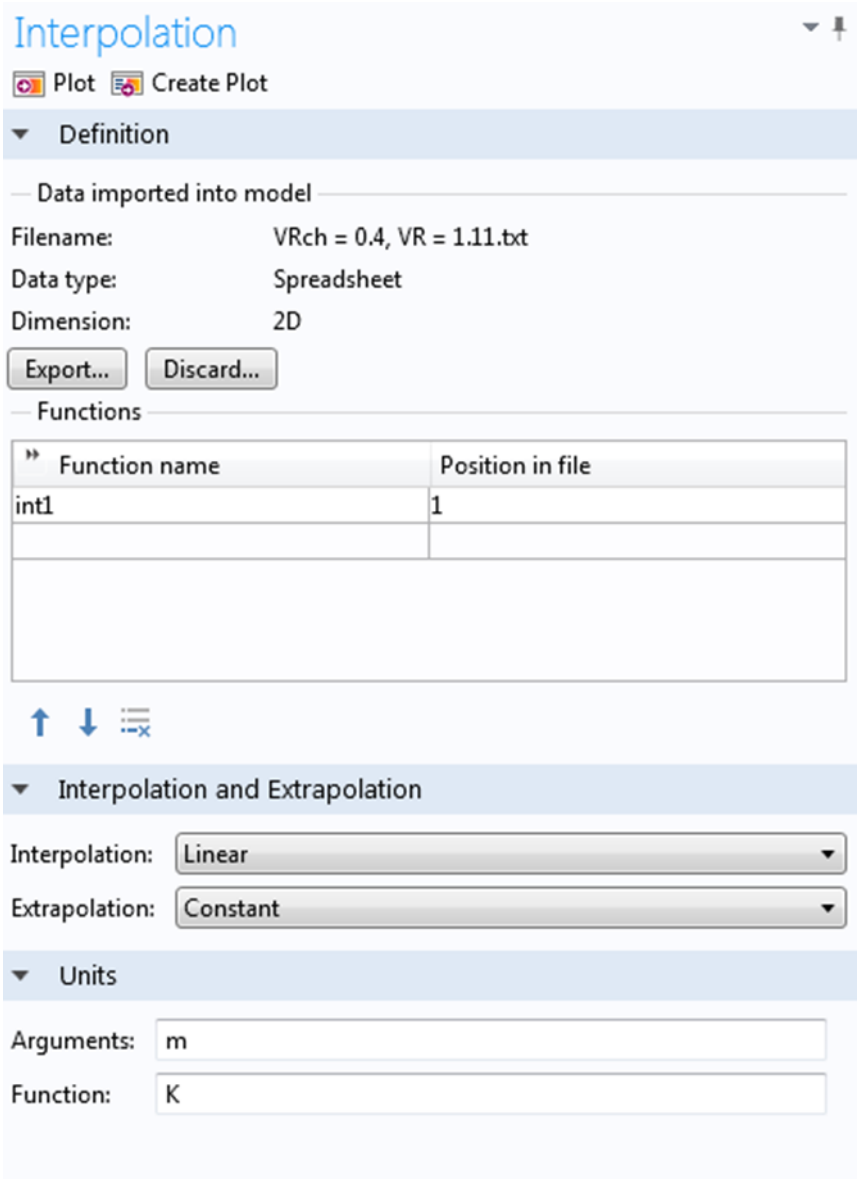

Figure A.11: Interpolation window after importing the text file

Define the Boundary Conditions

The default boundary conditions for each external surface are insulated boundary conditions (q" = 0). The boundary conditions that you set will override the default condition. You will therefore not need to apply boundary conditions to those for which you want an insulated boundary condition set. The interpolation function that was defined based on the 2D temperature distribution will be applied as a temperature boundary condition to the top surface. A natural convection boundary condition will be applied to the bottom surface.

1. Right click on "Heat Transfer in Solids" and select "Temperature" to set up the top surface boundary condition.
2. Click on the top surface in the Graphics window. The surface should become highlighted
3. In the box labeled "Temperature" enter the function call "int1(x,z)" as shown in Figure A.12 (a). The function *int1* is the interpolation function created earlier as seen in parentheses next to its listing in the Model Builder menu.
4. Right click on "Heat Transfer in Solids" and select Convective Heat Flux" to create the bottom boundary condition.
5. Select the bottom surface in the Graphics window, which should highlight it
6. This example will use a user-defined heat transfer coefficient, although Comsol can be used to model natural convection in the "Heat transfer coefficient" drop-down menu. Enter h = 5 W/(m^2·K) and T_{ext} = 298 K as shown in Figure A.12 (b).

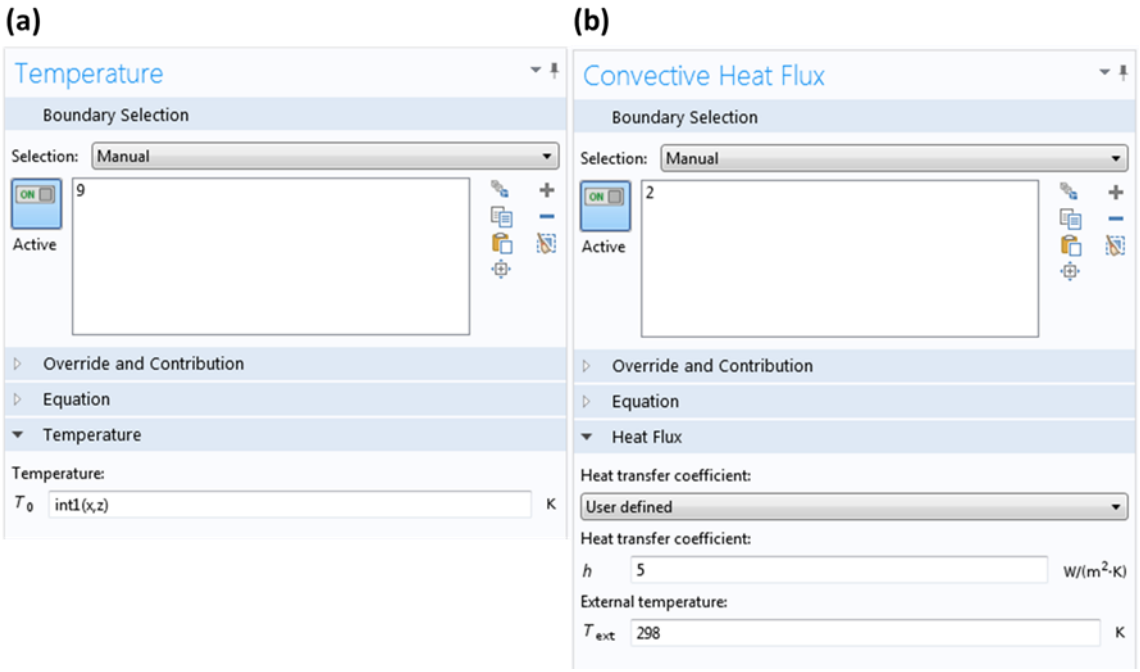

Figure A.12: Boundary conditions for (a) the top surface and (b) the bottom surface

Create the Mesh

The mesh used in this study had different resolution at different streamwise locations. To do that would require different geometric entities for the top surface, which this model does not have. For the sake of simplicity, this example will use a top surface mesh resolution of 1mm while the rest of the model will have a resolution of 4 mm.

1. Create the top surface mesh. Right click on "Mesh 1" in the Model Builder menu, hover the mouse over "More Operations" and select "Free Triangular". This will create the mesh "Free Triangular 1"
2. Select "Free Triangular 1" and click on the top surface to apply the mesh to that surface. The top surface should be highlighted.

3. Right click on “Free Triangular 1” and select “Size” This will create “Size 1”
4. Figure A.13 (a) shows the sizing parameters used. First click on “Custom” under “Element Size”. Comsol has a number of generic built in mesh sizes, but none of them are fine enough. Make sure to check the box next to the element size parameters you want to modify.
5. There is considerable room to understand these meshing parameters better. Hitting F1 on the keyboard brings up a Help menu on the right of the screen if you have questions about the parameters.
6. Click “Build Selected” to generate the top surface mesh. The mesh will appear once it is generated. It will be rather fine so you may have to zoom in to see the individual elements.
7. Now create the mesh for the rest of the model. Right click “Mesh 1” and select “Free Tetrahedral”. This will create “Free Tetrahedral 1” underneath “Free Triangular 1” That order is important as it will determine the order in which the mesh gets built. You should always make surface meshed before the body meshes.
8. If you select “Free Tetrahedral 1” you will see that the Geometric entity level is set to “Remaining”. This means that it will apply this mesh to everything that does not have a mesh assigned to it.
9. Right click on “Free Tetrahedral 1” and select “Size” to create and new Size feature
10. As for the top surface mesh, you will want to set the size of the mesh. Figure A.13 (b) shows the sizing parameters used.

11. Select “Mesh 1” and click “Build All” to generate the mesh. The mesh will display when it is complete. You will see affine mesh on the top surface that becomes coarser as it moves away from the top surface.
12. To see the mesh statistics, right click on “Mesh 1” and select “Statistics”

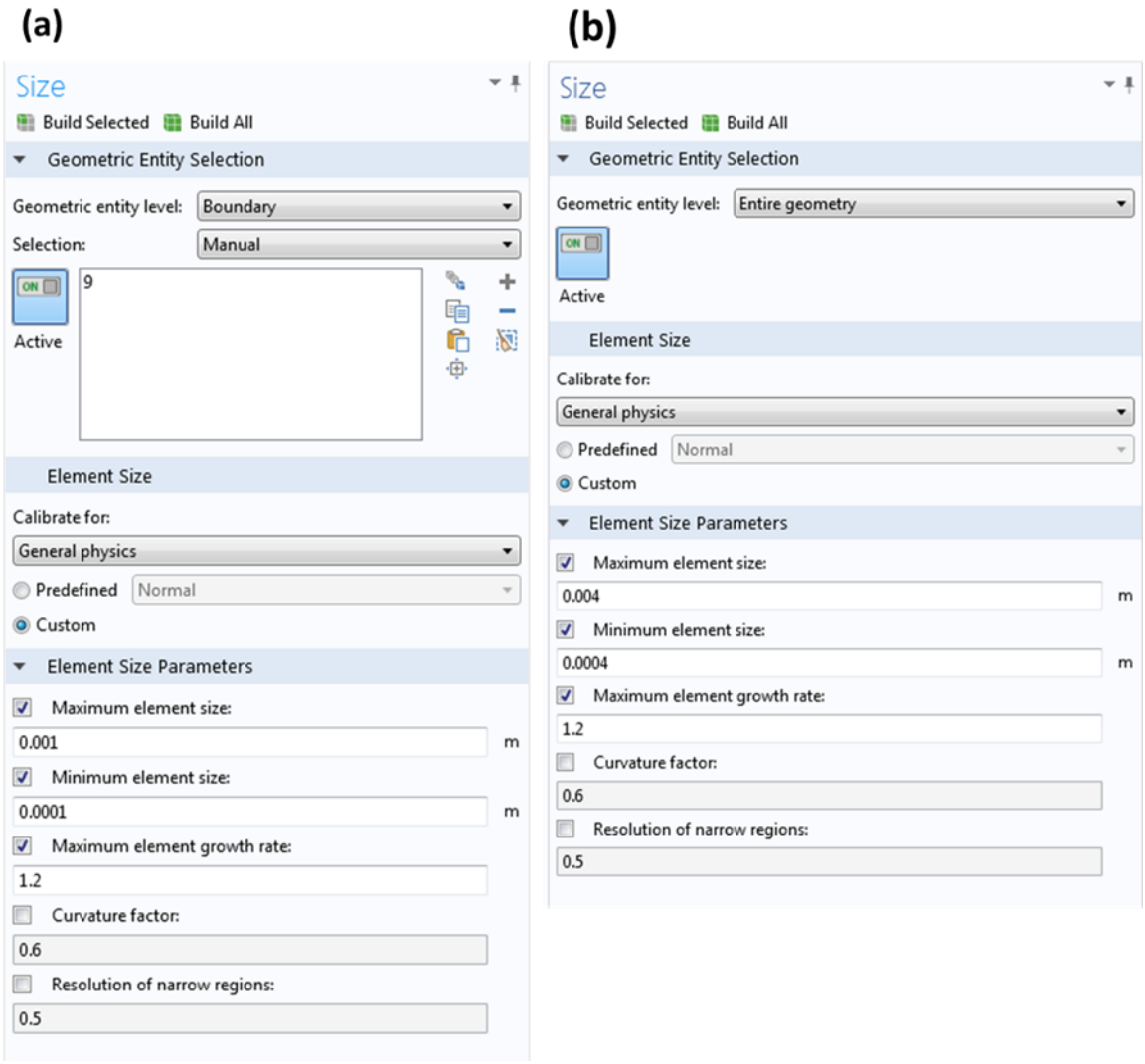

Figure A.13: Sizing parameters for (a) the top surface mesh and (b) the mesh for the rest of the model

Running and Exporting Data

As with the interpolation for the top surface, the solver will be executed by a Matlab script that automates this process. However, it is worthwhile running the solver in Comsol to get a feel for what the output looks like. It is also necessary to set up how the data will be output from Comsol.

1. Right clock on "Study 1" and select "Compute". The solver should run quickly due to the simple geometry and relatively low resolution mesh.
2. By default, Comsol will show you a plot of the temperature. There are a number of things you can do to plot other parameters. These will not be covered in this guide but are worth exploring.
3. Set up the output. Right click "Export" and select "Data", which will create "Data 1" and open up its menu in the middle box.
4. Figure A.14 shows how the output is set up to export data in this example.
5. First add the desired expressions, which are the interpolated surface temperature and the heat flux in the *y* direction on the top surface. To add the temperature, click the plus sign to the right of the heading "Expressions". This will open a menu with a wide range of options. Expand "Heat Transfer in Solids" then expand "Temperature" and double click on "Temperature (T)". This will add the temperature to the list of expressions below
6. Do the same for the heat flux, except expand "Heat Transfer in Solids" then "Domain Fluxes", then "Conductive Heat Flux" then double click "Conductive Heat Flux, y component (ht.dfluxy)" to add it to the list of expressions

7. Under the Output header, click “Browse” to select the desired output directory and type in the file name you want to save the output under. The file does not have to exist to save it.
8. There are a number of options for “Points to Evaluate in” and “Data format”. For this example, choose “Grid” and “Spreadsheet” respectively.
9. The output grid will cover the full range of x and z in increments of 0.4 mm and only use $y = 0$.
10. Click the data range button to the left of the box for x. This will bring up a window titled “Range” For entry method select “Step”. These values will all be in meters. Set it up to start at 0.004 m, take steps of 0.0004 m, and stop at 0.2 m. Then click “Add”. The desired range will appear in the box next to x.
11. Do the same for z starting at -0.048 m, stepping 0.0004 m, and ending at 0.048 m.
12. For y, set the entry method to “Number of Values”. Set it to start and stop at 0 and enter 1 for number of values.
13. Expand the “Advanced” section. Deselect “Include header” and select “Sort”. The header will make the output text files more difficult to read.
14. At the top of the Data window, click “Export” to export the data to the selected file location

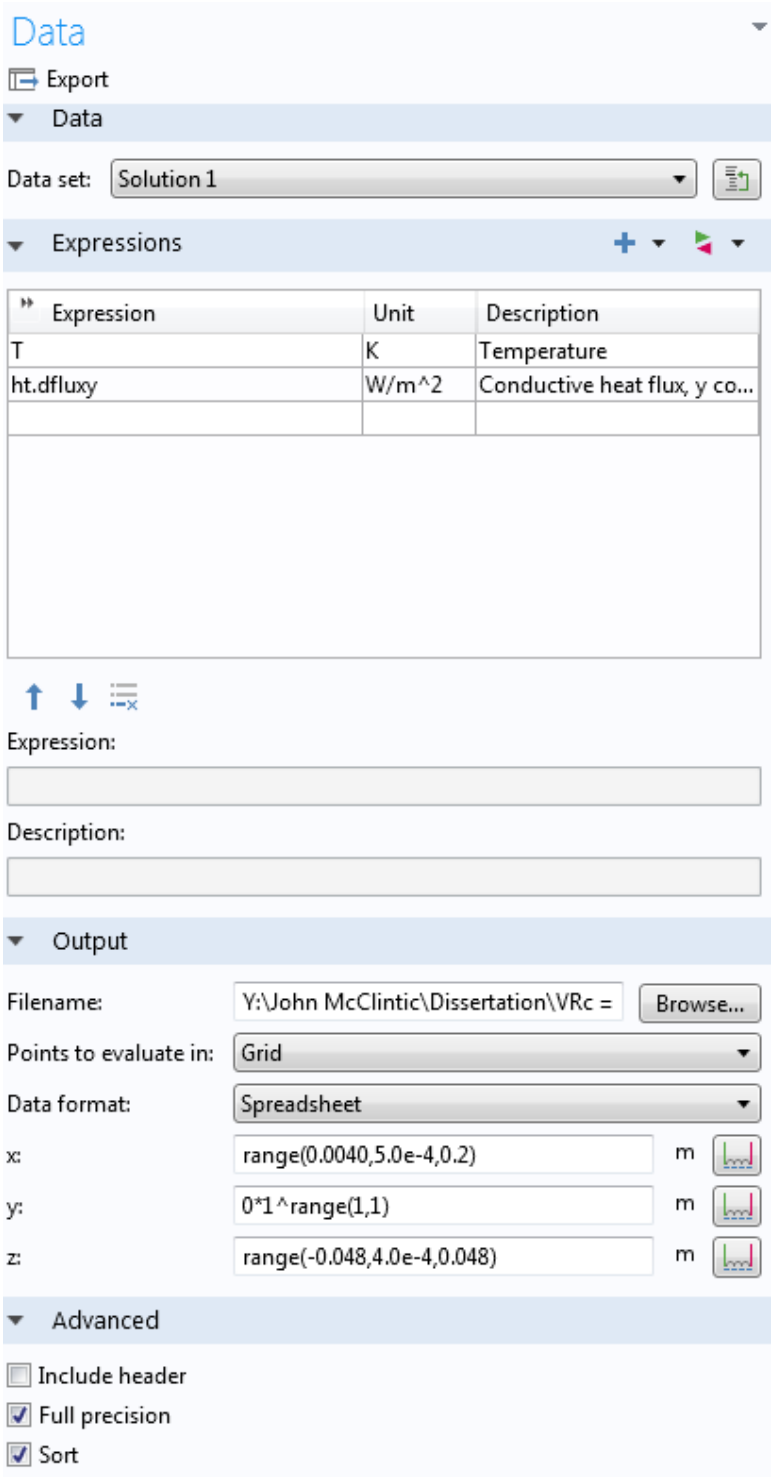

Figure A.14: Data export window set up as described in the instructions

Comsol Models Used in this Study

The models used in this study had finer meshes and more accurately represented the setup of the experimental facility. Table A.2 lists the names models used in this study and what they were used for. All models used for this study can be found in the directory G:\2014\Comsol and are available to those with access to the appropriate drive.

Table A.2: Comsol Models Used in this Study

Model Name	***Used For***
Large Channel 777 4mm mod	Axial 7-7-7 holes
Large Channel 777 5mm	Compound angle 7-7-7 holes film effectiveness
Large Channel 777 5mm HTCA	Compound angle 7-7-7 holes heat transfer coefficient augmentation

A.3.2 Running the Matlab Script to Automate Comsol

A Matlab script was used to automatically import the solution file, set boundary conditions, and export the data. The script is called comproc.m and has a corresponding Excel file comproc_input.xlsx. To use the script, you must first have a Comsol model set up as described above as well as (x, z, T) data in tab delimited text files. These files must be saved in the same directory as comproc and its Excel input file.

Open Matlab and Connect to the Comsol Server

You will need to set up Matlab such that it can communicate with Comsol.

1. Open Comsol Multiphysics 4.4 Server. This will open a command window that will indicate that it “started listening on port 2036”
2. Open Matlab
3. Set the current directory to C:\Program Files\COMSOL\COMSOL44\mli

4. In the Matlab command window enter `mphstart(2036)`. Once this has run successfully, the Comsol server command window will indicate that you have logged onto the server using port 2036. The command window will ask you for a username and password if this is your first time connecting to the server with your user account. Enter in the user name and password you use for your user account on the computer. You will not be asked for your password again.
5. Open *comproc* and set the run directory to the folder containing the script, input file, and text files.

Setup the Input File

The input Excel file, comproc_input.xlsx, is used to tell comproc which text files to read and which Comsol model to use. It has two tabs called "Conditions" and "Comsol Model"

1. In the Conditions tab, enter the names of the text files in the "File Names" column without the ".txt" appended to the file name. For each point, enter the corresponding mainstream and coolant temperature as well as the internal channel heat transfer coefficient.
2. In the Comsol Model tab, enter the desired Comsol model name without the ".mph" appended to it. The model directory will be updated in *comproc*
3. The remaining fields, except "Init. Interp" are derived from the Comsol model you will use. If you right click on "Study 1" in the Model Builder window in Comsol and select "Properties" you will open a Properties window. In that window, next to "Tag:" you will see "std1". This is the name that Comsol uses to identify the

study. That is the identifier that you want to enter into the Excel file for each field. You will probably only have to change the tags associated with the boundary conditions. Note that the model in the previous example did not have a coolant boundary condition and currently won't work with *comproc* without modification to either the model or Matlab code.

4. The "Init. Interp." Cell should be set to 1. This has *comproc* create a new interpolation function called by the name you give it in the "Interp Function" field. It is best to have Matlab create an interpolation function with a different tag than the one in model to avoid a whole host of potential errors.

Run the Matlab Script

1. First update the directories at the top of the script
    a. "dir_comsol" is the directory of the Comsol model. Make sure to end the string with a '\'
    b. "dir_output" is the save directory for the output files. The output files will be given the same name as the input files so make sure to save them in a different folder so you don't overwrite the input files.
2. Run *comproc*. This will likely take a few minutes per condition if you use a more complicated model than the example given above. The script will launch a progress window that shows the progress of solving each condition.

3. The output files will be of the same format as those output manually in the above example – a five column matrix with columns corresponding to x (m), y (m), z (m), T (K), and q'' (W/m^2) respectively.

Text of comproc.m

```
function comproc()

%-------------------------------------------------------------------------
----
% UPDATE THE DIRECTORY FOR THE COMSOL MODEL AND DATA OUTPUT

dir_comsol = 'W:\2014\Comsol\';
dir_output = 'W:\2014\1 Cross-Flow Project\Experiments 2016\161019
Reprocess\Comsol Process\';
%-------------------------------------------------------------------------
---
% This program works with the Comsol LiveLink for MatLab to run Comsol
% conduction simulations for measured surface temperature distributions
for
% the purpose of performing a three-dimensional conduction correction.
The
% conduction analysis requires a case without film cooling, "eta0", and
% cases with different film cooling configurations, "etam".
%
% The input files are:
%   comproc_input.xlsx - User input for blowing conditions and Comsol
model
%                        parameters
%   condition.txt - tab delimited text file providing surface positions
in
%                   meters and corresponding surface temperatures in
Kelvin
%
% The output files are:
%   condition.txt - text files providing location data in mm, surface
%                   temperatures in K, and surface heat flux in W/m^2
%
% Written By: John McClintic
% Date: 1/30/2014
%
% Revision Log:
%   2/11/14 JWM Removed the relianace on using eta0 to predict h0
%
%-------------------------------------------------------------------------
---
```

```
% Set up the computation
%-------------------------------------------------------------------------
---

fprintf('\n Setting up the computation... \n\n');

% Import Comsol library functions
import com.comsol.model.*
import com.comsol.model.util.*

% Turn on progress bar for Comsol solutions
ModelUtil.showProgress(true);

% Read input file
[nums, text] = xlsread('comproc_input_R.xlsx', 'Conditions');
[num2, text2] = xlsread('comproc_input_R.xlsx', 'Comsol Model');

% Text inputs
conditions = text(2:end,1);
Nc = length(conditions);

% Number Inputs
Tinf = nums(:,1);
Tc = nums(:,2);
hch = nums(:,3);

% Comsol Model Inputs
model_name = cell2mat(text2(1,2));
study_name = cell2mat(text2(2,2));
heat_transfer = cell2mat(text2(3,2));
coolant_BC = cell2mat(text2(4,2));
top_surf_BC = cell2mat(text2(5,2));
etam_Interp = cell2mat(text2(6,2));
export_data = cell2mat(text2(7,2));
init_interp = num2;

% Load Comsol Model
model_str = [dir_comsol model_name];
model = mphload(model_str);

% Physics Model - set MatLab variable names
std1 = model.study(study_name); % study name
ht = model.physics(heat_transfer); % heat transfer in solids
cool_temp = ht.feature(coolant_BC); % colant boundary condition
surf_temp = ht.feature(top_surf_BC); % top surface boundary condition

% Set MatLab variable
data1 = model.result.export(export_data);
```

```
data2 = model.result.export('data2');

% Run blowing conditions
%-----------------------------------------------------------------------
---

% Define/initialize interpolation function
if init_interp == 1
    etam = model.func.create(etam_Interp, 'Interpolation');
else
    etam = model.func(etam_Interp);
end

for i = 1:Nc

    fprintf(['\n Running blowing condition ' num2str(i) ' of '
num2str(Nc) '... \n\n'])

    % Read input data for interpolation function
    etam_str = [cell2mat(conditions(i)) '.txt'];
    etam.set('filename', etam_str);

    % Apply Boundary Conditions
    Tc_m = Tc(i);
    h_m = hch(i);
    cool_temp.set('Text', 1, num2str(Tc_m));
    cool_temp.set('h',1,num2str(h_m));
    surf_temp.set('T0',1,[etam_Interp '(x,z)']);

    % Compute
    std1.run

    % Export data as text file
    eta_save_str = [dir_output cell2mat(conditions(i)) '.txt'];

    data1.set('filename',eta_save_str);
    data1.run

%     temp_save_str = [dir_output cell2mat(conditions(i)) '_bot.txt'];
%     data2.set('filename',temp_save_str);
%     data2.run
end

% Save Comsol Model
%fprintf('\n Saving Comsol Model... \n\n');
%mphsave(model)

fprintf('\n Finished \n\n');
```

References

[1] Langston L. S., 2015, "Each Blade is a Single Crystal," *American Scientist*, **103**(1), pp. 30.

[2] Bogard, D. G. and Thole, K. A., 2006, "Gas Turbine Film Cooling," *J. Propulsion and Power*, **22**(2), pp. 249-270.

[3] Han J. C, Dutta, S., and Ekkad, S. V, 2000, *Gas Turbine Heat Transfer and Cooling Technology*, 1st ed. New York, USA: Taylor & Francis.

[4] Dees, J. E., 2010, "Experimental Measurements of Conjugate Heat Transfer on a Scaled-up Gas Turbine Airfoil with Realistic Cooling Configuration," The University of Texas at Austin, TX, USA, Ph.D. Dissertation.

[5] Wilkes, E. K., Anderson, J. B., McClintic, J. W., and Bogard, D. G., 2016, "An Investigation of Turbine Film Cooling Effectiveness with Shaped Holes and Internal Cross-Flow with Varying Operational Parameters," ASME Paper No. GT2016-56162.

[6] Greiner, N. J., Polanka, M. D., and Rutledge, J. L., 2015, "Scaling of Film Cooling Performance from Ambient to Engine Temperatures," *J. Turbomach*, **137**(7), pp. 071007.

[7] Thole, K. A., Sinha, A., Bogard, D. G., and Crawford, M. E., 1992, "Mean Temperature Measurements of Jets with a Crossflow for Gas Turbine Film Cooling Application," *Rotating Machinery Transport Phenomena*, edited by J.H. Kim and W. J. Yang, Hemisphere, NY, pp. 69-85.

[8] Harrison, K. L. and Bogard, D. G., 2008, "Use of the Adiabatic Wall Temperature in Film Cooling to Predict Wall Heat Flux and Temperature," ASME Paper No. GT2008-51424.

[9] Williams, R. P., Dyson, T. E., Bogard, D. G., and Bradshaw, S. D., 2012, "Sensitivity of the Overall Effectivness to Film Cooling and Internal Cooling on a Turbine Vane Suction Side," ASME Paper No. GT2012-69110.

[10] Bunker, R. S., 2005, "A Review of Shaped Hole Turbine Film-Cooling Technology," *J. Heat Transfer*, **127**, pp. 441-453.

[11] Schroeder, R. P. and Thole, K. A., 2014, "Adiabatic Effectiveness Measurements for a Baseline Shaped Film Cooling Hole," ASME Paper No. GT2014-25992.

[12] Gritsch, M., Schulz, A., and Wittig, S., 2003, "Effect of Internal Coolant Crossflow on the Effectiveness of Shaped Film-Cooling Holes," *J. Turbomach.*, **125**, pp. 547-554.

[13] Gritsch, M., Schulz, A., and Wittig, S., 1998, "Adiabatic Wall Effectiveness Measurements of Film-Cooling Holes with Expanded Exits," *J. Turbomach.*, **120**, pp. 549-556.

[14] Saumweber, C. and Schulz, A., 2008, "Comparison of the Cooling Performance of Cylindrical and Fan-Shaped Cooling Holes with Special Emphasis on the Effect of Internal Coolant Cross-Flow," ASME Paper No. GT2008-51036.

[15] Saumweber, C. and Schulz, A., 2012, "Effect of Geometry Variations on the Cooling Performance of Fan-Shaped Cooling Holes," *J. Turbomach.*, **134**, p.061008.

[16] Peng, W. and Jiang, P. X., 2012, "Experimental and Numerical Study of Film Cooling with Internal Coolant Cross-Flow Effects," *J. Exp. Heat Transfer*, **25**, pp. 282-300.

[17] Taslim, M. E. and Khanicheh, A., 2005, "Film Effectiveness Downstream of an Row of Compound Angle Holes," *J. Heat Transfer*, **127**, pp. 434-440.

[18] Bell, C. M., Hamakawa, H., and Ligrani, P. M., 2000, "Fim Cooling from Shaped Holes," *J. Heat Transfer*, **122**, pp. 224-232.

[19] Ganzert, W., Hildebrandt, T., and Fottner, L., 2000, "Systematic Experimental and Numerical Investigations on the Aerothermodynamics of a Film Cooled Turbine Cascade with Variation of the Cooling Hole Shape, Part I: Experimental Approach," ASME Paper No. 2000-GT-295.

[20] Dittmar, J., Schulz, A., and Wittig, S., 2002, "Assessment of Various Film Cooling Configurations Including Shaped and Compound Angle Holes Based on Large Scale Experiments," ASME Paper No. GT-2002-30176.

[21] McClintic, J. W., Klavetter, S. R., Winka, J. R., Anderson, J. B., Bogard, D. G., Dees, J. E., Laskowski, G. M., and Briggs, R., 2015, "The Effect of Internal Crossflow on the Adiabatic Effectiveness of Compound Angle Film Cooling Holes," *J. Turbomach.*, **137**, p.071006.

[22] Hay, N., Lampard, D., and Benmansour, S., 1983, "Effect of Crossflows on the Discharge Coefficient of Film Cooling Holes," *J. Eng. Power*, **105**, pp. 243-248.

[23] Bunker, R. S. and Bailey, J. C., 2000, "Film Cooling Discharge Coefficient Measurements in a Turbulated Passage with Internal Cross Flow," ASME Paper No. 2000-GT-0135.

[24] Gritsch, M., Saumweber, C., Schulz, A., Wittig, S., and Sharp, E., 2000, "Effect of Internal Coolant Crossflow Orientation on the Discharge Coefficient of Shaped Film-Cooling Holes," *J. Turbomach.*, **122**, pp. 146-152.

[25] Pietzryk, J. R., Bogard, D. G., and Crawford, M. E., 1989, "Hydrodynamic Measurements of Jets in Crossflow for Gas Turbine Applications," *J. Turbomach.*, **111**, pp. 139-145.

[26] Pietzryk, J. R., Bogard, D. G., and Crawford, M. E., 1989, "Effects of Density Ratios on the Hydrodynamics of Film Cooling," ASME Paper No. 89-GT-175.

[27] Leylek, J. H., and Zerkle, R. D., 1994, "Discrete-Jet Film Cooling: A Comparison of Computational Results with Experimnents," *J. Turbomach.*, **116**, pp. 358-368.

[28] Issakhanian, E., Elkins, C. J., and Eaton, J. K., 2012, "In-Hole and Mainflow Velocity Measurements of Low-Momentum Jets in Crossflow Emanating from Short Holes," *J. Exp. Fluids*, **53**, pp. 1765-1778.

[29] Hyams, D. G. and Leylek, J. H., 1997, "A Detailed Analysis of Film Cooling Physics Part III: Streamwise Injection with Shaped Holes," ASME Paper No. 97-GT-271.

[30] Brittingham, R. A. and Leylek, J. H., 1997, "A Detailed Analysis of Film Cooling Physics Part IV: Compound-Angle Injection with Shaped Holes," ASME Paper No. 97-GT-272.

[31] Oliver, T. A., Anderson, J. B., Bogard, D. G., Moder, R. D., and Laskowski, G., 2017, "Implicit LES for Shaped-Hole Film Cooling Flow," ASME Paper No. GT2017-63314.

[32] Lloyd, S. and Brown, A., 1986, "Velocity and Turbulence Fields in Pipe Entrance Regions in the Presence of Cross Flows," *J. Eng. Gas Turbines and Power*, **108**, pp. 498-503.

[33] Thole, K. A., Gritsch, M., Schulz, A., and Wittig, S., 1998, "Flowfield Measurements for Film-Cooling Holes with Expanded Exits," *J. Turbomach.*, **120**, pp. 327-336.

[34] Peterson, S. D. and Plesniak, M. W., 2002, "Short-Hole Jet-in-Crossflow Velocity Field and its Relationship to Film-Cooling Performance," *J. Exp. Fluids*, **33**, pp. 889-898.

[35] Peterson, S. D. and Plesniak, M. W., 2004, "Evolution of Jets Emanating from Short Holes into Crossflow," *J. Fluid Mech.*, **503**, pp. 57-91.

[36] Peterson, S. D. and Plesniak, M. W., 2007, "Flow Structure and Skin Friction in the Vicinity of a Streamwise-Angled Injection Hole Fed by a Short Pipe," *J. Exp. Fluids*, **43**, pp. 627-638.

[37] Kohli, A. and Thole, K. A., 1998, "Entrance Effects of Diffused Film-Cooling Holes," ASME Paper No. 98-GT-402.

[38] Crabb, D., Durao, D. F. G., and Whitelaw, J. H., 1981, "A Round Jet Normal to a Crossflow," *J. Fluids Eng*, **103**, pp. 142-153.

[39] Andreopoulos, J. and Rodi, W., 1984, "Experimental Investigation of Jets in a Crossflow," *J. Fluid Mech.*, **138**, pp. 93-127.

[40] Kelso, R. M., Lim, T. T., and Perry, A. E., 1996, "An Experimental Study of Round Jets in Cross-flow," *J. Fluid Mech.*, **306**, pp. 111-114.

[41] Haven, B. A., Yamagata, D. K., Kurosaka, M., Yamawaki, S., and Maya, T., 1997, "Anti-Kidney Pair of Vortices in Shaped Holes and their Influence on Film Cooling Effectiveness," ASME Paper No. 97-GT-45.

[42] Berger, P. A. and Liburdy, J. A., 1998, "A Near-Field Investigation into the Effects of Geometry and Compound Angle on the Flowfield of a Row of Film Cooling Holes," ASME Paper No. 98-GT-279.

[43] Schroeder, R. P. and Thole, K. A., 2015, "Effect of High Freestream Turbulence on Flowfields of Shaped Film Cooling Holes," ASME Paper No. GT2015-43339.

[44] McClintic, J. W., Dyson, T. E., Bogard, D. G., and Bradshaw, S. D., 2013, "Mean and Turbulent Velocity Profile Measurements on the Suction Side of a Film Cooled Turbine Vane," ASME Paper No. GT2013-94931.

[45] Anderson, J. A., Wilkes, E. K., McClintic, J. W., and Bogard, D. G., 2016, "Effects of Freestream Mach Number, Reynolds Number, and Boundary Layer Thickness on Film Cooling Effectiveness of Shaped Holes," ASME Paper No. GT2016-56512.

[46] Moffat, R. J., 1985, "Using Uncertainty Analysis in the Planning of an Experiment," *J. Fluids Eng.*, **107**, pp. 173-178.

[47] Klavetter, S. R., McClintic, J. W., Bogard, D. G., Dees, J. E., Laskowski, G. M., and Briggs, R., 2015, "The Effect of Rib Turbulators on Film Cooling Effectiveness

of Round Compound Angle Holes Fed by an Internal Cross-Flow," ASME Paper No. GT2015-43947.

[48] Boyd, E. J., McClintic, J. W., Chavez, K. F., and Bogard, D. G., 2014, "Direct Measurement of Heat Transfer Coefficient Augmentation at Multiple Density Ratios," *J. Turbomach.,* **139**, pp. 011005.

[49] Stewart, W. R. and Bogard, D. G., 2015, "Experimental Thermal Field Measurements of Film Cooling Above the Suction Surface of a Turbine Vane," *J. Eng. Gas Turbines Power*, **137**, pp. 102604.

[50] Dyson, T. E., McClintic, J. W., Bogard, D. G., and Bradshaw, S. D., 2013, "Adiabatic and Overall Effectiveness for a Fully Cooled Turbine Vane," ASME Paper No. GT2013-94928.

[51] Tavoularis, S., 2005, *Measurement in Fluid Mechanics*, New York, USA: Cambridge University Press.

[52] Anderson, J. B., Boyd, E. J., and Bogard, D. G., 2015, "Experimental Investigation of Coolant-to-Mainstream Scaling Parameters with Cylindrical and Shaped Film Cooling Holes." ASME Paper No. GT2015-43072.

[53] Anderson, J. B., McClintic, J. W., Bogard, D. G., Dyson, T. E., and Webster, Z. D., 2017, "Freestream Flow Effects of Film Effectiveness and Heat Transfer Coefficient Augmentation for Compound Angle Shaped Holes," ASME Paper No. GT2017-64853.

[54] Davidson, F. T., Kistenmacher, D. A., and Bogard, D. G., 2014, "Film Cooling with a Thermal Barrier Coating: Round Holes, Craters, and Trenches," *J. Turbomach.*, **136**(4), pp. 041007.

Vita

John McClintic grew up in Katy, Texas and graduated from James E. Taylor High School in May 2007. He attended Baylor University in Waco, Texas and received his Bachelor of Science in mechanical engineering in 2011. Shortly afterward he made the short (in terms of geographic distance) but long (in terms of hours spent on I35 and cultural differences) trip to Austin, Texas to begin graduate school. He has worked for Dr. David Bogard as a graduate research assistant studying gas turbine film cooling for almost 6 years. He originally intended to only pursue a master's degree (which he attained in May of 2013), but he enjoyed his research more than he thought he would, so he decided to stick around to get his Ph.D. Among his non-academic contributions to the laboratory, John is perhaps most proud of no one becoming seriously injured/maimed/vaporized during his tenure as Grand Moff of Safety, developing an improved metric for evaluating the quality of football score predictions, coining the term "Taco Tuesday on Wednesday", and the critical role he played in convincing Dr. David Bogard and Dr. Karen Thole [2] to sing karaoke during the 2013 IGTI conference in San Antonio.

Permanent email: johnwmcclintic@gmail.com

This dissertation was typed by the author